

# Development of Hybrid Deterministic–Statistical Models for Irradiation Induced Microstructural Evolution

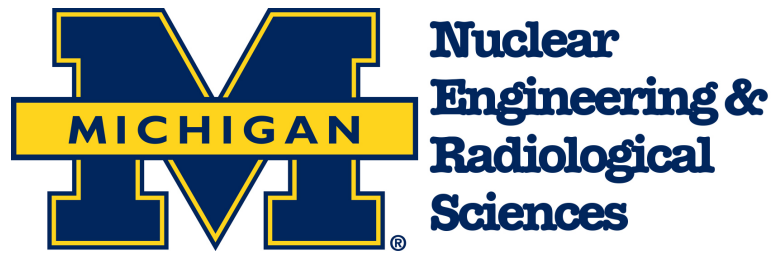
by

Efraín Hernández–Rivera

A dissertation submitted in partial fulfillment  
of the requirements for the degree of  
Doctor of Philosophy  
(Nuclear Engineering and Radiological Sciences)  
in The University of Michigan  
2015

Doctoral Committee:

Professor Lumin Wang, Co–Chair  
Manager Veena Tikare, Co–Chair, Sandia National Laboratories  
Professor Fei Gao  
Professor Wei Lu



© Efraín Hernández-Rivera 2015  

---

All Rights Reserved

To my wife *Lichi*, who has been by my side through all this mess.

## ACKNOWLEDGEMENTS

I am very grateful to Rackham Graduate School, the Department of Nuclear Engineering and Radiological Sciences, the University of Michigan and Sandia National Laboratories for all the financial support and other resources provided throughout my graduate school years. I would not have been able to complete this work without the variety of resources made available to me from all these bodies.

I would like to thank my advisors, Dr. Lumin Wang and Dr Veena Tikare. The flexibility granted by Dr. Wang allowed me to explore research areas well beyond the scope of my original projects. I would also like to acknowledge Dr. Wang's effort in identifying such a unique problem to study, and explaining his experimental observations and their big picture significance. A special thanks goes to Dr. Tikare who agreed to take me under her wing and teach me the basics of computational materials methods. Dr. Tikare gave me an opportunity that most people would not have granted to a person with my scientific background. Without these opportunities, none of this work would have been possible. Further, the amount of time invested in teaching me the ropes on writing manuscripts and presentations are truly appreciated. I would also like to thank my dissertation committee, Dr. Fei Gao and Dr. Wei Lu, for accepting to serve on my doctoral committee and provide feedback on the development of this manuscript.

I would like to thank my colleagues for their assistance and support throughout my years in the doctoral program. My initial years in graduate school allowed me to train in a variety of interesting instruments like transmission electron microscopy.

This training was mostly provided by Pantip Ampornrat and Alex P. Berg. Through my initial tenure at UM, I greatly benefited from the encouragement and conversations with Brian Kitchen, Michael McMurtrey, Eva Sunny and Jonathan Wierschke. Also, I would like to thank Dr. Kundar Li for the discussions on his phase field model and introducing me to computational methods. A most special thank you goes to Peggy Jo Gramer. Whether it was trying to encourage me, helping me out when things looked less than bright or just distracting me during stressful times, Peggy was always there to help.

Extended thanks goes to Cristina Garcia-Cardona, Dr. Fred Gelbard, Dr. Eric Homer, Dr. Steve Plimpton and Dr. Aidan Thompson for their guidance and suggestion on the development and implementation of the C++ models. I am also appreciative of the discussions and friendship provided by my Sandia office neighbors Victor Figueroa, Dr. Carlo Jove and Carlos Lopez.

Lastly, I would like to thank my family. My parents, Efrain and Zory, as well as my brother Jesus and sister Karissa, for their unconditional support and encouragement over the years. My wife, Elizabeth Colon, for her love and patience even in times of stress and uncertainty and my son Armando for giving me perspective during trying times.

In all, thanks to the people who made this dissertation possible, even those who put together a nice L<sup>A</sup>T<sub>E</sub>X template for me to use. Lastly, this work was partly supported by the U.S. Department of Energy's National Nuclear Security Administration under contract DE-AC04-94AL85000 and the Basic Energy Science under contract DE-FG02-02ER46005.

# TABLE OF CONTENTS

DEDICATION . . . . .	ii
ACKNOWLEDGEMENTS . . . . .	iii
LIST OF FIGURES . . . . .	viii
LIST OF TABLES . . . . .	xix
LIST OF APPENDICES . . . . .	xx
LIST OF ABBREVIATIONS . . . . .	xxi
ABSTRACT . . . . .	xxiii
<b>CHAPTER</b>	
<b>I. Introduction and Background . . . . .</b>	<b>1</b>
1.1 Radiation Damage Physics . . . . .	2
1.1.1 Sputtering . . . . .	2
1.1.2 Radiation Induced Segregation . . . . .	7
1.1.3 Radiation Induced Amorphization . . . . .	14
1.1.4 Radiation Swelling . . . . .	18
1.2 Semiconductor Properties . . . . .	22
1.2.1 Energy Band Gap . . . . .	25
1.2.2 Quantum Confinement . . . . .	26
1.3 Radiation Induced Nano-Structuring . . . . .	26
1.3.1 Embedded Nano-Structures . . . . .	28
1.3.2 Surface Nano-Structures . . . . .	35
1.4 Modeling of Radiation Effects . . . . .	42
1.4.1 Bradley-Harper Model . . . . .	42
1.4.2 Monte Carlo Modeling . . . . .	44
1.4.3 Phase Field Modeling . . . . .	46
1.5 Comments on the Formation of Nano-porous Structures . . . . .	48
1.5.1 Qualitative Models . . . . .	49

<b>II. Development of the Hybrid Model</b>	52
2.1 Microstructural Representation	52
2.1.1 Spin	53
2.1.2 Phase	53
2.1.3 Concentration	55
2.2 Radiation Damage	55
2.2.1 Binary Collision Approximation	56
2.2.2 Defect Survivability	63
2.3 Conventional Formulation	68
2.3.1 Flux in a Multi-Component System	69
2.4 Chemical Potential Definition	71
2.4.1 Equilibrium of a Multi-Phase System	72
2.5 Free Energy Functional	74
2.6 Phenomenological Equations for a Quaternary System	75
2.6.1 Surface Migration, Grain Growth and Phase Transformation	76
2.7 Coupling of the Deterministic and Statistical Models	77
2.7.1 Advantage Over Conventional Models	79
2.8 Stochastic Parallel PARTicle Kinetic Simulator	80
<b>III. Research Mission Statement</b>	82
<b>IV. Mathematical Concepts and Numerical Methods</b>	84
4.1 Taylor Expansion	84
4.2 Finite Difference Methods	85
4.2.1 Approximation of the Diffusion Equation	88
4.3 Capillarity Driven Flux	92
4.3.1 Mathematical Treatment of the Curvature	93
4.3.2 Discrete Approximation of the Curvature	95
4.4 Euler-Lagrange	97
<b>V. Numerical Simulation of Radation Induced Segregation: Influence on Precipitate Kinetics</b>	99
5.1 Introduction	99
5.2 Model Framework	101
5.2.1 Microstructural and Compositional Representation	101
5.2.2 Radiation Damage	102
5.2.3 Phenomenological Behavior	103
5.2.4 Thermodynamics of the System	104
5.2.5 Phenomenological Equations	107



5.2.6	Discretization of the Phenomenological Equations . . . . .	111
5.2.7	Phase Transformations . . . . .	114
5.3	Results and Discussion . . . . .	114
5.3.1	Effects of Radiation Defect on Precipitate Growth . . . . .	115
5.3.2	Uniform Irradiation of Polycrystalline Matrix . . . . .	124
5.3.3	Medium and High Energy Irradiation . . . . .	126
<b>VI.</b>	<b>Numerical Simulation of the Formation of Nano-Porous Networks . . . . .</b>	<b>133</b>
6.1	Introduction . . . . .	134
6.2	Inter-granular Bubble Swelling . . . . .	135
6.2.1	Model Framework . . . . .	136
6.2.2	Results and Discussion . . . . .	143
6.3	Nano-porous Network Formation and Swelling . . . . .	148
6.3.1	Model Framework . . . . .	150
6.3.2	Results and Discussion . . . . .	158
<b>VII.</b>	<b>Summary . . . . .</b>	<b>181</b>
7.1	Future Work . . . . .	184
<b>APPENDICES</b>	<b>. . . . .</b>	<b>187</b>
<b>BIBLIOGRAPHY</b>	<b>. . . . .</b>	<b>221</b>

## LIST OF FIGURES

### Figure

1.1	Schematic showing the ion induced sputtering and ion implantation processes. . . . .	3
1.2	Sputtering yield of silicon (Si) as a function of: (left) incident ion energy, and (right) incident ion atomic number (extracted from [6]). The solid circles data is from <i>Andersen and Bay</i> [7] and the plus signs correspond to Stopping and Range of Ions in Matter (SRIM) simulations [5]. . . . .	5
1.3	Evolution of the partial sputtering yields of a PtSi target as a function of dose. . . . .	7
1.4	In the presence of defects, diffusion can occur by exchange of the defect and atom site positions. . . . .	8
1.5	Representation of RIS in a binary, 50% A–50%B, system showing (a) the vacancy concentration profile generated by the flow of vacancies to the grain boundary due to a counter diffusion of A and B atoms, (b) the interstitial concentration profile generated by the flow of interstitials to the grain boundary due to diffusion of A and B atoms through the interstitial sites, and (c) the resulting concentration profiles for A and B . . . . .	12
1.6	Types of lattice defects. (a) Frenkel pair formed on a crystalline lattice, where the vacancy (square) is in the lattice atom position and the interstitial (gray circle) is the displaced atom now in the interstitial position. (b) Schottky is a vacancy defect that retains its stoichiometry, i.e. neutral charge. The defect is formed when both an anion (black) and cation (gray) leave their respective lattice sites. For non–ionic crystals it means a simple vacancy. . . . .	14
1.7	High resolution transmission electron microscopy (HRTEM) of a 1.5 MeV $Kr^+$ irradiated $Ca_2La_8(SiO_4)_6O_2$ single crystal showing: (A) undamaged crystalline lattice; (B) a small subcascade damage at the center of the crystal; and (C) a larger cascade or overlap of subcascade damage regions . . . . .	15

1.8	Comparison of experimental measurement of amorphous fraction accumulation as a function of dose with curves fit to various models for radiation induced amorphization (extracted from [17]). . . . .	16
1.9	Critical amorphization dose as a function of temperature for CuTi irradiated with 1 MeV electrons and ions, all at a dose rate of $1 \times 10^{-3}$ dpa/s. The hatched area represents the conditions where the crystalline and amorphous phases can coexist (extracted from [18]).	17
1.10	(top) TEM of two stainless steel grains showing the high dislocation density in the dark grain and the voids on the light grain [29] and (bottom) micrographs of voids in stainless steel [30]. . . . .	19
1.11	SEM of a fuel with burnup of 23 GWd/t after it was annealed. (a) inter- and intragranular bubbles nucleated and diffused to the grain boundaries, and (b) close up showing the different distribution of bubbles. It is expected that the intragranular bubbles migrate to the grain boundaries where they coalesce into the larger intergranular bubbles [26]. . . . .	20
1.12	Swelling as a function of temperature on nickel irradiated to a fluence of $5 \times 10^{19}$ $n/cm^2$ [32]. . . . .	21
1.13	(a) A void (outlined by dashed lines) nucleated near the interstitial dislocation loop. (b–d) Stage 1 growth of the void, where it grew in length but not in thickness. The length growth direction is indicated by the yellow arrow. The specimen is irradiated over a dose range of 0.95–1.17 displacement-per-atom (d.p.a.). Scale bar, 5 nm. [33]. . .	23
1.14	(a) First vacancy layer nucleates on the top of the (0001) facet as indicated by the yellow arrow. (b) The spreading of the vacancy layer on the (0001) facet, the size of the vacancy layer is designated by the dashed lines. (c) Vacancy layer extends over the whole (0001) facet surface. (d) Subsequent nucleation of a new vacancy layer. Scale bar, 5 nm. . . . .	24
1.15	(a) Volume expansion $\Delta z$ as a function of the ion fluence $N_i$ for room temperature irradiated Ge with 380 keV I- and Au-ions under an angle of $\Theta = 7^\circ$ . The solid lines exemplify the linear dependence whereas the dotted line points to the general trend. In (b) the influence of the ion rate $\Phi$ on the volume expansion is shown for the irradiation with 380 keV I-ions [28]. . . . .	25
1.16	Density of states in one band of a semiconductor as a function of dimension (reproduced from [35]). . . . .	27
1.17	The temperature dependence of amorphization dose for 1.5 MeV $Kr^+$ irradiated Ge [20]. . . . .	29
1.18	Radiation-induced nano-porous structure formation in amorphous germanium (Ge) after 1.5 MeV $Kr^+$ irradiation at room temperature to doses of: (a) $7.0 \times 10^{14}$ ; (b) $3.0 \times 10^{15}$ ; (c) $6.0 \times 10^{15}$ ; (d) $1.0 \times 10^{16}$ ; (e) $2.0 \times 10^{16}$ ; and (f) $2.7 \times 10^{16}$ $ions\ cm^{-2}$ [19]. . . . .	30

1.19	Implant damage map for self implants into Ge: threshold dose values are $5.0 \times 10^{13} \text{ cm}^2$ for amorphization, $2.0 \times 10^{15} \text{ cm}^2$ for void formation, and $4.0 \times 10^{15} \text{ cm}^2$ for porous structure formation. Boxed symbol represents crystallinity, filled symbols represent continuous amorphization, half-filled symbols represent void clustering, and open symbols represent porous formation. All implants were done at room temperature. (Figure copied from Darby et al. [37]. The references to the data used are given by them.) . . . . .	31
1.20	Window of radiation endurance. Map showing the window of radiation resistance (triangular area) in terms of the diameter of the foam ligaments and the dose-rate for the irradiation conditions explored in this work: 45 keV Ne ions into Au foam target at room temperature [38]. . . . .	33
1.21	Irradiation of nanofoams, experimental results. Nanoporous Au irradiation at 77 K with 45 keV Ne+ to a dose of $4.5 \times 10^{14}/\text{cm}^2$ (1.5dpa) at 300 K. (a) Unirradiated sample, including small area diffraction (SAD) pattern showing that the ligaments are polycrystalline. (b) Bright-field TEM image of np-Au after irradiation. (c) Irradiation of nanofoams, computer simulation. Small region of the sample with 45% porosity and a $\sim 5$ nm ligament size, $\sim 110$ ps after a cascade began, melted and recrystallized the tip of a ligament. Atomic displacements larger than the lattice parameter $a_0$ are shown with red indicating more than $4a_0$ [38]. . . . .	33
1.22	a) Cross-sectional SEM image GaSb nano-porous layer irradiated with 1 MeV Au <sup>+</sup> to $1 \times 10^{14} \text{ ions cm}^{-2}$ . Inserts show b) the surface layer (tilted to $10^\circ$ off axis), c) the presence of fully formed nano-porous region, and d) a transition regime in which the pores blend into the substrate. e) Same sample at an angled perspective, showing the incident ion beam direction, surface layer, nano-porous layer, and crystalline substrate [34]. . . . .	34
1.23	scanning electron microscopy (SEM) images of morphological evolution of gallium arsenide (GaAs) at various incident angles: (a) $0^\circ$ ; (b) $0^\circ$ , viewed from $52^\circ$ to sample normal; (c) $20^\circ$ ; (d) $25^\circ$ ; (e) $30^\circ$ ; (f) $40^\circ$ ; (g) $50^\circ$ ; and (h) $60^\circ$ . Ion energy 5 keV, flux $1.5 \times 10^{15} \text{ cm}^{-2} \text{ s}^{-1}$ , bombardment time 5 mins (scale bar 1 $\mu\text{m}$ ) [24]. . . . .	37
1.24	(Left) Cross-sectional transmission electron microscopy (TEM) of a single quantum dot (droplet), and (right) energy dispersion spectroscopy (EDS) showing the composition of the quantum dot. Ion energy 5 keV, flux $1.5 \times 10^{15} \text{ cm}^{-2} \text{ s}^{-1}$ , incidence angle $35^\circ$ [24]. . . . .	38
1.25	SRIM calculation of the species sputtering, as averaged for a given number of incident ions. We see that the number of ions sputtered deviates significantly, but the average is consistent with increasing dose. Simulation conditions used were those that yield quantum dots, given in Figure 1.24. . . . .	38

1.26	(a) bright field (BF) TEM images of the nanocones, inset: zoom on the tip showing a polycrystalline structure. (b) SEM cross-section images of a surface irradiated at an incidence angle of $60^\circ$ . (c) scanning transmission electron microscopy (STEM) high-angle annular dark-field (HAADF) images of the nanocones. (d) electron energy loss spectroscopy (EELS) spectrum imaging a tip. Ga is represented in green, Sb in blue, and O in red [42]. . . . .	39
1.27	Formation of nano-walls due to low (a) energy [44] or (b) low fluence [28]. From the work by <i>Steinbach et al.</i> we can see that the nano-walls degrade as a function of fluence, which yields a “netlike” nano-porous structure. . . . .	40
1.28	Schematic representation of the microstructural evolution of Ge with increasing ion dose; the starting material is single crystal Ge, but with increasing dose an amorphous layer is formed; as the dose increases further, small clusters of near-surface pores nucleate; as the dose increases further, the pores cover the whole surface and elongate into the wafer, forming the nanostructured morphology; as the dose increases further, the pores elongate further and the material experiences a large out-of-plane expansion with the nanostructured region existing on top of a nonporous amorphous layer. In all cases, the surface roughness and roughness of the amorphous/crystalline interface increase with increasing ion dose. [36] . . . . .	41
1.29	Schematic of an undulated surface being irradiated from the top. The shaded regions represent the energy being deposited, which can be assumed to be Gaussian shaped. This initial undulation of the surface is due to the natural material roughness and the stochasticity of the radiation damage processes. . . . .	43
1.30	Dependence of the best-fit quadratic coefficient $S_X(\theta)$ and theoretical curves $S_X(\theta) = S_X^{eros.}(\theta) + S_X^{redist.}(\theta)$ on deviation from normal ion incidence. $S_X^{eros.}(\theta)$ is from BH theory modified by the Yamamura correction function with no free parameters. $S_X^{redist.}(\theta)$ is our implementation of the Yamamura correction on the CV redistributive model with a single free parameter as discussed in the text. [47]. . .	44
1.31	Drawing of two different types of interfaces: a) sharp, and b) diffuse. The red region represents a precipitate and the blue the matrix . . .	47
1.32	Formation and evolution, in arbitrary time units, of nanowalls under a medium ion energy irradiation as calculated by Eq. 1.30. [44]. . .	49
1.33	Qualitative model describing the formation of the nano-structures. (i) The point defects are created by ion implantation, with the more mobile interstitials migrating. (ii) Voids nucleation during the early stage of irradiation. (iii) Surviving interstitial atoms migrate and aggregate under the walls, increasing their height. (iv) The voids grow perpendicular to the surface until they burst. . . . .	50

1.34	Adaptation of the <i>Nitta</i> model by <i>Perez-Bergquist</i> to explain the formation of a “transition layer” and a quasi-stable intact surface layer. The transition layer is formed as the ions are able to penetrate deeper into the highly porous target. . . . .	51
2.1	Schematic of a polycrystalline material as defined by its grain ID, phase and concentration and represented by a digitized voxelated microstructure. a) Representation of the grain ID, where each color defines a particular grain orientation. b) The phase of each particular grain is visualized for this $\alpha$ (blue)– $\beta$ (red) system. c) The smoothly varying concentration field of the binary system. If looking at the concentration from left to right we go from a high concentration of $A$ ( $C_a \rightarrow 1$ , $C_b \rightarrow 0$ ) to a low concentration ( $C_a \rightarrow 0$ , $C_b \rightarrow 1$ ) with a smooth variation in between. . . . .	54
2.2	Illustration of a Monte Carlo BCA (SRIM) calculated $\text{Ga}^+$ ion tracks as they travel through a Ge substrate after entering through the surface, depth = 0 Å. Each colored dotted line represents a particular path for the given colored ion. . . . .	56
2.3	TRIM simulation of 1 MeV $\text{Kr}^+$ irradiation on amorphous Ge. (green) Curves correspond to the left axis and were obtained from the <i>damage event</i> file, and (blue) Curve corresponds to the right axis and was obtained from the <i>energy to recoil</i> file. . . . .	59
2.4	Representation of fitting and randomization of the recoil energy deposited under the same condition as in 2.3. The stars represent the random deposited energy at depths $z = (120, 320, 600)$ nm. . . . .	62
2.5	(Atom displacement statistics for single 1 keV Ar+ impact on (left) amorphous and (right) crystalline Si at 50° incidence angle MD and BCA. [80] . . . . .	63
2.6	Comparison of an experimental SIMS profile of boron implanted into silicon with profiles simulated using capture and CPU intensive process of keeping track of the point radius values of $0.22a$ , $0.43a$ , $0.50a$ and $0.85a$ for an energy defects created by all cascades, and yet, within the error of 15 keV, tilt angle of 0°, and rotation angle of 0° [83]. . . . .	66
2.7	Comparison of experimental SIMS profiles of boron implanted into silicon at doses of $1 \times 10^{13}$ , $5 \times 10^{14}$ , $2 \times 10^{15}$ , and $8 \times 10^{15} \text{ cm}^{-2}$ with profiles simulated with the damage model for (a) an energy of 15 keV, tilt angle of 0°, and rotation angle of 0°, and (b) an energy of 35 keV, tilt angle of 7°, and rotation angle of 30°. [83]. . . . .	67
2.8	Use of the common tangent construction rule to determine the state that yields equilibrium conditions. . . . .	73
2.9	Representation of a surface diffusion event where a void voxel (white) exchanges location with a matter voxel (blue). We can see the ensembles (a) before and (b) after the exchange. It is evident that the new configuration has a lower overall energy, i.e. decreased interface. The dots identify the voxels of interest. . . . .	78

2.10	Representation of a feature growth event where a feature 1 voxel (white) grows at the expense of the feature 2 voxel (blue). We can see the ensembles (a) before and (b) after the change. It is evident that the new configuration has a lower overall energy, i.e. decreased interface. The dots identify the voxels of interest. . . . .	78
2.11	The main advantages of each computational approach are exploited in order to develop a hybrid model that is able to efficiently model microstructural evolution, with the added benefits of being robust and retaining the correct kinetics and physics. . . . .	79
4.1	Representation of different type of FDM schemes. Each scheme shows the respective points that need to be sampled in order to approximate a first order derivative. . . . .	87
4.2	Graphical depiction of (a) forward, (b) backward, and (c) centered finite-divided-difference approximations of the first derivative [95]. .	89
4.3	Cell map defined for computational convenience. The summation in Equation 4.15 follows the logic represented by this map. . . . .	91
4.4	Diagram of a digitized free surface, defined as the interface between a void (green) and matter (blue) space. Two arrangements where the presence of a surface will influence the flux equation as shown. This finite difference stencil yields a second order error, $\propto(h^2)$ . Careful consideration must be applied when choosing how to set up the no flux conditions where needed. . . . .	93
4.5	Basic schematic of the Ostwald ripening process. Due to their larger curvature, the smaller features are less thermodynamically stable, which leads to their dissolution and growth of the larger features. (Taken and adapted from [101].) . . . . .	94
4.6	Representation of a 3D voxelated surface where the void voxels are not shown and the voxels shown represent a single phase. Each voxel has 26 neighbors surrounding it which can contribute to the curvature approximation. . . . .	96
5.1	Diagram showing the expected growth behavior of $\beta$ -precipitates on an irradiated $\alpha$ -matrix material. As the generated point defects diffuse to the sinks (phase boundaries), an associated atomic flux will influence microstructural evolution behavior. . . . .	104
5.2	Composition dependent bulk free energy functional for the binary two-phase system. These curves were chosen as to be comparable to the NiSi system for $\bar{C}_{Si} \sim 0.13$ , $T < 900 K$ . . . . .	106
5.3	NiSi phase diagram (from Massalski [114]). . . . .	107
5.4	Schematic of a high energy ion damage distribution, e.g. swift ions. Since the ion is highly energized, it travels through a large section of the target producing slightly gradual radiation damage. If the simulation is only interested in a region (blue square) away from the peak damage and surface, radiation damage can be assumed to be uniform through the simulation domain. . . . .	116

5.5	Schematic representation of the radiation influenced precipitate growth. As radiation induced mobile $B$ atoms move towards the $\alpha - \beta$ interfaces, Ostwald ripening is suppressed, leading to slower precipitate growth kinetics. . . . .	117
5.6	Microstructural evolution of the $\beta$ precipitates (red) as a function of time for the unirradiated and high irradiation dose simulations. Radiation leads to appreciable changes in the grain size, shape and distribution. The feature phase order parameter is shown. (Time units are in Monte Carlo steps.) . . . . .	118
5.7	Precipitate growth curves for the unirradiated and irradiated cases. It is evident that radiation leads to the presence of smaller precipitates at longer times. The radiation damage units mean approximate average number of defects created per time unit on each pixel. . . .	120
5.8	The inverse of the precipitate growth exponential decreases with increasing radiation damage rate. This reveals how the system's evolution goes from pure Ostwald ripening to radiation retarded kinetics. Interestingly, the data fits nicely to an equation of the $1/n = a \cdot K_0^{1/n_{ost}} + b$ form. This indicates that inverse exponentials scale with the inverse exponential for Ostwald ripening. . . . .	122
5.9	Average concentration of point defects as a function of time for the irradiated cases. The top curves correspond to the vacancy concentration ( $\bar{C}_v$ ) and the bottom curves correspond to the interstitial concentration ( $\bar{C}_i$ ). . . . .	123
5.10	Solute concentration profiles for the different cases simulated. It is clear that the radiation induced quasi-stability of smaller precipitates has an influence on the equilibrium cobcentrations. Hence, with higher damage, more of the smaller precipitates grow and/or persist. . . . .	125
5.11	Growth of the $\beta$ film along the $\alpha$ matrix grain boundary. By simulating irradiation of a bi-crystal $\alpha$ matrix with a random distribution of $\beta$ precipitates, the development and growth of the secondary phase is observed. The grain ID, and concentration distributions of $B$ atoms and interstitials are shown. . . . .	127
5.12	Shape of the deposited energy distributions used in the low (green) and high (blue) ion energy simulations. The ions with higher energy have a larger range, meaning that they deposit most of their energy deeper into the target. The surface is located at zero depth, $d = 0 \cdot L$ . . . . .	128
5.13	Microstructure of an irradiated target after 10,000 MCS for a low energy ion beam. The simulated target is being irradiated through the surface, the "top" of the image. . . . .	130
5.14	Microstructure of an irradiated target after 10,000 MCS for a high energy ion beam. The simulated target is being irradiated through the surface, the "top" of the image. . . . .	131



5.15	Concentration distribution profile across the microstructure for the low and high ion beam energy cases. The films and precipitates can be distinguished by the width of the “step”–like higher concentration. The irradiated surface is located at 1500 <i>px</i> (top). . . . .	132
6.1	Micrographs showing inter– and intra–granular bubbles. (a) SEM fractographs of the fuel with burnup of 23 GWd/t after annealing at 1800° C × 5 <i>h</i> [26]. (b) Advanced development of grain-boundary porosity: this fuel was ramped under similar conditions to that in Fig. 4 (of White) but maintained at 1800°C for 30 min [121]. . . . .	136
6.2	Simulation space showing the frame (blue outer box), microstructural domain (polycrystalline material) and empty space in between these two regions. The empty space, i.e. vacuum domain, allows swelling of the microstructural domain. . . . .	138
6.3	Microstructural representation of a bubble nucleation and coalescence in a polycrystalline material. Bubbles are nucleated along grain boundaries where they diffuse and form the interlinked bubble networks. . . . .	142
6.4	Schematic of the swelling algorithm. (left) A grain boundary site is flagged to undergo a swelling event, leading to the calculation of the random swelling direction. (right) The step–wise site exchange that leads to the swollen microstructure. . . . .	143
6.5	Microstructure after undergoing irradiation induced bubble swelling. (a) 3D swollen microstructure at time for percolation, (b) select view of grains showing advanced stage (well past percolation) swelling, (c) all the inter–granular bubbles present within the microstructural domain and (d) percolating bubble at time for percolation. . . . .	146
6.6	Measured swelling from the expanding microstructural domain dimensions as a function of time. The blue data represents the measured swelling and the green represents an 83% reduction in the calculated swelling times. . . . .	147
6.7	Comparison of the time for percolation between microstructures with initial porosities of 0% and 5%. The abrupt increase of largest the bubble volume (number of voxels) marked by the vertical lines denote the time for percolation. . . . .	148
6.8	Bubble size distribution for the two cases simulated. It is evident that a much lower bubble content is needed for percolation to take place for the $\rho = 95\%$ case. The inserts refer to bubbles that were larger than 500 voxels. . . . .	149
6.9	Schematic of a voxelated surface showing the difference in free surface area between two surface voxels. Site <i>a</i> will have a lower surface area, meaning that the more defects will be annihilated by site <i>b</i> . The arrangement shown indicates that voxel <i>a</i> and <i>b</i> have 3 and 5 free faces.	156

6.10	Example of the void swelling mechanism showing defect accumulation and volumetric expansion. As the material is irradiated, the defect density is increased as shown by the different shades of blue (lighter = more vacancies). Eventually enough defects are accumulated that a void is nucleated (white). Defects will then diffuse towards the newly created surface regions. . . . .	159
6.11	Qualitative representation of the radiation damage profiles used to assess the coupled swelling model. The uniform case considers an equal probability of damage and energy deposition regardless of the voxel location. The planar case sets a distribution that peaks at the center of the target in the depth direction, where $z = L_3^l$ or $z = L_3^h$ is the irradiated surface. The figure on the right helps visualizing the distribution along the $xz$ - or $yz$ -planes. . . . .	161
6.12	Average concentration for the point defects as a function of time. The green curve corresponds to the vacancy concentration ( $\bar{C}_v$ ) and the blue curve correspond to the interstitial concentration ( $\bar{C}_i$ ). . . . .	162
6.13	Evolution of the bulk microstructural domain at the onset of swelling, an intermediate time and at steady state. The microstructure seems to arrange into a stable configuration that remains generally unchanged for the last 4,000 <i>MCS</i> . . . . .	163
6.14	Cross sectional view of the microstructural evolution showing the development of the porous network. The stabilization of the porous network can be better appreciated from these views. . . . .	165
6.15	Void size distribution for (top) experimentally measured pore sizes [125], and (bottom) the uniform radiation simulation. The simulation distributions are able to capture the interlinkage between the individual voids while the is not straightforward for the experimental measurements. Notice that the experimental and computational distributions measure different parameters. Further, the simulations have “flexible” axes to allow for visualization of the data. . . . .	166
6.16	Single frame cross sectional views of the microstructural evolution of the void nucleated nano-porous structure. The simulations show the effects of the diffusivity magnitude. The three views represent different structuring stages: early initial void nucleation (left); preceding time step to reaching a stable configuration (center); and final configuration where steady state has been achieved (right). . . . .	168
6.17	Porosity evolution for the different magnitude cases, identified by the order of magnitude of the given value. As the defects diffuse faster, a less porous stable microstructure is achieved. This is due to defects being removed faster and restraining void nucleation. . . . .	169
6.18	Porosity of the stable configuration as a function of the interstitial diffusivity. With less mobile defects, the microstructure is able to nucleate and grow more voids leading to a more porous configuration. . . . .	170

6.19	Single frame cross sectional views of the microstructural evolution of the void nucleated nano-porous structure. The simulations show the effects of the diffusivities' ratio. The three views represent different structuring stages: early initial void nucleation (left); preceding time step to reaching a stable configuration (center); and final configuration where steady state has been achieved (right). . . . .	171
6.20	Porosity evolution for the varying diffusivities' ratio cases. The reference point used corresponds to the simulation that leads to the most porous microstructure for the diffusivity magnitude study, i.e. $D_i \rightarrow 10^{-4}$ . It's interesting that while making the interstitials increasingly faster than vacancies barely influences the microstructural evolution, the case of faster vacancies has a very noticeable effect on the microstructure. . . . .	172
6.21	Qualitative comparison of the experimental [19] and the computational results (this dissertation). Visual inspection reveals that slow diffusing defects with slightly faster interstitials yield to a more sensitive and proper stable configuration. The computational results are from single frame cross sectional views of the previously discussed simulations. Notice that the experimental results were analyzed (computationally filtered) in order to obtain a sharper image that provides a more accurate description of a single frame cross sectional view. . . . .	174
6.22	Cross sectional views of the microstructural evolution showing the development of the porous network. It is clear that the interlinked porous network forms in stages depending on the evolution of the defect concentration. . . . .	177
6.23	Cross sectional views of the microstructural evolution showing the vacancy compositional distribution. Since the average defect concentrations were shown to behave similarly for the uniform case, only the vacancy distribution is displayed. The defect distribution closely aligns with the radiation damage profile. . . . .	178
6.24	Planar views of the damaged microstructures exhibits a peculiar swelling behavior where expansion is faster in the region where the porous network forms. As the porous networks extend to the remaining region, the microstructural domain seems to reach a uniformly swollen configuration. The dashed box is fixed in location and size to compare the dimensional changes over time. . . . .	179
6.25	Porosity evolution is sensitive to the radiation damage distribution. An interesting observation is that while the uniform radiation seems to reach a stable configuration relatively quickly, the planar distribution does not achieve a stable microstructural arrangement. . . . .	180

E.1	Sketch illustrating methodology used to calculate discrete curvature. The lower-left white dot shows the concept of neighbor shells, where each color surrounds the neighbors considered for a given $\mathcal{N}$ -shell: red corresponds to 8 neighbors ( $\mathcal{N} = 1$ ), green to 24 ( $\mathcal{N} = 2$ ) and yellow to 48 ( $\mathcal{N} = 3$ ). For $\mathcal{N} = 2$ , the curvature of the upper-right white dot is proportional to 16, which gives $\kappa = 0.25$ calculated using Equation E.13. . . . .	214
E.2	Free energy curves for the minimum curvature configuration. As the curvature changes, these curves move and the solubility changes (insert for $\mathcal{N} = 2$ ) . . . . .	214
E.3	Concentration profile for the matrix-precipitate (insert) system after equilibrium has been reached. The concentration is taken across the center of the precipitate, as shown by the white line in the insert. The concentration at the interfaces for all cases are very similar and is highlighted by the high resolution of the y-axis. . . . .	215
E.4	Microstructural evolution showing grain growth on the left, and concentration evolution and coarsening of the $\alpha$ (blue) and $\beta$ (red) phases on the right for the $\mathcal{N} = 1$ case. We show the spin and concentration distributions for: (top to bottom) $t = 464, 4640$ and $46416$ <i>MCS</i> . . . . .	216
E.5	Grain growth curves for hPPF and our simplified model with shells $\mathcal{N} = 1$ and 2. We can see that all three curves are virtually identical. . . . .	217
E.6	3D simulation of a polycrystalline microstructural evolution using the discrete curvature definition ( $\mathcal{N}_{3D} = 1$ ). The top figures show the concentration evolution, while the bottom shows the microstructural (grain id) evolution. The grain growth exponential was found to be in good agreement with the 2D cases, Table E.2. . . . .	218
F.1	Fiber or cell wall thickness as a function of ion fluence for InSb, GaSb, and Ge irradiated with 1 MeV Au+ ions. . . . .	220
F.2	Self diffusivities for crystalline Ge and GaSb as a function of temperature. . . . .	220

## LIST OF TABLES

### Table

1.1	Effect of solute size on RIS [13, 14, 15] . . . . .	13
2.1	Constant values which define the ZBL screening function. . . . .	58
2.2	General characteristics of the Potts kinetic Monte Carlo (PMC) and the phase field models. . . . .	80
5.1	Numerical values of the parameterization variables for the energetic configuration. The values used are separated into enthalpic and entropic sections. The values shown here are technically the non-dimensionalized values as defined in Section 5.2.5.2. . . . .	106
5.2	Values for the non-dimensionalized phenomenological and Potts' interfacial energy variables. . . . .	112
5.3	Fitted grain growth exponential value, $R^n - R_0^n = kt$ , for the different cases studied. A growth exponential of $n = 3$ is indicative of Ostwald ripening kinetics [99, 100]. . . . .	119
6.1	Comparison of real life and computational modeling of fission gas behavior. These characteristics describe the fission gas generation and transport (based of [122]). . . . .	139
6.2	Parameterization values used for the inter-granular bubble swelling simulation. The parameters correspond to nucleation, pore migration and grain growth rates, as identified. . . . .	144
6.3	Numerical values of the parameterization variables for the rate theory and kinetic equations. The units of the parameters have been set to represent <i>cm</i> and <i>s</i> . . . . .	160
D.1	Typical dump output file. This dump file outputs data showing the site ID, $x, y$ and $z$ position, spin, and vacancies and interstitials concentrations for a SPPARKS' time of $\sim 168$ MCS. The values correspond to the frame region. . . . .	205
E.1	Numerical values of the model's parameterization variables used in the presented simulations. . . . .	215
E.2	Summary of the grain growth exponential inverse, $1/n$ , for the hPPF model and a series of discrete curvature calculations with varying $\mathcal{N}$ . . . . .	215

## LIST OF APPENDICES

### Appendix

A.	Evolution Equations for a Quaternary System . . . . .	188
B.	Mathematical Formulation of a Continuum Surface's Curvature . . . . .	196
C.	Comments on Numerical Approximation to the Phenomenological Equations . . . . .	200
D.	Pseudocode and Output Data Layout . . . . .	203
E.	Sharp Interface hybrid Potts-phase field . . . . .	206
F.	Comments on the Dependence of <i>Fiber</i> Diameter on Diffusivity . . . . .	219

## LIST OF ABBREVIATIONS

**As** arsenic

**Au** gold

**BCA** binary collision approximation

**BF** bright field

**BH** Bradley–Harper

**EDS** energy dispersion spectroscopy

**EoS** equation of state

**EELS** electron energy loss spectroscopy

**FDM** *finite difference methods*

**FTCS** forward–time central–space

**Ga** gallium

**GaAs** gallium arsenide

**GaSb** gallium antimonide

**Ge** germanium

**hPPF** hybrid Potts–phase field

**HAADF** high-angle annular dark-field

**HRTEM** High resolution transmission electron microscopy

**I** iodine

**InSb** indium antimonide

**kMC** kinetic Monte Carlo

**MC** Monte Carlo  
**MD** molecular dynamics  
**MPI** message passing interface  
**nPBC** non-periodic boundary conditions  
**PBC** periodic boundary conditions  
**PDE** partial differential equation  
**PMC** Potts Monte Carlo  
**RIS** radiation-induced segregation  
**Sb** antimony  
**SEM** scanning electron microscopy  
**Si** silicon  
**SPPARKS** Stochastic Parallel PARTicle Kinetic Simulator  
**SRIM** Stopping and Range of Ions in Matter  
**STEM** scanning transmission electron microscopy  
**TEM** transmission electron microscopy  
**TRIM** Transport of ions in matter  
**ZBL** Ziegler-Biersack-Littmark



# ABSTRACT

Development of Hybrid Deterministic–Statistical Models for Irradiation Induced  
Microstructural Evolution

by

Efraín Hernández–Rivera

Chairs: Lumin Wang and Veena Tikare

Ion irradiation holds promise as a cost–effective approach to developing structured nano–porous and nano–fibrous semiconductors. Irradiation of certain semiconductors leads to the development of these structures, with exception of the much desired silicon. Hybrid deterministic–statistical models were developed to better understand the dominating mechanisms during structuring.

This dissertation focuses on the application of hybrid models to two different radiation damage behavior: (1) precipitate evolution in a binary two–phase system and (2) void nucleation induced nano–porous structuring. Phenomenological equations defining the deterministic behavior were formulated by considering the expected kinetic and phenomenological behavior. The statistical component of the models is based on the Potts Monte Carlo (PMC) method. It has been demonstrated that hybrid models efficiently simulate microstructural evolution, while retaining the correct kinetics and physics. The main achievement was the development of computational methods to simulate radiation induced microstructural evolution and highlight which processes and materials properties could be essential for nano–structuring.

Radiation influenced precipitate evolution was modeled by coupling a set of non-linear partial differential equations to the PMC model. The simulations considered the effects of dose rate and interfacial energy. Precipitate growth becomes retarded with increased damage due to diffusion of the radiation defects countering capillarity driven precipitate growth. The effects of grain boundaries (GB) as sinks was studied by simulating precipitate growth in an irradiated bi-crystalline matrix. Qualitative comparison to experimental results suggest that precipitate coverage of the GB is due to kinetic considerations and increased interfacial energy effects.

Void nucleation induced nano-porous/fibrous structuring was modeled by coupling rate theory equations, kinetic Monte Carlo swelling algorithm and the PMC model. Point defect (PD) diffusivities were parameterized to study their influence on nano-structuring. The model showed that PD kinetic considerations are able to describe the formation of nano-porous structures. As defects diffuse faster, void nucleation becomes limited due to the fast removal of the defects. It was shown that as the diffusivities' ratio diverges from unity, the microstructures become statistically similar and uniform. Consequently, the computational results suggest that nano-pore structuring require interstitials that are much faster than the slow diffusing vacancies, which accumulate and cluster into voids.

# CHAPTER I

## Introduction and Background

Ion irradiation of materials has been studied for decades, with a vast body of work focusing on radiation damage of alloys. There are several uses of ion irradiation, which range from materials processing to accelerated simulation of neutron radiation under nuclear reactor environments. Use of these techniques lead to the observation of different types of radiation effects. These effects range in time and spatial scales. Some of these effects are well understood, e.g. radiation induced segregation, whilst other are mostly are qualitatively described, e.g. radiation induced nano-porous structures. This work aims to close this gap by coupling well established theory to qualitative models.

In recent years, interest on the use of ion beam modifications of semiconductors has been increasing. Radiation induced nano-structuring promises to be an efficient and economical tool for the generation of quantum-confined photo-electronics. One of the most coveted nano-structure is silicon nano-wires, which have been shown to allow for the tuning of its photonic properties by controlling the structural size. These structures have been achieved through different methods [1], except ion irradiation. On the other hand, ion irradiation has been proven to lead to the formation of the desired nano-structures on germanium and a variety of III-V semiconductors.

Even though this work focuses on radiation effects on semiconductors, radiation

related physical processes are similar for most materials. Therefore, we begin by looking at general theory of radiation damage on materials. This chapter also looks at the different types of radiation induced nano-structures known to happen under certain irradiation conditions focusing on the formation of nano-porous networks. Furthermore, the current modeling techniques used to explain the formation of these types of nano-structures are briefly discussed.

## 1.1 Radiation Damage Physics

As energized ions travel through a target material, there is a probability that the ion will physically interact with the target atoms. This probability depends on several factors, which include ion and target properties. Once the ion interacts with the material, several types of event and/or processes are possible. Some of these include: sputtering, radiation-induced segregation (RIS), amorphization and swelling. All of these processes have a significant influence on microstructural evolution. This section goes over the essential theory related to these different radiation damage mechanisms. It has been suggested that several of these mechanisms are critical in the formation of the desired structures.

### 1.1.1 Sputtering

Ion beam interaction with materials can lead to surface erosion or removal of surface and near surface atoms, otherwise known as *sputtering*. As kinetic energy is deposited into the target atoms through nuclear collisions, the atoms become displaced from their equilibrium lattice position and can eventually be ejected from the surface. This phenomena is characterized by the sputtering yield

$$Y = \frac{\text{average number of emitted atoms}}{\text{incident particle}}. \quad (1.1)$$

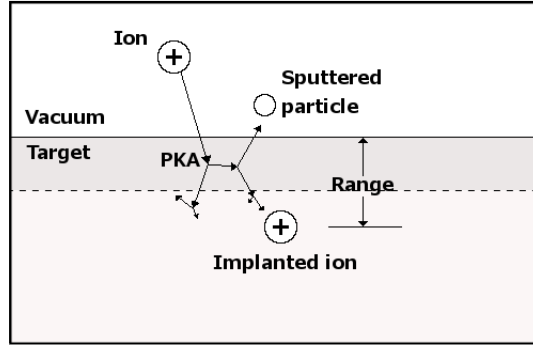


Figure 1.1: Schematic showing the ion induced sputtering and ion implantation processes.

Sputtering is an important radiation effect to consider, especially when dealing with low to mid-range energetic ions (less than a few tens of  $keV$ ), where most of the energy is deposited in the sub-surface region. For these conditions, typical values for the sputtering yield range between 0.5–20.

The mechanism that leads to sputtering is a complex one that includes several nuclear collisions within the collision cascade region. A schematic depicting the sputtering/implantation process is shown in Figure 1.1. The figure shows a gray shaded region where there is a high probability that an energized particle-atom collision can lead to sputtering of the target atoms. This region is usually considered to be a couple atomic layers. As the ion displaces atoms from their lattice positions, these can undergo several collision and deflections. It is also possible that some of these displaced atoms will be backscattered. The backscattered atoms can then be ejected from the surface if they arrive there with enough energy. These atoms make up most of the sputtered atoms. On the regime previously described, the sputtering yield is proportional to the number of displaced target atoms. This is properly described by Sigmund’s model [2]. This is also known as the linear cascade sputtering regime [3].

The sputtering yield depends on the target material properties, the ion beam characteristics and the experimental setup. In the linear sputtering regime, for normal

incidence in a monatomic material, the sputtering yield can be defined as [2]

$$Y = \Lambda \cdot F_D(E_0), \quad (1.2)$$

where  $\Lambda$  is the material factor and  $F_D(E_0)$  is the amount of energy deposited per unit length due to nuclear collisions by an ion with  $E_0$  initial energy. The material factor is defined by the target material properties and can be approximated as [4]

$$\Lambda \approx \frac{4.2}{NU_0} \left[ \frac{nm}{eV} \right], \quad (1.3)$$

where  $N$  is the atomic density of the target material and  $U_0$  is the surface binding energy. The amount of energy being deposited into the target is dictated by the experimental setup, e.g. the energized ion, the target material properties and angle of incidence. It can be calculated by

$$F_D(E_0) = \alpha N S_n(E_0) \quad (1.4)$$

where  $\alpha$  is a correction factor that accounts for the atom-ion mass difference and the angle of incidence, and  $S_n(E_0)$  is the nuclear stopping cross-section for an ion with  $E_0$ . There have been several derivations for the nuclear stopping cross-section, which is highly sensitive to both ion and target atom characteristics. A very good approximation can be achieved by use of the ZBL potential function [5]. The term  $NS_n$  describes the amount of energy that is lost by the ion due to nuclear collisions and can be written as  $dE_0/dx|_n$ . Then, the general equation for the sputtering yield is given by

$$\begin{aligned} Y &\approx 4.2 \frac{\alpha S_n(E_0)}{U_0} \\ &= 4.2 \underbrace{\alpha \frac{dE_0}{dx}|_n}_{\text{Energy deposited}} \underbrace{(NU_0)^{-1}}_{\text{Material properties}} \end{aligned} \quad (1.5)$$

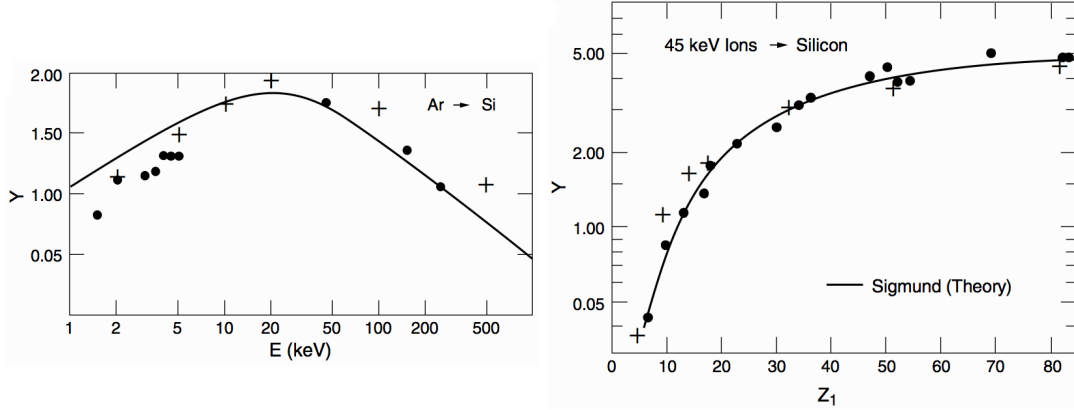


Figure 1.2: Sputtering yield of Si as a function of: (left) incident ion energy, and (right) incident ion atomic number (extracted from [6]). The solid circles data is from *Andersen and Bay* [7] and the plus signs correspond to SRIM simulations [5].

Figure 1.2 shows the dependence of the sputtering yield on beam characteristics. For the energy dependence, we see that initially the yield is increased until the ion is given enough energy to penetrate deep into the target material when the yield begins to decrease. As for the incident ion type, it can be seen that the yield increases since larger ions are more efficient at transferring their energy to the lattice atoms. We see that the sputtering yield increases with the effectiveness to deposit energy in the surface region.

For targets that have more than one atomic element, the probability of sputtering a given species is different. The difference in the probability of sputtering arises from the fact that different atoms' ability to transfer energy due to nuclear collisions are very dissimilar, i.e. energy transfer efficiency due to mass ratios. Therefore, we will have one component being sputtered at a faster rate than the other leading to surface compositional changes. For an  $AB$  alloy, the sputtering yield of the  $A$  component is [8, 9]

$$Y_A = \sum_{n=1}^{\infty} p_A^{(n)} C_A^{(n)} \quad (1.6)$$

where  $p_A^{(n)}$  is the effective yield of sputtering an  $A$  atom from the  $n - th$  atomic layer and  $C_A^{(n)}$  is the concentration of  $A$  atoms in the  $n - th$  layer. Essentially, the species specific sputtering yield, i.e. partial sputtering yield, is the probability of sputtering an atom from a given depth times the probability of finding that species at the given depth. Since sputtering can be considered to be a phenomena occurring at the few top atomic layers of the target, we can say that partial sputtering yield is proportional to the surface concentration, i.e.  $C_A^{(n)} = C_A^s$ . The ratio of sputtering yields is given by

$$\frac{Y_A}{Y_B} = \frac{p_A}{p_B} \cdot \frac{C_A^s}{C_B^s} = r \frac{C_A^s}{C_B^s}, \quad (1.7)$$

where  $r$  is the sputtering factor and it accounts for differences in surface binding energies, sputtering escape depth probability and efficiency of energy transfer within the collision cascade.

When steady state has been achieved, the ratio of the partial sputtering yields is required to be the equal to the ratio of the bulk concentrations due to mass conservation

$$\frac{Y_A(\infty)}{Y_B(\infty)} = \frac{C_A^b}{C_B^b}, \quad (1.8)$$

which leads to the following equation for the surface concentration ratio

$$\frac{C_A^s(\infty)}{C_B^s(\infty)} = \frac{1}{r} \frac{C_A^b}{C_B^b}. \quad (1.9)$$

Now, let's consider a system where  $A$  is preferentially sputtered over  $B$ , i.e.  $Y_A(0) > Y_B(0)$ . As we continue to sputter the target atoms, the surface will become  $B$ -rich and  $A$ -depleted, leading to an increase and decrease in  $Y_B$  and  $Y_A$ , respectively. This will continue until steady state has been achieved, as shown in Figure 1.3. This phenomena limits the amount of matter that can be implanted into the target surface region. For a binary target being irradiated with a beam flux



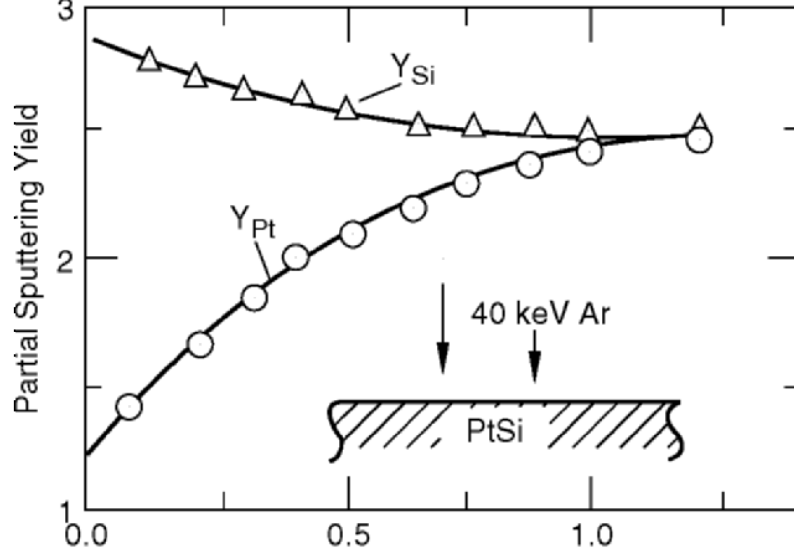


Figure 1.3: Evolution of the partial sputtering yields of a PtSi target as a function of dose [10].

( $\text{ion} \cdot \text{cm}^{-2} \cdot \text{s}^{-1}$ ), the number of sputtered atoms is given by [8, 9]

$$\frac{dN}{dt} = \frac{dN_A^{sp}}{dt} + \frac{dN_B^{sp}}{dt} = (Y_A + Y_B)\phi. \quad (1.10)$$

The authors were also able to show that the net change in component concentration at the surface of the target is given by

$$\frac{dN_i}{dt} = \left( C_i^b \frac{\alpha}{\Omega^b} - Y_i \right), \quad (1.11)$$

where  $i$  stands for the component  $i$ ,  $\alpha$  is the volume removed per incident ion and  $\Omega^b$  is the average atomic volume in the bulk.

### 1.1.2 Radiation Induced Segregation

One can think of point defect diffusion as the positional exchange between a defect and the atomic species, Figure 1.4. These atoms yield their lattice position allowing the defects to diffuse until reacting with other defects or reaching a sink. Then, we can think of a diffusion event as the rate at which an atom and defect species exchange

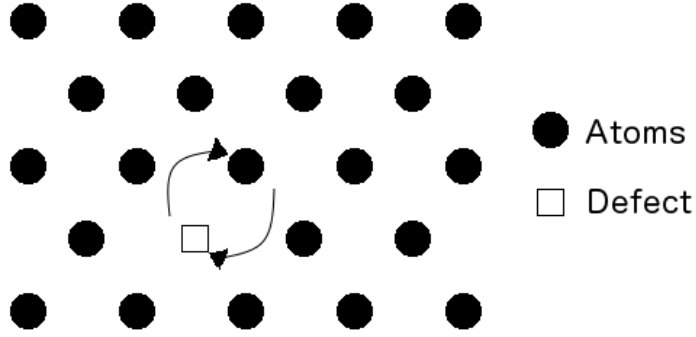


Figure 1.4: In the presence of defects, diffusion can occur by exchange of the defect and atom site positions.

site. The diffusion rate can be characterized as the probability of being next to an atom exchange site (concentration) times the rate at which the events are attempted

$$D_i^j = \frac{\lambda^2}{6} \nu N_j \quad (1.12)$$

where  $\lambda$  is the (jump) distance between species  $i$  and  $j$ ,  $\nu$  is the frequency with which an exchange is attempted and  $N_j$  is the number of  $j$  species neighboring  $i$ . Since radiation events lead to the formation of a wide range of defects, we need to account for these defects. Considering a lattice that has several types of defects, we can write an equation for the *radiation enhanced diffusion*

$$D_{rad} = D_v N_v + D_i N_i + D_{2v} N_{2v} + \dots = \sum_{d=i,v}^{\mathcal{D}} D_d N_d \quad (1.13)$$

where  $D_d$  are the diffusion coefficient through the specific mechanisms defined by the  $b$  subscript. As is evident from Equation 1.12, as the amount of defects increase due to ion irradiation, then the diffusivity will increase correspondingly.

Radiation damage leads to the formation of point defects within the collision cascade known as *interstitials* and *vacancies*. The evolution of the interstitial and

vacancy defects are generally described by the rate theory equations developed at Argonne National Laboratory

$$\frac{\partial C_i}{\partial t} = \mathcal{K}_0 - \mathcal{K}_{iv}C_iC_v - \mathcal{K}_{is}C_iC_s + \nabla \cdot (D_i \nabla C_i) \quad (1.14a)$$

$$\frac{\partial C_v}{\partial t} = \mathcal{K}_0 - \mathcal{K}_{iv}C_iC_v - \mathcal{K}_{vs}C_vC_s + \nabla \cdot (D_v \nabla C_v), \quad (1.14b)$$

where  $\mathcal{K}_0$  is the defect production rate,  $\mathcal{K}_{iv||vi}$  is the defect recombination rate,  $\mathcal{K}_{xs}$  is the reaction rate between the  $x$ -defect and its sinks. Many of the initial point defects tend to recombine or annihilate at different sinks, but as radiation damage is increased these will accumulate. They can also become mobile at higher temperatures, which can lead to enhanced net fluxes away from the concentration gradient.

Accumulation of the point defects created by ion irradiation can lead to the oversaturation point defects within the target material. This oversaturation can lead to the formation of larger scale damage by agglomeration of the defects, e.g. dislocations and voids. Furthermore, these point defects diffuse in the opposite direction to their gradient, which leads to a corresponding chemical component flux, as shown in Figure 1.5 for a binary system. If we consider each defect diffusion event to be directly related to an atomic diffusion, we can say that a net vacancy flux is equal and opposite in direction of the atomic flux through the vacancy mechanism, i.e.

$$\mathbf{J}_v = -\mathbf{J}_A^v - \mathbf{J}_B^v. \quad (1.15)$$

Similarly, for the interstitial flux and atomic flux through the interstitial mechanism, we have

$$\mathbf{J}_i = \mathbf{J}_A^i + \mathbf{J}_B^i. \quad (1.16)$$

Combining these two equations, we can write the following equation for the net atomic

flux

$$\mathbf{J}_i - \mathbf{J}_v = (\mathbf{J}_A^i + \mathbf{J}_A^v) + (\mathbf{J}_B^i + \mathbf{J}_B^v) = \mathbf{J}_A + \mathbf{J}_B. \quad (1.17)$$

Figure 1.5 shows the diffusion of defects toward the defect sink (grain boundary) in a binary system. We see that the flux of  $A$  atoms is larger than the flux of  $B$  through the vacancy mechanism and vice versa through the interstitial mechanism. In other words, there is a net flux of  $A$  away from the sink and of  $B$  toward the sink, i.e.  $D_A^v > D_B^v$  and  $D_A^i < D_B^i$ . This leads to enrichment of  $B$  around the grain boundary.

Mass conservation relates the concentration evolution to the atomic flux, as stated by Fick's second law

$$\frac{\partial C_A}{\partial t} = -\nabla \cdot \mathbf{J}_A \quad (1.18a)$$

$$\frac{\partial C_B}{\partial t} = -\nabla \cdot \mathbf{J}_B. \quad (1.18b)$$

While there could be terms related to more complex defects, e.g. di-vacancies, there are assumed to be negligible as they are less likely to exist and much slower. To define the component specific flux, we need to consider all the diffusion mechanisms. Therefore, the flux for the specific components in the binary system are given by [11]

$$\mathbf{J}_A = -\chi D_A \nabla C_A - D_A^i \nabla C_i + D_A^v \nabla C_v \quad (1.19a)$$

$$\mathbf{J}_B = -\underbrace{\chi D_B \nabla C_B}_{\text{Chemical flux}} - \underbrace{D_B^i \nabla C_i}_{\text{Interstitial flux}} + \underbrace{D_B^v \nabla C_v}_{\text{Vacancy flux}} \quad (1.19b)$$

where  $\chi$  is a term used to account for the difference between the concentration and chemical potential gradients. Since we are considering a binary system, we can say that  $C_A + C_B = 1$ , i.e.  $\nabla C_A = -\nabla C_B$ . Then, we can define the total flux of the

defect as

$$\mathbf{J}_i = -\Omega(D_A^i - D_B^i)C_i\chi\nabla C_A - D_i\nabla C_i \quad (1.20a)$$

$$\mathbf{J}_v = \Omega(D_A^v - D_B^v)C_v\chi\nabla C_A - D_v\nabla C_v \quad (1.20b)$$

where  $\Omega$  is the average atomic volume. Implementing the flux equations into the concentration evolution equations, the radiation induced segregation can be described as

$$\frac{\partial C_A}{\partial t} = -\nabla \cdot \mathbf{J}_A = \nabla \cdot [D_A\chi\nabla C_A + \Omega C_A(D_A^i\nabla C_i - D_A^v\nabla C_v)] \quad (1.21a)$$

$$\frac{\partial C_i}{\partial t} = -\nabla \cdot \mathbf{J}_i = \nabla \cdot [D_i\nabla C_i + \Omega\chi C_i(D_A^i - D_B^i)\nabla C_A] + \mathcal{K}_0 - R \quad (1.21b)$$

$$\frac{\partial C_v}{\partial t} = -\nabla \cdot \mathbf{J}_v = \nabla \cdot [D_v\nabla C_v + \Omega\chi C_v(D_B^v - D_A^v)\nabla C_A] + \mathcal{K}_0 - R \quad (1.21c)$$

where  $R$  includes all the types of reactions rates at the sinks, e.g. recombination of point defects. Taking into account that we can directly relate the concentration  $A$  to the concentration of  $B$ , we only need a three partial differential equation (PDE) equation set to fully describe the radiation induced segregation phenomena.

One important aspect of RIS that we must keep in mind is the effect of solute size to the overall segregation characteristics [12]. To reduce atomic lattice strain energy, the smaller sized solute atoms will most likely preferentially diffuse through the interstitial mechanism, while the larger sized atoms will diffuse through the vacancy mechanism. All of this can be readily predicted by strain energy considerations since interstitial sites occupy smaller volumes than vacancy sites. As *Frenkel pair* are created, shown in Figure 1.6, we will have diffusion of the defects towards the sinks. Considering that atoms diffuse in the same and opposite direction of interstitials and vacancies, respectively, and taking into consideration strain energy reduction, we can expect enrichment of the smaller and depletion of the larger solute atoms around

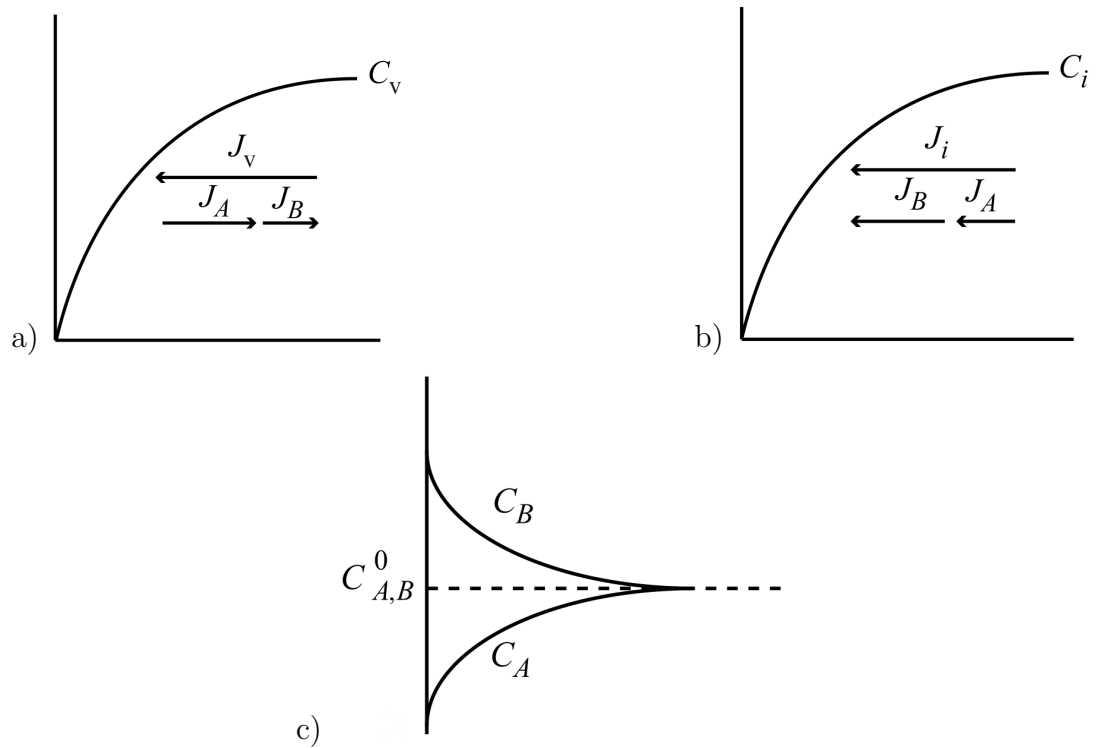


Figure 1.5: Representation of RIS in a binary, 50% A–50%B, system showing (a) the vacancy concentration profile generated by the flow of vacancies to the grain boundary due to a counter diffusion of A and B atoms, (b) the interstitial concentration profile generated by the flow of interstitials to the grain boundary due to diffusion of A and B atoms through the interstitial sites, and (c) the resulting concentration profiles for A and B [11].

the sinks. Table 1.1 shows the effect of solute size on RIS for a variety of materials. As can be seen, the solute size is a very effective predictor of the direction of solute segregation with respect to the sink.

Table 1.1: Effect of solute size on RIS [13, 14, 15]

Solute-Solvent	Volume Misfit (%)	Predicted Segregation Direction	Observed Segregation Direction
Pd-Cu	-20	+	+
Pd-Fe	-27	+	+
Pd-Mo	-3	+	+
Pd-Ni	-26	+	+
Pd-W	-2	+	+
Al-Ge	-37	+	+
Al-Si	-45	+	+
Al-Zn	-19	+	+
Fe-Cr	+4	-	-
Mg-Cd	-19	+	+
Ti-Al	-3	+	+
Ti-V	-26	+	+
Ni-Al	+52	-	-
Ni-Au	+55	-	-
Ni-Be	-29	+	+
Ni-Cr	+1	-	-
Ni-Ge	-5	+	+
Ni-Mn	+32	-	-
Ni-Mo	+31	-	-
Ni-Sb	+21	-	-
Ni-Si	-16	+	+
Ni-Ti	+57	-	-
Cu-Ag	+44	-	-
Cu-Be	-34	+	+
Cu-Fe	-8	+	+
Cu-Ni	-7	+	+
*SS-Ni	-3	+	+
*SS-Cr	+5	-	-
*SS-Si	-3	+	+
*SS-C	+54	-	-
*SS-Mn	+3	-	-
*SS-Mo	+36	-	-
*SS-Cu	+9	-	-

\*SS refers to 316 stainless steel from [14]

Extracted from [11]

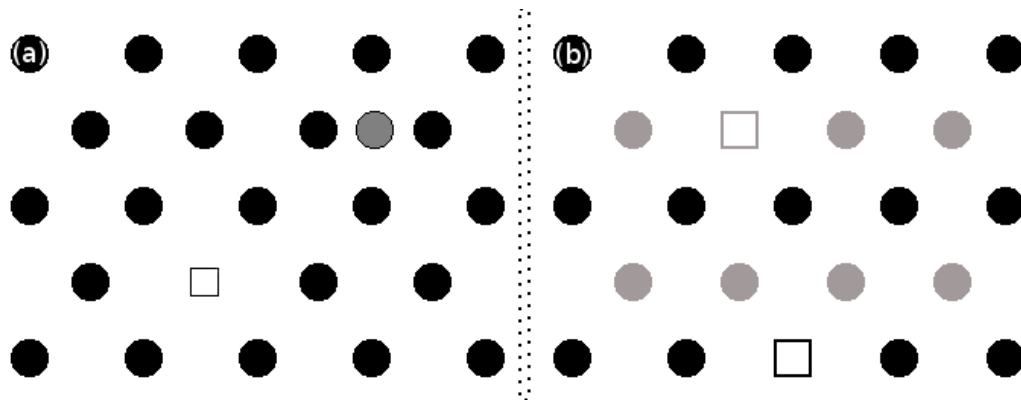


Figure 1.6: Types of lattice defects. (a) Frenkel pair formed on a crystalline lattice, where the vacancy (square) is in the lattice atom position and the interstitial (gray circle) is the displaced atom now in the interstitial position. (b) Schottky is a vacancy defect that retains its stoichiometry, i.e. neutral charge. The defect is formed when both an anion (black) and cation (gray) leave their respective lattice sites. For non-ionic crystals it means a simple vacancy.

### 1.1.3 Radiation Induced Amorphization

Nuclear and electronic interactions between energized ions and target lattice atoms lead to the formation of different types of lattice defects, e.g. Frenkel pairs and Schottky defects Figure 1.6. These types of defects alter the lattice long range ordering, which defines the crystallinity of the target. When enough atoms have been displaced from their ground state lattice positions, the long range periodicity of the crystal becomes compromised. An example is shown in Figure 1.7, where a complex crystalline structure has been bombarded by Kr ions. The lattice disordering in the region where one or more radiation events, e.g. elastic collisions, took place is evident. Eventually, enough lattice disordering will cause most of the long range arrangement to be lost and the material is said to become amorphous.

Several models that describe the formation and evolution of the amorphized lattice have been developed over the past four decades, at least. The models are based on two general types: the direct impact and the defect accumulation models. The former is based on the material's heterogeneous amorphization within the collision cascade, while the latter treats amorphization as a homogeneous event when the



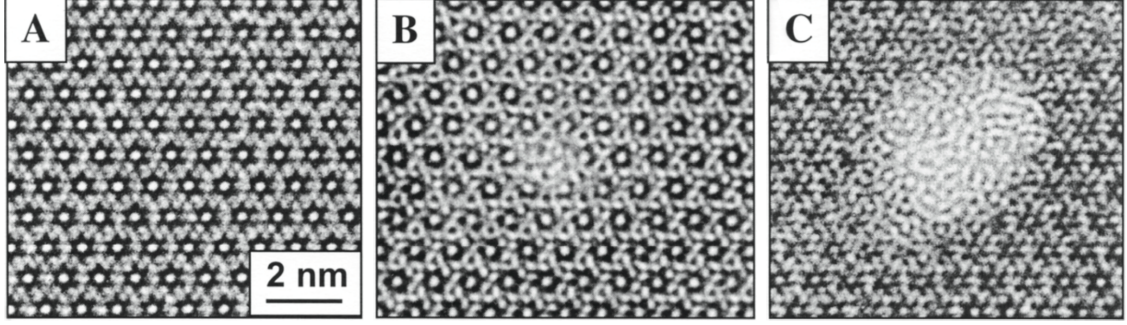


Figure 1.7: HRTEM of a 1.5 MeV  $Kr^+$  irradiated  $Ca_2La_8(SiO_4)_6O_2$  single crystal showing: (A) undamaged crystalline lattice; (B) a small subcascade damage at the center of the crystal; and (C) a larger cascade or overlap of subcascade damage regions [16]

accumulation of local point defects reaches a critical value. Most recent models are a form of the defect accumulation model that takes into consideration the heterogeneous amorphization process [16].

An example of the rate of amorphization by direct impact can be expressed as

$$\frac{\partial f_a}{\partial t} = \sigma_a(1 - f_a)\phi \quad (1.22)$$

where  $f_a$  is the fraction of amorphous material,  $\sigma_a$  is the cross section of amorphization and  $\phi$  is the ion flux. A solution to Equation 1.22 gives a function for the amorphous fraction

$$f_a = 1 - \exp(-\sigma_a D_\phi) \quad (1.23)$$

where  $D_\phi \equiv f(\phi, t)$  is the ion dose. The defect accumulation model predicts a sigmoidal amorphous fraction function [16]. Another example is for the case of requiring the overlap of three cascades for the formation of an amorphous region. For such a case, we have

$$f_a = 1 - \left[ 1 + \sigma_t D_\phi + \frac{(\sigma_t D_\phi)^2}{2} \right] \exp(-\sigma_t D_\phi) \quad (1.24)$$

where  $\sigma_t$  is the total cross section.

A way to define the onset of complete amorphization of a material is with the crit-

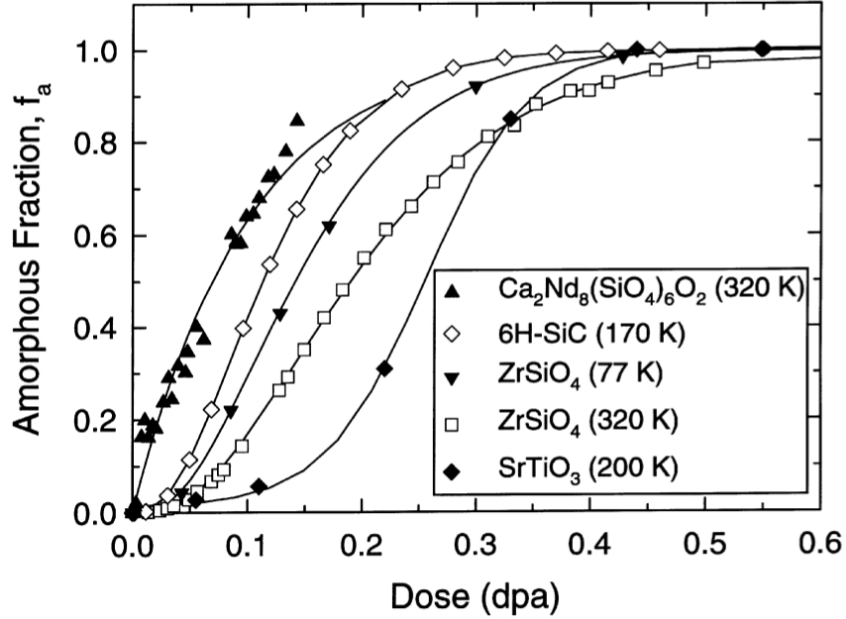


Figure 1.8: Comparison of experimental measurement of amorphous fraction accumulation as a function of dose with curves fit to various models for radiation induced amorphization (extracted from [17]).

ical amorphization dose. An important factor to consider when looking at the critical amorphization dose is temperature, which can cause healing of the radiation induced defects. Figure 1.9 shows the dependence of the critical dose on temperature. As the temperature increases the defects become more mobile and are able to heal faster i.e. annihilate. Hence, the critical amorphization dose increases with temperature to overcome this healing effect. We can also see that there is a critical temperature,  $T_c$ , at which defect healing is faster than the rate of amorphization, thus amorphization cannot be achieved. This temperature is sensitive to the projectile ion energy and mass, and the dose rate. On the other hand, the temperature can be high enough that it can supplement to the disordering of the lattice by enabling the lattice atoms to become mobile.

Amorphization has been used as a mechanism to explain the formation of complex radiation induced nano-structures, discussed in Section 1.3. For example, *Wang et al.* [19, 20] have suggested target amorphization as a precursor to the formation of

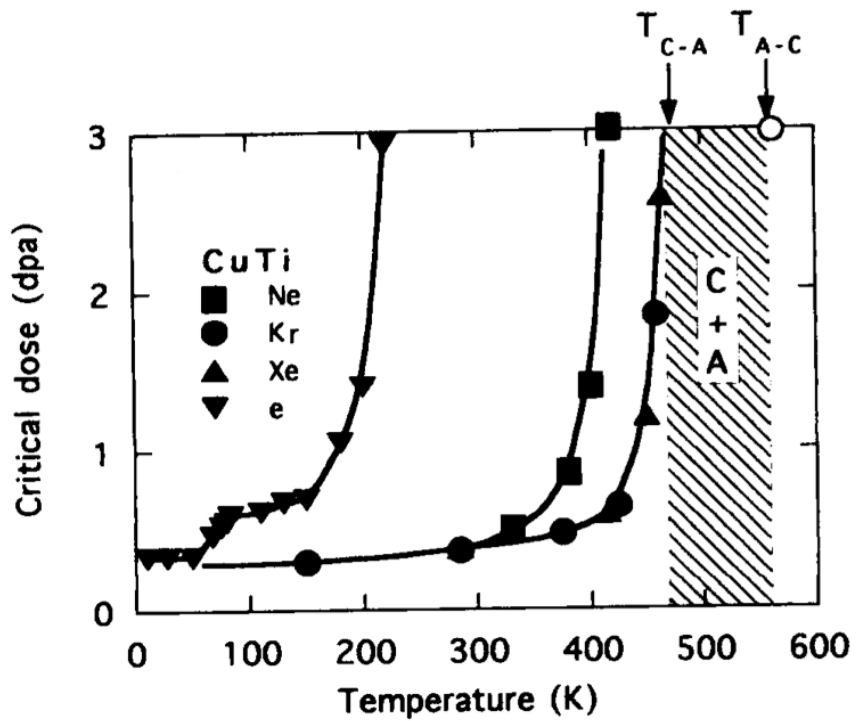


Figure 1.9: Critical amorphization dose as a function of temperature for CuTi irradiated with 1 MeV electrons and ions, all at a dose rate of  $1 \times 10^{-3}$  dpa/s. The hatched area represents the conditions where the crystalline and amorphous phases can coexist (extracted from [18]).

embedded nano-porous structures. They have shown complete amorphization of a Ge electron transparent target before the nucleation and growth of the void network. A three stage transition is suggested where complete amorphization occurs at a fluence of  $\phi_a = 1.2 \times 10^{14} \text{ ions/cm}^2$ , large density of small void nucleation at  $\phi_{vn} = 7 \times 10^{14} \text{ ions/cm}^2$  and final formation of a quasi-stable nano-porous structure at  $\phi_{np} = 8.5 \times 10^{15} \text{ ions/cm}^2$ . Similar behavior has been observed in GaSb [21] and indium antimonide (InSb) [22, 23]. High resolution transmission electron microscopy reveal that the highly amorphized fibers indeed contain nano-crystals embedded on the amorphous matrix. The nano-crystals possibly form from the amorphized matrix due to ion beam heating and thermal spiking in the material [22]. Another example is the formation of surface Ga quantum dots from the ion irradiation of a GaAs target [24]. In-situ observation of the evolution of the self-ordered quantum dots exhibit a behavior similar to the movement of liquid droplets on top of a surface.

#### 1.1.4 Radiation Swelling

Swelling is the isotropic volumetric increase in an irradiated material due to void or bubble formation and growth. This phenomena was first observed for fast breeder reactor under operational conditions, when the stainless steel cladding was observed to have undergone extreme structural changes. Figure 1.10 shows a couple of TEM micrographs with nucleated intragranular voids within the stainless steel grains. *Cawthorne* and *Fulton* showed that the swelling was due to the formation of these intragranular voids [25]. These voids can be observed to grow with an evident faceted shape. This is clear indication of void nucleation in a crystalline structure. Ceramics, such as nuclear fuels, have been observed to swell as well. In this case, most of the swelling is due to the trapping of the fission gas products in bubbles. This bubble swelling has been shown to happen from the formation of both inter- and intragranular, Figure 1.11 [26]. More recently, studies have shown that the for-

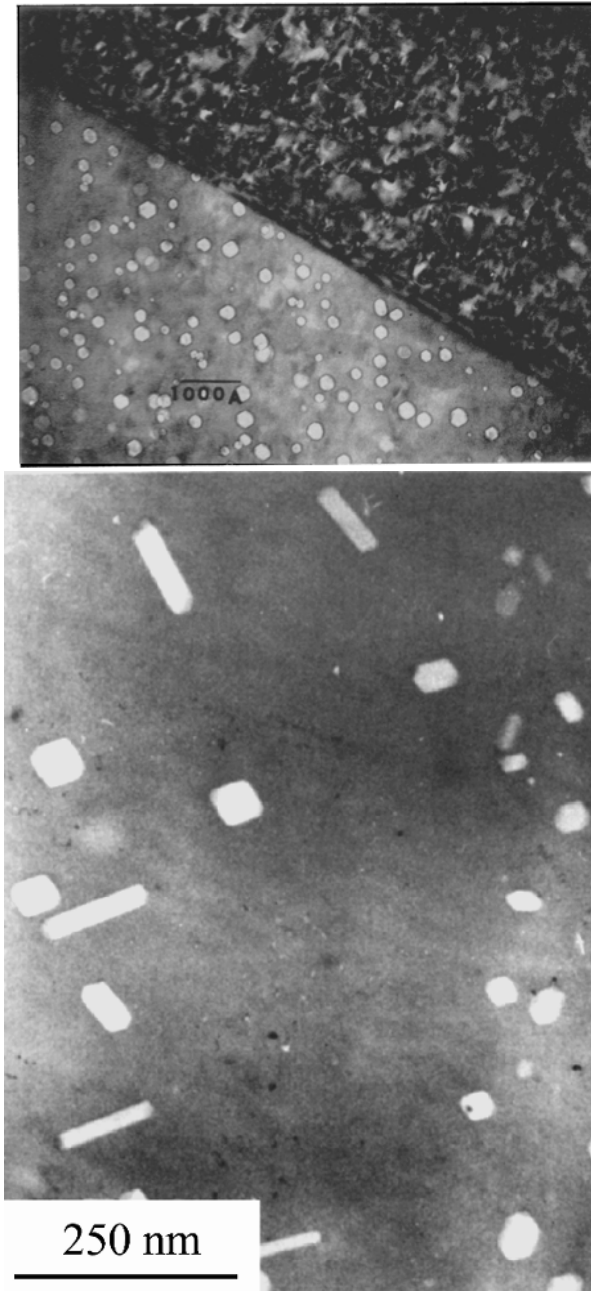


Figure 1.10: (top) TEM of two stainless steel grains showing the high dislocation density in the dark grain and the voids on the light grain [29] and (bottom) micrographs of voids in stainless steel [30].

mation of porous nano-structures in ion irradiated semiconductors leads to extreme increase in volume [19, 27, 28].

Many parameters have been shown to enhance or suppress swelling, and some-

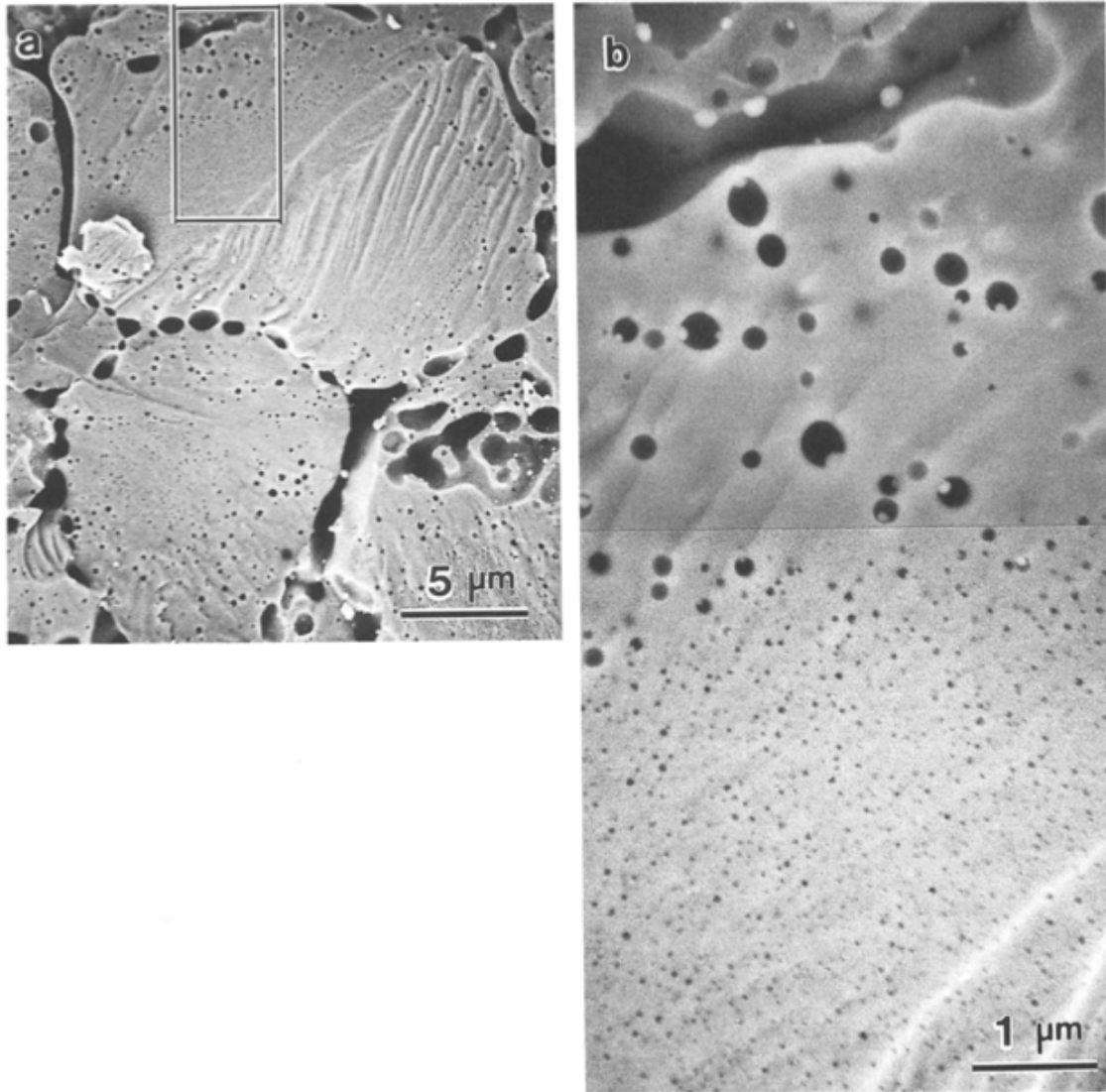


Figure 1.11: SEM of a fuel with burnup of 23 GWd/t after it was annealed. (a) inter- and intragranular bubbles nucleated and diffused to the grain boundaries, and (b) close up showing the different distribution of bubbles. It is expected that the intragranular bubbles migrate to the grain boundaries where they coalesce into the larger intergranular bubbles [26].

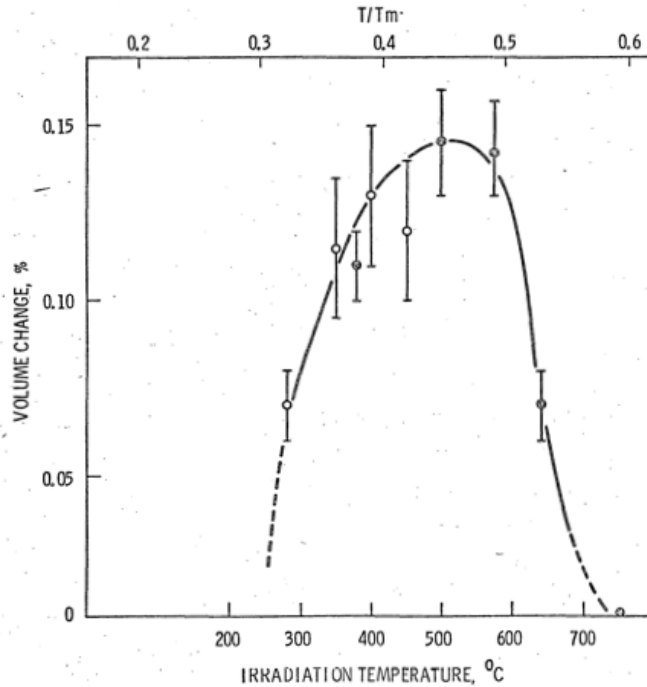


Figure 1.12: Swelling as a function of temperature on nickel irradiated to a fluence of  $5 \times 10^{19} \text{ n/cm}^2$  [32].

times both depending on the parameters magnitude. Some of these parameters include fluence, flux, microstructure, stress, temperature, *in. al.* [11, 31]. A way of understanding the dependence swelling has on these parameter is by understanding how these parameters affect the defects generated in the material. For instance, from Figure 1.12, we can see that swelling is low and with a positive slope at lower temperatures, peaks at intermediate temperatures, and decreases at higher temperatures. This is a fairly typical depiction of the effect of temperature on swelling in metals. This can be explained by the fact that at low temperatures vacancies have low mobility, which means that they can agglomerate and grow voids. As for high temperatures vacancies are emitted from the voids, shrinking the voids.

Void swelling in crystalline metals has been the subject of study for several decades. It is understood that voids nucleate by accumulation of point defect vacancies and these becoming stable in the lattice sites. They tend to coalesce into voids in the high energy crystal planes (facets) of the crystalline structure. A recent

TEM study was able to capture the nucleation and growth of a highly faceted void in magnesium irradiated by an electron beam [33]. The nucleation and “longitudinal” growth of the void is shown in Figure 1.13, while the “thickness” growth is shown in Figure 1.14. They argue that the initial growth in length is dominated by the slow nucleation kinetics of vacancy layers on basal facets and anisotropic vacancy diffusivity, while the thickness growth is driven by trying to reduce surface energy. These mechanisms are believed to be same ones that lead to the formation of the voids in Figure 1.10. While these mechanisms are able to explain the formation of these faceted voids in crystalline materials, the precise method by which voids nucleate in the amorphized semiconductors is still not well understood. Obviously, a completely different mechanism is to be expected, which leads to the very dissimilar resulting microstructures.

Of special interest to this work, is the recent studies by *Steinbach et. al.* where they irradiated Ge(100) with iodine (I) and gold (Au). The results showed that the ion species is an important swelling variable. The initial stages of void swelling are very similar with a linear increase followed by a saturation regime, which yields comparable nano-porous structures. Then, the I irradiated sample experiences an abrupt increase in swelling, which the authors attribute to a change in the nano-structure. They report the formation of a layer of differently distributed pores, which they term *netlike* porous structure. They suggest that the difference in swelling evolution is due to chemical properties of the ion beam. It should be clarified that similar structures were observed on Au irradiated GaSb as discussed in Section 1.3.1.

## 1.2 Semiconductor Properties

Semiconductors are those materials that have conductivity properties that are between those of good conductors (e.g. metals) and insulators. These materials can



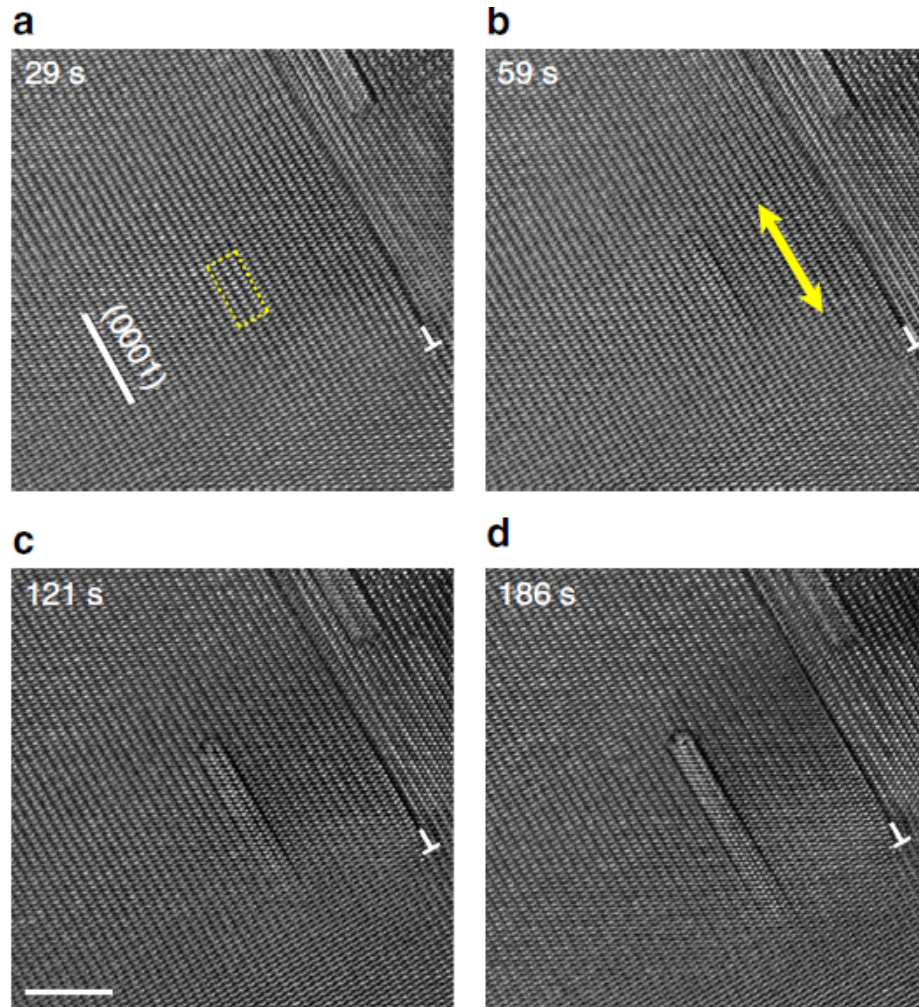


Figure 1.13: (a) A void (outlined by dashed lines) nucleated near the interstitial dislocation loop. (b–d) Stage 1 growth of the void, where it grew in length but not in thickness. The length growth direction is indicated by the yellow arrow. The specimen is irradiated over a dose range of 0.95–1.17 displacement-per-atom (d.p.a.). Scale bar, 5 nm. [33].

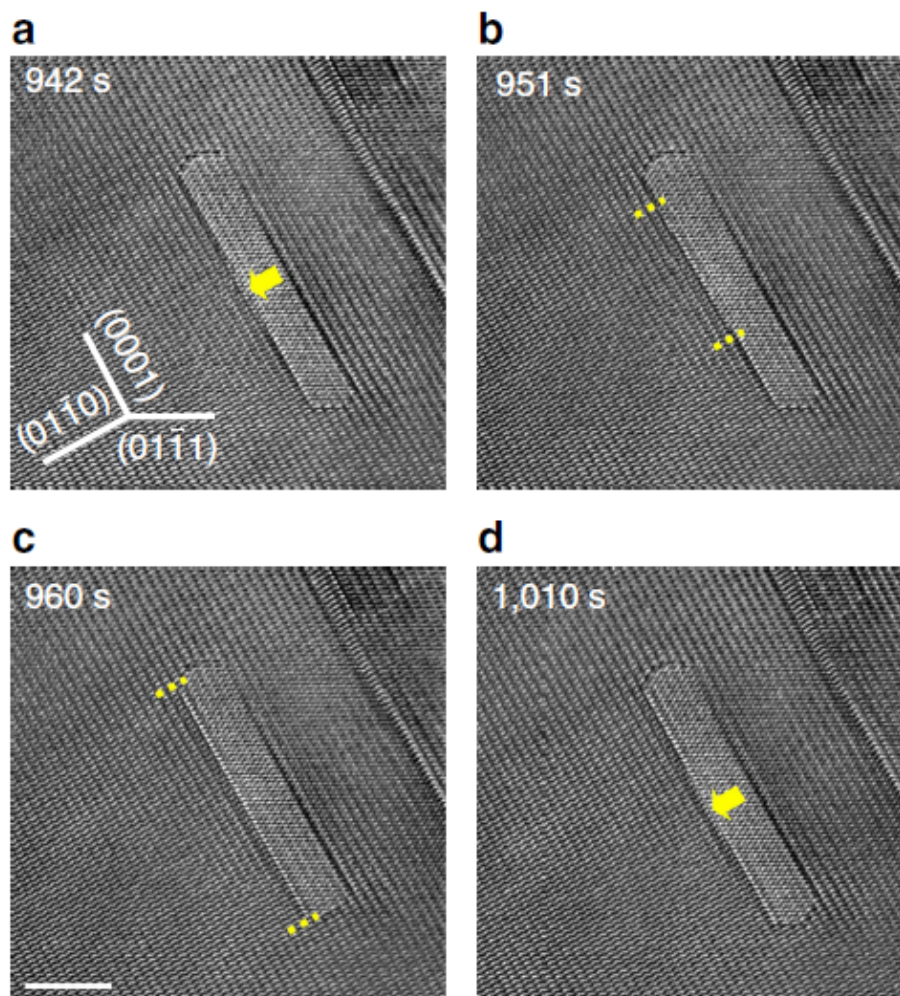


Figure 1.14: (a) First vacancy layer nucleates on the top of the (0001) facet as indicated by the yellow arrow. (b) The spreading of the vacancy layer on the (0001) facet, the size of the vacancy layer is designated by the dashed lines. (c) Vacancy layer extends over the whole (0001) facet surface. (d) Subsequent nucleation of a new vacancy layer. Scale bar, 5 nm.

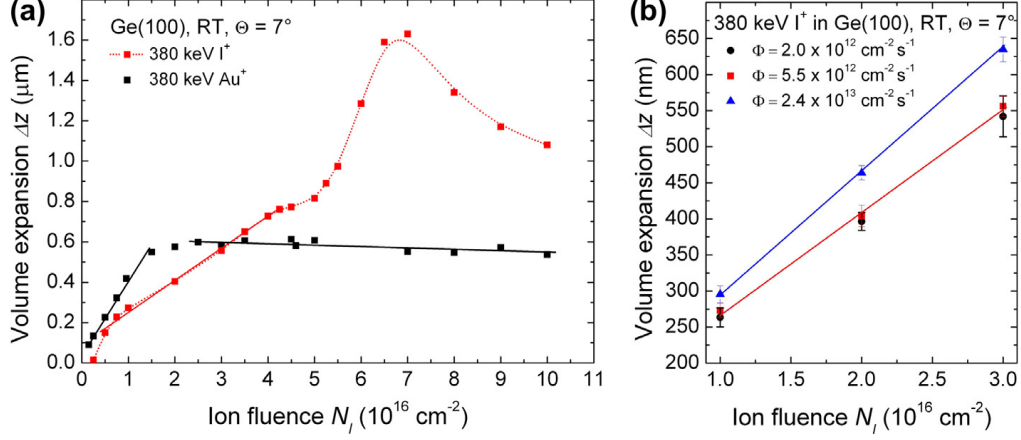


Figure 1.15: (a) Volume expansion  $\Delta z$  as a function of the ion fluence  $N_i$  for room temperature irradiated Ge with 380 keV I- and Au-ions under an angle of  $\Theta = 7^\circ$ . The solid lines exemplify the linear dependence whereas the dotted line points to the general trend. In (b) the influence of the ion rate  $\Phi$  on the volume expansion is shown for the irradiation with 380 keV I-ions [28].

also be defined as materials with a narrow band gap,  $E_g = 0.02 - 2.5 \text{ eV}$ , which is the energy range where no electron states can exist. These unique properties can be tailored by use of impurities, application of external forces (e.g. electric fields), and spatial structuring. There has been a recent push on the latter to develop nano-sized structures, which relates to the quantum confinement phenomena. The main objective of structuring such materials is the expected increase in efficiency of photo-electronic devices.

### 1.2.1 Energy Band Gap

The band gap refers to the energy difference between the valance and conduction bands in materials, which is the energy required to free an outer shell electron from its orbit. This electron then becomes a free charge carrier through the material. Matter with a large band gap are considered insulators, ones with smaller gaps semiconductors, and those with very small or no band gaps are conductors. Therefore, the energy band gap is the preferred material parameter used to describe the electrical conductivity properties of a solid.

Semiconductors have played a crucial role in the recent advances in electronic and optical modern technologies. Therefore, there is great interest in developing complex semiconductor material structures, especially *intrinsic semiconductors* like Ge and Si. Of these, the latter is the most desirable semiconductor for photoelectronic applications because of its larger band gap, which enables its uses at room temperatures. While Ge can and is widely used, the need to provide cooling is restrictive in the applicability of Ge based devices.

### 1.2.2 Quantum Confinement

When the semiconductor spatial dimensions are similar to the wavelength of the electron wave function, the electronic and optical properties of the material deviate substantially from the bulk material's properties. This phenomena is known as *quantum confinement*, and when achieved the energy band gap is increased. This leads to a blue shift in the optical properties as the size the size of the features decreases. On a bulk medium, the density of states is a continuum, as the dimensions are decreased the density changes until it becomes discretized when the particles are quantum-confined, Figure 1.16. Considering currently developed structures, quantum dots confine in three dimensions, quantum wires in two dimensions, and quantum wells in one dimension. This capability to change the material's properties by controlling the spatial dimensions has increased interest on semiconductor self-assembled structuring. We should keep in mind that ion beam irradiation has been used to generate some of these structures in a wide range of materials (e.g. Ge [19], gallium antimonide (GaSb) [34], GaAs [24], *in. al.*).

## 1.3 Radiation Induced Nano-Structuring

Ion beam processing has been used to develop complex material structures through ion beam mixing, ion beam deposition and, more recently, ion beam nano-structuring.

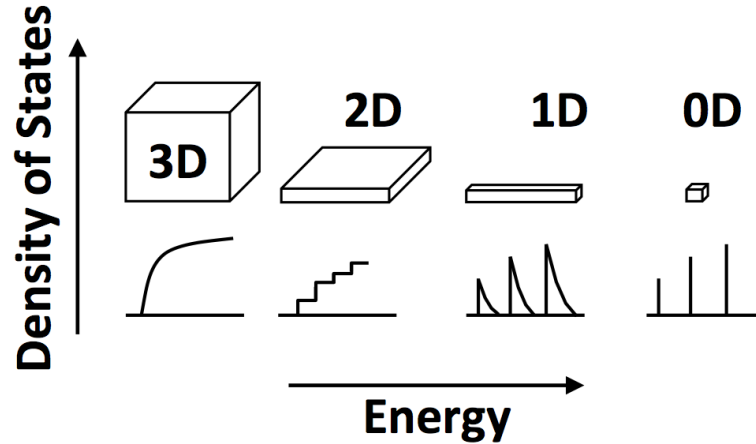


Figure 1.16: Density of states in one band of a semiconductor as a function of dimension (reproduced from [35]).

Different semiconductor materials have been observed to self-assemble into different nano-sized structures depending on the material and the irradiation conditions. Under certain conditions, the size and distribution of the self-assembled nano-structures can also be controlled. If the nano-structures can be finely tuned by changing the irradiation conditions, ion beam nano-structuring has the potential to be an effective and economy way of manufacturing quantum confining structures. On the other hand, the parameters that lead to the formation of these structures seem to be highly dependent on the irradiated material. For example, nano-porous structures have been developed under a wide range of materials [34, 23, 19, 28, 36], but has been elusive under the much desired silicon. This has been rather puzzling since these two materials have comparable properties that are usually used to study radiation damage effects. Hence, we wish to understand the true controlling mechanisms that lead to the formation of these structures. Lastly, we can divide the different types of structures into two generic categories: bulk embedded and surface structures. While we want to focus on the mechanisms that lead to the formation of the nano-porous networks, we briefly discussed both types for completeness.

### 1.3.1 Embedded Nano-Structures

When the incident ion beam has enough energy, ions are able to travel deep into the target where most of the lattice damage occurs. An intriguing feature observed on high energy ion irradiated semiconductors, is the formation of extensively interlinked nano-porous networks. In this section we look at the formation of these volumetric nano-structures.

#### 1.3.1.1 Nano-porous structure

Nano-porous networks on a Ge TEM specimen was observed by *Wang et al.* when trying to study radiation damage tolerance in amorphous structures [19, 20]. The development of radiation resistant materials has been one of the most intriguing materials challenges, especially in the nuclear energy industry. A way to describe radiation tolerance is “materials that are able to accommodate excess defects created during irradiation”. One of the material structures of interest are amorphous or disordered materials, i.e. materials lacking long range atomic ordering/periodicity. It was believed that since no long range ordering is present in these materials, irradiation would not lead to further disordering and defects could be easily accommodated in the structure.

In order to study the radiation tolerance of amorphous structures, *Wang et al.* irradiated Ge past its critical amorphization dose [19, 20], Figure 1.17. Through *in situ* TEM they observed that further irradiation leads to the formation of a highly porous uniformly distributed nano-structure, Figure 1.18. The resulting porous network suggested that the amorphous structure does not make a good radiation resistant material as clearly the material’s structural properties have been critically altered. Soon after the critical amorphization dose is realized nucleated small void-like features were observed. It can be expected that they start to nucleate at smaller fluences, and that they were not observed due to instrument limitations. It should be pointed

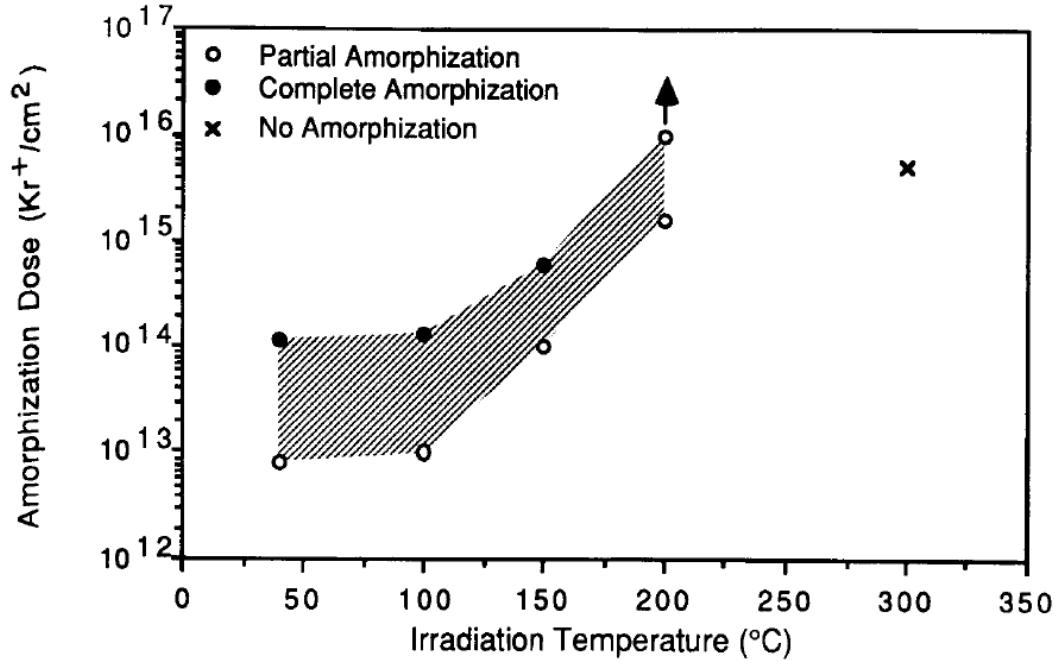


Figure 1.17: The temperature dependence of amorphization dose for 1.5 MeV Kr<sup>+</sup> irradiated Ge [20].

out that even though they are referred to as voids, the characteristics of their formation are very likely not equivalent to those of the formation of voids in crystalline materials. The process followed in the formation of the nano-porous networks can be easily appreciated by looking the “implant damage map”, Figure 1.19. We can see that as we increase the ion fluence we must transition through an amorphous region in order to achieve the nano-porous structure. Therefore, it seems that amorphization of the material is a precursor for the formation of the nano-porous networks.

Figure 1.18 shows the evolution of the microstructure with increasing irradiation dose. We can see that initially the small voids grow by absorption of radiation generated vacancies and coalesce until they lose their circular-like shape. They also report that once the circular shaped voids have evolved into the more complex porous structure, no more voids are observed to form and the existing ones simply grow without coalescing. Further, past a dose of  $8.5 \times 10^{15} \text{ ions cm}^{-2}$  the microstructure becomes fairly stable and further irradiation does not change the microstructure significantly.

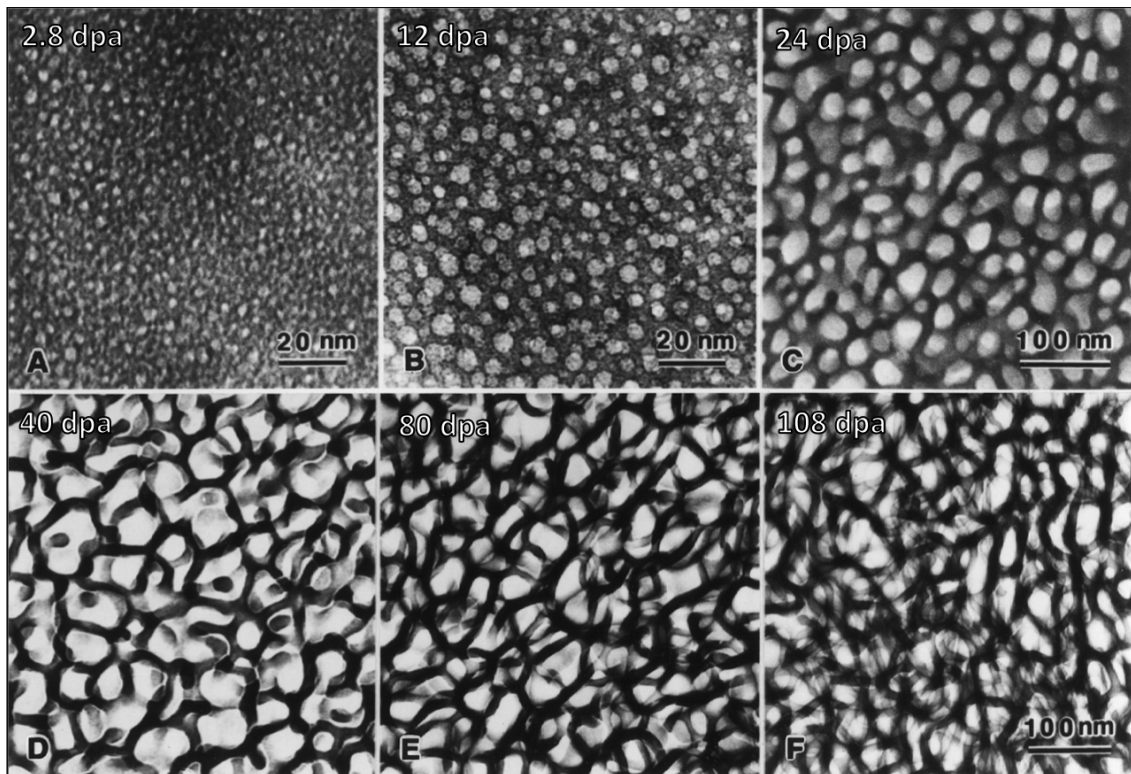


Figure 1.18: Radiation-induced nano-porous structure formation in amorphous Ge after 1.5 MeV  $Kr^+$  irradiation at room temperature to doses of: (a)  $7.0 \times 10^{14}$ ; (b)  $3.0 \times 10^{15}$ ; (c)  $6.0 \times 10^{15}$ ; (d)  $1.0 \times 10^{16}$ ; (e)  $2.0 \times 10^{16}$ ; and (f)  $2.7 \times 10^{16}$   $ions\ cm^{-2}$  [19].



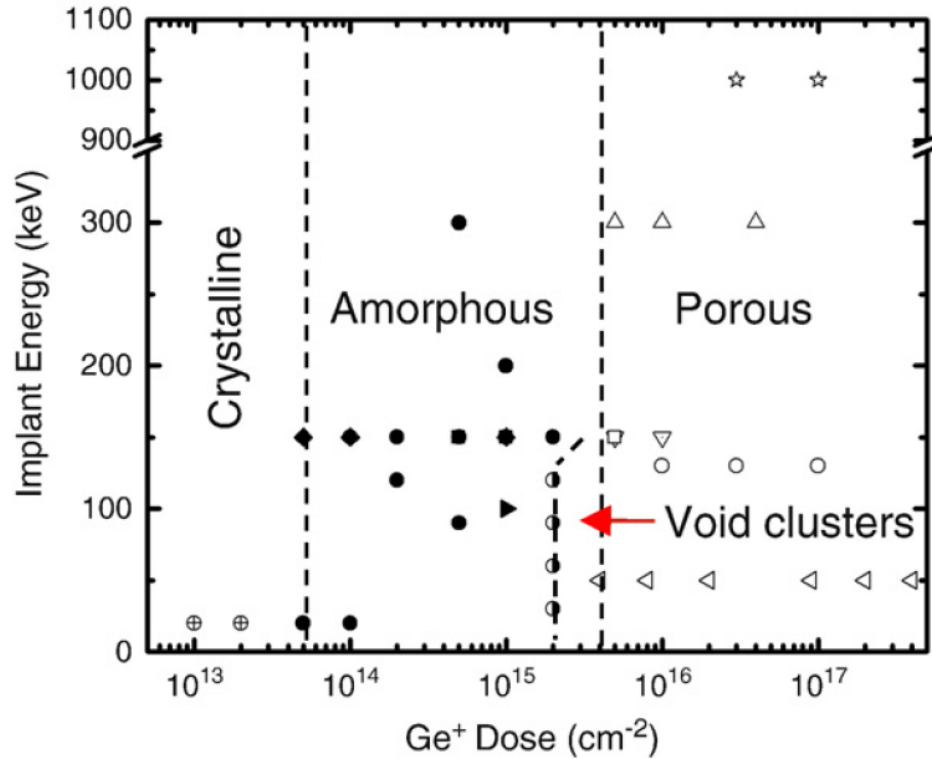


Figure 1.19: Implant damage map for self implants into Ge: threshold dose values are  $5.0 \times 10^{13} \text{ cm}^2$  for amorphization,  $2.0 \times 10^{15} \text{ cm}^2$  for void formation, and  $4.0 \times 10^{15} \text{ cm}^2$  for porous structure formation. Boxed symbol represents crystallinity, filled symbols represent continuous amorphization, half-filled symbols represent void clustering, and open symbols represent porous formation. All implants were done at room temperature. (Figure copied from Darby et al. [37]. The references to the data used are given by them.)

This nano-porous network stability is not completely understood, but a likely explanation is that the high porosity allows the ions to freely travel through the target causing minimum damage to the material. This along the fact that these porous structures have a very large surface-to-volume ratio can lead to fast healing of the defects that are created. Recent work on nano-porous Au shows that there are critical “fiber” diameters at which radiation damage will be readily annealed, Figure 1.20 [38]. *Briga et al.* argue that if the fibers are too large they will accumulate defects leading to clustering, e.g. into voids. If they are too small, collision cascades will lead to melting and breakage of the fibers. Either case leading to unstable microstructures. The damage tolerance window was computationally calculated from molecular dynamics simulations and experimentally validated, Figure 1.21. It was suggested that there is an essential balance between the damaged production and the enhanced annealing due to the large surface area.

Similar structures have been formed on binary III-V semiconductors like GaSb [34, 21] and InSb [23]. These high ion energy irradiated materials also lead to the formation of embedded nano-porous structures. *Perez-Bergquist et al.* reported the formation of a “intact” surface layer, Figure 1.22. The formation of distinct nano-scale porous regions as a function of depth was observed from cross sectional micrographs. First, we can see a uniform surface layer located at the irradiated surface. This layer deteriorates with increasing dose as the porous region leads to expansion of the subsurface region<sup>[34]</sup>. Under this layer there is a nano-porous structure with uniformly spaced pores and “fibers” that extends most of the damaged region. This layer thickness is energy and dose dependent, increasing with both of these parameters. Lastly, at the end of the porous layer, Figure 1.22(d), there is a nano-porous network nucleation layer. The pores in this region are much smaller ( $\sim 20\%$ ) than the pores in the uniform region. This region is referred to as a transition region between the nano-porous and bulk material.

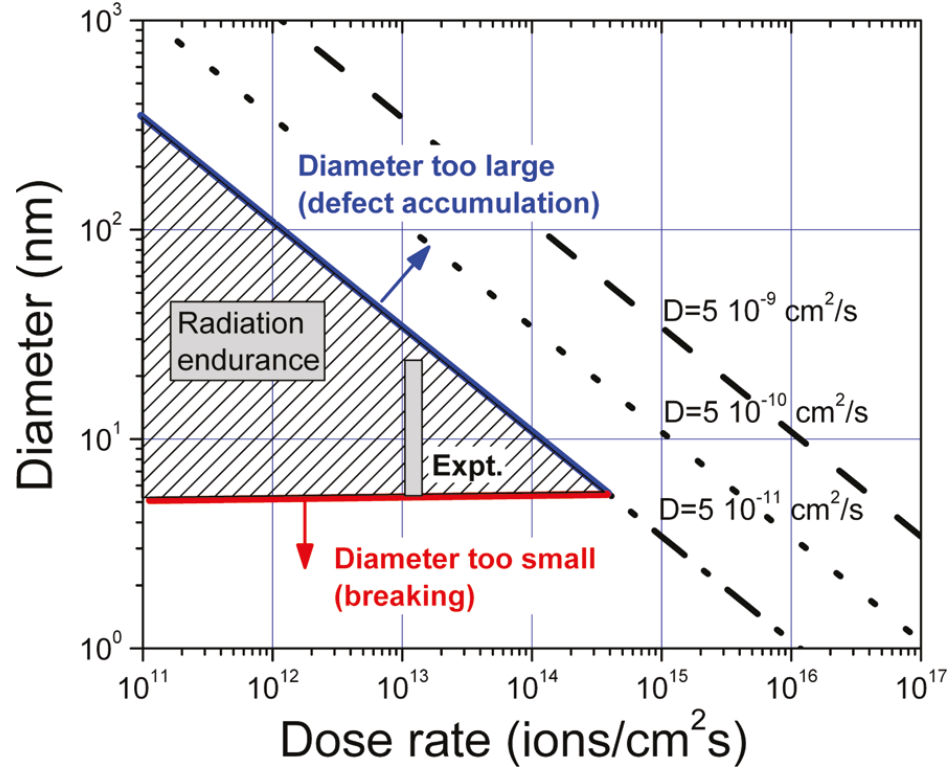


Figure 1.20: Window of radiation endurance. Map showing the window of radiation resistance (triangular area) in terms of the diameter of the foam ligaments and the dose-rate for the irradiation conditions explored in this work: 45 keV Ne ions into Au foam target at room temperature [38].

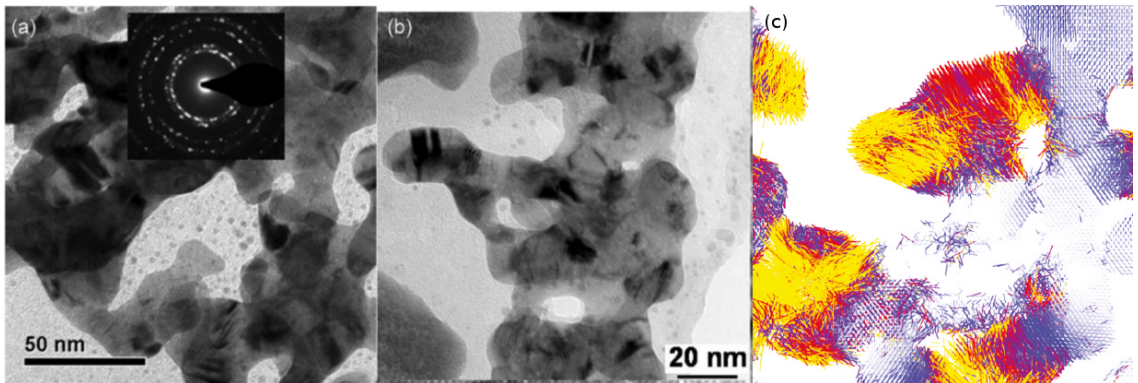


Figure 1.21: Irradiation of nanofoams, experimental results. Nanoporous Au irradiation at 77 K with 45 keV Ne+ to a dose of  $4.5 \times 10^{14}/cm^2$  ( $1.5 dpa$ ) at 300 K. (a) Unirradiated sample, including small area diffraction (SAD) pattern showing that the ligaments are polycrystalline. (b) Bright-field TEM image of np-Au after irradiation. (c) Irradiation of nanofoams, computer simulation. Small region of the sample with 45% porosity and a  $\sim 5$  nm ligament size,  $\sim 110$  ps after a cascade began, melted and recrystallized the tip of a ligament. Atomic displacements larger than the lattice parameter  $a_0$  are shown with red indicating more than  $4a_0$  [38].

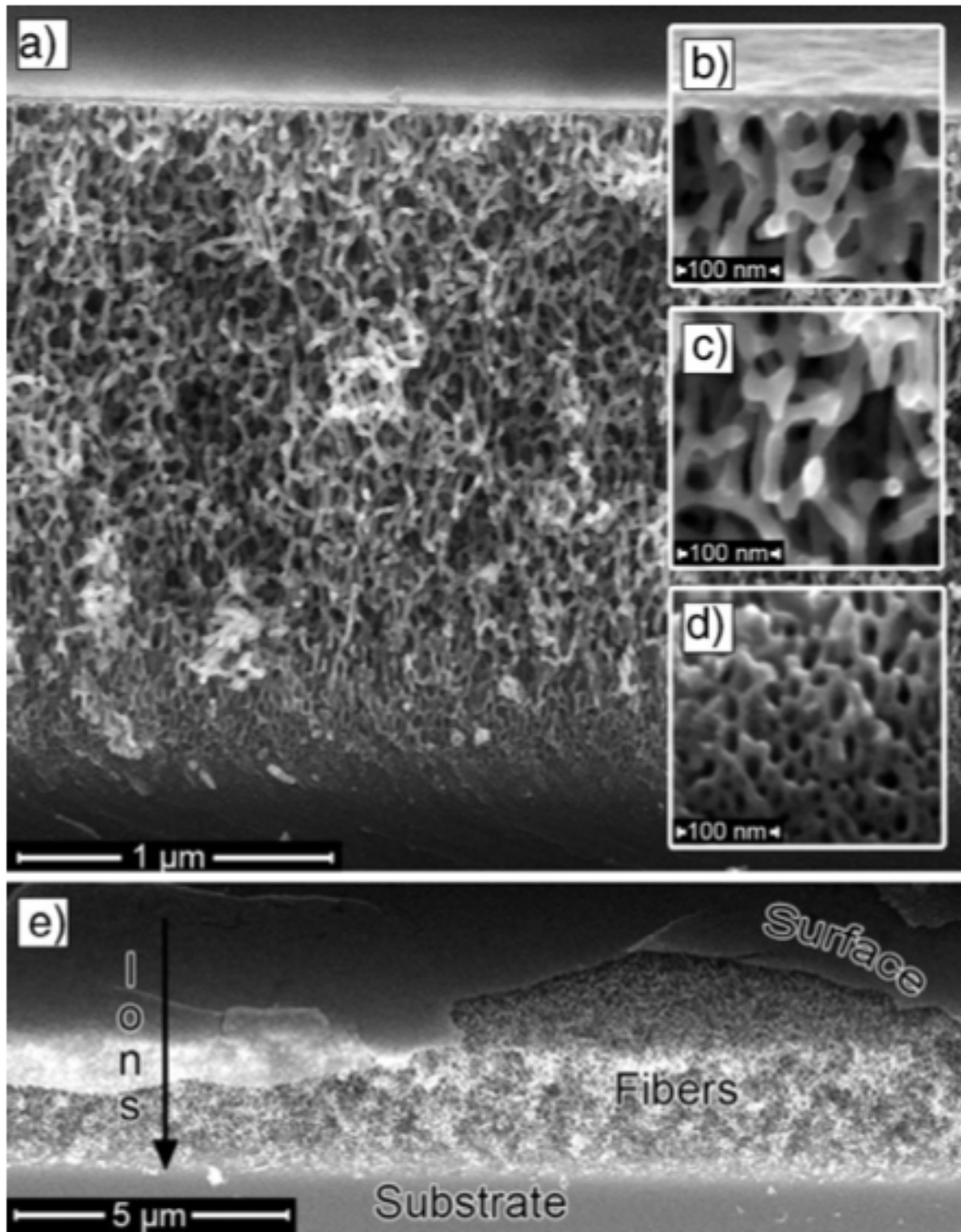


Figure 1.22: a) Cross-sectional SEM image GaSb nano-porous layer irradiated with 1 MeV Au<sup>+</sup> to  $1 \times 10^{14} \text{ ions cm}^{-2}$ . Inserts show b) the surface layer (tilted to 10° off axis), c) the presence of fully formed nano-porous region, and d) a transition regime in which the pores blend into the substrate. e) Same sample at an angled perspective, showing the incident ion beam direction, surface layer, nano-porous layer, and crystalline substrate [34].

It should be mentioned that attempts to generate these nano-porous structures in Si substrates has proven more challenging. Even though several methods have been successful in synthesizing Si nano-fibers [1], ion irradiation has not been shown to generate the desired nano-structure. *Perez-Bergquist et al.* did show the formation of porous micron-scale structures, “nano-caves”, by varying the radiation temperature [27], but were not able to generate nano-porous structures similar to the ones observed in Ge. Due to the importance of Si in the electronics field, it is of great interest to understand the mechanisms that enable the formation of said structures in Ge but not in Si. Lastly, we must acknowledge that it has been suggested that the formation of these unique structures are due to bubble swelling or sputtering. Even though the work by Wang was performed with Kr-ion irradiation, the high energy (range of  $\sim 700$  nm) and small size of the sample ( $\sim 100$  nm TEM sample) means that most of the ions traveled through the Ge. In fact, Wang reports that it is expected that  $< 1\%$  of Kr was deposited. Furthermore, similar structures have been observed with a wide range of non-noble gas ion irradiation. As for the case of sputtering, it is not expected to be able to explain the formation of the nano-porous structure deep into the bulk of the material. Additionally, GaSb has been observed to retain an intact surface layer even after a well-defined nano-porous network has been developed.

### 1.3.2 Surface Nano-Structures

Several surface nano-structures have been developed through ion beam irradiation. In order to generate these structures, the material needs to be irradiated by low to mid energy ions. Otherwise the ions would penetrate deep into the material depositing most of the ions’ energy away from the surface. The formation of these structures has been attributed to sputtering and surface diffusion mechanisms, as discussed in Section 1.4.1. In this section we will look at surface quantum dots,

nano-cones and nano-wall formation.

### 1.3.2.1 Quantum dots

Quantum dots are of interest due to their potential applications in transistors, solar cells and diodes. Ion irradiation has been used to generate them on monatomic (Si [39] and Ge [40]) and binary (GaAs [24] and GaSb [41]) semiconductors. The size and spatial distribution of the ion irradiation induced quantum dots is very sensitive to the irradiation conditions. For instance, *Wei et al.* showed that GaAs quantum dots tend to self-assemble into highly periodic hexagonal-like patterns as the ion beam incidence angle deviates from the surface normal, Figure 1.23. Continuous bombardment increases the extent of the highly ordered pattern. The highly periodic patterning is partly attributed to a shadowing effect of the angled ion beam by the droplets, once these are formed. As the angle and ion bombardment (i.e. dose) increases more energy is deposited in the surface region of the target, which enhances the nano-structuring phenomena. Furthermore, they show that the quantum dots formed on top of the GaAs target are arsenic (As)-depleted, Figure 1.24. This could be explained through sputtering mechanisms, since As has a larger preferential sputtering yield, as argued by [24]. Figure 1.25 shows a SRIM Monte Carlo sputtering calculation [5], which corroborates the expected preferential sputtering of As.

### 1.3.2.2 Nano-cones

A comparable structure formed during low to mid energy ion irradiation of certain binary semiconductors are nano-cones. These have been shown to form in InSb [23] and in GaSb [42]. As can be seen from Figure 1.26, the cones grown in the direction of the beam. This is in contradiction with predictions of sputtering and surface diffusion models that predict the formation of nano-ripples [43]. Another interesting feature is the chemical segregation and depletion of antimony (Sb) in certain regions of the

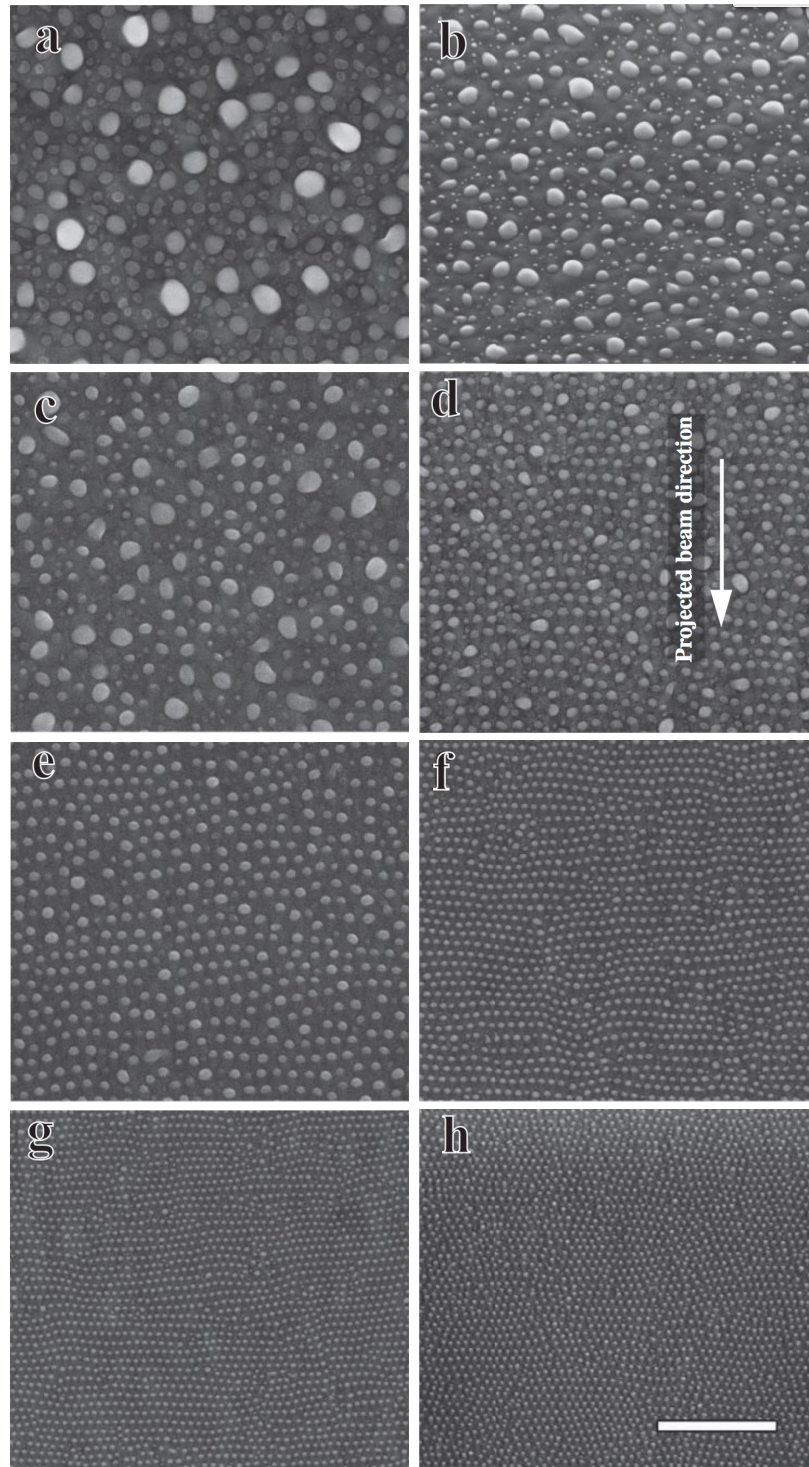


Figure 1.23: SEM images of morphological evolution of GaAs at various incident angles: (a)  $0^\circ$ ; (b)  $0^\circ$ , viewed from  $52^\circ$  to sample normal; (c)  $20^\circ$ ; (d)  $25^\circ$ ; (e)  $30^\circ$ ; (f)  $40^\circ$ ; (g)  $50^\circ$ ; and (h)  $60^\circ$ . Ion energy 5 keV, flux  $1.5 \times 10^{15} \text{ cm}^{-2} \text{ s}^{-1}$ , bombardment time 5 mins (scale bar  $1 \mu\text{m}$ ) [24].

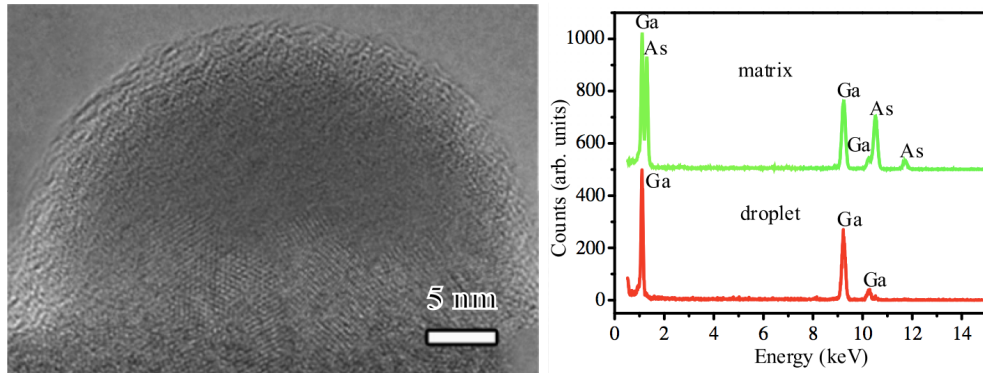


Figure 1.24: (Left) Cross-sectional TEM of a single quantum dot (droplet), and (right) EDS showing the composition of the quantum dot. Ion energy 5 keV, flux  $1.5 \times 10^{15} \text{ cm}^{-2} \text{ s}^{-1}$ , incidence angle  $35^\circ$  [24].

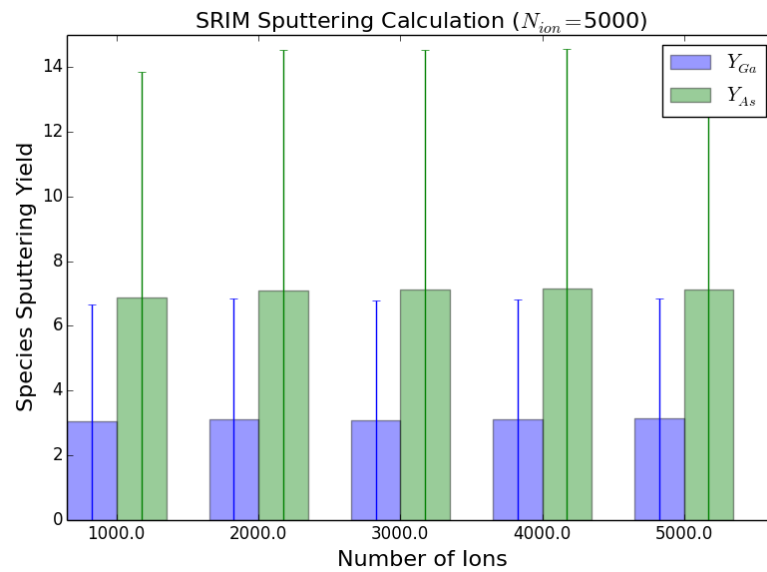


Figure 1.25: SRIM calculation of the species sputtering, as averaged for a given number of incident ions. We see that the number of ions sputtered deviates significantly, but the average is consistent with increasing dose. Simulation conditions used were those that yield quantum dots, given in Figure 1.24.



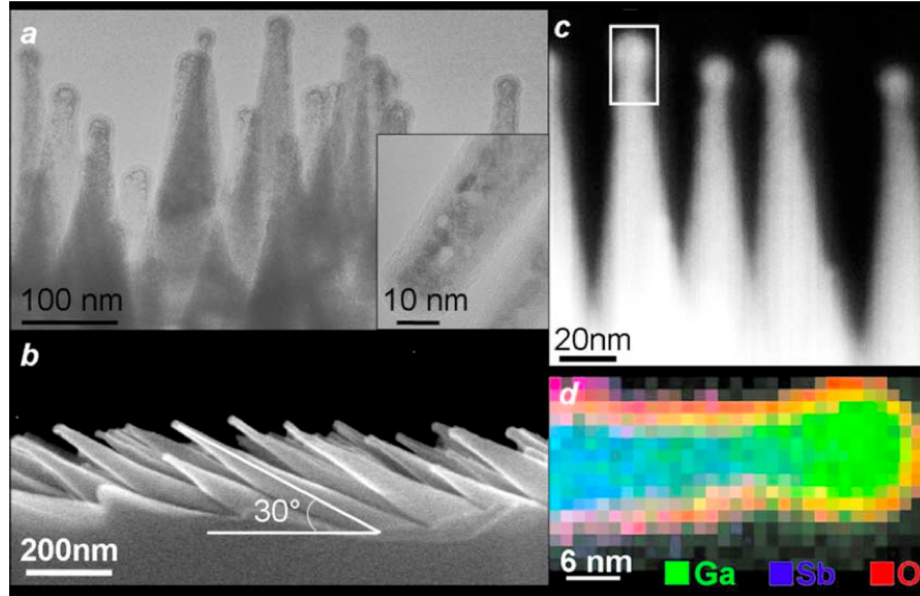


Figure 1.26: (a) BF TEM images of the nanocones, inset: zoom on the tip showing a polycrystalline structure. (b) SEM cross-section images of a surface irradiated at an incidence angle of  $60^\circ$ . (c) STEM HAADF images of the nanocones. (d) EELS spectrum imaging a tip. Ga is represented in green, Sb in blue, and O in red [42].

cones, Figure 1.26(d), which is attributed to the slightly higher preferential sputtering of Sb. A mechanism for the formation of the segregated cones was suggested by *LeRoy et al.* that combines preferential sputtering of Sb and surface diffusion of Ga to the tip of the cone. The mechanism consist of three stages: (i) preferential sputtering leading to the formation of gallium (Ga)-rich dots; (ii) a Ga-rich surface leads to the sputtering of Ga and depression of the region around the dot to form the cones; and (iii) quasi-equilibrium sputtering of Ga from the Ga-rich tip and the cone walls, and surface diffusion of Ga from the cone walls to the tip. This surface diffusion provides a continuous supply of Ga to the tip as this is being sputtered.

### 1.3.2.3 Nano-walls

In beam ion energy has a great deal of influence in the type of nano-structure generated during irradiation. Even when irradiating the same materials, the energy deposition distribution will dictate which type of nano-structure will result. For ex-

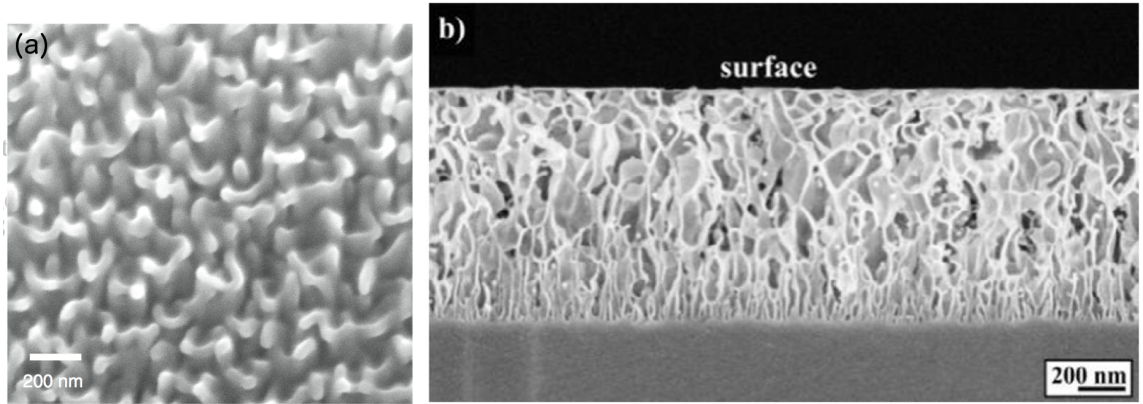


Figure 1.27: Formation of nano-walls due to low (a) energy [44] or (b) low fluence [28]. From the work by *Steinbach et al.* we can see that the nano-walls degrade as a function of fluence, which yields a “netlike” nano-porous structure.

ample, as previously discussed, high energy ion (MeV) irradiation of Ge will lead to the formation of individual fiber-like nano-porous networks, while low to mid-range energies yield nano-wall like features. Even though the resulting microstructures are quite different, the general mechanisms leading to these structures are very similar. Figure 1.28 [36] shows a schematic of the mechanism for the formation of the nano-walls. As for the nano-porous networks, we first have amorphization of the target, nucleation and coalescence of the defects and finally extension of the observed structures. Irradiation fluence also seems to have a similar effect to the energy on the type of structure that is generated [28]. Energy deposition distributions could once again explain the differences in the target structuring. It should be pointed out that these nano-wall could possibly be the precursor structure to the fiber-like nano-porous structuring, although they do achieve a stable structure. Similar energy deposition dependence on nano-structuring behavior has been reported for other types of semi-conductors, e.g. InSb [23].

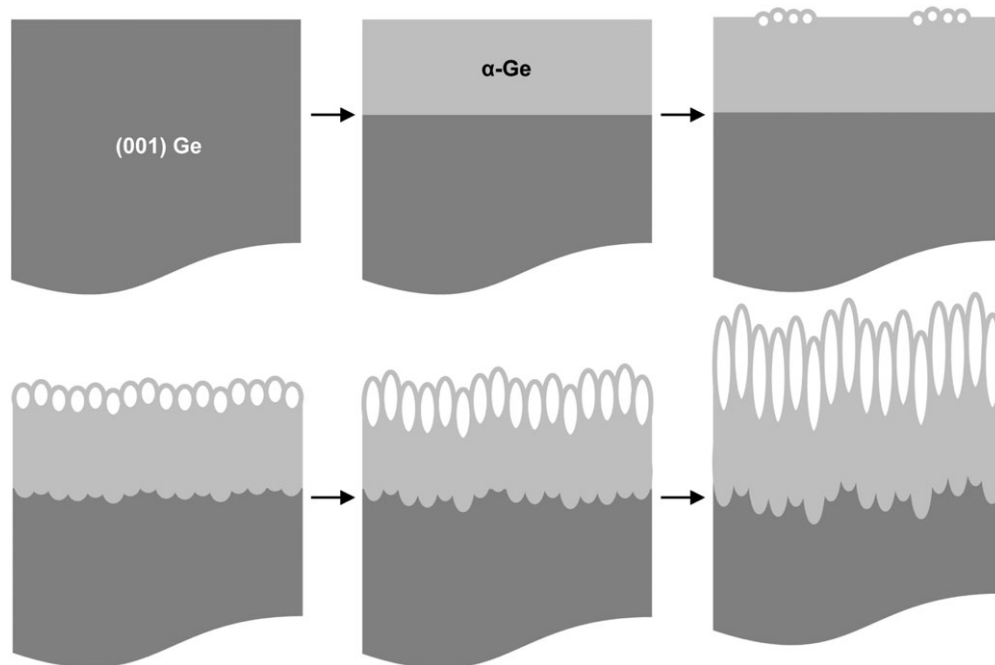


Figure 1.28: Schematic representation of the microstructural evolution of Ge with increasing ion dose; the starting material is single crystal Ge, but with increasing dose an amorphous layer is formed; as the dose increases further, small clusters of near-surface pores nucleate; as the dose increases further, the pores cover the whole surface and elongate into the wafer, forming the nanostructured morphology; as the dose increases further, the pores elongate further and the material experiences a large out-of-plane expansion with the nanostructured region existing on top of a nonporous amorphous layer. In all cases, the surface roughness and roughness of the amorphous/crystalline interface increase with increasing ion dose. [36]

## 1.4 Modeling of Radiation Effects

This work focuses on the development of computational numerical models that are able to simulate the unique radiation induced microstructural changes previously discussed. Computational models have been extensively used to model different types of radiation related changes in materials. In this section, we briefly examine several models and computational techniques that have been employed in the simulation of radiation induced effects.

### 1.4.1 Bradley–Harper Model

Ion irradiation induced sputtering has been suggested as the controlling mechanism for the formation of the nano–structures presented earlier. This is especially true of the surface nano–structures, Section 1.3.2. These were studied in depth by *Sigmund* [45], when he developed a theory to explain how the surface local curvature influences the total sputtering yield. Basing their model on Sigmund’s theory, Bradley–Harper (BH) developed a model that accounts for both sputtering and surface diffusion as the main mechanisms for the formation of radiation induced surface structures. According to Sigmund’s theory, regions down the slope in the valley have a larger energy deposition than regions close to the peak, Figure 1.29. Therefore, as detailed in Section 1.1.1, since the sputtering yield is proportional to the energy deposited by the ion, the sputtering yield at the valley is larger than at the peak. This leads to an enhancement of any small intrinsic roughness that may be present.

Bradley–Harper showed that during low energy ion irradiation, the target is subjected to surface instability mechanisms where sputtering and surface diffusion lead to roughening and smoothing of the surface, respectively. BH developed a continuum

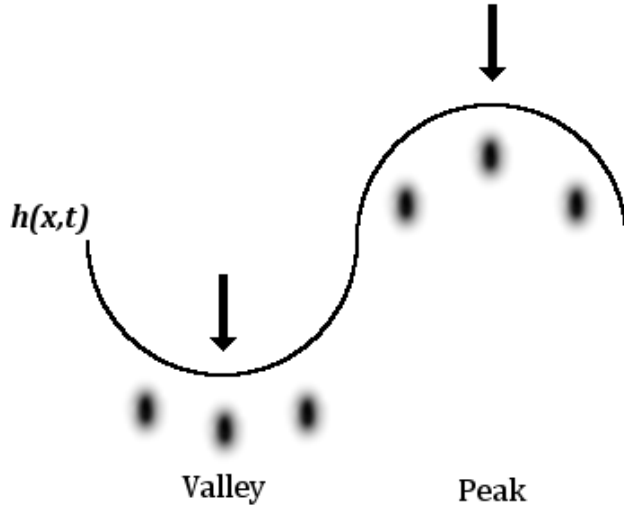


Figure 1.29: Schematic of an undulated surface being irradiated from the top. The shaded regions represent the energy being deposited, which can be assumed to be Gaussian shaped. This initial undulation of the surface is due to the natural material roughness and the stochasticity of the radiation damage processes [46].

PDE for the surface height,  $z = h(\mathbf{x}, t)$ , to model radiation induced nano-ripples,

$$\frac{\partial h}{\partial t} \approx \underbrace{-v_0(\theta) + v'_0(\theta) \frac{\partial h}{\partial x} + \frac{fa}{n} Y_0(\theta) \left[ \Gamma_1(\theta) \frac{\partial^2 h}{\partial x^2} + \Gamma_2(\theta) \frac{\partial^2 h}{\partial y^2} \right]}_{\text{Sputtering}} - \underbrace{B \nabla^2 \nabla^2 h}_{\text{Surface Diffusion}} \quad (1.25)$$

where  $v_0$  is the rate of erosion of the planar surface,  $f$  is the ion flux,  $a$  is the average depth of energy deposition,  $n$  is the atomic density,  $Y_0$  is the sputtering yield,  $\Gamma_{1,2}$  are geometric curvature dependent coefficients, and  $B$  is a surface diffusion coefficient. The terms grouped under *sputtering* lead to surface instability, while the terms under *surface diffusion* stabilize the surface. This model has been useful in describing surface ripple formation during the initial linear stages.

Lastly, we should point out that recently *Madi et al.* argued that the mechanism that control the surface evolution is the mass redistribution of the atoms not sputtered [47]. Fitting of grazing incidence small angle X-ray scattering experimental data to curvature coefficients derived from the BH and mass redistribution models seem to agree with their assertions, Figure 1.30. A reasonable explanation to why

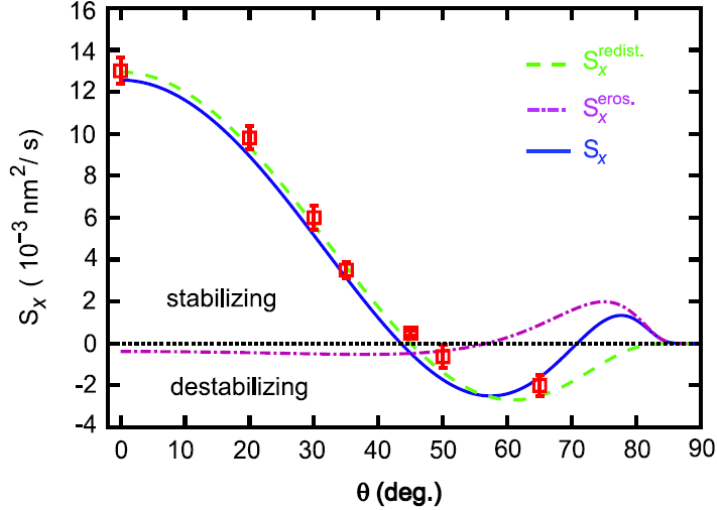


Figure 1.30: Dependence of the best-fit quadratic coefficient  $S_X(\theta)$  and theoretical curves  $S_X(\theta) = S_X^{\text{eros.}}(\theta) + S_X^{\text{redist.}}(\theta)$  on deviation from normal ion incidence.  $S_X^{\text{eros.}}(\theta)$  is from BH theory modified by the Yamamura correction function with no free parameters.  $S_X^{\text{redist.}}(\theta)$  is our implementation of the Yamamura correction on the CV redistributive model with a single free parameter as discussed in the text. [47].

mass redistribution could cause such surface nano-structuring is due to lattice mismatching of the reordered atoms. This mismatch increases the local elastic strain energy. To offset this strain energy, quantum dots could form on the surface, which in turn increases the surface energy. This has been proven as the controlling mechanism for the formation of quantum dots (or *islands*) during heteroepitaxial growth [48, 49]. This process is known as *Stranski-Krastanov* growth.

### 1.4.2 Monte Carlo Modeling

One of the most widely used modeling techniques for simulating microstructural evolution consists of random sampling of the different allowable ensembles, i.e. configurations, otherwise known as Monte Carlo (MC) methods. MC methods have been applied to several material's microstructural (grain growth [50, 51], texture evolution [51], heteroepitaxial growth [52]), intragranular bubble swelling [53], as well as wide range of radiation damage parameters [5], *inter alia*. In general, Monte Carlo methods are a computational tool that relies on the stochastic nature of certain pro-

cesses in order to model them.

One of the most employed variant of the MC methods is known as the Potts, or  $Q$ -state, MC method [54], which was developed as a generalized extension of the Ising model [55]. Each one of these  $q_i$ -states can be a representation of the material's local phase, grain orientation, *inter alia* [56]. The Potts model is a discrete statistical model, which has been extensively applied to grain growth kinetics [50, 57]. For the standard implementation, the Hamiltonian of the system is given by the equation of state

$$H = E_{gb} \sum_{i=1}^N \sum_{j=1}^n (1 - \delta_{q_i q_j}) \quad (1.26)$$

where  $E_{gb}$  is a measure of the grain boundary/interface energy,  $N$  is the number of particles in the system,  $n$  is the number of neighbors surrounding site  $i$  and  $\delta_{q_i q_j}$  is the Kronecker delta which is given by

$$\delta_{ij} = \begin{cases} 1, & i = j \\ 0, & i \neq j \end{cases} \quad (1.27)$$

The equation of state has been adapted to include several types of energetic contributions suitable for different applications, e.g. strain energy and bulk free energy [53] and polycrystal plasticity energy [58]. The system energy allows us to determine if a certain ensemble is favorable, i.e. if a transition is likely to occur. An example would be grain growth where site  $i$  attempts to change states to that of site  $j$ ,  $q_i \rightarrow q_j$ . To determine whether the change will be allowed, the standard Metropolis algorithm can be employed. Therefore, the probability that this particular exchange will happen is given by following the Boltzmann statistics, such that

$$P_{q_i \rightarrow q_j} = \begin{cases} 1, & \Delta H \leq 0 \\ \exp\left(-\frac{\Delta H}{k_B T}\right), & \Delta H > 0 \end{cases} \quad (1.28)$$

where  $\Delta H$  is the change in the energy of the system before and after the exchange,  $k_B$  is the Boltzmann constant and  $T$  is the absolute temperature. The temperature parameter  $T$  does not represent the actual experimental temperature, but a parameter of the probability of transition between states. The transition probability is then compared to a uniformly distributed random number,  $RN = [0, 1)$ , to determine the *transition acceptance*

$$k_{ac} = \begin{cases} \text{accept} & RN < P_{q_i \rightarrow q_j} \\ \text{reject} & RN \geq P_{q_i \rightarrow q_j} \end{cases} \quad (1.29)$$

### 1.4.3 Phase Field Modeling

The phase field method has also been used to simulate many of the same phenomena as the MC methods, e.g. grain growth [59, 60]. The main difference between the two techniques is the way that they achieve a solution to the system: MC is based on stochastic sampling of ensembles by use of discrete fields and phase field solves sets of PDEs that describe the evolution of continuum fields *deterministically*. The fundamental idea of this method is to define smoothly varying *fields* that describe the state of the system.

Each parameter of interest will be defined by its own *order parameter* (field), such that the set of order parameters are able to describe the phenomena of interest, e.g. microstructural evolution. For example, let's consider an order parameter that represent the actual phase of the material,  $q$  composed of a precipitates within a matrix. Then the order parameter is  $q = 0$ ,  $q = 1$  and  $0 < q < 1$  for the precipitate, matrix and interfaces, respectively. This is schematically shown in Figure 1.31 for the interface between the matrix and precipitate. This particular order parameter can be considered to be like the plot shown in Figure 1.31(b), which is known as a diffuse interface. In other words, the transition between the precipitate and the matrix is



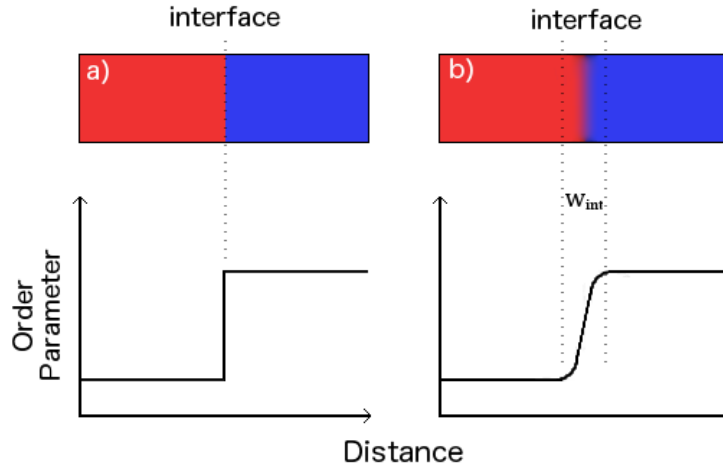


Figure 1.31: Drawing of two different types of interfaces: a) sharp, and b) diffuse. The red region represents a precipitate and the blue the matrix

not *sharp*, but continuous and characterized by the interface width,  $w_{int}$ .

#### 1.4.3.1 Cahn–Hilliard Equation

An important implementation of the phase field model was developed by Cahn–Hilliard to study spinodal decomposition. They derived the Cahn–Hilliard equation to describe the evolution of the concentration field, which is driven by the chemical potential [61, 62, 63, 64]. This model was later extended by *Allen* and *Cahn* to couple the concentration and phase fields to describe microstructural evolution [65]. The Cahn–Hilliard equation has been very useful for material scientists in simulating a wide variety of phenomena.

The Cahn–Hilliard model has been also applied to the modeling of the formation of the porous nano–structures, discussed in Section 1.3.1.1 [44, 66]. This is, to the best of the author’s knowledge, the first and only attempt at modeling the formation of the porous nano–structures. There have been other Cahn–Hilliard models developed to model bubble [67] and void [68, 69, 70] swelling of metals, but not the formation of the extended microstructures previously discussed. *Li et al.* implemented an adapted Cahn–Hilliard equation, which includes terms for the defect creation ( $\xi_0$ ),

recombination ( $\xi_{rc}$ ) and re-deposition ( $\xi_{rd}$ ) rates

$$\frac{\partial\phi}{\partial t} = \underbrace{\xi_0 - \xi_{rc}(1 - \phi) - \xi_{rd}\phi}_{\text{Radiation damage}} + \underbrace{\frac{M}{N^2}\nabla^2\left(\frac{\partial g}{\partial\phi} - 2k\nabla^2\phi\right)}_{\text{Cahn-Hilliard}} \quad (1.30)$$

where  $\phi$  is the order parameter,  $M$  is the mobility,  $N$  is the number of atomic sites per unit volume,  $k$  is the gradient energy coefficient and  $g(\phi)$  is given by the regular solution equation

$$g(\phi) = g_v\phi + g_a(1 - \phi) + k_BNT[\phi\ln\phi + (1 - \phi)\ln(1 - \phi)] + \Omega N\phi(1 - \phi). \quad (1.31)$$

*Li et al.* were able to produce very elegant results, Figure 1.32, but they had significant shortcomings like the lack of a physical connection between the experimental parameters and the computational ones. This is true of most models, but no clear relationships could be established between the kinetics controlling rates and the physical processes. Furthermore, Li's model essentially is solving the spinodal decomposition of a two well system, much too similar as many other spinodal decomposition models. Hence, while the results yield very interesting microstructures it is complicated to attribute the resemblance to the adaptation of the Cahn-Hilliard model.

## 1.5 Comments on the Formation of Nano-porous Structures

The mechanisms that lead to the formation of the porous nano-structure have been debated ever since they were first observed. Due to their initial spherical shape and since krypton was used as the irradiating projectile of the Ge, it was suggested that the nano-pores were Kr nano-bubbles. As Wang explained, the ion range of Kr in Ge under the experimental conditions is  $\sim 700$  nm. They also point out that the irradiated sample was electron transparent, i.e. with a thickness of  $< 100$  nm. Therefore, it is expected that most of the ions travel through the transparent target.

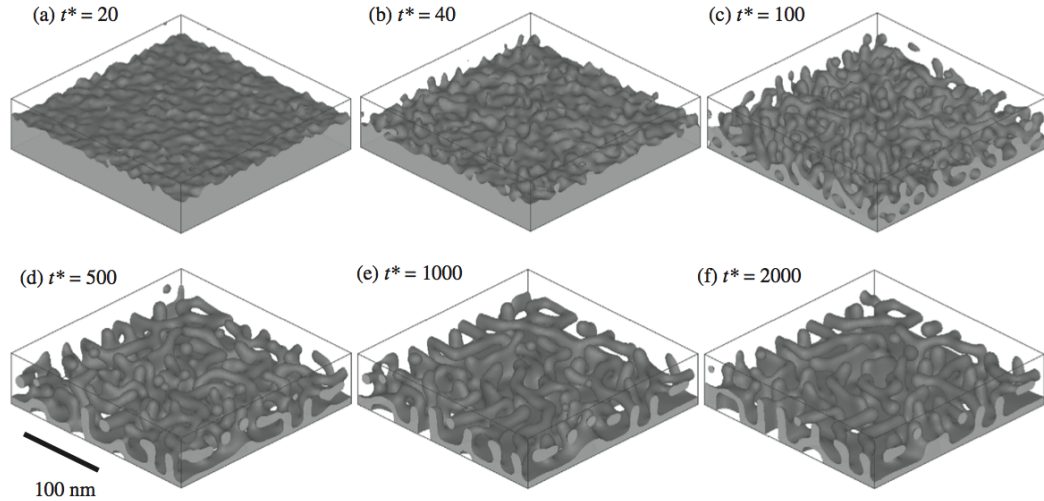


Figure 1.32: Formation and evolution, in arbitrary time units, of nanowalls under a medium ion energy irradiation as calculated by Eq. 1.30. [44].

More recently, metallic ions have been used to generate similar structures, which seem to discredit the notion that the nano-porous structures are a result of gases nucleating nano-bubbles.

Another mechanism suggested is that of extreme sputtering. This argument can be invalidated by the recent observation of the embedded nano-pores under an intact surface layer. Also, the nano-porous region has been observed to grown in thickness deeper into the target with irradiation dose and energy. Hence, even if there was sputtering at the end of the ion range, it would be redeposited into the surrounding fibers. Perhaps working as a mechanism to grow the fibers, which has not been observed.

### 1.5.1 Qualitative Models

From all the qualitative descriptions of the phenomena that leads to the formation of the nano-porous structures, *Nitta et al.* [71] presented the most compelling one. As the material is irradiated, mobile point defects are created within the target matrix. The interstitials that survive recombination rapidly diffuse to the free surface (sink) where they are annihilated. Meanwhile, the vacancies remain in close vicinity to

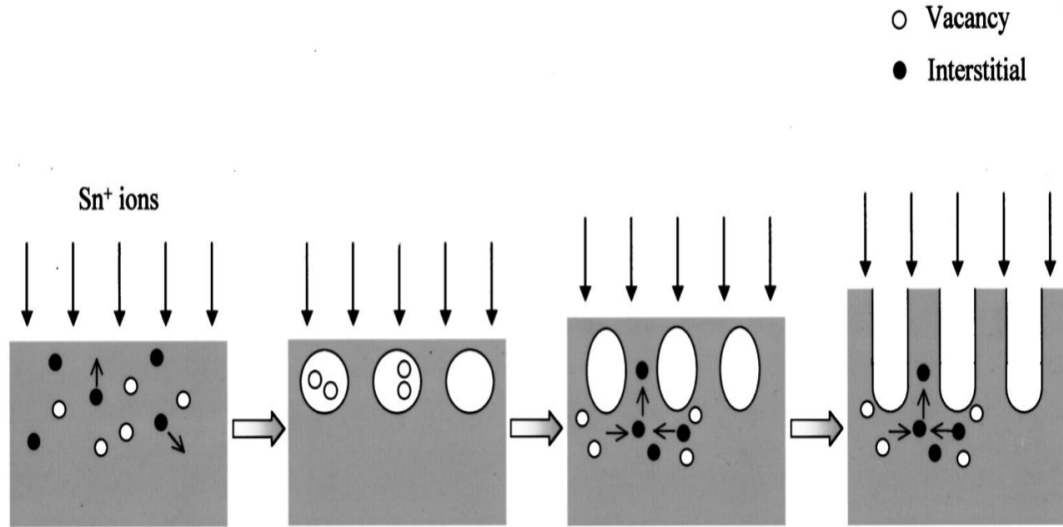


Figure 1.33: Qualitative model describing the formation of the nano-structures. (i) The point defects are created by ion implantation, with the more mobile interstitials migrating. (ii) Voids nucleation during the early stage of irradiation. (iii) Surviving interstitial atoms migrate and aggregate under the walls, increasing their height. (iv) The voids grow perpendicular to the surface until they burst.

where they were created, where they can nucleate into voids. Vacancy annihilation at the void surface then leads to the growth of the void in the downward direction, while interstitial diffusion along the walls separating the voids leads to the walls increasing their height. In their description, these two mechanisms lead to the formation of the columnar features shown in Figure 1.33. The model describes the formation of the nano-walls discussed in Section 1.3.2.3. *Perez-Bergquist et al.* [34] extended this qualitative model to include the formation of the embedded nano-porous networks and the nucleation of the transition zone, as discussed in Section 1.3.1.1. Figure 1.34 shows a schematic of *Perez-Bergquist's* qualitative model.

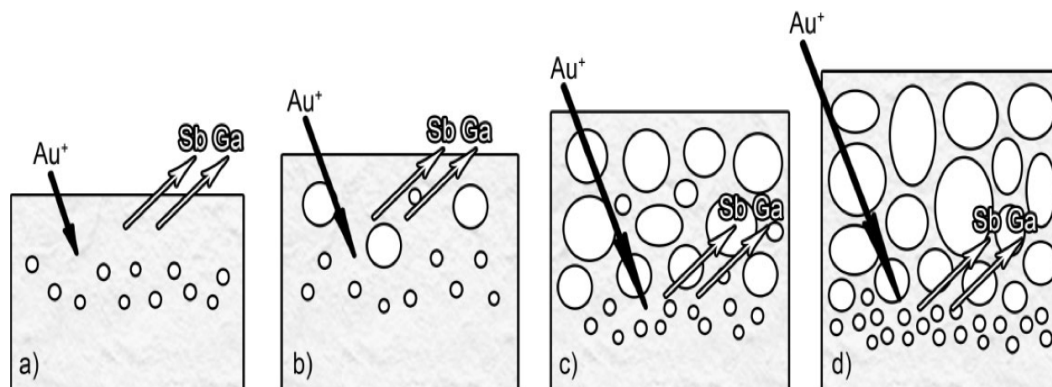


Figure 1.34: Adaptation of the *Nitta* model by *Perez-Bergquist* to explain the formation of a “transition layer” and a quasi-stable intact surface layer. The transition layer is formed as the ions are able to penetrate deeper into the highly porous target.

## CHAPTER II

# Development of the Hybrid Model

Ion irradiation induced nano-structuring is a multi-scale multi-physics phenomena that cannot be trivially explained. This is especially true for the embedded nanoporous structures, which has different types of features that span several orders of magnitude. There have been attempts at modeling these phenomena as explained in Section 1.4.3.1 [72, 44, 66]. Unfortunately, these models lack elements that are able to properly couple and describe these physical processes. In order to enhance the previous attempts at modeling these phenomena, a multi-scale model that combines deterministic and statistical methods has been developed. The motivation for using a deterministic-statistical hybrid model is trying to draw from the advantages that each of these computational approaches provide. This chapter discusses the development of the computational model that aims at properly approximately describing these multi-scale processes.

### 2.1 Microstructural Representation

The hybrid model can be executed in rectangular (2D) or cuboid (3D) geometries, as defined by SPPARKS (discussed in Section 2.8). These geometries are digitized into a voxelated mesh, where each voxel's state is defined by a set of continuum and discretized fields. The correct description of the microstructure is given by these

fields which can be representative of: atomic and defect composition (continuum), and phase, spin or feature (discrete). Each mesh voxel within the simulation domain has a corresponding set of different fields describing its particular state, as discussed in the next sections. These parameters are tailored for each model and discussed for each individual simulation.

### 2.1.1 Spin

The spin order parameter ( $s$ ) is an integer discrete value that is assigned to each voxel and it identifies the site’s “energetic state” level. It can be representative of different state characteristics like grain orientation, texture, inter alia. Therefore, the model is able to simulate single, polycrystalline materials and amorphous (or materials lacking long range crystallinity), depending on the simulation specifics. Figure 2.1 shows a polycrystalline microstructure where each color represents a given grain orientation. Interfaces, in this example a grain boundary, are identified by the interface between two differently colored voxels. One of the main uses for this parameter is for grain growth calculation using the Potts Monte Carlo model.

### 2.1.2 Phase

The phase order parameter ( $q$ ), much like the spin, is an integer discrete value that describes the voxel’s thermodynamic state. Therefore, it is essential for the respective thermodynamic calculations. One main difference between spins and phases is that while a phase can have several grain orientations (spins), a single crystal will be composed of a single phase. This field must be carefully defined for each particular simulation, especially when employing models that make use of the free energy functionals, e.g. Cahn–Hilliard model. Furthermore, it should be pointed out that this field could be used to define different types of features. For instance, we could define a void to be a particular phase in a swelling model. Other features which have

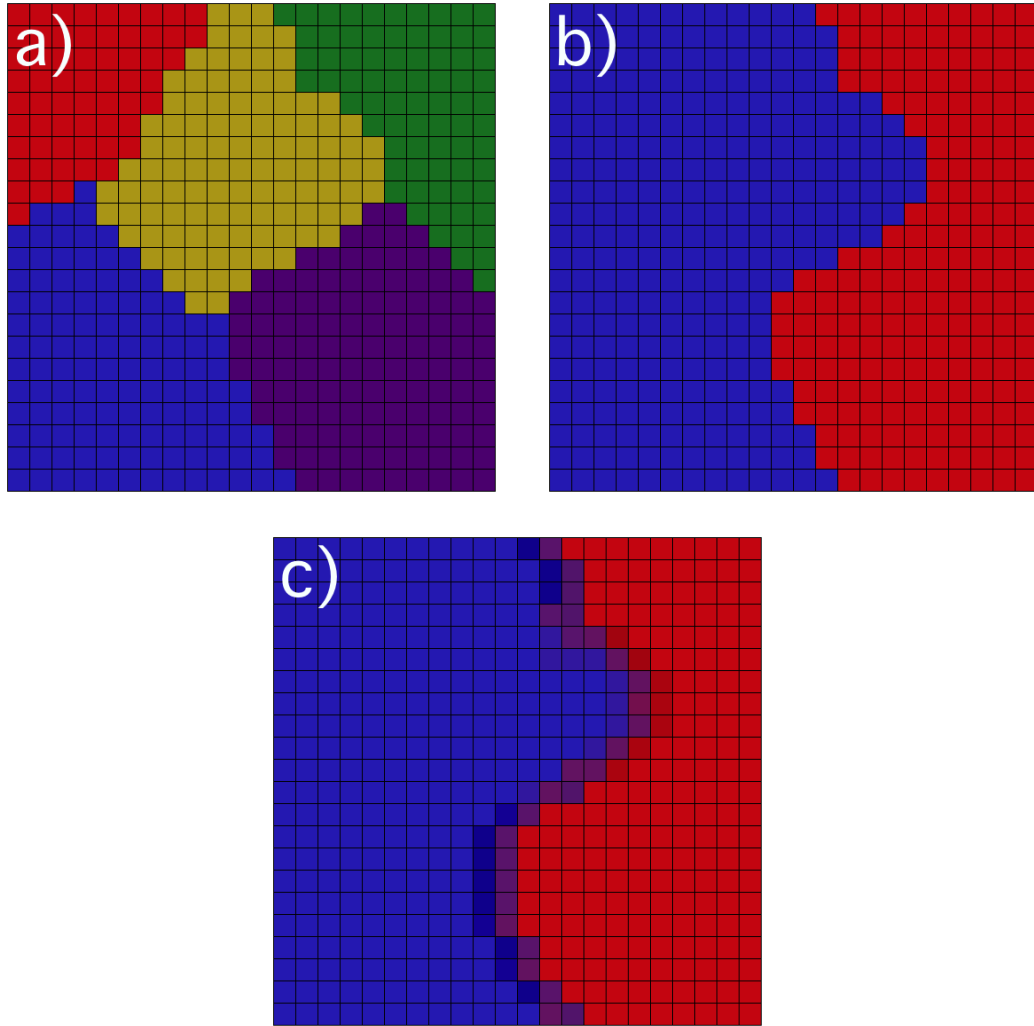


Figure 2.1: Schematic of a polycrystalline material as defined by its grain ID, phase and concentration and represented by a digitized voxelated microstructure. a) Representation of the grain ID, where each color defines a particular grain orientation. b) The phase of each particular grain is visualized for this  $\alpha$ (blue)– $\beta$ (red) system. c) The smoothly varying concentration field of the binary system. If looking at the concentration from left to right we go from a high concentration of  $A$  ( $C_a \rightarrow 1$ ,  $C_b \rightarrow 0$ ) to a low concentration ( $C_a \rightarrow 0$ ,  $C_b \rightarrow 1$ ) with a smooth variation in between.



been used in the past include: bubbles, defect clusters, and precipitates.

### 2.1.3 Concentration

Depending on the model, we can have multiple order parameters to represent the concentration of a variety of elements, e.g. binary systems, or chemical and defect concentration. These are continuous fields that represent the fraction of a given component

$$C_i = \frac{n_i}{\sum_{i=1}^N n_i} \in \mathbb{R} : (0 \leq C_i \leq 1). \quad (2.1)$$

where  $n_i$  is the number of the  $n$ -field which relates to the  $i$  component and  $N$  is the total number of components associated to the  $n$ -field. The evolution of these fields are driven by diffusional forces, and are directly coupled with the discrete fields previously discussed. These fields are intrinsically linked to the systems' energy through the equation of state (EoS).

## 2.2 Radiation Damage

One of the difficulties of being able to physically describe the formation of the nano-porous structures is that processes that occur at the atomistic scale have such a pronounced effect on the morphological evolution. In other words, the radiation damage caused at the atomistic scale leads to effects that are evident at the meso-scale, e.g. RIS. Several computational models and/or techniques have been developed to simulate these type of atomic scale events. Some of these techniques include: binary collision approximations [5, 73], molecular dynamics [74] and kinetic Monte Carlo [75]. Our model incorporates the use of SRIM to obtain general description of the radiation damage generated from collision events. For instance, SRIM calculates the number of defects generated by binary collision approximations.

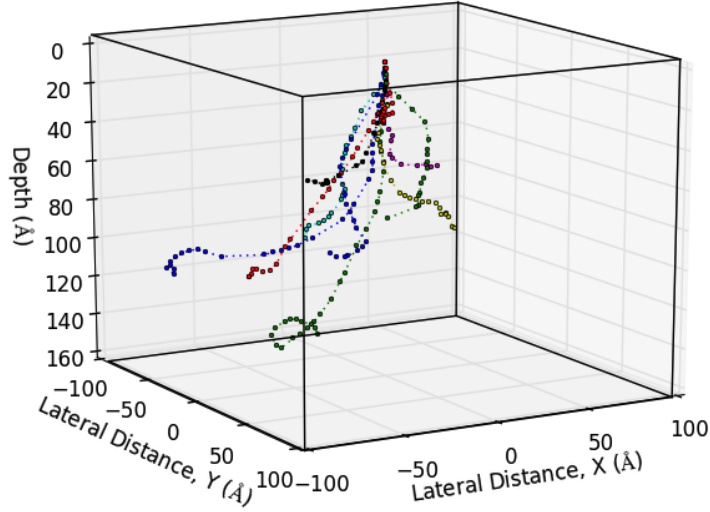


Figure 2.2: Illustration of a Monte Carlo BCA (SRIM) calculated  $\text{Ga}^+$  ion tracks as they travel through a Ge substrate after entering through the surface, depth = 0 Å. Each colored dotted line represents a particular path for the given colored ion.

### 2.2.1 Binary Collision Approximation

The binary collision approximation (BCA) is a computational technique used to efficiently simulate ion range and defect production in materials, Figure 2.2. BCA models have been developed for crystalline targets, e.g. MARLOWE [76], which share similarities to molecular dynamics in that specific collision events can only happen in well defined sites. By including crystallinity we can incorporate phenomena like channeling, which will influence important radiation damage characteristics like the range of ions. The other type of BCA model is for materials lacking long range ordering, i.e. amorphous materials. Simply, no long range atomic ordering is accounted for, which by default leads to the assumption of an amorphous material. These type of BCAs employ stochastic methods to determine the collision properties, e.g. Monte Carlo models. For both variations, the ion trajectory is approximated to be a straight path with deflections due to binary (ion–target atom) collisions.

The collision parameters for a BCA model influencing deflection of the projectiles

are determined by solving the scattering integral, or *general orbital equation*, between colliding particles,

$$\theta = \pi - b \int_{r_{min}}^{\infty} \frac{dr}{r^2 \sqrt{1 - \left(\frac{b}{r}\right)^2 - \frac{V(r)}{\eta E_0}}} \quad (2.2)$$

where  $b$  is the impact parameter,  $r$  is the distance between the colliding particles,  $V(r)$  is the interatomic potential,  $\eta$  is an ion–atom mass parameter and  $E_0$  is the ion incoming energy. The solution to the scattering integral gives us information about the scattering angle and the amount of energy that is lost by the ion to the target. The Monte Carlo BCA randomly determines the collision and scattering conditions for the next target atom, considering only the material density. This random choice of collision parameters in effect treats the target material as amorphous.

### 2.2.1.1 Stopping and Range of Ions in Matter

SRIM is a suite of programs, which include a Monte Carlo BCA algorithm. It includes the Transport of ions in matter (TRIM) code, which is one of the most widely known and used software for the calculation of radiation damage to a first approximation [5]. This software uses Monte Carlo methods, alongside target properties like the density, to determine the impact parameter, which yields information about how much radiation damage can be expected on average.

The TRIM program makes use of the of the Ziegler–Biersack–Littmark (ZBL) universal interatomic potential

$$V_{ZBL}(R) = \frac{z_1 z_2 e^2}{aR} \Phi_U(R) \quad (2.3)$$

where  $z_{1,2}$  are the atomic number for the ion and atom, respectively,  $e$  is the electronic charge,  $a$  is the screening radius,  $R$  is the reduced interatomic separation ( $R \equiv r/a$ ),

Table 2.1: Constant values which define the ZBL screening function.

n	$A_n$	$B_n$
1	0.18180	3.2000
2	0.50990	0.9423
3	0.28020	0.4029
4	0.02817	0.2016

and  $\Phi(R)$  is the universal screening function, given by

$$\Phi_U(R) = \sum_{i=1}^4 A_i \exp(-B_i \cdot R) \quad (2.4)$$

where the fitting constant values  $A_i$  and  $B_i$  were obtained from averaging of approximate potentials for randomly selected atomic pairs and are given in Table 2.1.

One of the main advantages to the TRIM code, is the use of the ‘‘MAGIC’’ formula to determine the uniformly random distribution of scattering angles [77, 78]. The MAGIC formula is defined as

$$\cos\left(\frac{\theta}{2}\right) = \frac{B + R_c + \Delta}{R_0 + R_c} \quad (2.5)$$

where  $B = b/a$ ,  $R_c = \rho/a$  and  $\rho$  is the radii of curvature,  $R_0 = r_0/a$  and  $r_0$  is the sum of the distance of closest approach, and  $\Delta = \delta/a$  and  $\delta$  is the sum of the correction terms. The MAGIC formula is the essential component that made TRIM a viable tool to approximate radiation damage by allowing a semi-analytical solution to the scattering angle equation [5]. By obtaining the scattering angle with use of the MAGIC formula, instead of solving Equation 2.2, computing speeds are increased by up to  $50\times$ .

We should note that the stochastic nature of TRIM’s solution to the scattering integral fundamentally treats the target material as amorphous. Hence, instead of having periodic positions where events can happen we allow a statistical distribution of such probable positions. This makes TRIM a good tool to approximate the char-

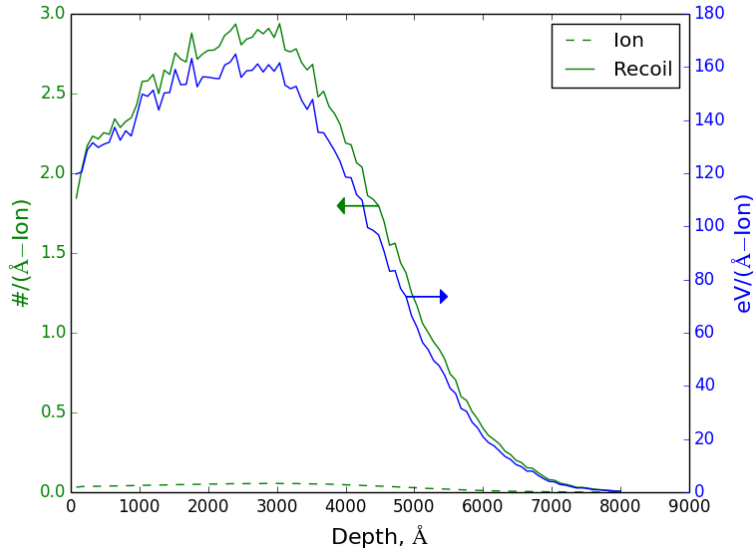


Figure 2.3: TRIM simulation of 1 MeV  $\text{Kr}^+$  irradiation on amorphous Ge. (green) Curves correspond to the left axis and were obtained from the *damage event* file, and (blue) Curve corresponds to the right axis and was obtained from the *energy to recoil* file.

acteristics of the radiation damage in the nano-porous networks since amorphization has been established as a precursor to the formation of these structures.

### 2.2.1.2 SRIM Calculated Damage

TRIM calculations can give us a first order approximation of the amount of damage that is introduced as a function of dose. After a large TRIM simulation, i.e. enough MC runs to obtain a smooth damage profile distribution, we obtain a suitable average to the amount of radiation damage. Figure 2.3 shows a TRIM simulation of 30,000 Kr ions irradiating an amorphous Ge substrate. We are mainly interested in two of the TRIM calculations: damage event and energy to recoil. These calculations are used to determine the extent of damage introduced into the microstructure.

These radiation damage distributions represent an average of the radiation effects at a given depth. For example, at a depth of  $\sim 300 \text{ nm}$ , on average, each  $\text{Kr}^+$ -ion will deposit about  $1.6 \text{ keV/nm}$ . These distributions can be nicely fitted by Gaussian

distributions

$$\Upsilon(z) = \Upsilon_0 \cdot \exp\left(-\left[\frac{z - \bar{z}}{\sqrt{2}\sigma}\right]^2\right) \quad (2.6)$$

where  $\Upsilon(z)$  is either the damage or energy deposited at depth  $z$ ,  $\Upsilon_0$  is a parameter to define the distribution's "amplitude",  $\bar{z}$  is the average depth at which the distribution peaks and  $\sigma$  is the standard deviation. In this way we could model the radiation damage in our system by using carefully defined Gaussian distributions. While the approach used by Li et al. in his adapted Cahn–Hilliard model is based in similar fundamental thinking, in their work all defects are introduced spontaneously at the beginning of the simulation.

The rate at which atoms are displaced by atom–ion interactions can be given by

$$R_d \equiv N \int_{\check{E}}^{\hat{E}} \phi(E_0) \sigma_D(E_0) dE_0 \quad (2.7)$$

where  $N$  is the atomic density,  $\check{E}$  and  $\hat{E}$  are the minimum and maximum ion energies,  $\phi(E_0)$  is the energy dependent ion flux, and  $\sigma_D(E_0)$  is the energy dependent displacement cross section. This rate gives us the probability that a projectile with some energy will interact with the lattice atoms cause radiation damage. Instead of solving this type of equation, we approximate the probability of collision to be proportional to TRIM's damage calculation, or more accurately to the normal distribution used to simulate the damage distribution

$$\begin{aligned} p_d(\mathbf{x}) &= p_d^0 \cdot \exp\left(-\left[\frac{\mathbf{x} - \bar{\mathbf{x}}}{\sigma}\right]^2\right) \\ &= p_d^0 \cdot \exp\left(-\left[\frac{x - \bar{x}}{\sigma}\right]^2\right) \exp\left(-\left[\frac{y - \bar{y}}{\sigma}\right]^2\right) \exp\left(-\left[\frac{z - \bar{z}}{\sigma}\right]^2\right). \end{aligned} \quad (2.8)$$

where  $p_d^0$  is a normalized peak probability of a radiation event taking place located near the ion range and  $\mathbf{x}$  is the Cartesian coordinate. While technically TRIM's

damage calculation provides the number of defects that were created at a certain depth, we assume that this is directly proportional to the probability of collision.

There is an inherent stochasticity to the radiation processes, and the process described for calculating the probability of collision is deterministically, to some extent. To account for the aleatory nature of the radiation processes, we can “randomize” the energy deposited distribution. This approach is better understood by examining Figure 2.4. The TRIM calculation gives us a distribution profile for the amount of energy deposited by ion as a function of depth,  $E_{dep}(\mathbf{x})$ . We then perform a Gaussian fit to this distribution, which gives us a maximum energy deposited threshold. This threshold is used to calculate the amount of energy deposited during the simulation by multiplying by a uniformly distributed random number

$$E_{dep}^{sim} = \mathcal{RN} \cdot E_{dep}^{Gaus} \quad (2.9)$$

where  $\mathcal{RN} \in \mathbb{R} : [0, 1)$  is the random number. Using these distributions, we are able to simulate the creation of defects within our model. For example, on Figure 2.4, the TRIM calculated data is fitted to a Gaussian distribution shown in green and blue, respectively. The fitted distribution is then used to determine how much energy was deposited at a particular depth by randomly choosing an amount of energy bounded by the fitted curve, shown as stars. These values are then used to calculate the number of radiation defects introduced in our model. While this could add to the link between the model and the physical processes, it does not significantly change the simulation results.

Lastly, it should be noted that most of the created defects calculated by the TRIM simulation arise from the recoil atoms, instead of the projectile ion. This is clearly shown in Figure 2.3, where the recoil curve is orders of magnitude larger than the ion curve. Therefore, in this work we will only consider defect generation from the recoil

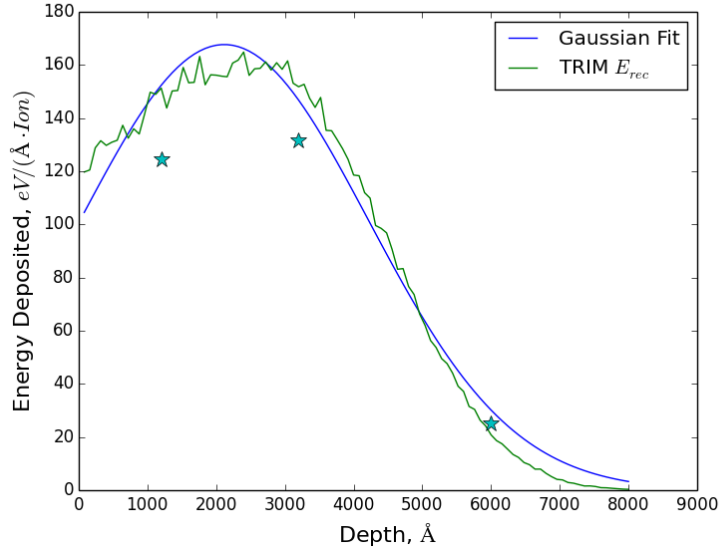


Figure 2.4: Representation of fitting and randomization of the recoil energy deposited under the same condition as in 2.3. The stars represent the random deposited energy at depths  $z = (120, 320, 600)$  nm.

atoms. Furthermore, while this concept of randomizing average calculated values, SRIM could be used to obtain ion paths similar to the ones shown in Figure 2.2. These paths could then be sampled by use of a kinetic Monte Carlo algorithm. This would give an even more accurate simulation of the radiation damage.

### 2.2.1.3 Shortcomings to the BCA Model

TRIM is widely used to describe the radiation damage characteristics, especially by experimentalist as a first order approximation. Recent comparative studies between BCA and molecular dynamics (MD) [79, 80], suggest that there are some shortcomings with the crystal and Monte Carlo BCA models. One clear shortcoming arises from amorphization mechanisms, which BCA models are not able to simulate. *Bukonte et.al.* also showed that BCA models are not capable of accurately capturing small displacements in both crystalline and amorphous materials, when compared to MD models. They also suggest that the Monte Carlo BCA model better describes crystalline material irradiation than it does amorphous material irradiation Figure 2.5.



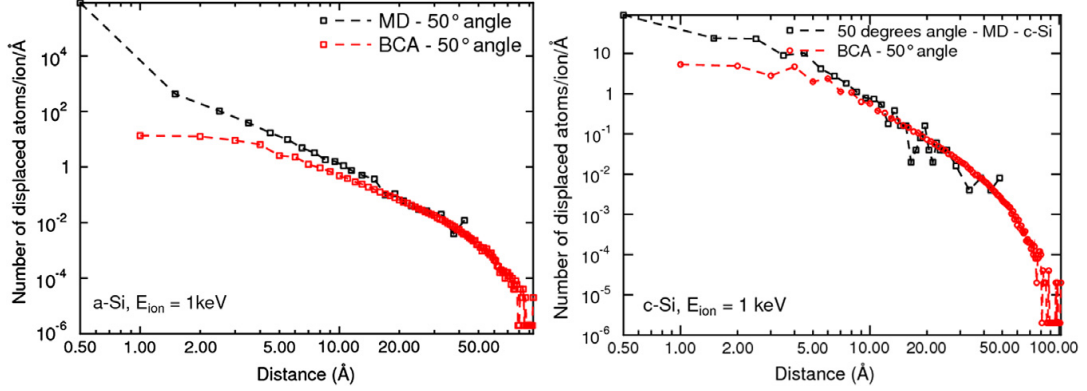


Figure 2.5: (Atom displacement statistics for single 1 keV Ar+ impact on (left) amorphous and (right) crystalline Si at 50° incidence angle MD and BCA. [80]

Even though BCA models might be fundamentally flawed, we incorporate them in the calculation of radiation damage in our model as they do provide acceptable approximations.

### 2.2.2 Defect Survivability

For non-diffusive/reactive defects, as the ones calculated by TRIM, we need to approximate how many of the created defects survive the collision cascade and quenching stages. Before determining how many defects survive the highly unstable cascades and go on to modify the microstructure at larger scales, we need be able to approximate how many instantaneous defects are created. From TRIM we obtain the amount of energy that was transferred, through nuclear collisions, from the ion or primary knock-on atom to the lattice atoms. As these atoms are displaced, we generate a wide range of point defects, which we calculate by use of the Kinchin-Pease model [81]

$$\eta(E_T) = \begin{cases} 0, & E_T < E_d \\ 1, & E_d < E_T \leq 2E_d \\ \frac{E_T}{2E_d}, & 2E_d < E_T < E_c \\ \frac{E_c}{2E_d}, & E_T \geq E_c \end{cases} \quad (2.10)$$

where  $\eta(E_T)$  is the number of defects created when  $E_T$  energy was transferred,  $E_d$  is the threshold displacement energy and  $E_c$  is the cut-off energy associated to electronic energy loss. This is the most basic model, and many other adaptations have been developed [11]. Nevertheless, it is the standard approach followed by TRIM and we implement it as a first order approximation.

The Kinchin–Pease model we can approximate how many defects were created during the radiation event. The model does not account for the evolving microstructure nor does it retain memory of any previous event. Therefore, it does not account for defect reactions like recombination or annihilation at sinks. As can be expected from such a simple model, Kinchin–Pease overestimates the number of defects present after the quenching stage. In order to properly account for the recombined point defects, we use the approach described by *Hobler* [82]. Let’s consider two defects that are separated by a distance  $d_{ij}$ . The probability of these defects “seeing” each other to then recombine is dependent on the magnitude of their separation distance. If this distance is less or equal than the *capture radius* ( $r_{cap}$ ) we assume that the defects are able to recombine. Work on what this capture radius is and how it is implemented to a *cumulative damage* model has yielded consistent trends [83, 84]. Following approach outlined by Hobler et al., the number of defects surviving the cascade quenching period is given by

$$\eta_{surv}(E_T) = \eta(E_T) \cdot f_{rec} \cdot f_{pre} \quad (2.11)$$

where  $\eta$  is the Kinchin–Pease calculated number of Frenkel pairs,  $f_{pre}$  is the probability of a newly created defect annihilating itself with a pre-existing defect, and  $f_{rec}$  is the fraction of defects that survive recombination during the collision cascade. The  $\eta(E_T)$  can be calculated from the TRIM results as discussed in Section 2.2.1.2. The fraction of defects remaining after recombining with pre-existing defects is proportional to the recombination probability ( $p_{rec}$ ). To obtain a relationship between these two parameters, let’s consider the four probable events which the defects can

undergo and how they affect the Frenkel pairs.

- Both defects recombine with a pre-existing defect, which leads to a net change of one less Frenkel pair. This event will have a probability of  $p_{-FP} = p_{rec} \cdot p_{rec} = p_{rec}^2$ .
- Both defects survive the quenching stage, leading to a net increase of one Frenkel pair. Since the probability of not recombining is  $(1 - p_{rec})$ , this event will have a probability of  $p_{+FP} = (1 - p_{rec})(1 - p_{rec}) = (1 - p_{rec})^2$ .
- Either the interstitial or the vacancy defect recombines, while the other defect survives. This leads to no change in the number of Frenkel pairs and has a probability of  $p_0 = p_{rec}(1 - p_{rec})$ .

Taking these processes into consideration, we can express the parameter  $f_{pre}$  as

$$\begin{aligned}
 f_{pre} &= \sum_{i=1}^4 p_i \cdot \Delta FP_i \\
 &= (+1) \cdot p_{rec}^2 + (-1) \cdot (1 - p_{rec})^2 + 2 \cdot (0) \cdot p_{rec}(1 - p_{rec}) \\
 &= (1 - 2p_{rec})
 \end{aligned} \tag{2.12}$$

where  $\Delta FP_i$  is the net change of number of Frenkel pairs and  $p_i$  is the probability of that change taking place. The recombination probability is given by

$$p_{rec} \equiv \frac{N_i + N_v}{4N_{sat}} \approx \frac{N_v}{2N_{sat}} \tag{2.13}$$

where  $N_i$  and  $N_v$  are the local concentration densities of pre-existing interstitials and vacancies defects, and  $N_{sat}$  is point defect saturation concentration density. For simplicity, here we have made the approximation, as Hobler et al., that  $N_i \approx N_v$  since they are created in equal numbers. With this assumption, the probability of recombining and not recombining will be identical, which leads to  $p_{rec} = (1 - p_{rec}) =$

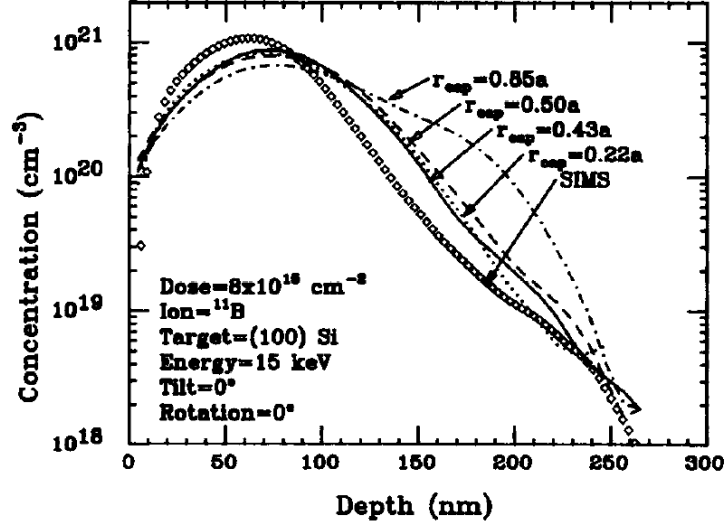


Figure 2.6: Comparison of an experimental SIMS profile of boron implanted into silicon with profiles simulated using capture and CPU intensive process of keeping track of the point radius values of  $0.22a$ ,  $0.43a$ ,  $0.50a$  and  $0.85a$  for an energy defects created by all cascades, and yet, within the error of 15 keV, tilt angle of  $0^\circ$ , and rotation angle of  $0^\circ$  [83].

$0.5$  and  $N_v = N_{sat}$ . This saturation parameter is defined by the capture radius

$$N_{sat} = \frac{1}{2} \left( \frac{4\pi r_{cap}^3}{3} \right)^{-1} = \frac{3}{8\pi r_{cap}^3} \quad (2.14)$$

where the  $1/2$  terms stems from the fact that at saturation the probability of recombining is equal to the probability of surviving. The capture radius describes the critical distance between defects at which they are able to recombine. Studies on  $B^+$  irradiated crystalline Si suggests that the capture radius can be defined as

$$r_{cap} = f \cdot a_0 \quad (2.15)$$

where  $a_0$  is the lattice constant and  $f$  is a correction factor that ranges between  $0.22$ – $0.5$ , Figure 2.6 [83]. They implemented the cumulative model to the MARLOWE program obtaining fairly good agreement for a capture radius of  $r_{cap} = 0.43s_0$ . By

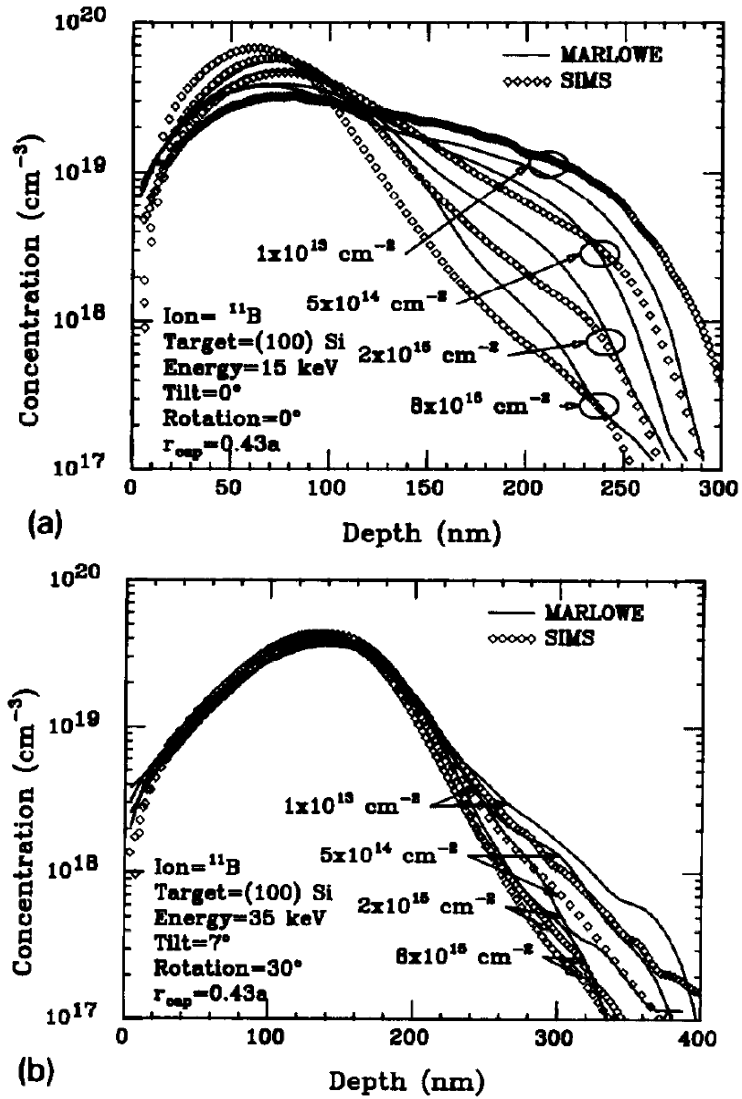


Figure 2.7: Comparison of experimental SIMS profiles of boron implanted into silicon at doses of  $1 \times 10^{13}$ ,  $5 \times 10^{14}$ ,  $2 \times 10^{15}$ , and  $8 \times 10^{15} \text{ cm}^{-2}$  with profiles simulated with the damage model for (a) an energy of 15 keV, tilt angle of  $0^\circ$ , and rotation angle of  $0^\circ$ , and (b) an energy of 35 keV, tilt angle of  $7^\circ$ , and rotation angle of  $30^\circ$ . [83].

combining Equations 2.11 and 2.12, we get the *defect survivability*

$$\eta_{surv}(E_T) = \eta(E_T) \cdot f_{rec} \cdot (1 - 2p_{rec}) \quad (2.16)$$

which is the number of expected surviving defects that will influence how the microstructure evolves at the mesoscales. This parameter is then incorporated into the defect evolution equations, as detailed in the next sections. While this approach was developed for crystalline materials, it is assumed that it will be an acceptable approximation for both crystalline and amorphous materials. Perhaps adapting the different correctional constants could be an appropriate way of tailoring the model for amorphous materials. Furthermore, we need to keep in mind that by definition amorphous materials do not have periodic lattice sites which accommodate point defects. In fact, to the best of my knowledge, there is no consensus on how to define point defects on amorphous structures. Therefore, we treat these defects as concentration densities.

## 2.3 Conventional Formulation

As outlined in Section 1.1.2, the creation of radiation defects can lead to chemical changes in the target material. We incorporate a similar model to the one detailed in the previous chapter, but we adapt the set of governing equation to include driving forces that are based on thermodynamics. A clear distinction between our model and the one previously developed by *Wiedersich et al.* is the use of chemical potentials, which drives the atomic chemical solubility to a thermodynamic equilibrium.

We can define the system such that the concentration for each individual component  $i$  is the fraction of said component present and adding all the individual components equals one, i.e.

$$\sum_{i=1}^N C_i = 1. \quad (2.17)$$

Then, we can rewrite this equation in a way that one component becomes dependent

on the rest

$$C_N = 1 - \sum_{i=1}^{N-1} C_i \quad (2.18)$$

where we have reduced the number of elements that we need to explicitly track. Using this relationship, we can define the compositional evolution of the system by a set of  $N - 1$  PDEs describing the diffusional evolution. Each one of these equations has the general form

$$\frac{\partial C_i}{\partial t} = -\nabla \cdot \mathbf{J}_i \quad (2.19)$$

where  $\mathbf{J}_i$  is the flux vector for the  $i$ -component. A well accepted definition to the flux is given by Fick's first law

$$\mathbf{J}_i = D_{ij} \nabla C_i \quad (2.20)$$

where  $D_{ij}$  is the diffusion coefficient of element  $i$  through the  $j$  mechanism. However, this ignores all the driving forces exerted on the  $i$ -component by all the other components present on the system. These cannot be ignored as they are intrinsically linked as evident from Equation 2.18. Following the work by *Balluffi et al.* [85], the next section gives a general description of the proper treatment of the evolution equations.

### 2.3.1 Flux in a Multi-Component System

The manner in which an element will diffuse on a generic system depends on the driving forces acting upon it, as described by the flux. The fluxes can be conventionally defined as a function of all the different driving forces

$$\mathbf{J}_i = f(\mathbf{F}_i, \mathbf{F}_{i+1}, \dots, \mathbf{F}_N), \quad (2.21)$$

such that all components have an influence on the flux of  $i$ , and vice versa. By performing a first order Taylor expansion, we get a generalized equation for the flux

$$\mathbf{J}_i = \sum_{j=1}^N L_{ij} \mathbf{F}_j \quad (2.22)$$

where  $L_{ij} = \partial \mathbf{J}_i / \partial \mathbf{F}_j$  is evaluated at equilibrium and is often termed the Onsager matrix of phenomenological coefficients. In this model, the driving force ( $\mathbf{F}$ ) can be the concentration and/or chemical potential gradient. For a volume fixed frame of reference, we can set

$$\sum_{j=1}^N L_{ij} \mathbf{F}_j = \sum_{j=1}^N \mathcal{J}_j = 0, \quad (2.23)$$

where  $\mathcal{J}_j^1$  is the flux related to the  $j$ -component driving force. Rewriting Equation 2.23, we get

$$\mathcal{J}_N = - \sum_{j=1}^{N-1} \mathcal{J}_j \quad (2.24)$$

This approach allows us to reduce the set of equations by removing  $N^{th}$  flux as dependent. As outlined by *Balluffi et al.*, the entropy production rate, given by Equation 6.5 from [85], is proportional to the scalar product of all fluxes and the gradient of a thermodynamic potential. In other words, each flux can be multiplied by it's *conjugate* force in order to obtain the entropy rate. Then, using Equation 2.24, we get

$$T\dot{\mathcal{S}} = - \sum_{j=1}^N \mathcal{J}_j \cdot \nabla \psi_j = - \sum_{j=1}^{N-1} \mathcal{J}_j \cdot \nabla (\psi_j - \psi_N) \quad (2.25)$$

where the conjugate force is

$$\mathbf{F}_j = -\nabla(\psi_j - \psi_N). \quad (2.26)$$

---

<sup>1</sup>The vector notation was omitted for nomenclature convenience.



Therefore, Equation 2.19 can be rewritten as

$$\frac{\partial C_i}{\partial t} = \nabla \cdot \left( \sum_{j=1}^{N-1} L_{ij} \nabla (\psi_j - \psi_N) \right) \quad (2.27)$$

where the conjugate forces can be chemical potential or concentration gradients, depending on the particular simulation, and the Onsager coefficients ( $L_{ij}$ ) can be diffusivities or mobilities. This is equivalent to Fick's second law, but here we explicitly account for the forces that all elements exert on element  $i$ , which contribute to its evolution.

## 2.4 Chemical Potential Definition

One of the major misunderstood concepts of the phenomenological evolution equations is that the driving force can be simply defined as the slope of the free energy curves. While under certain arrangements this turns out to be true when setting the chemical potential as the driving force, we need to understand the conceptually accurate definition of the chemical potential. On a multi-component multi-phase system, we need to use the true definition of the chemical potential to describe the correct thermodynamics of the system. The following derivation is based on the work done by *Lupis* [86].

If we define the Gibbs bulk free energy of the system as a function of the molar components, we get

$$f_G = n \tilde{f}_G \equiv \sum_{i=1}^N n_i \tilde{f}_{G,i} \quad (2.28)$$

where  $\tilde{f}_{G,i}$  is the molar Gibbs free energy and  $n_i$  is the number of moles of the  $i$ -component. Then, the chemical potential can be defined as the partial derivative of

the Gibbs energy with respect to the number of moles

$$\mu_i = \frac{\partial f_G}{\partial n_i} = \tilde{f}_G \left( \frac{\partial n}{\partial n_i} \right)_{n_{k \neq i}} + n \left( \frac{\partial \tilde{f}_G}{\partial n_i} \right)_{n_{k \neq i}} \quad (2.29)$$

As shown in Appendix A, this equation can be rewritten in terms of the concentration as

$$\mu_i = \tilde{f}_G + \sum_{j=1}^{N-1} (\delta_{ij} - C_j) \left( \frac{\partial \tilde{f}_G}{\partial C_j} \right)_{n, C_N} \quad (2.30)$$

where  $\delta_{ij}$  is the Kronecker delta and  $C_i$  is the concentration (in molar fraction) of  $i$ . This definition is also known as the partial molar Gibbs free energy and it is convenient to define the chemical potential this way since bulk free energies are usually experimentally measured in molar terms. As an example, let's consider a quaternary system, i.e. a system defined by the presence of four elemental components. Using Equation 2.30, and setting  $C_4 = 1 - C_1 - C_2 - C_3$ , we have

$$\mu_1 = \tilde{f}_G + (1 - C_1) \frac{\partial \tilde{f}_G}{\partial C_1} - C_2 \frac{\partial \tilde{f}_G}{\partial C_2} - C_3 \frac{\partial \tilde{f}_G}{\partial C_3} \quad (2.31a)$$

$$\mu_2 = \tilde{f}_G - C_1 \frac{\partial \tilde{f}_G}{\partial C_1} + (1 - C_2) \frac{\partial \tilde{f}_G}{\partial C_2} - C_3 \frac{\partial \tilde{f}_G}{\partial C_3} \quad (2.31b)$$

$$\mu_3 = \tilde{f}_G - C_1 \frac{\partial \tilde{f}_G}{\partial C_1} - C_2 \frac{\partial \tilde{f}_G}{\partial C_2} + (1 - C_3) \frac{\partial \tilde{f}_G}{\partial C_3} \quad (2.31c)$$

$$\mu_4 = \tilde{f}_G - C_1 \frac{\partial \tilde{f}_G}{\partial C_1} - C_2 \frac{\partial \tilde{f}_G}{\partial C_2} - C_3 \frac{\partial \tilde{f}_G}{\partial C_3} \quad (2.31d)$$

where the chemical potential  $\mu_i$  is the conjugate variable for element  $i$ .

#### 2.4.1 Equilibrium of a Multi-Phase System

The chemical potential of a material at a given concentration is often obtained by the *method of intercepts*. For a multi-phase material, thermodynamics want to drive the system to an equilibrium, which determines the concentration for material of each particular phase. This equilibrium concentration can be determined by the

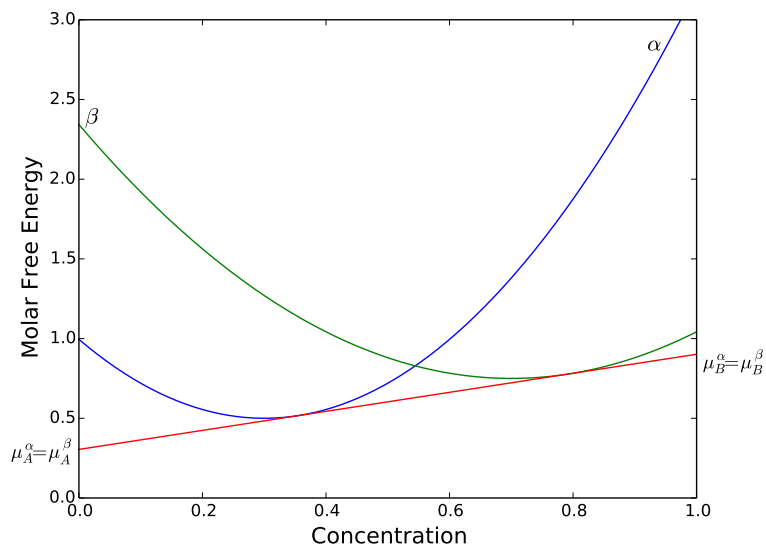


Figure 2.8: Use of the common tangent construction rule to determine the state that yields equilibrium conditions.

method of intercepts. This can be graphically represented by the *common tangent construction*, Figure 2.8. The equilibrium state for the  $\alpha\beta$  system is achieved when the conditions

$$\mu_A^\alpha = \mu_A^\beta$$

and

$$\mu_B^\alpha = \mu_B^\beta$$

are met. Under these conditions, the equilibrium system wants to drive the respective phases to their equilibrium concentration, given by the intercept of the common tangent to the phase curve. If the phases were thermodynamically influenced by other forces, e.g. hydrostatic pressures, the thermodynamic state of the system will change. This would then change the equilibrium conditions, and give a different set of equilibrium concentrations.

## 2.5 Free Energy Functional

Apart from the need to understand the driving mechanisms that lead to the formation of the radiation induced nanostructures, this work was motivated by the phase field work done by *Li et al.* [72, 44, 66]. In their work, to describe the thermodynamic state they use the regular solution, which has a double well in the concentration field. In essence, they provide a given defect density distribution and allow basic spinodal decomposition to drive the system into a porous looking microstructure. While basic spinodal decomposition drives the evolution, the adapted model does account for different mechanisms directly related to radiation damage. To some extent, this misrepresents many of the real processes taking place. Nonetheless, they showed that their approach may be capturing some fundamental thermodynamical behavior as they are able to produce structures that resemble the ones observed experimentally.

The free energy functional gives us the amount of energy that is stored within the system for a given state, where the state is defined by the order parameters discussed earlier in the chapter. A commonly used definition for the free energy functional in phase field simulations is the one given by *Cahn-Hilliard* [61, 62, 63]

$$F_{CH} = \int_V \left( f_0 + \frac{\gamma}{2} |\nabla C|^2 \right) dV \quad (2.32)$$

where  $f_0$  is the bulk chemical free energy,  $\gamma$  is the interfacial energy gradient coefficient and  $C$  is the order parameter that characterizes the interface. The  $\gamma$ -term also gives a measure of the thickness of the diffuse interface. *Li et al.* used the regular solution equation as the bulk chemical free energy. Due to the intriguing similarities between the experimental results and Li's computational simulations, their thermodynamic description should be examined in models simulating the formation of the nanoporous structures. In fact, similar double well equations have been used to simulate bubble and void swelling [70, 67]. It should be noted that this functional could be

easily adapted to incorporate other energetic terms depending on the forces that might influence the system thermodynamics.

## 2.6 Phenomenological Equations for a Quaternary System

To illustrate the implementation of the true chemical potentials into the evolution equations, let's work an example for a quaternary system. This corresponds to a simple binary system where we treat the interstitial and vacancy defects as inherent “atomic” components

$$C_A + C_B + C_i + C_v = 1$$

where the interstitial and vacancy terms include both atomic components, i.e.  $C_i = C_i^A + C_i^B$ . Using this relationship, we can describe the evolution of the system by the use of  $N - 1 = 3$  equations. From Equation 2.27 and using the chemical potential as the conjugate force, we have

$$\frac{\partial C_A}{\partial t} = \nabla \cdot [M_{AA}\nabla(\mu_A - \mu_B) + M_{Ai}\nabla(\mu_i - \mu_B) + M_{Av}\nabla(\mu_v - \mu_B)] \quad (2.33a)$$

$$\frac{\partial C_i}{\partial t} = \nabla \cdot [M_{ii}\nabla(\mu_i - \mu_B) + M_{iA}\nabla(\mu_A - \mu_B) + M_{iv}\nabla(\mu_v - \mu_B)] \quad (2.33b)$$

$$\frac{\partial C_v}{\partial t} = \nabla \cdot [M_{vv}\nabla(\mu_v - \mu_B) + M_{vA}\nabla(\mu_A - \mu_B) + M_{vi}\nabla(\mu_i - \mu_B)] \quad (2.33c)$$

where  $\mu_i$  is the chemical potential of component  $i$  and  $M_{ij}$  is the mobility of the  $j$  component through the  $i$  mechanism. By employing the true definition of the chemical

potential, Equation 2.31a, we have

$$\frac{\partial C_A}{\partial t} = \nabla \cdot \left[ M_{AA} \nabla \left( \frac{\partial \tilde{F}}{\partial C_A} \right) + M_{Ai} \nabla \left( \frac{\partial \tilde{F}}{\partial C_i} \right) + M_{Av} \nabla \left( \frac{\partial \tilde{F}}{\partial C_v} \right) \right] \quad (2.34a)$$

$$\frac{\partial C_i}{\partial t} = \nabla \cdot \left[ M_{ii} \nabla \left( \frac{\partial \tilde{F}}{\partial C_i} \right) + M_{iA} \nabla \left( \frac{\partial \tilde{F}}{\partial C_A} \right) + M_{iv} \nabla \left( \frac{\partial \tilde{F}}{\partial C_v} \right) \right] \quad (2.34b)$$

$$\frac{\partial C_v}{\partial t} = \nabla \cdot \left[ M_{vv} \nabla \left( \frac{\partial \tilde{F}}{\partial C_v} \right) + M_{vA} \nabla \left( \frac{\partial \tilde{F}}{\partial C_A} \right) + M_{vi} \nabla \left( \frac{\partial \tilde{F}}{\partial C_i} \right) \right] \quad (2.34c)$$

where  $\tilde{F}$  is the bulk molar free energy functional. For convenience, we can rewrite this set of equations as

$$\frac{\partial C_A}{\partial t} = \nabla \cdot [M_{AA} \nabla \hat{\mu}_A + M_{Ai} \nabla \hat{\mu}_i + M_{Av} \nabla \hat{\mu}_v] \quad (2.35a)$$

$$\frac{\partial C_i}{\partial t} = \nabla \cdot [M_{ii} \nabla \hat{\mu}_i + M_{iA} \nabla \hat{\mu}_A + M_{iv} \nabla \hat{\mu}_v] \quad (2.35b)$$

$$\frac{\partial C_v}{\partial t} = \nabla \cdot [M_{vv} \nabla \hat{\mu}_v + M_{vA} \nabla \hat{\mu}_A + M_{vi} \nabla \hat{\mu}_i] \quad (2.35c)$$

where we set  $\hat{\mu}_i \equiv \partial \tilde{F} / \partial C_i$  for nomenclature convenience. It should be noted that is we set the mixed diffusion terms to zero, i.e.  $M_{i \neq j} = 0$ , we obtain the customary definition of the phenomenological equations. Numerically solving these equations we can model the compositional changes of each individual component, keeping in mind that  $C_B$  can be obtained as a function of these three components.

### 2.6.1 Surface Migration, Grain Growth and Phase Transformation

Microstructural evolution is a complex and multi-stage process, which can seldomly be described by a single type of event. Some events being considered throughout this work include: surface migration, and grain and/or phase changes. The surface migration event can occur when a void voxel (white) is located next to a matter voxel (blue). An exchange of voxel values occurs such that the corresponding order parameter is conserved Figure 2.9. On the other hand, feature growth does lead to a

non-conserved equilibrium where one feature grows at the expense of the other Figure 2.10. Both cases lead to a minimization energy ensemble, i.e. smoother surfaces. The energy is minimized by means of the standard Metropolis algorithm [87]. Hence, for sites that have been identified as having a likelihood for change the Maxwell–Boltzmann distribution is assumed to describe the probability of these changes taking place. Therefore, these changes are accepted by following Maxwell–Boltzmann statistics, which can be derived from statistical mechanical thermodynamics considerations. These events will be discussed with more detail as implemented. Now, the probability of an *event* taking place, is a function of the ensemble’s energy before and after the *event*. If the free energy functional ( $F$ ) describes the energetic state of the ensemble, the probability that the *event* will be accepted is

$$P_{event} = \begin{cases} 1, & \Delta F \leq 0 \\ \exp\left(-\frac{\Delta F}{k_B T}\right), & \Delta F > 0 \end{cases} \quad (2.36)$$

where  $\Delta F$  is the change in energy before and after the *event*,  $k_B$  is the Boltzmann constant and  $T$  is the absolute temperature. Proper coupling of all these processes will describe the complete microstructural evolution.

## 2.7 Coupling of the Deterministic and Statistical Models

One of the main objectives of this work is the improvement on the model developed by Li. The approach used to achieve this is by coupling deterministic and statistical methods in order to describe microstructural evolution. The model presented here was inspired by the hybrid Potts–phase field (hPPF) model developed by *Homer et al.*, Figure 2.11 [88, 89, 90]. While they are able to individually capture the correct kinetics and physics related to microstructural evolution, we attempt to leverage on their respective computational advantages and weaknesses through the hybrid

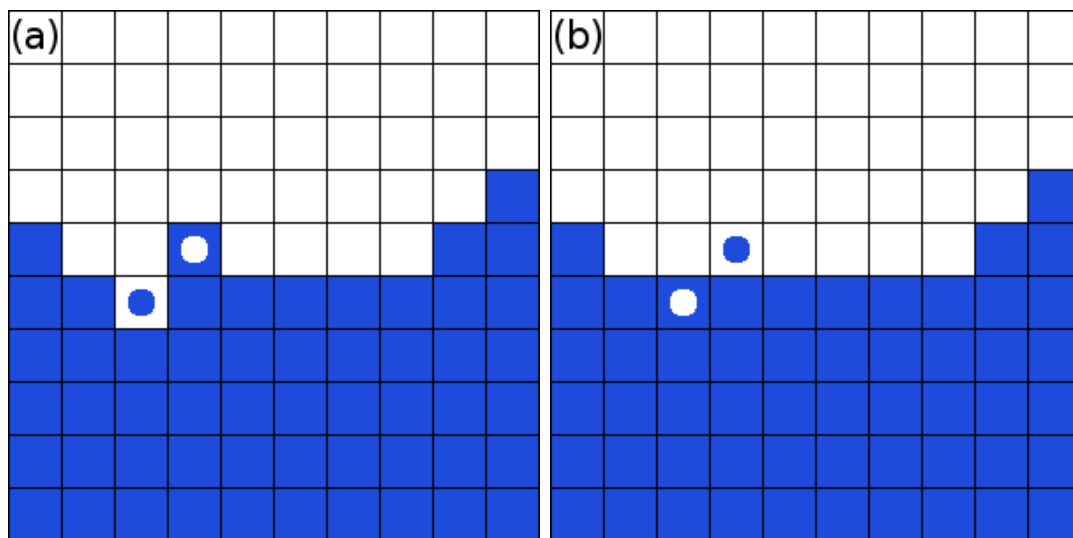


Figure 2.9: Representation of a surface diffusion event where a void voxel (white) exchanges location with a matter voxel (blue). We can see the ensembles (a) before and (b) after the exchange. It is evident that the new configuration has a lower overall energy, i.e. decreased interface. The dots identify the voxels of interest.

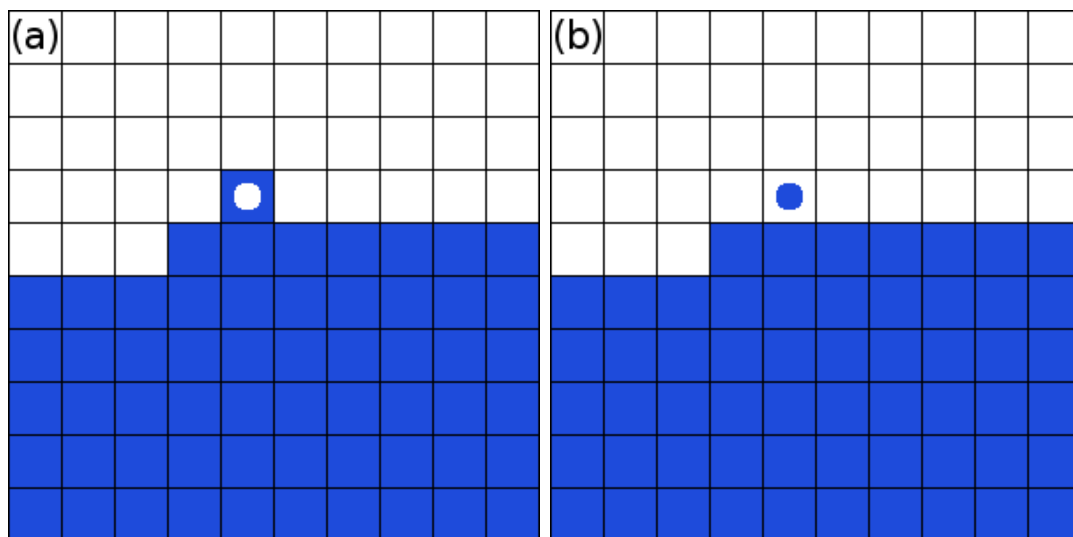


Figure 2.10: Representation of a feature growth event where a feature 1 voxel (white) grows at the expense of the feature 2 voxel (blue). We can see the ensembles (a) before and (b) after the change. It is evident that the new configuration has a lower overall energy, i.e. decreased interface. The dots identify the voxels of interest.



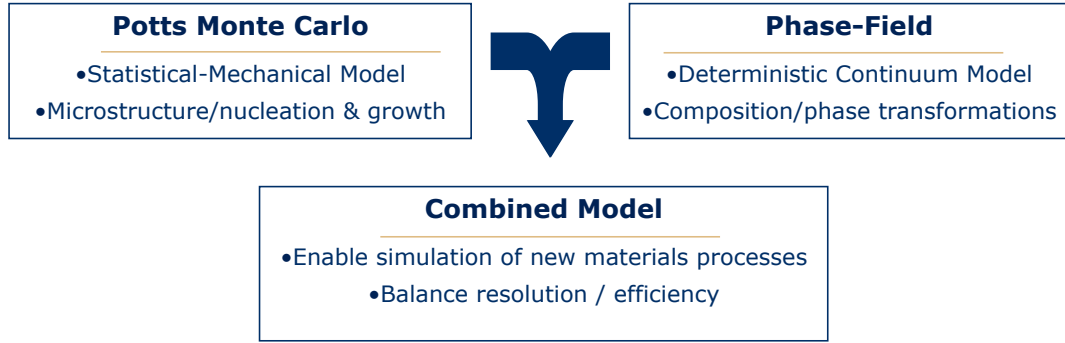


Figure 2.11: The main advantages of each computational approach are exploited in order to develop a hybrid model that is able to efficiently model microstructural evolution, with the added benefits of being robust and retaining the correct kinetics and physics.

model, Table 2.2. Homer et al. demonstrated that the hybrid model efficiently and accurately simulates complex microstructural evolution problems by capitalizing each methods' strengths, e.g. grain growth by capillarity. The coupling consists of allowing the PMC model to simulate generic microstructural evolution like grain growth, while the phase field model handles the evolution of the smoothly varying continuum fields like concentrations. The latter is achieved by numerically solving the corresponding PDEs. Therefore, the set of PDEs normally required by the phase field model can be greatly reduced as the generic microstructure can be represented as discretized elements. A pseudo-code describing the flow of the model is shown in Appendix D. This approach provides a more robust method to modeling certain behavior which might be stochastic and/or deterministic in nature.

### 2.7.1 Advantage Over Conventional Models

The model presented here combines a Potts Monte Carlo model and a phase field model to create the hybrid model. Both of these have been extensively used for simulating microstructural changes [50, 57, 59]. Although very useful, both models do have some shortcomings. While Potts Monte Carlo has been shown to accurately simulate grain growth kinetics, it is quite difficult to model the evolution of con-

Table 2.2: General characteristics of the Potts kinetic Monte Carlo (PMC) and the phase field models.

<i>CON's</i>	<i>PRO's</i>
<b>Continuum Model: PF</b>	
<ul style="list-style-type: none"> <li>○ Finer space and time grids for complicated energy functionals</li> <li>○ Developing functionals that couple all parameters is challenging</li> </ul>	<ul style="list-style-type: none"> <li>○ Readily available time dependent evolution equations</li> <li>○ Relatively easy to construct energy functionals</li> </ul>
<b>Statistical Model: PMC</b>	
<ul style="list-style-type: none"> <li>○ Poor simulating continuum fields</li> </ul>	<ul style="list-style-type: none"> <li>○ Can incorporate the kinetics, thermodynamics and topological characteristics</li> <li>○ Simple, intuitive and easy to code</li> </ul>

tinuous fields. On the other hand, phase field models are excellent simulating such behavior, but can become prohibitively expensive as we introduce order parameters, e.g. different grain orientations. To simulate these, this method requires large sets of PDEs to fully describe realistic microstructures. Furthermore, to accurately model the continuous field evolution across interfaces, the phase field models need high resolution meshing to simulate the diffuse interfaces. This can substantially increase the computational expenses. Therefore, by correctly coupling both models we take advantage of each model's strength. By coupling these models we can improve the computational efficiency while producing very accurate solutions.

## 2.8 Stochastic Parallel PARTicle Kinetic Simulator

SPPARKS [91, 92] is a C++ Monte Carlo framework developed at Sandia National Laboratories that provides several types of kinetic Monte Carlo algorithms. These have been implemented to simulate a wide range of microstructural evolution behavior as showcased in, e.g. fission gas transport in fuels [92]. The models developed have been implemented such that they are compatible with SPPARKS' framework in order to take advantage of its scalability. In general, the models developed make

use of the on-lattice rejection kinetic Monte Carlo algorithm. SPPARKS handles the generation of the simulation space/sites, and the manner in which particular voxel is sampled. The scalability and portability afforded by SPPARKS were the main motivations to develop these models under the framework. While many of the simulations were performed on a 12-core Mac Pro desktop, the larger simulations were performed on Sandia's cluster facilities. All codes are written as to allow either two or three dimensional simulations. Furthermore, it can be run as a single process or as massively parallel processes using a message passing interface (MPI), where SPPARKS is solely responsible for managing the communication aspects. However, it should be pointed out that for the more elaborate models, extra communication across processor boundaries was needed to be applied.

## CHAPTER III

### Research Mission Statement

While a large body of work has been produced experimentally studying microstructural evolution of ion irradiation induced nano-structures, the same cannot be said of computational efforts. This is due in part to the fact that the controlling mechanisms that lead to the formation of these structures are not well understood. Although there are well established theories that do provide some insight on the development of such structures, these are mostly focused on crystalline materials. Therefore, models developed need to be adapted such that the lack of long range atomic ordering is taken into consideration. Hybrid deterministic-statistical models have been developed in order to address some of these issues. Such models have not been applied to radiation induced microstructural evolution until these works. Computational models allow for an economical approach to better understand the mechanisms that lead to the formation of nano-structures of interests. Hence, they are very useful in the search of the controlling mechanisms that lead to the formation of the desired microstructures.

The main objectives of this thesis is to develop a model that can help us understand how different radiation related processes influence the formation of the nano-porous networks. By developing these hybrid models, it is expected to have an efficient and flexible approach to study these processes. Here are the steps taken in order to

developed and test the numerical models:

- The implementation of the hybrid Potts–phase field (hPPF) to a sharp interface microstructure. The original hPPF model was adapted to use the discrete sharp interfaces to account for interfacial energies. The model implements a discrete curvature, which is able to describe interfacial energy. To demonstrate the adapted model, grain growth by capillarity was simulated and it was compared to the original hybrid model. The adapted hPPF was found to be robust and to retain the correct kinetics and physics [93]. This exercise was performed in order to familiarize myself with deterministic–statistical models and obtain a direct method to calculate the thermodynamic state of a sharp interface.
- The application of the hybrid deterministic–statistical model to a radiation induced microstructural evolution test problem. This model incorporates rate theory, phase field and Potts Monte Carlo to simulate the behavior of precipitates within a matrix. To test the hybrid model with radiation defect formation as discussed in Section 2.2.1.2, it was applied to a generic phase precipitation and growth kinetics case. The details of this model are found on Chapter V. The model simulates the effects that radiation induced defects and subsequent RIS has on the precipitation evolution kinetics.
- The coupling of rate theory equations to a kinetic Monte Carlo volumetric void swelling. This model implements rate theory equations to govern the behavior of the radiation defects, which in turn are used to nucleate void lattices. This type of model where the actual volume change can be simulated enables us to generate nano–porous microstructures. A general case was simulated to generate highly porous microstructures where the behavior described in Section 1.3.1.1 can be observed. The details of this model and its implementation can be found in Chapter VI.

## CHAPTER IV

# Mathematical Concepts and Numerical Methods

The main mathematical concepts and techniques used in this work are discussed in this chapter. In order to solve the complex non-linear fourth order PDEs used to describe the system's evolution, we need to rely on numerical methods since unique and exact solutions are not readily available. Although analytical solutions have been suggested, e.g. *Ugurlu et al.* [94], these equations are still of major interests amongst mathematicians and physical scientists.

### 4.1 Taylor Expansion

The *Taylor series* is one of the most important mathematical techniques used in the field of numerical methods. This series can be used to approximate the value of a function at a point, given the function's and its derivatives' values at another point [95]. It is a series expansion of a function  $f(x)$  centered around a point  $x = a$ , which has infinite number of derivatives and we can find them all about  $x = a$ . For an infinite number of terms and *centering* around  $x_i$ , we have

$$f(x_i + h) = f(x_{i+1}) = \sum_{n=0}^{\infty} \frac{f^{(n)}(x_i)}{n!} h^n \approx \sum_{n=0}^N \frac{f^{(n)}(x_i)}{n!} h^n + R_n \quad (4.1)$$

where  $h = x_{i+1} - x_i$  is the step size,  $N$  is the  $n - th$  number of terms used for the approximation of  $f$  and  $R_n$  is the remainder term and defined as

$$R_n = \frac{f^{(n+1)}(\xi)}{(n+1)!} h^{n+1} = \mathcal{O}(h^{n+1}) \quad (4.2)$$

where  $\xi$  is a value for  $x$  that lies between  $x_i$  and  $x_{i+1}$  and  $\mathcal{O}(h^{n+1})$  is known as the *truncation error*. As evident from Equation 4.1, Taylor expansion gives the exact value of  $f(x_{i+1})$  for a summation of an infinite number of derivatives. Further, the accuracy of the approximation will be improved as we increase the number of terms ( $N$ ) that are included on the series. Hence, for a finite number of summation terms, Taylor expansion provides an approximation to the desired value. On the other hand, for most cases, a few terms will result in a reasonable approximation. Furthermore, we have some control over the accuracy of the approximation. For instance, by making  $h$  smaller, according Equation 4.2, the remainder should become smaller.

As evident from Equation 4.1, there is an inherit error that will be present for all Taylor expansions since an infinite sum is unpractical, which is related to the *remainder* term Equation 4.2. As previously mentioned, we can tailor this error by increasing or decreasing the spatial step size,  $h$ , and the number of terms in the summation chosen. For example, say that we chose  $n - th$  terms such that we get either  $\mathcal{O}(h)$  or  $\mathcal{O}(h^2)$  truncation errors. Then, halving the step size will reduce the error by a half or a quarter, respectively. Furthermore, by properly manipulating the Taylor series, we are able to derive the *finite difference equations* used in this work to approximate solutions to the set of PDEs.

## 4.2 Finite Difference Methods

Non-linear partial differential equations, as the Cahn–Hilliard equation, are usually very strenuous to solve analytically if at all possible, hence numerical methods

are employed. A simple approach commonly used is known as the *finite difference methods* (FDM), which has been applied to a wide range of engineering and scientific problems [96, 97]. This is a relatively straightforward and intuitive approach, but careful considerations must be taken as to obtain accurate approximations. In a way, FDM is in part an applied *art form* [98], which employs scientific computing principles to approximate differential equation. The phenomenological equations derived in Section 2.3 are approximately solved using this mathematical technique. While these equations are representative of a general formulation, the same concepts can be applied to other PDEs used on the different models developed.

As mentioned before, FDM is a scientific art form such that many types of approximations can be derived. The approximation chosen will depend on computational limitations, desired accuracy, *inter alia*. Some more common schemes include the *forward* difference method, also known as the Euler forward method,

$$\Delta f_i \equiv f_{i+1} - f_i, \tag{4.3}$$

the *backward* difference scheme

$$\Delta f_i \equiv f_i - f_{i-1}, \tag{4.4}$$

and the *centered* difference scheme

$$\Delta f_i \equiv f_{i+1} - f_{i-1}, \tag{4.5}$$

all of which can be used to approximate first order derivatives. Figure 4.1 shows a graphical representation of these schemes applied to a first order derivative on a 1D three point system. The proper points of interest for all schemes can be easily identified, which tell us the site's whose value are needed in order to approximate the



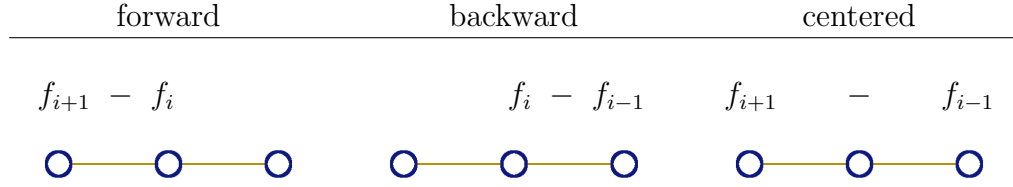


Figure 4.1: Representation of different type of FDM schemes. Each scheme shows the respective points that need to be sampled in order to approximate a first order derivative.

solution.

The Taylor series can be manipulated in different ways such that we can derive the schemes described with their corresponding truncation errors. For instance, let us consider the first order derivative of  $y$

$$y' = \frac{dy}{dx}. \quad (4.6)$$

The different schemes can be derived by expanding Equation 4.1, for the forward ( $+h$ ) case

$$y(x_i + h) = y(x_i) + hy' + \mathcal{O}(h). \quad (4.7)$$

Rearranging for the derivative of interest, we have

$$y' = \frac{y(x_i + h) - y(x_i)}{h} + \mathcal{O}(h), \quad (4.8)$$

and for the backward ( $-h$ ) scheme

$$y' = \frac{y(x_i) - y(x_i - h)}{h} + \mathcal{O}(h). \quad (4.9)$$

For the centered case we need to extend in both directions ( $\pm h$ ) and then combine

both equations, which gives

$$y' = \frac{y(x_i + h) - y(x_i - h)}{2h} + \mathcal{O}(h^2). \quad (4.10)$$

From the discussion in Section 4.1, we expect the centered scheme to provide a more accurate approximation to  $y'$ . This is graphically represented in Figure 4.2, where the approximation is shown as the slope between the points of interest, Figure 4.1. We can graphically appreciate that the centered scheme yields a more accurate approximation for the *true* derivative (slope), as expected from the Taylor expansion analysis.

#### 4.2.1 Approximation of the Diffusion Equation

The PDEs that describe the compositional evolution of the different continuum order parameters discussed earlier are differentiated with respect to time and space. A generally used scheme to numerically solve similar equations, e.g. the heat equation, is the forward–time central–space (FTCS), which has been successfully applied to diffusional equations problems [88, 89, 99, 49]. Hence, the phenomenological equations derived in Section 2.6 were numerically solved by using the FTCS scheme. This scheme couples the forward and centered schemes in such a way that we get a  $\mathcal{O}(\Delta t, h^2)$  order accurate solution. Let's consider a basic diffusional equation with constant mobilities and interfacial energy defined by the Cahn–Hilliard equation,

$$\frac{\partial f}{\partial t} = M \left[ \nabla^2 \frac{\partial f_0}{\partial f} + \gamma \nabla^4 f \right]. \quad (4.11)$$

Here we have three distinct orders of differential equations which were solved using the FTCS scheme. Let's examine each one individually and for simplicity let's assume a one dimensional case. The biharmonic equation of  $f$  requires the Taylor expansion with several spatial considerations, i.e.  $nh$  where  $n = [-2, 2]$ . More clearly, for the centered scheme we need to perform four Taylor expansions about  $x_i$  to obtain

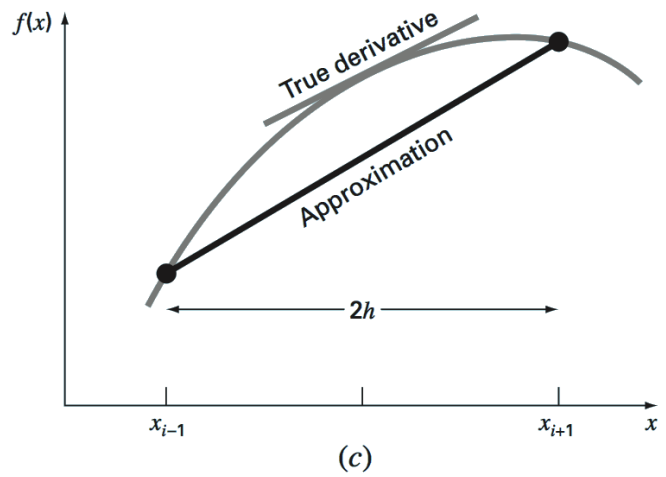
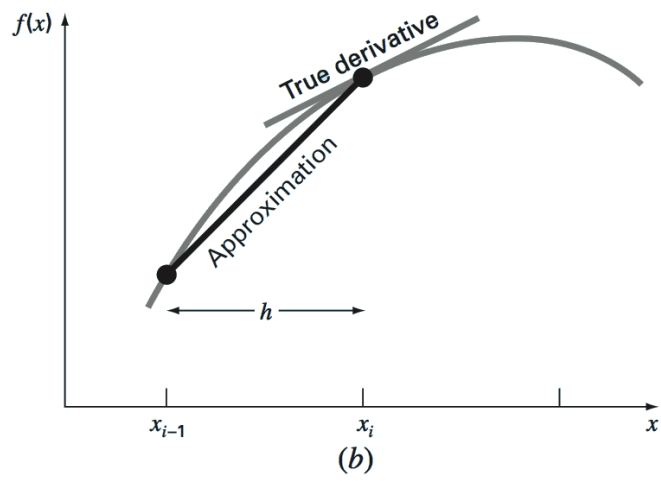
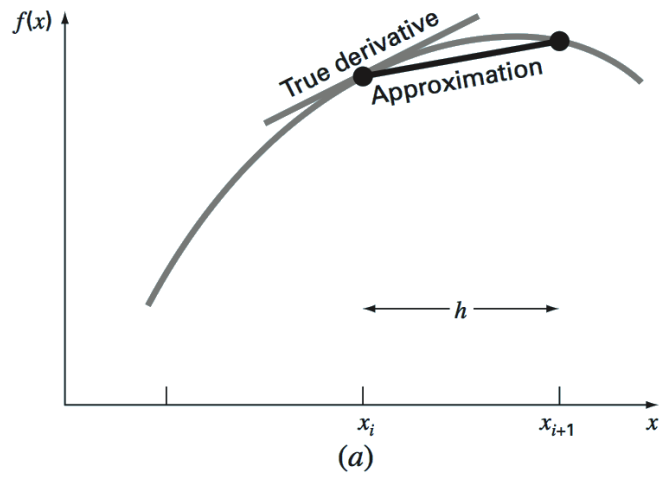


Figure 4.2: Graphical depiction of (a) forward, (b) backward, and (c) centered finite-divided-difference approximations of the first derivative [95].

an approximation to the biharmonic equation. This set of expansions can then be combined in a way that yields an error order of  $\mathcal{O}(h^2)$ . The resulting approximation is

$$\nabla_x^4 f = \frac{\partial^4 f}{\partial x^4} \approx \frac{f_{i+2} - 4f_{i+1} + 6f_i - 4f_{i-1} + f_{i-2}}{h^4} + \mathcal{O}(h^2) \quad (4.12)$$

where the nomenclature has been simplified,  $f(x \pm nh) = f(x_{i \pm n}) = f_{i \pm n}$ . Similarly, for the Laplacian of  $f$ , using  $n = [-1, 1]$  we have

$$\nabla_x^2 \left( \frac{\partial f_0}{\partial f} \right) = \nabla_x^2 \hat{\mu} = \frac{\partial^2 \hat{\mu}}{\partial x^2} \approx \frac{\hat{\mu}_{i+1} - 2\hat{\mu}_i + \hat{\mu}_{i-1}}{h^2} + \mathcal{O}(h^2) \quad (4.13)$$

where  $\hat{\mu} \equiv \partial f_0 / \partial f$  as described earlier. Finally, combining Euler's equation for the temporal differentiation with the approximations given by Equations 4.12 and 4.13, we can approximate the value of  $f$  at  $i$  for the next time step as

$$f_i^{n+1} \approx f_i^n + \Delta n M \left[ \gamma \left( \frac{f_{i+2} - 4f_{i+1} + 6f_i - 4f_{i-1} + f_{i-2}}{h^4} \right) + \frac{\hat{\mu}_{i+1} - 2\hat{\mu}_i + \hat{\mu}_{i-1}}{h^2} \right] + \mathcal{O}(\Delta n, h^2). \quad (4.14)$$

As can be appreciated, we need the values of the four nearest neighbors in any given Cartesian direction in order to approximate the next time step value. The form of the approximation shown here is valid for a system with periodic boundary condition. This solution to the PDE system is implemented through explicit methods. One advantage of using explicit methods is that we can achieve really accurate solutions, as long as we choose proper discretization parameters, i.e.  $(\Delta n, h)$ . Even though implicit methods have been used to numerically solve similar systems of equations, it has been observed that the explicit FTCS approach is better at handling discontinuities (or shocks) to the continuum fields [99]. Since we are continuously adding defects (or shocking the continuum order parameter), we rely on the use of the explicit solution.

Due to the way in which connectivity is defined by the SPPARKS framework,

cmap[5]	cmap[3]	cmap[6]
cmap[0]	i	cmap[1]
cmap[4]	cmap[2]	cmap[7]

Figure 4.3: Cell map defined for computational convenience. The summation in Equation 4.15 follows the logic represented by this map.

Figure 4.3, and considering a three dimensional space, we can re-write this equation for simplicity when coding as

$$f_i^{n+1} \approx f_i^n + \frac{\Delta n M}{h^2} \sum_{d=1}^D \sum_{j=-1}^1 \left[ (\hat{\mu}_{i_d+j} - \hat{\mu}_i) + \frac{\gamma}{h^2} (f_{i_d+2j} - 4f_{i_d+j} + 3f_i) \right] \quad (4.15)$$

$$= f_i^n + \frac{\Delta n M}{h^2} \sum_{d=1}^D \sum_{j=-1}^1 \hat{\mathcal{J}}_{dj} \quad (4.16)$$

where  $D$  is the simulation space dimension,  $\hat{\mathcal{J}}_{dj}$  is defined for nomenclature convenience as the flux between the site and its neighbors, i.e. terms within the bracket, and the  $i_d$  nomenclature stands for the site in the dimensional direction  $d$ . This approach could be introducing an extra error that arises from the approximation of the Laplacian of the chemical potential. As explained in Appendix C, depending on the definition of  $f_0$ , there may be terms that have been dropped from the differentiation for computational ease. The omission of these terms has been observed to not influence the stability and/or final solution of the microstructural evolution.

For simulations with non-periodic boundary conditions, i.e. free surfaces, we need to account for the respective boundary conditions. Figure 4.4 shows a free surface, which is defined as the interface between a void region (green outline) and a matter

region (blue outline). The sites whose information is required to approximate the biharmonic are outlined in maize. One of the more evident boundary conditions across a void–matter interface is that of no diffusion. Therefore, the flux across the domain boundary is set to zero

$$\mathbf{n} \cdot \mathbf{J} = 0 \quad \partial\Omega \tag{4.17}$$

where  $\Omega$  is the domain space. This boundary condition will lead to a modification of the way we discretized the PDEs, Equation 4.15. For an arrangement as the one shown in Figure 4.4(a), there will be diffusion only between sites on the  $\overrightarrow{ix_{ip1}}$ ,  $\overrightarrow{ix_{im1}}$  and  $\overrightarrow{iy_{im1}}$  directions. For this case it is fairly straightforward how to set the flux in the  $\overrightarrow{iy_{ip1}}$  direction to zero, i.e.  $\hat{\mathcal{J}}_{y_{ip1}} = 0 \rightarrow \hat{\mu}_i = \hat{\mu}_{y_{ip1}}$  and  $f_{y_{ip2}} = f_{y_{ip1}} = f_i$ . On the other hand, correctly setting the flux for the case shown in Figure 4.4(b) is not as trivial. This is because of the biharmonic contribution in the  $+y$  direction. While there is a contribution from the  $y_{ip1}$  site, the fact that  $y_{ip2}$  is a void means that it cannot contribute to diffusion. Hence, this needs to be accounted for numerically. If not properly set, the continuum order parameters were found not to be conserved.

### 4.3 Capillarity Driven Flux

The models developed throughout this thesis have made use of sharp interface to define grain boundaries and free surfaces. While the original hPPF model was shown to accurately simulate grain growth kinetics driven by Ostwald ripening mechanisms [100], Figure 4.5, a direct approach to handle sharp interfaces was needed. This is especially true for the cases where we have free surfaces since we treat these as being 100% void, i.e. they have no concentration. In order to achieve this, the phenomenological equations were adapted as to replace the Cahn–Hilliard diffuse interfacial energy with a discrete sharp interfacial energy [93]. The sharp interfacial

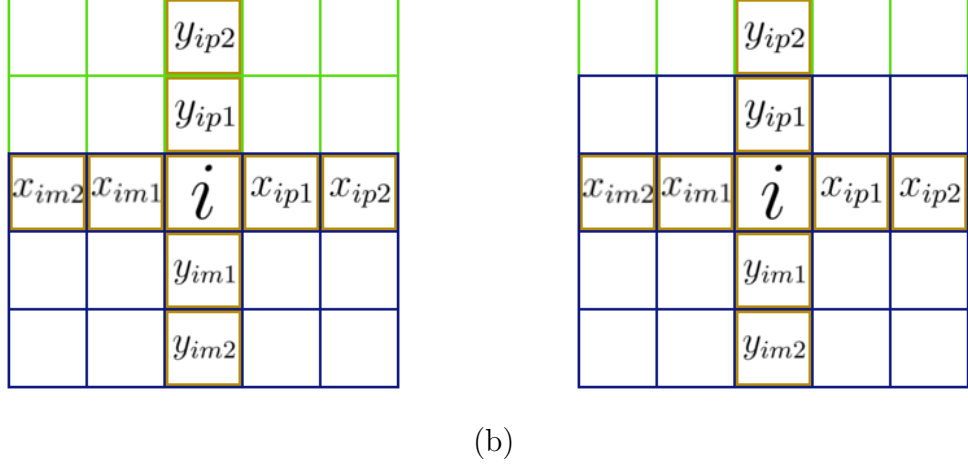


Figure 4.4: Diagram of a digitized free surface, defined as the interface between a void (green) and matter (blue) space. Two arrangements where the presence of a surface will influence the flux equation as shown. This finite difference stencil yields a second order error,  $\iota(h^2)$ . Careful consideration must be applied when choosing how to set up the no flux conditions where needed.

energy is shown to be related to the curvature

$$\frac{\delta F}{\delta C} = \gamma \frac{\delta S}{\delta C} = \gamma \frac{\delta V}{\delta C} \frac{\delta S}{\delta V} = \gamma \Omega \frac{8\pi R \delta r}{4\pi R^2 \delta r} = \frac{2\gamma \Omega}{R} \equiv \gamma \Omega \kappa \quad (4.18)$$

where  $S$  is the surface area,  $\gamma$  is the surface energy,  $\Omega$  is the molar volume change and  $\kappa$  is the curvature. The development of the discrete interfacial energy hPPF can be found in Appendix E. While the contribution here are made through the development of the sharp interfacial energy method, let's look at common methods used to define and treat curvature.

### 4.3.1 Mathematical Treatment of the Curvature

Whenever you have a continuum field defining surface, e.g. level set theory [102, 103], the curvature can be defined in terms of the continuum field. In fact, if we consider the Cahn–Hilliard interfacial energy term to be analogous to a curvature measure, we can see that as we move away from the interface it should approach zero

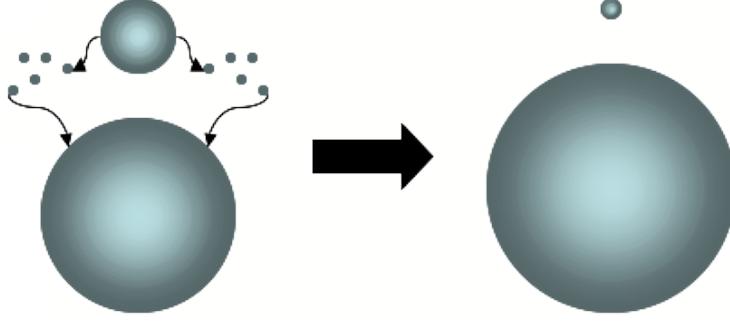


Figure 4.5: Basic schematic of the Ostwald ripening process. Due to their larger curvature, the smaller features are less thermodynamically stable, which leads to their dissolution and growth of the larger features. (Taken and adapted from [101].)

since the equal-phase region should have the same concentration

$$\lim_{d \rightarrow \infty} \nabla^2 C = 0. \quad (4.19)$$

Let's consider that the concentration defines the a *curved surface* ( $s$ ) which is used to identify interfaces. The curvature can then be defined as the divergence of the normal vector,

$$\hat{\mathbf{n}} = \frac{\nabla C}{|\nabla C|}, \quad (4.20)$$

at any point in that in the curve, which gives

$$\kappa = \nabla \cdot \hat{\mathbf{n}} = \nabla \cdot \left( \frac{\nabla C}{|\nabla C|} \right). \quad (4.21)$$

Applying the chain rule to expand this definition of the curvature, we get

$$\kappa = \frac{\nabla^2 C}{|\nabla C|} - \sum_{i=x}^{\{y,z\}} \frac{\nabla_i C}{|\nabla_i C|^3} \left( \nabla_i C \nabla_{ii} C + \sum_{j=x}^{\{y,z\}} (1 - \delta_{ij}) \nabla_j C \nabla_{ij} C \right) \quad (4.22)$$



where

$$\nabla_i = \frac{\partial}{\partial i} \tag{4.23a}$$

$$\nabla_{ij} = \frac{\partial^2}{\partial i \partial j} \tag{4.23b}$$

This definition of the curvature is fairly complex and finding a numerical approximation could present challenges. From Appendix E, we see that the rate change of the concentration is proportional to the Laplacian of the curvature, i.e.  $\dot{C} \propto \nabla^2 \kappa$ . Therefore, an even more intricate expression would need to be numerically solved. This could become computationally expensive, especially as we add order parameters. A detailed derivation of these equations can be found in Appendix B.

### 4.3.2 Discrete Approximation of the Curvature

A discrete curvature equation was developed in order to use the sharp interface defining the boundary between different features, Appendix E. Analogous definitions to the discrete curvature have been applied to cellular automata simulations of solidification processes [104]. The discrete curvature is defined as

$$\kappa_i = \frac{\sum_{j=1}^{n_s} (1 - \delta_{q_i q_j}) - n_{base}}{n_s} \tag{4.24}$$

where  $q_i$  is the phase of site  $i$ ,  $n_s$  is a normalizing parameter which can be the number of surrounding neighbors being considered on the curvature calculation and  $n_{base}$  is the reference state that yields a curvature of zero for a flat surface. Even though this looks similar to the Potts interfacial energy, an important distinction is that we consider unlike *phase* sites. This is so that each phase is able to find its corresponding equilibrium concentration. As an example, if we look at Figure 4.6, the dark blue cell is a free surface site with 17 unlike phase surrounding sites (not shown). This value would replace the sum term from the discretized curvature equation. This definition

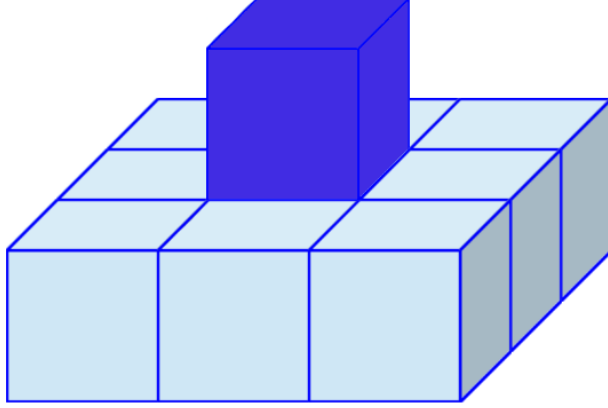


Figure 4.6: Representation of a 3D voxelated surface where the void voxels are not shown and the voxels shown represent a single phase. Each voxel has 26 neighbors surrounding it which can contribute to the curvature approximation.

of the curvature allows for more accurate approximations by allowing a larger number of surrounding sites to be sampled, as discussed in Appendix E.

Its important to note that even for the sharp interfaces employed by our models, we can still apply the complex curvature equations shown earlier. This could be done by calculating the normal of the sharp interface [105]

$$\hat{\mathbf{n}}_d = \sum_{j=1}^{n_s} \frac{(1 - \delta_{ij})d_{ij}}{|(1 - \delta_{ij})d_{ij}|} \quad (4.25)$$

where  $d_{ij}$  is the distance vector between sites  $i$  and its neighbor  $j$

$$d_{ij} = \sum_{d=1}^D (x_{d,j} - x_{d,i}) \cdot \mathbf{e}_d \quad (4.26)$$

where  $x_{d,i}$  is the position of site  $i$  in the  $d$  direction and  $\mathbf{e}_i$  is the unit vector in the  $d$  direction. Hence, for the ensemble shown in Figure 4.6 the unit normal vector points upwards.

## 4.4 Euler–Lagrange

The literature often shows the Cahn–Hilliard equation and the resulting phenomenological equation with seldom mention of how one leads to the other. For clarity, the derivation is discussed here. Starting from the Cahn–Hilliard free energy functional,

$$F = \int_{\Omega} (f_0 + \gamma |\nabla C_i|^2) dV = \int_{\Omega} f(\mathbf{x}, f_0, C_i, \nabla C_i) dV, \quad (4.27)$$

and arriving to the well know Cahn–Hilliard phenomenological equation, Equation 4.11, is not trivial. In fact, Cahn–Hilliard employed the Euler–Lagrange equation to obtain the variational change of the free energy functional with respect to the concentration. Let’s consider the free energy functional to be the system’s total Gibbs free energy. The chemical potential of component  $i$  is

$$\mu_i = \frac{\partial G}{\partial C_i} \equiv \frac{\delta F}{\delta C_i} \quad (4.28)$$

where we have defined the chemical potential to be equivalent to the variational derivative of  $F$  with respect to  $C_i$ . This is consistent with the definition of the chemical potential and thermodynamic principles since we are minimizing the free energy of the system. Applying the Euler–Lagrange equation gives

$$\frac{\delta F}{\delta C_i} = \frac{\partial I}{\partial C_i} - \frac{d}{dx} \frac{\partial I}{\partial \nabla C_i} \quad (4.29)$$

where  $I$  is the integrand of the free energy functional, Equation 4.27. For simplicity, let’s consider a 1 dimensional space. Combining Equations 4.27 and 4.29, we obtain

$$\frac{\delta F}{\delta C_i} = \frac{\partial}{\partial C_i} \left[ f_0 + \gamma \left( \frac{\partial C_i}{\partial x} \right)^2 \right] - \frac{d}{dx} \left( \frac{\partial}{\partial C_i / \partial x} \left[ f_0 + \gamma \left( \frac{\partial C_i}{\partial x} \right)^2 \right] \right) \quad (4.30)$$

and by performing the respective operations, the right hand side results in

$$\frac{\partial f_0}{\partial C_i} + \gamma \frac{\partial}{\partial C_i} \left( \frac{\partial C_i}{\partial x} \right)^2 - \frac{d}{dx} \left( \frac{\partial f_0}{\partial C / \partial x} + 2\gamma \frac{\partial C_i}{\partial x} \right) = \frac{\partial f_0}{\partial C_i} - 2 \frac{d}{dx} \left( \gamma \frac{\partial C_i}{\partial x} \right) \quad (4.31)$$

where the two terms cancel to zero since the gradient of  $C_i$  is independent of the concentration and the bulk volumetric energy ( $f_0$ ) is independent of the concentration gradient, respectively. Assuming that the surface energy is constant, this yields the more recognizable Cahn–Hilliard equation

$$\frac{\delta F}{\delta C_i} = \frac{\partial f_0}{\partial C_i} - 2\gamma \frac{\partial^2 C_i}{\partial x^2}. \quad (4.32)$$

The solution of this PDE will result in the composition profile with stationary values, i.e. maxima, minima or saddle points [61].

A recent derivation provides an easier way to articulate the final result of the derivation just shown [106]

$$F = \int_{\Omega} G(\mathbf{x}, C, \nabla C) d\Omega = \int_{\Omega} G(x_i, \dots, x_n, C, C_{x_1}, \dots, C_{x_n}) d\Omega \quad (4.33)$$

where  $C_{x_i} = \partial C / \partial x_i$ . Again, using the Euler–Lagrange equation, they arrive to the expression

$$\frac{\delta F}{\delta C} = \frac{\partial G}{\partial C} - \sum_{i=1}^n \frac{\partial}{\partial x_i} \frac{\partial G}{\partial C_{x_i}} = \frac{\partial G}{\partial C} - \nabla \cdot \frac{\partial G}{\partial \nabla C}, \quad (4.34)$$

which provides “cleaner” nomenclature and perhaps a straightforward way of understanding the resulting derivation. More importantly, it could be easily applied to any free energy functional of their particular form, Equation 4.33. If the same integrands are chosen, this equation yields the same result as the one shown.

## CHAPTER V

# Numerical Simulation of Radiation Induced Segregation: Influence on Precipitate Kinetics

Irradiation of materials has been shown to lead to accelerated and/or non thermodynamically driven microstructural changes. This behavior is driven by the radiation induced defects. These changes in microstructural evolution present themselves as nucleation of phases away from thermodynamic equilibrium [107, 108] and/or abnormal crystallization kinetics [109]. It is important to understand how microstructures evolve as a function of radiation damage as microstructural characteristics are related to the materials' macroscopic properties. This is especially true in the nuclear energy industry where one of the main limiting factors of reactor performance are due to material degradation. This chapter focuses on the development and implementation of a hybrid model that incorporates the radiation-induced segregation (RIS) rate theory formulation. A brief introduction to the problem followed by model specifics and results discussion are presented.

### 5.1 Introduction

Radiation damage of materials has been a subject of interest for many decades, which spans several fields including outer space satellite application [110] and the

energy sector [11, 31]. Models like the one developed by *Wiedersich et al.* have been used to interpret experimentally observed behavior like RIS [111, 112]. In fact, the RIS model has been used to qualitatively explain the observed formation of thermodynamically unstable phases on irradiated *NiSi* systems [113]. The RIS model postulates that as materials are irradiated the created defects diffuse towards different types of sinks and can be annihilated at different rates, e.g. interstitial and vacancy removal at the free surfaces. The difference in the atomic diffusivities then leads to a net depletion or enrichment of a given atomic component around the sinks. For instance, a binary (*AB*) alloy where the *B* atoms diffuse faster through the interstitial mechanism will lead to enrichment of *B* in the vicinity of the sinks. Possibly leading to precipitation of non-thermodynamically stable phases.

Models like *Wiedersich's* have proven effective at simulating the chemical evolution of materials under irradiation. However, it fails to capture other complex and synergistic effects related to the overall microstructural evolution, e.g. grain and/or precipitate evolution. To address this gap, a new type of hybrid model was developed where these phenomena can be more easily computationally implemented. This hybrid deterministic-statistical model couples a set of non-linear partial differential equations (PDE) to a Potts Monte Carlo model. The set of PDEs uses phase field and rate theory models to simulate the chemical evolution of the atomic components and point defects, respectively. The Potts Monte Carlo model is used to simulate phase and precipitate growth kinetics. This hybrid model was applied to a generic binary (*AB*) system by studying how the microstructural evolution is affected by different radiation conditions. The hybrid model's deterministic and statistical methods efficiently model the synergistic processes taking place due to the radiation damage being produced. It should be noted that understanding irradiation affects microstructures evolution is very important to areas like reactor safety and integrity. Improving these has implications on our ability to reach the much needed manageable, safe and

reliable energy production levels required for the future.

## 5.2 Model Framework

A chemically binary ( $AB$ ) system with thermodynamic characteristics that define a two-phase material are studied. Radiation damage is introduced in the form of point defects densities, i.e. interstitial and vacancy concentration. To simulate the evolution of these components, a set of deterministic PDEs was derived. The PDEs link the diffusion of the atomic and defect components, and how the behavior of a given component affects others. The processes modeled that lead to microstructural evolution include: diffusion of the atomic ( $A$  and  $B$ ) and defect ( $i$  and  $v$ ) components; precipitate growth and phase transformation. The model is based on the diffuse interfacial hybrid Potts-phase field model *Homer et al.* [88, 89, 90], but is further developed to simulate radiation damage and its effects on diffusion. While the simulation could be easily extended to 3-dimensions, the work presented here was carried out on a 2-dimensional simulation mesh.

### 5.2.1 Microstructural and Compositional Representation

As it was described in Section 2.1, the model uses both continuum and discrete order parameters to describe the complete microstructure. The set of continuum order parameters are the atomic ( $C_a$  and  $C_b$ ) and point defect ( $C_i$  and  $C_v$ ) concentrations, which are defined by Equation 2.1. The discrete order parameters represent the grain ID/orientation ( $s$ ) and phases ( $q$ ), i.e. distinct features. Furthermore, simulations considering irradiation of an exposed free surface, both of the discrete order parameters are set to an identical value that represents a vacuum. These order parameters enable the full description of the microstructural evolution.

Simulations without free surfaces have periodic boundary conditions (PBC), while the ones with free surfaces have PBC on the horizontal-direction only, i.e. the direc-

tion that does not have a free surface. This makes the latter case’s simulation space a semi–infinite solid with an irradiated free surface in direct contact with a vacuum. This boundary is included for computational reasons, allowing simpler implementation of the discretized equations as discussed in Section 4.2.1.

### 5.2.2 Radiation Damage

Radiation damage is introduced into the system in the form of radiation induced point defects. The amount of defects which contribute to the microstructural evolution are calculated in a two step process. First, a probability of collision,  $p_{coll}$ , is calculated and compared to a random number ( $RN \sim U[0, 1) : \{RN|0 \leq RN < 1\}$ ). Depending on the particular simulation, this probability will have a uniform (constant probability) or Gaussian–like profile. The particular distribution will be discussed for each respective simulation. To determine the amount of energy being deposited on average per pixel at a given location, is given by a depth dependent normal distribution

$$E_T(\mathbf{x}) = E_0 \cdot E_n \exp\left(-\left[\frac{\mathbf{x} - \bar{\mathbf{x}}}{\sigma}\right]^2\right) \quad (5.1)$$

where  $\mathbf{x} = x \cdot \hat{i} + y \cdot \hat{j} + z \cdot \hat{z}$  is the position vector for a given pixel,  $E_T$  is energy deposited at  $z$ –depth,  $E_0$  is the ion beam energy,  $E_n$  is a parameter to define the distribution’s “amplitude”,  $\bar{\mathbf{x}}$  is the average range of the ions traveling through the irradiated target and  $\sigma$  is the standard deviation. A more realistic damage profile could be implemented by using the SRIM BCA model, Section 2.2.1, to calculate the expected distribution of the created defects [5]. These distributions could then be fitted to Equation 5.1. From the amount of energy deposited, the number of defects created at a given depth are approximated. The Kinchin–Pease model [81] is used to calculate the number of defects being created by a given collision cascade and its resulting energy deposition. These defects are assumed to be created in Frenkel pairs, i.e. each collision creates an equal number of interstitials and vacancies. The defects



created by the collision cascade are mostly very unstable and annihilated during the collision cascade collapse. Therefore, the defects of interest are the ones that survive past the quenching stage. The *defect survivability* is given by Equation 2.11. These are the defects that directly contribute to the microstructural evolution. The procedure of how these are calculated has been outlined in detail on Section 2.2.1.2.

### 5.2.3 Phenomenological Behavior

Radiation induced segregation models have been developed to explain the behavior of irradiated alloys that show chemical depletion/enrichment at generic sinks, e.g. grain boundaries. Figure 5.1 shows a schematic of this type of behavior. As irradiation induced defects are created, these want to diffuse towards the respective sinks. In this case, the main sink being the  $\alpha - \beta$  phase interface. Assuming that the predominant diffusion mechanism is a site exchange mechanism, the defect diffusion behavior will be closely linked to an atomic diffusion. These phenomena can be mathematically described by fully coupling the phenomenological diffusional behavior. An approach similar to *Wiedersich's*, and outlined in Section 1.1.2, is employed in the development of the phenomenological partial differential equations. Considering the chemical diffusion of the system, the evolution of the system is defined by the different fluxes

$$J_i^a + J_i^b = J_i \quad (5.2a)$$

$$J_v^a + J_v^b = -J_v \quad (5.2b)$$

$$J_a + J_b = J_i - J_v \quad (5.2c)$$

where  $J_x^y$  stands for the flux of defect  $x$  through  $y$ 's site. An important point that these equations communicate that the atomic components migrate in the same and opposite directions as the interstitials and vacancies, respectively. Therefore, let's say

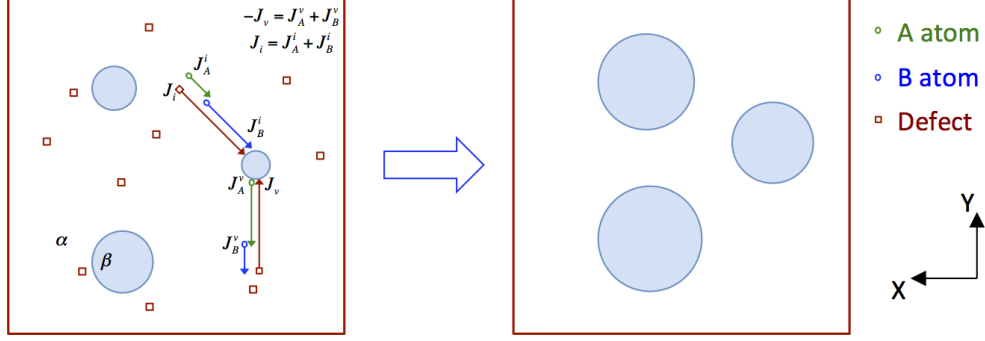


Figure 5.1: Diagram showing the expected growth behavior of  $\beta$ -precipitates on an irradiated  $\alpha$ -matrix material. As the generated point defects diffuse to the sinks (phase boundaries), an associated atomic flux will influence microstructural evolution behavior.

that  $A$  atoms preferentially diffuse through the vacancy mechanism and the  $B$  atoms through the interstitial mechanism. As defects diffuse towards the interface, the  $A$  atoms migrate away from the interface and the  $B$  atoms towards the interface. Thus, there is a net depletion of  $A$  and enrichment of  $B$  around the interface, which leads to growth of the  $\beta$  phase precipitates, as shown in Figure 5.1.

#### 5.2.4 Thermodynamics of the System

The model deterministically drives the system towards an equilibrium state as dictated by the equation of state (EoS), which is given by the Ginzburg–Landau equation, also known as the Cahn–Hilliard’s free energy functional,

$$F_{EoS} = \int_{\mathcal{V}} (G + \gamma |\nabla C_b|^2) dV \quad (5.3)$$

where  $\mathcal{V}$  is a bounded domain in an infinite medium,  $G$  is the bulk free chemical energy and  $\gamma$  is the interfacial gradient energy coefficient. The interfacial energy is given by the diffuse interfaces across distinct phases, which are defined by gradient of the atomic concentration across the interface. Radiation damage is an extremely complicated parameter to measure and quantify for modeling purposes. Therefore,

the energetic contribution associated to radiation damage is incorporated as point defect density terms [108]. The bulk free chemical energy is given by entropic and phase dependent enthalpic energetic components. The enthalpic energy terms are characterized by a phase dependent polynomial equation of the form

$$G_q = k_0(C_b - C_0)^2 + k_1(C_b - C_1)^2 + \begin{cases} k_\alpha(C_b - C_\alpha)^2 & q = \alpha \\ k_\beta(C_b - C_\beta)^2 & q = \beta \end{cases} \quad (5.4)$$

where  $q$  denotes the pixel's phase and the  $k$ 's are parameterization variables with units of *energy*. The values used for the parameterization variables are shown in Table 5.1. Figure 5.2 shows the polynomial curves used during this work. These polynomial equations were designed as to yield a system that is comparable to a bulk matrix with  $\sim 12.7$  at.%Si and precipitates with  $\sim 25$  at.%Si, Figure 5.3. These concentrations were chosen from the experimental work by Potter et al. For the entropic term, the ideal solution of mixing equation for a quaternary system is used

$$G_m = E_i^f C_i + E_v^f C_v + \omega_{ab} C_a C_b + k_B T [C_a \ln C_a + C_b \ln C_b + C_i \ln C_i + C_v \ln C_v] \quad (5.5)$$

where  $E_i^f$  is the energy of formation for the  $i$  defect,  $\omega_{ab}$  is the interaction parameter between  $A$  and  $B$  atoms,  $k_B$  is the Boltzmann constant,  $T$  is the absolute temperature and  $C_a = 1 - C_b$ . The increase of energy to the system due to the radiation energy deposited to the target is indirectly incorporated through this equation. The bulk free chemical energy is then given by adding Equations 5.4 and 5.5. Parameterization variables values were chosen as to yield a microstructure that simulates Ostwald ripening precipitate evolution.

Table 5.1: Numerical values of the parameterization variables for the energetic configuration. The values used are separated into enthalpic and entropic sections. The values shown here are technically the non-dimensionalized values as defined in Section 5.2.5.2.

Parameterization Variable	Values
$C_0$	$1.00 \times 10^{-1}$
$C_1$	$2.75 \times 10^{-1}$
$C_\alpha$	$5.00 \times 10^{-2}$
$C_\beta$	$3.00 \times 10^{-1}$
$k_0$	3.00
$k_1$	3.00
$k_\alpha$	5.00
$k_\beta$	5.00
$E_i^f$	8.00
$E_v^f$	5.00
$\omega_{ab}$	$8.00 \times 10^{-1}$
$\mathcal{J}$	$2.15 \times 10^{-2}$

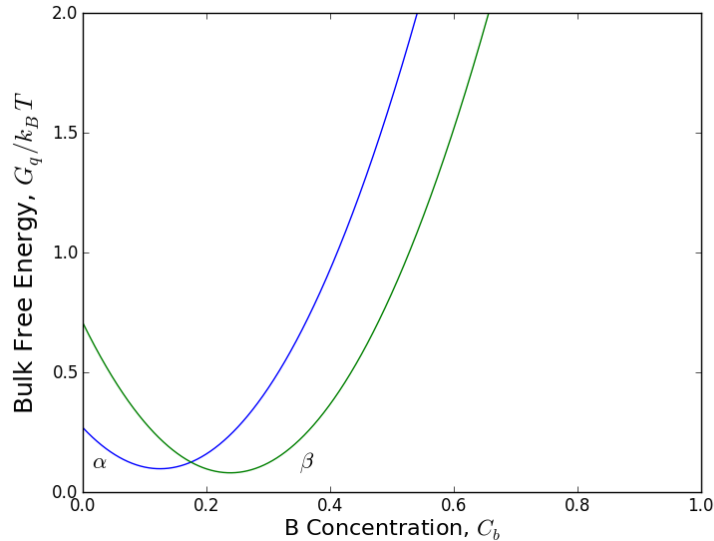


Figure 5.2: Composition dependent bulk free energy functional for the binary two-phase system. These curves were chosen as to be comparable to the NiSi system for  $\bar{C}_{Si} \sim 0.13$ ,  $T < 900$  K.

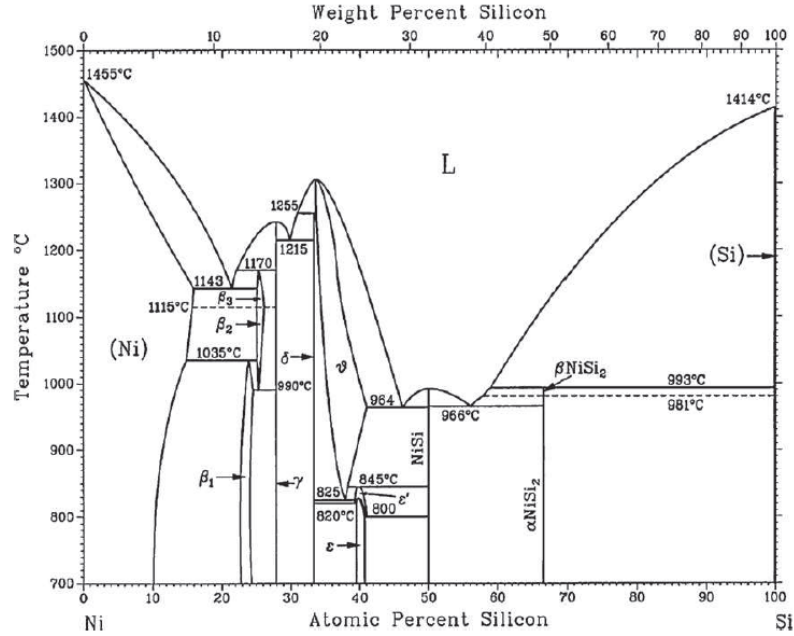


Figure 5.3: NiSi phase diagram (from Massalski [114]).

### 5.2.5 Phenomenological Equations

Since the point defects are treated as atomic entities, it can be argued that the model simulates a quaternary system,

$$C_a + C_b + C_i + C_v = 1.$$

But, since it can be assumed that  $C_{a,b} \gg C_{i,v}$ , this relationship can be approximated as

$$C_a + C_b = 1. \quad (5.6)$$

where the  $C_a$  and  $C_b$  are the  $A$  and  $B$  atomic conserved concentration, respectively. The defect concentrations are not conserved, as they can be created and annihilated through different mechanisms. In fact, the average defect concentration is expected to increase until a steady state is achieved [11, 109]. By coupling the evolution equations for the atomic and defect components, the model can simulate the microstructural evolution of the system by solving the set of three phenomenological equations. Set-

ting the chemical potential as the driving force, the chemical evolution of each atomic component in a system containing  $n = i, j, \dots, n_t$  components is given by

$$\frac{\partial C_i}{\partial t} = \nabla \cdot \mathbf{J}_i = \nabla \cdot \left[ \sum_{j=1}^{n_t-1} M_{ij} \nabla \hat{\mu}_j \right] \quad (5.7)$$

where the  $M_{ij}$  terms are the mobilities of the each atomic component through the different diffusion mechanisms and

$$\hat{\mu}_j \equiv \mu_j - \mu_{n_t} = \frac{\partial F}{\partial C_i} \quad (5.8)$$

is the true driving force, Section 2.6. This can be shown by using the true definition of the chemical potential for a multi-phase multi-component system [86]

$$\mu_i = F + \sum_{j=1}^{n_t-1} (\delta_{ij} - C_j) \frac{\partial F}{\partial C_j} \quad (5.9)$$

where  $F$  can be set to be the EoS and  $\delta_{ij}$  is the Kronecker delta.

The RIS model developed by *Wiedersich* similarly couples a set of rate theory equations to simulate atomic and defect compositional evolution. However, this hybrid model uses the chemical potential gradient as the driving force for the chemical components, instead of the compositional gradient. This allows the respective phases to be driven to their appropriate thermodynamic equilibrium concentrations, as opposed to continually deplete or enrich the regions around sinks [115]. It should be noted that the RIS work does suggest the implementation of a parameter that accounts for the difference between the chemical potential and concentration gradients. This was not further explored in this work. Adapting Equation 5.7 to include radia-

tion damage related events as in *Wiedersich*, we have

$$\frac{\partial C_i}{\partial t} = \frac{\eta_s}{\Delta t} + \nabla \cdot (D_{ii} \nabla C_i + D_{ib} \nabla C_b) - k_{iv} C_i C_v - \sum_{j=1}^{n_i^s} S_{i,j} \quad (5.10a)$$

$$\frac{\partial C_v}{\partial t} = \frac{\eta_s}{\Delta t} + \nabla \cdot (D_{vv} \nabla C_v - D_{vb} \nabla C_b) - k_{iv} C_i C_v - \sum_{j=1}^{n_v^s} S_{v,j} \quad (5.10b)$$

$$\frac{\partial C_b}{\partial t} = \nabla \cdot (M_{bb} \nabla [\hat{\mu}_b - \gamma \nabla^2 C_b] + D_{bi} \nabla C_i - D_{bv} \nabla C_v) \quad (5.10c)$$

where  $\eta_s(\Delta t)$  is the concentration of surviving defects during irradiation time  $\Delta t$ , the  $D_{ij}$  are the diffusion coefficients,  $k_{iv} = k_{vi}$  is the point defect recombination rate and the sums are the rate of defect removal at the different  $S$  sinks. The work presented here considers the free surface and the  $\alpha - \beta$  interface to be the only sinks. These sinks are incorporated by setting a boundary condition of constant defect concentration at the interfaces

$$C_{i,v}(\mathbf{x} = \text{interface}) = C_{i,v}^{eq}. \quad (5.11)$$

Furthermore, a zero flux boundary condition is applied to the pixels at the interface between the free surface and vacuum, i.e. no flux between the irradiated target and voided space

$$J \cdot \mathbf{n} = 0 \quad \text{on } \partial \mathcal{V} \quad (5.12)$$

where  $\mathbf{n}$  is the surface unit normal.

### 5.2.5.1 Comments on Diffusion and Mobility Parameters

An important distinction between this model and *Wiedersich*'s is that this work sets the chemical potential to be the driving force of the chemical evolution equation. It is quite common for the diffusivity and mobility to be related by  $M = CD/k_B T$ , which is only true for certain systems. By applying the chain rule to the flux' driving

force, we have

$$M_{ij}\nabla\hat{\mu}_j = M_{ij}\frac{\partial\hat{\mu}_j}{\partial C_j}\nabla C_j = \Theta_j M_{ij}\nabla C_j = D_{ij}\nabla C_j \quad (5.13)$$

where  $\hat{\mu}$  is the difference in the true chemical potentials as defined in Equation 5.8. For simplicity, the mobility scaling parameter ( $\Theta_j$ ) has been defined in order to conveniently compare the diffusivity and mobility. Note that if the chemical potential is defined by the regular solution equation in a monatomic single phase material,  $\mu = \mu_0 + k_B T \ln C$ , the commonly used relationship between  $D_{ij}$  and  $M_{ij}$  is obtained by this method.

From Equation 5.10, it can be appreciated that the model includes the use of a variety of diffusion coefficients,  $D_{ij}$ . These are termed: self-diffusion ( $i = j$ ) and inter-diffusion ( $i \neq j$ ) coefficients. The inter-diffusion coefficient, i.e. diffusion of a given component assisted by the diffusion of another component, is given by

$$D_{ij} = p_{n=i} \cdot \frac{\omega\lambda^2}{2 \cdot \mathcal{D}} = C_i D_j \quad (5.14)$$

where  $p_{n=i}$  is the probability that an adjacent site  $n$  is occupied by an  $i$  type component,  $\omega$  is the frequency at which an exchange is attempted,  $\lambda$  is the average jump distance and  $\mathcal{D}$  is the system's dimensionality. This standard definition was adapted by allowing the probability to be equivalent to the concentration  $C_i$  ( $= p_{n=i}$ ) times the diffusivity constant parameter (often called the pre-exponential), which includes the remaining terms. For self-diffusion, the diffusion coefficient is simply set to  $D_{ii} = D_i$ .

### 5.2.5.2 Non-dimensionalization and Scales

For computational convenience, the standard approach to non-dimensionalizing the Cahn-Hilliard equation is employed. A set of normalizing parameters are defined such that they allow the non-dimensionalization of Equations 5.10 and scale the



different driving forces with simple scalar(s). The normalizing parameters are, for energy

$$\mathcal{E} = k_B T, \quad (5.15)$$

and length

$$l = \sqrt{\frac{\gamma}{\mathcal{E}}} = \sqrt{\frac{\gamma}{k_B T}} \quad (5.16)$$

where the interfacial energy constant,  $\gamma$ , has units of  $length^2 \cdot energy$  giving  $l$  units of length. Finally, using the standard approach and Equation 5.13, the normalized time is

$$\tau = \frac{l^2}{M_{bb}\mathcal{E}} = \frac{\Theta_b l^2}{D_{bb}\mathcal{E}} \quad (5.17)$$

where the mobility,  $M_{bb}$ , has units of  $length^2/(energy \cdot time)$  and  $\Theta_b$  has units of  $energy$  giving the time normalization parameter units of  $time$ . By using these parameters to non-dimensionalize the energy, spatial and time units correspondingly, the Equations 5.10 can be re-written in their non-dimensional forms

$$\frac{\partial C_i}{\partial \tilde{t}} = \frac{\eta_s}{\Delta \tilde{t}} + \tilde{\Theta}_b \tilde{\nabla} \cdot \left( \frac{D_i}{D_b} \tilde{\nabla} C_i + C_i \tilde{\nabla} C_b \right) - \tilde{k}_{iv} C_i C_v - \tilde{S}_{fs} - \tilde{S}_{\alpha\beta} \quad (5.18a)$$

$$\frac{\partial C_v}{\partial \tilde{t}} = \frac{\eta_s}{\Delta \tilde{t}} + \tilde{\Theta}_b \tilde{\nabla} \cdot \left( \frac{D_v}{D_b} \tilde{\nabla} C_v - C_v \tilde{\nabla} C_b \right) - \tilde{k}_{iv} C_i C_v - \tilde{S}_{fs} - \tilde{S}_{\alpha\beta} \quad (5.18b)$$

$$\frac{\partial C_b}{\partial \tilde{t}} = \tilde{\nabla} \cdot \left( \tilde{\nabla} \left[ \frac{\partial \tilde{G}}{\partial C_b} - \tilde{\nabla}^2 C_b \right] + \tilde{\Theta}_b C_b \left[ \frac{D_i}{D_b} \tilde{\nabla} C_i - \frac{D_v}{D_b} \tilde{\nabla} C_v \right] \right) \quad (5.18c)$$

where the non-dimensional parameters are identified by a ‘‘tilde’’ and given by  $\tilde{t} = t/\tau$ ,  $\tilde{k}_{iv} = \tau k_{iv}$ ,  $\tilde{\Theta}_b = \Theta_b/\mathcal{E}$ ,  $\tilde{G} = G/\mathcal{E}$ ,  $\tilde{\nabla} = l\nabla$  and  $\tilde{S} = \tau S$ .

## 5.2.6 Discretization of the Phenomenological Equations

Due to the complexity of finding an exact solution to the set of PDEs described above, the hybrid model is numerically approximated by discretizing the equations.

Table 5.2: Values for the non-dimensionalized phenomenological and Potts’ interfacial energy variables.

Non-dimensional Variable	Value
$\tilde{D}_i/D_b$	$9.50 \times 10^{-1}$
$\tilde{D}_v/D_b$	$9.50 \times 10^{-2}$
$\tilde{\Theta}_b$	$3.72 \times 10^1$
$\tilde{k}_{iv}$	$1.00 \times 10^{-3}$
$\tilde{S}_{fs}$	BC ( $C = C^{eq}$ )
$\tilde{S}_{\alpha\beta}$	$\tilde{S}_{fs}$

This is achieved by employing finite difference methods, more precisely the FTCS scheme, Section 4.2.1. Further, explicit methods are used to solve the complex set of PDEs’. The amount of energy stored within each digitized pixel is given by the free energy functional, Equation 5.3, which can be written as

$$F = \sum_{i=1}^N F_i = \sum_{i=1}^N (G_{q,i} + G_{m,i} + \gamma |\nabla C_{b,i}|^2) \quad (5.19)$$

where  $N$  is the number of pixel sites in the simulation space. Considering events that lead to phase transformations, the Cahn–Hilliard term does not accurately measure the interfacial energy change. This is due to the Cahn–Hilliard equation only considering the continuum order parameter while the phase change is characterized by a discrete instantaneous order parameter change. Therefore, for the sole purpose of comparing the thermodynamic state change during such events, the Potts Monte Carlo method is used to measure interfacial energy. By using the PMC interfacial energy, Equation 5.19 can be re-written as

$$F_d = \sum_{i=1}^N F_{d,i} = \sum_{i=1}^N \left( G_{q,i} + G_{m,i} + \mathcal{J} \sum_{j=1}^n [1 - \delta_{s(i)s(j)}] \right) \quad (5.20)$$

where  $n$  is the number of surrounding neighbors and  $\mathcal{J}$  is the adjacent element interaction energy.

Applying the standard FTCS finite difference scheme to Equations 5.10, results in an approximation for the concentration value for the next time step

$$C_i^{t+1} = C_i^t + \frac{\Delta \tilde{t}}{\tilde{h}^2} \cdot \sum_{i=1}^{2 \cdot \mathcal{D}} \mathbf{J}_{n=i} \quad (5.21)$$

where  $\mathcal{D}$  is the simulation space dimensionality and  $\mathbf{J}_{n=i}$  is the net flux across the digitized boundary (pixel edge for  $2\mathcal{D}$  and voxel face for  $3\mathcal{D}$ ) between sites  $n$  and  $i$ . The net flux equation, as apparent from examining Equation 5.10, for each components' discretized form will be slightly different to match the corresponding driving forces. Therefore, as a generic example, let's consider Equation 5.10c. The net flux across the boundary for this case is

$$\begin{aligned} \mathbf{J}_{n=i} = & \left[ \left( \frac{\partial \tilde{G}}{\partial C_{b,n}} - \frac{\partial \tilde{G}}{\partial C_{b,i}} \right) - \left( \frac{C_{b,2n} - 4C_{b,n} + 3C_{b,i}}{\tilde{h}^2} \right) \right] \\ & + \tilde{\Theta}_{b,i} \bar{C}_b \left[ \frac{D_i}{D_b} (C_{i,n} - C_{i,i}) - \frac{D_v}{D_b} (C_{v,n} - C_{v,i}) \right] \end{aligned} \quad (5.22)$$

where  $\bar{C}_b = (C_{b,n} + C_{b,i})/2$  is the average concentration of  $B$ , and the  $i, n$  and  $2n$  subscripts stand for the different sites of interest: self, first neighbors and second neighbors, respectively. The sites constituting the calculation's "sites of interest" are shown in Figure 4.4. The regular second order centered approximations in space ( $\mathcal{O}(h^2)$ ) of the Laplacian and the biharmonic operators are attained when performing the sum over  $2 \cdot \mathcal{D}$ , Equation 5.21. Adaptations to the term in large square brackets in Equation 5.22 were employed for instances where the second neighbor is a void site as to reflect the no flux boundary condition between the vacuum and target regions. This allows for conservation of the continuum order parameters which define the atomic components.

### 5.2.7 Phase Transformations

The change in the chemical bulk free energy with sharp interfacial energy, Equation 5.20, dictates whether a transition between thermodynamic states will take place. The energetic contribution of the radiation damage is incorporated in the form of excess point defects. In addition, the radiation induced depletion/enrichment of the different chemical components in the irradiated region can be considered another indirect energetic component arising from the radiation damage. The precipitates are allowed to grow and shrink by minimizing the EoS by means of the standard Metropolis algorithm. For a site  $i$ , a neighboring site  $n$  is randomly selected and its grain ID and phase are adopted. Following Boltzmann statistics, the probability of accepting the configurational change is given by

$$P_i = \begin{cases} 1, & \Delta F_{d,i} \leq 0 \\ \exp\left(-\frac{\Delta F_{d,i}}{k_B T}\right), & \Delta F_{d,i} > 0 \end{cases} \quad (5.23)$$

where  $\Delta F_{d,i} = F_{d,i}^{trial} - F_{d,i}^{initial}$  is the change in bulk free energy of the system between the attempted (trial) and the initial configurations. The sharp interfacial energy EoS is given by Equation 5.20. When the trial configuration is accepted, the phase transformation events are accompanied by an instantaneous removal of excess point defects. This simulates the decrease in energy as the microstructure “relaxes” to a more stable microstructure.

## 5.3 Results and Discussion

To test the model, several irradiation conditions are simulated on bulk and surface irradiated materials. The different radiation conditions can be defined as uniform and non-uniform. Uniform irradiation assumes that the ion range is much deeper into the target than the domain being simulated, Figure 5.4. The non-uniform cases consider

irradiation of a surface with medium and high energy irradiation profiles, as relative to each other. Generally, the simulations look at irradiation of an  $\alpha$ -matrix with an initial density ( $\rho_0^\beta$ ) of  $\beta$ -precipitates. These configurations are meant to be analogous to the thermodynamic state for a Ni 12.7 at.%Si system at elevated temperatures,  $T > 700 K$ .

These simulations were performed on the SPPARKS framework to take advantage of the massive parallel features [91, 92]. The simulation space is digitized into a static pixelated uniform mesh. Each pixel is defined to be  $\sim 4 nm^2$ , which translates into precipitates with initial diameter of  $\sim 6 nm$ . These parameters were chosen to be comparable to the micrographs shown in [113]. The mesh has full PBC for Sections 5.3.1 and 5.3.2. For Section 5.3.3 the mesh has semi-infinite conditions, i.e. PBC in the  $x$ -direction, but no flux boundary conditions on the  $z$ -direction. This simulates irradiation of the target from a voided region through the free surface. General kinetic and thermodynamic conditions used were such that  $D_i/D_v \sim 10$  and  $E_i^f > E_v^f$ , meaning that interstitials are faster and less thermodynamically able to form than vacancies. Further, another consideration taken into choosing the parameterization variables values was such that Ostwald ripening kinetics resulted for the non-irradiated case.

Lastly, even though thermodynamic characteristics similar to NiSi were used in the implementation of the model, actual material properties corresponding to this system were not used. Hence, evolution of the irradiated NiSi system is not being claimed.

### 5.3.1 Effects of Radiation Defect on Precipitate Growth

Tangible effects on the kinetics of microstructural evolution behavior are to be expected due to the presence of irradiation induced point defects. These defects will influence the atomic diffusion mechanisms. To get a general idea on the influence that

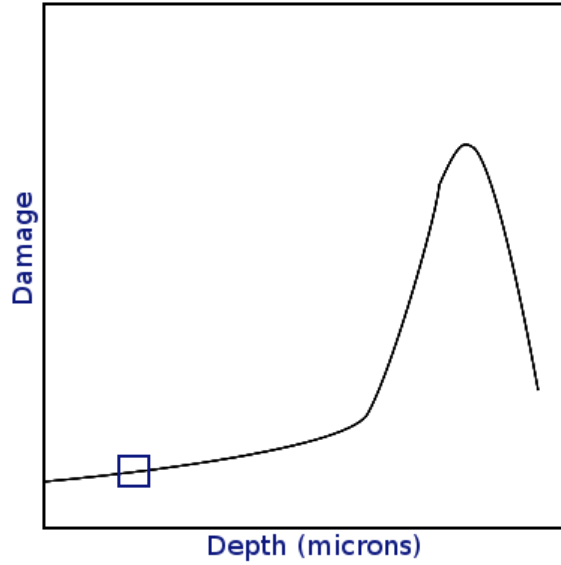


Figure 5.4: Schematic of a high energy ion damage distribution, e.g. swift ions. Since the ion is highly energized, it travels through a large section of the target producing slightly gradual radiation damage. If the simulation is only interested in a region (blue square) away from the peak damage and surface, radiation damage can be assumed to be uniform through the simulation domain.

radiation damage has on microstructural evolution, the results of a non-irradiated and uniform irradiation distribution simulations are compared, Figure 5.6. These simulations contain an initial  $\sim 2\%$  density of  $\beta$  precipitates sites. Figure 5.6 shows particular feature phases, clearly identifying the sharp interfaces between the respective phases ( $\alpha$  =blue and  $\beta$ =red). From visual inspection the resulting microstructure, it is clear that accounting for radiation induced defects has an important role on the shape and distribution of the  $\beta$  precipitates. The density of  $\beta$  precipitates present in the matrix at the end of the simulation is proportional to the radiation dose. This is due to the fact that increasing the number of point defects in the system leads to a departure from Ostwald ripening capillarity driven kinetics to radiation defect diffusion controlled kinetics. In other words,  $B$  atoms diffuse to both high and low curvature interfaces due to the introduced point defect gradients. These mechanisms are schematically represented in Figure 5.5. For high dose simulations, the precip-

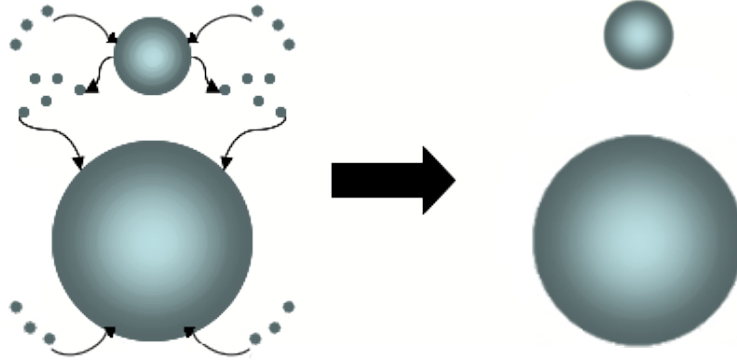


Figure 5.5: Schematic representation of the radiation influenced precipitate growth. As radiation induced mobile  $B$  atoms move towards the  $\alpha - \beta$  interfaces, Ostwald ripening is suppressed, leading to slower precipitate growth kinetics.

itates are much more asymmetrical. These were observed to lead to detachment of very small clusters ( $\sim 3$  pixels) in the vicinity of larger precipitates. These form due to an increase in the local energy from the creation of defects in the vicinity of the precipitates.

To better appreciate the effect that radiation has on the precipitate growth kinetics, several simulations for different dose rates were performed. The precipitate growth curves for these are shown in Figure 5.7. It is clear that as radiation dose rate increases, precipitate growth becomes suppressed. The suppression stems from having the excess defects diffuse towards the  $\alpha - \beta$  interfaces. Therefore, smaller precipitates are able to grow at the expense of depletion of the  $\alpha$  matrix. Further, this is influenced by the formation of smaller precipitates, which arises from detachment of the irregularly shaped larger precipitates and/or nucleation. These smaller precipitates also lead to the increasing deviation from the average radius, as evidenced by the larger error bars. Assuming that the growth behavior follows scaling growth with allometry, these curves can be fitted to the generic grain growth equation

$$\langle R \rangle^n - \langle R_i \rangle^n = kt \quad (5.24)$$

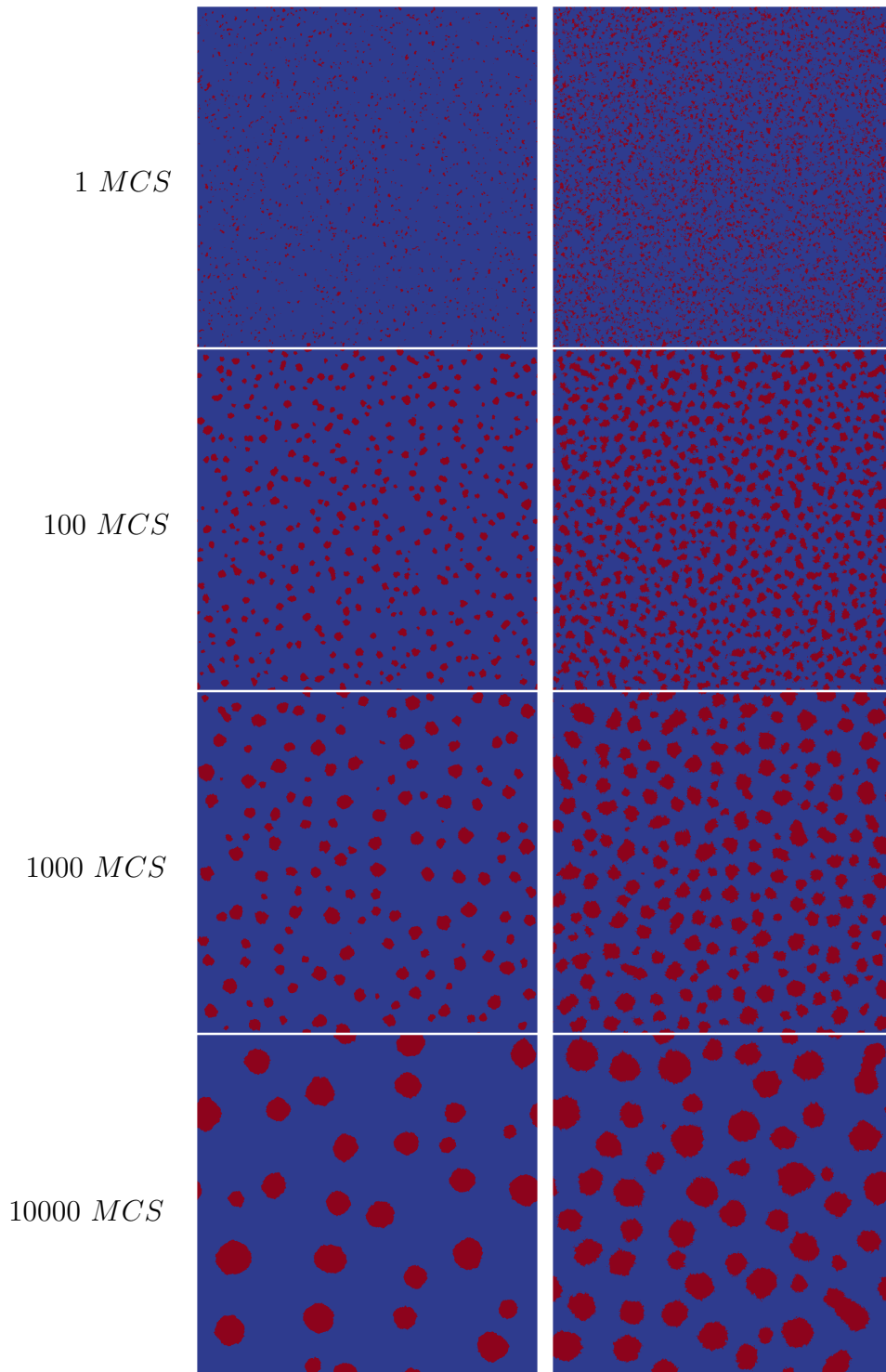


Figure 5.6: Microstructural evolution of the  $\beta$  precipitates (red) as a function of time for the unirradiated and high irradiation dose simulations. Radiation leads to appreciable changes in the grain size, shape and distribution. The feature phase order parameter is shown. (Time units are in Monte Carlo steps.)



Table 5.3: Fitted grain growth exponential value,  $R^n - R_0^n = kt$ , for the different cases studied. A growth exponential of  $n = 3$  is indicative of Ostwald ripening kinetics [99, 100].

Dose [ $\#/(MCS \cdot px)$ ]	0	$\sim 10^{-1}$	$\sim 10^0$	$\sim 10^1$
$n$	3.04	3.35	3.62	4.21

where  $\langle R \rangle$  is the average grain radius,  $\langle R_i \rangle$  is the initial average grain radius,  $n$  is the grain growth exponential,  $k$  is a temperature and radiation sensitive constant and  $t$  is time. Fitting resulting values where  $n, k$  and  $\langle R_i \rangle$  are fitting constants, is summarized in Table 5.3. It's clear that the exponential value increases with increasing irradiation dose, meaning that precipitate growth was suppressed.

### 5.3.1.1 Discussion on the Dependence to Radiation Damage

A more rigorous approach to describe the evolution of the precipitates was developed by Nelson, Hudson and Mazey, i.e. the NHM model [116],

$$\frac{dR}{dt} = -\xi K_0 \Omega + \frac{3DC}{4\pi RC_p} - R^2 D \rho \quad (5.25)$$

where  $\xi K_0$  gives the displacement rate planar density (dpa per unit area per second),  $\Omega$  is the atomic volume,  $D$  is the diffusivity,  $C$  is the total amount of solute ( $= C_p + C_m$ ) in the system and  $\rho$  is the precipitate density. This equation suggests that the growth rate is expected to decrease linearly with increasing irradiation damage rate. The common representation of precipitate growth curves, in a log-log plot, clearly shows behavior of scaling growth with allometry. Therefore, the precipitate growth exponentials were plotted as a function of the dose rate. From Figure 5.7, the slope of the log-log curves gives the inverse grain growth exponential. This can

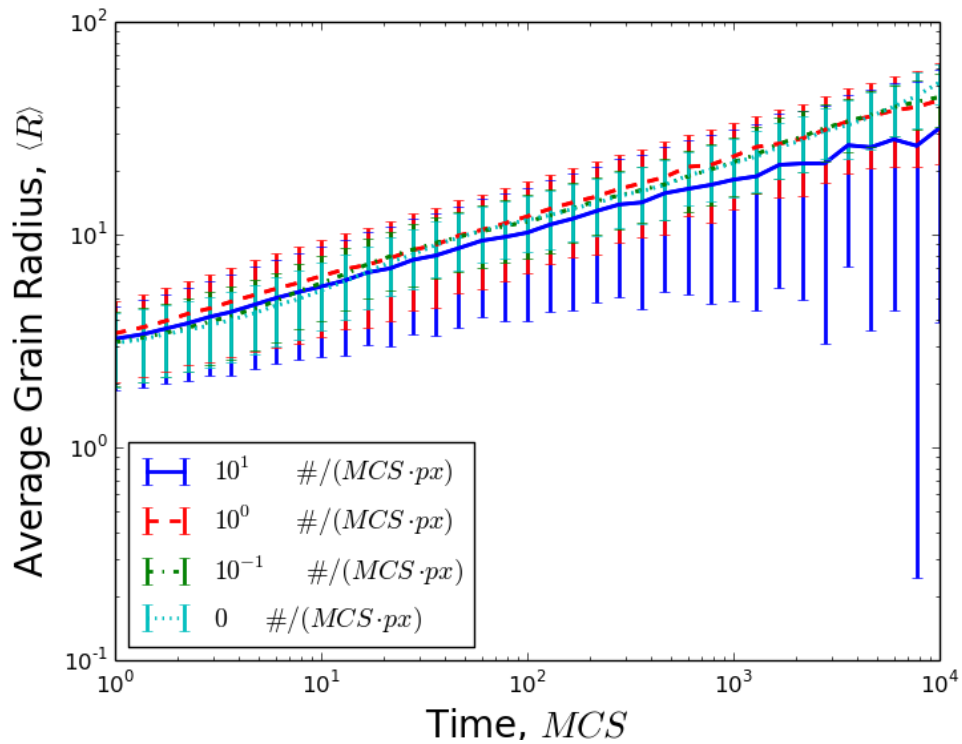


Figure 5.7: Precipitate growth curves for the unirradiated and irradiated cases. It is evident that radiation leads to the presence of smaller precipitates at longer times. The radiation damage units mean approximate average number of defects created per time unit on each pixel.

be mathematically expressed as

$$\langle R \rangle^n \propto t \rightarrow n \ln \langle R \rangle \propto \ln t \quad \therefore \quad \frac{1}{n} \equiv \frac{\Delta \ln \langle R \rangle}{\Delta \ln t}$$

where the values of  $n$  have been tabulated, Table 5.3. Taking the derivative with respect to time,

$$\frac{\Delta \ln \langle R \rangle}{\Delta \ln t} \equiv \frac{\partial \ln \langle R \rangle}{\partial \ln t} = \frac{t}{R} \frac{\partial \langle R \rangle}{\partial t} \equiv \frac{1}{n}, \quad (5.26)$$

which suggests that the precipitate growth inverse exponential is proportional to the damage rate planar density,  $-\xi K_0 \Omega$ . Since the microstructure is constantly evolving, the best representation of this can be obtained by plotting the inverse exponential as a function of the damage rate, Figure 5.8. It is clear that increasing damage rate, the rate at which precipitates grow is lessened. This figure could be interpreted as a representation of precipitate growth evolution deviation from Ostwald ripening kinetics as a function of damage rate, i.e.

$$\lim_{\phi \rightarrow 0} n \rightarrow n_{Ost} = 3$$

as expected.

### 5.3.1.2 Point Defect Behavior and Concentration Profile

The radiation characteristic regime can be studied by looking at the average defect concentration in the microstructure, Figure 5.9. Each of the irradiation cases (color coded) has upper and lower curves corresponding to the vacancy and interstitial average concentration, respectively. These curves behave as expected for a material irradiated at low temperature and intermediate sink density [11, 109]. This entails that the simulations follows: (i) a linear defect build up regime, (ii) followed by annihilation of the faster interstitials as they arrive to the sinks, and lastly (iii)

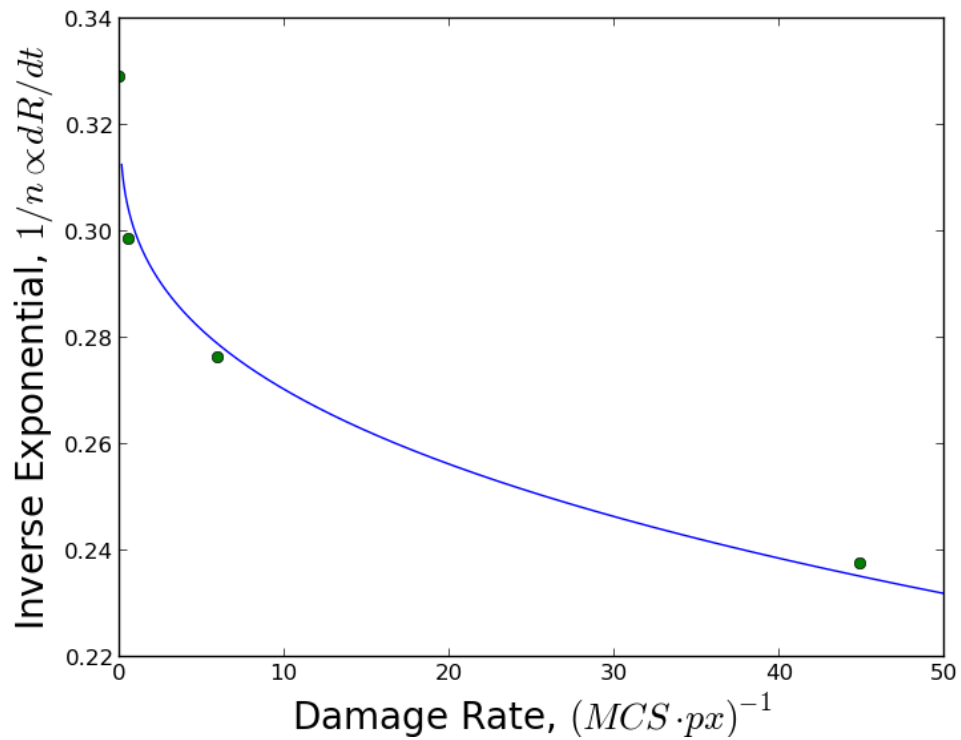


Figure 5.8: The inverse of the precipitate growth exponential decreases with increasing radiation damage rate. This reveals how the system's evolution goes from pure Ostwald ripening to radiation retarded kinetics. Interestingly, the data fits nicely to an equation of the  $1/n = a \cdot K_0^{1/n_{Ost}} + b$  form. This indicates that inverse exponentials scale with the inverse exponential for Ostwald ripening.

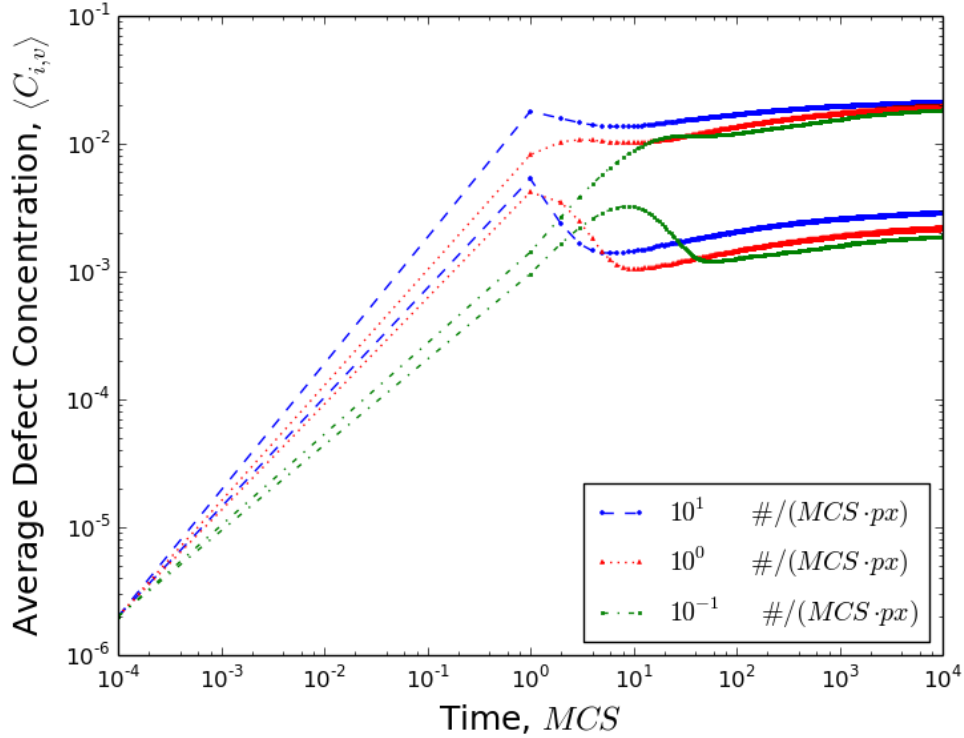


Figure 5.9: Average concentration of point defects as a function of time for the irradiated cases. The top curves correspond to the vacancy concentration ( $\bar{C}_v$ ) and the bottom curves correspond to the interstitial concentration ( $\bar{C}_i$ ).

reaching steady state as vacancies reach the sinks at which point defect densities saturate. This behavior is more evident from the low irradiation dose case. For the high irradiation dose case, too many defects are initially created, which are highly unstable leading to an initial decrease in defect concentration. It is possible that such a high dose is not realistically sustainable, and other type of damage needs to be incorporated to properly simulate very high dose effects, e.g. ion beam milling.

Plotting the solute concentration along the center of the simulation space, Figure 5.10, shows that quasi-equilibrium concentrations depend on the damage rate. Nonetheless, equivalent behavior of matrix and precipitate phases reaching an equilibrium concentration is shown for all the different simulations. The precipitate concentration varies more noticeably between the non-irradiated (Ostwald ripening) and

higher damage rate cases. However, there is a notable differences between the non-irradiated and low dose cases, Figure 5.10(b). For the irradiated cases, the matrix and precipitate have quasi-equilibrium concentrations that are well below thermodynamic equilibrium, as given by the common tangent rule. This is due to: a) irradiation provides mechanisms where smaller  $\beta$ -precipitates are quasi-stable leading to a larger precipitate density; and b) the system is assumed to conserve mass. Analytical models have been developed where the precipitate solute concentration is found to increase with damage rate, e.g. Wilkes' model [117]. The reason why this differs from the observed computational results is that the hybrid model accounts for the chemical potential as a driving force, leading to a constrained and conserved system. A previous iteration of the model [115] which relied on the concentration gradients to serve as driving forces for microstructural evolution, as in Wilkes' work, does show unconstrained compositional evolution of the precipitated phases. A way of countering this computational artifact is to include a solute infinite source. This is equivalent to having solute diffuse from a region away from the high radiation damage, to a reduced extent.

### 5.3.2 Uniform Irradiation of Polycrystalline Matrix

Radiation damage has been observed to induce nucleation and growth of stable secondary-phase films near surface sinks [15]. How these nucleated phases behave depends on different parameters, like the thermal history and pre-irradiation microstructure. This is well demonstrated on the work by *Potter et al.*, where a Ni-12.7 at.%Si was heat treated and irradiated. To study the role of grain boundaries in an irradiated microstructure, an irradiated bi-crystalline (two grain microstructure)  $\alpha$ -matrix with  $\sim 4\%$   $\beta$ -precipitates density randomly distributed was simulated. Figure 5.11 shows the microstructural (grain ID) and compositional evolution results. The two large grains, dark and light blue squares, correspond to the  $\alpha$ -phase, while

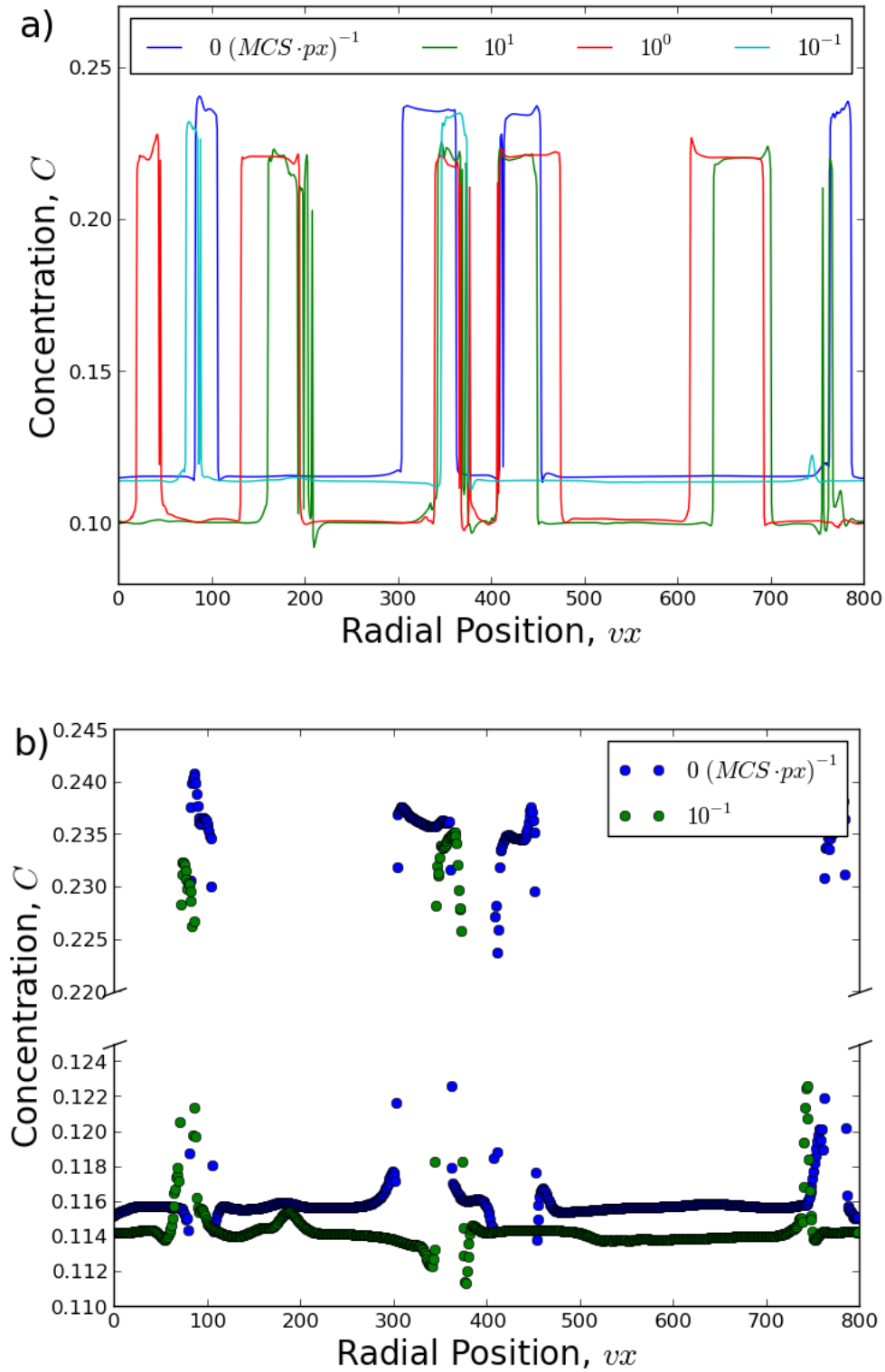


Figure 5.10: Solute concentration profiles for the different cases simulated. It is clear that the radiation induced quasi-stability of smaller precipitates has an influence on the equilibrium cobconcentrations. Hence, with higher damage, more of the smaller precipitates grow and/or persist.

the smaller features are the  $\beta$ -precipitates. The  $\beta$ -phase can be easily identified by looking at the “ $C_b$ ”-column, which shows the equilibrium chemical concentration under irradiation conditions, and the last column shows the interstitial defect concentration. Sharp interfacial boundaries can be distinguished for the abrupt concentration decrease (darker blue curves) since boundaries behave as infinite defect sinks. Only the interstitial defects concentration are shown since all boundaries are treated equally and have the same sink strength for either defect, Figure 5.11( $C_i$ ).

During the initial stages many of the precipitates in the vicinity of the  $\alpha - \alpha$  grain boundary get “trapped” by the grain boundary due to thermodynamics (surface tension). These grow and coalesce forming a  $\beta$  film along the grain boundary, while the precipitates in the matrix bulk grow similarly to the precipitates discussed in Section 5.3.1. An interesting effect observed was that in order to achieve complete coverage of a precipitated film along the grain boundary, the element (surface) interaction energy needed to be increased by  $\sim 40\%$ . When lower interfacial energy were used similar trapping and coverage along the grain boundary with elongated (lenticular shaped)  $\beta$ -features were observed, but the film did not result in a continuous feature. It is reasonable to expect the surface energy to increase by this amount, and has been shown to do so on ion irradiated polymers [118] and laser irradiated copper [119]. This increase in surface energy can be attributed to the fact that these interfaces act as damage sinks, which leads to less thermodynamically stable structures in the surface region. This dependence on increased surface energies for complete coverage suggests that RIS is only partially responsible for the observed film precipitation on irradiated NiSi.

### 5.3.3 Medium and High Energy Irradiation

Another important aspect that needs to be considered is related to the damage probability distributions described in Section 5.2.2. This is studied by looking at cases



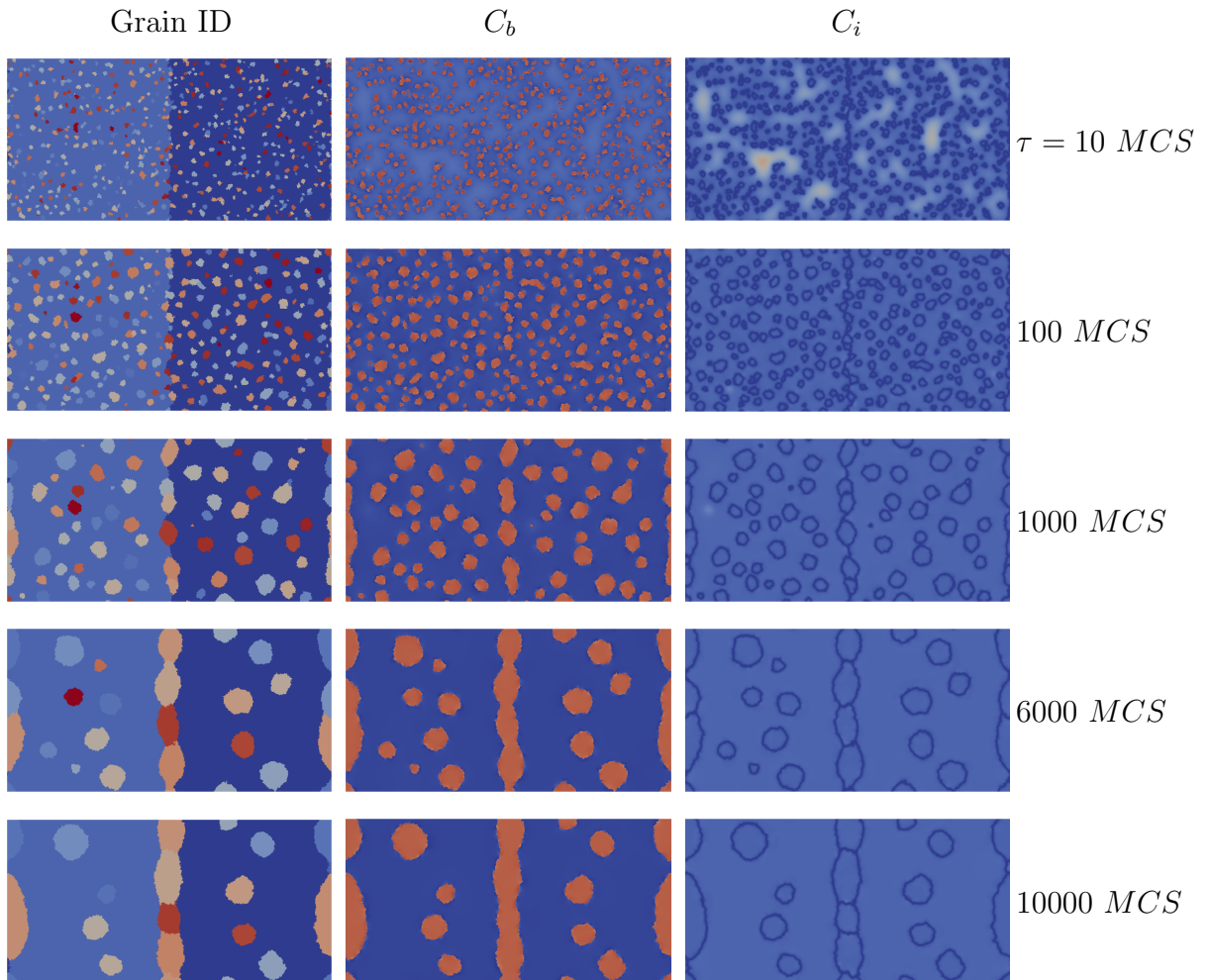


Figure 5.11: Growth of the  $\beta$  film along the  $\alpha$  matrix grain boundary. By simulating irradiation of a bi-crystal  $\alpha$  matrix with a random distribution of  $\beta$  precipitates, the development and growth of the secondary phase is observed. The grain ID, and concentration distributions of  $B$  atoms and interstitials are shown.

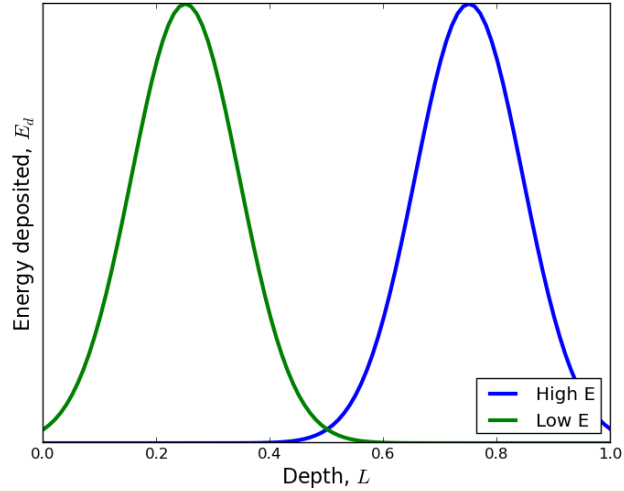


Figure 5.12: Shape of the deposited energy distributions used in the low (green) and high (blue) ion energy simulations. The ions with higher energy have a larger range, meaning that they deposit most of their energy deeper into the target. The surface is located at zero depth,  $d = 0 \cdot L$ .

where the ion range is close and far from the exposed free surface. This is analogous to having low and high ion energy irradiation. These conditions are handled by employing energy deposition distributions that peak at depths of  $\mathbf{x}(E_T^{peak}) \sim 0.25L$  and  $\sim 0.75L$  for low and high ion energy, respectively. The parameter  $L$  is the vertical length (depth)

$$\mathbf{x} = \{(x, z) : 0 \leq x \leq H, 0 \leq z \leq L\} \quad (5.27)$$

where the simulation has been defined in a 2 dimensional space with maximum dimensions of  $H$  and  $L$ . The distributions have general Gaussian shapes as shown in Figure 5.12. As before, the initial microstructure consists of  $\beta$ -precipitates within an  $\alpha$ -matrix. Note that the probability of collision was remained unchanged and the energy deposition was the only parameter adjusted. Therefore, the defects formation behavior is the main controlling parameter being studied.

The results shown correspond to the final microstructure after 10,000 *MCS*, as the goal is to compare the two resulting microstructures. Both cases have a very

similar microstructure, but with features that align with their corresponding energy deposition distribution. These features are: a continuous  $\beta$ -film and circular precipitates away from the damaged region that evolved by Ostwald ripening. Away from the peak dose region, the damage rate is negligible, which leads to capillarity driven precipitate growth behavior as discussed in Section 5.3.1. One interesting difference between the two damage profiles is that the isolated precipitates for the high ion energy simulation are slightly larger ( $54.33 \pm 16.39 px$ ) than the ones for the low energy case ( $48.36 \pm 12.81 px$ )<sup>1</sup>. This is due to diffusion of the solute atoms as the point defect diffuse away from the high defect concentration gradient towards the free surface sink. There is a net solute diffusion away from the peak damage region, i.e. precipitated film, for both cases. However, the high energy case has the added effect of having two “forces” attracting the excess defects, instead of one: (1) the circular precipitate interfaces and (2) the exposed surface. This extra attractive force enhances solute diffusion from the matrix, which resulted in the slightly larger circular precipitates.

The concentration distributions illustrate that there seems to be a significant difference between the film and precipitate’s equilibrium concentrations. Therefore, the concentration profile for both simulations is plotted, Figure 5.15. It is evident that precipitates for both cases have a slightly higher equilibrium concentration than the continuous films. This can be explained by the fact that the system is conserving mass, i.e. there is a finite amount of  $B$  that can be supplied to the  $\beta$ -phase. Hence, as more  $\beta$ -phase is precipitated in a narrow region,  $B$  becomes depleted in the immediate vicinity in order to reach a quasi-equilibrium. Therefore, the area surrounding the radiation induced film has a precipitate density,  $A_\beta/A_\alpha$ , too large to satisfy true thermodynamic equilibrium. This is equivalent to the observed dependence on dose rate previously discussed.

---

<sup>1</sup>While these are statistically equivalent precipitate average sizes, the differences are likely a real result arising from the difference in damage distributions that needs to be examined further.

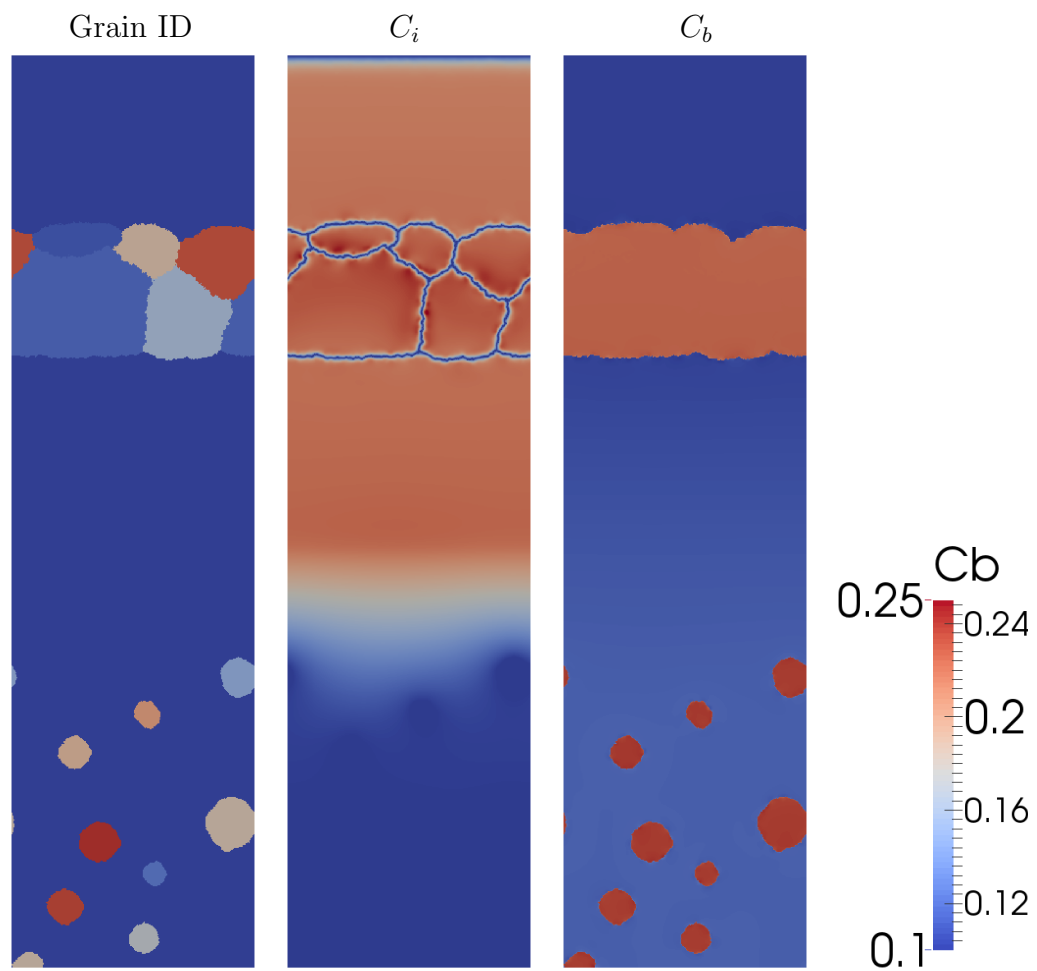


Figure 5.13: Microstructure of an irradiated target after 10,000 MCS for a low energy ion beam. The simulated target is being irradiated through the surface, the “top” of the image.

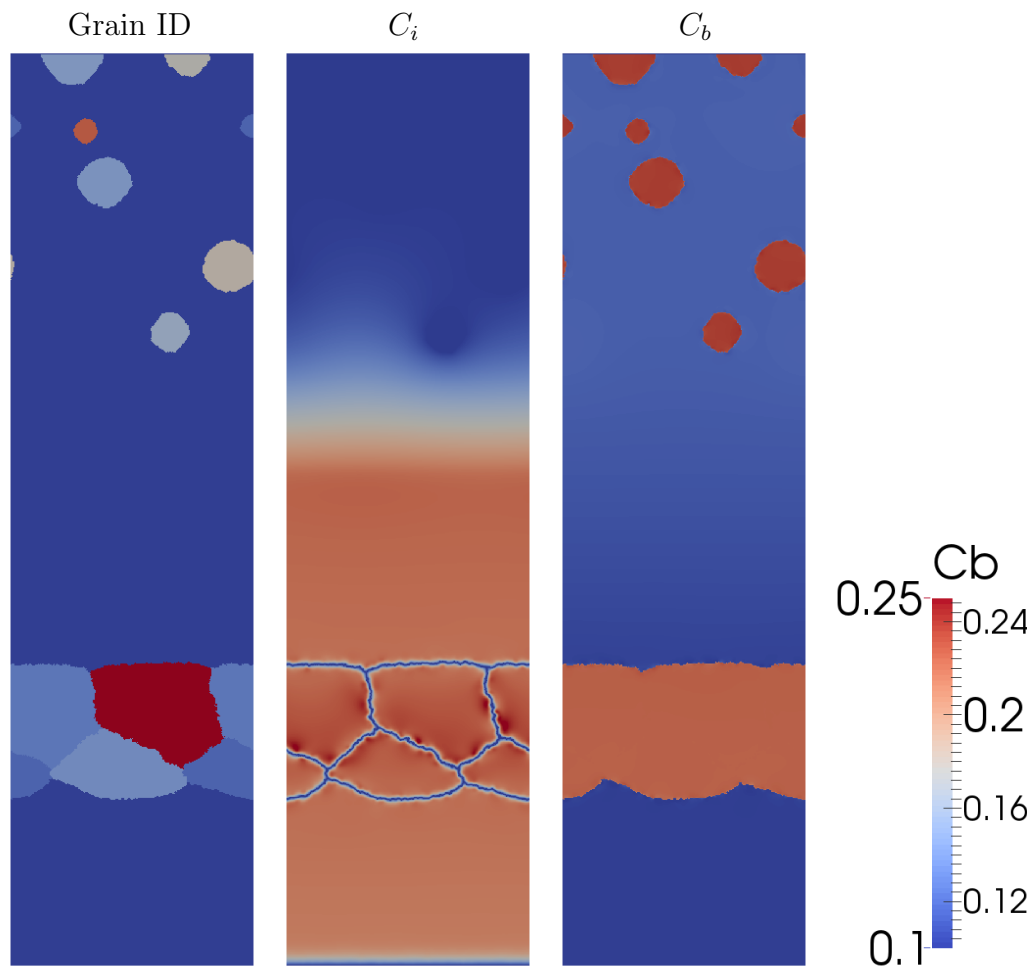


Figure 5.14: Microstructure of an irradiated target after 10,000 MCS for a high energy ion beam. The simulated target is being irradiated through the surface, the “top” of the image.

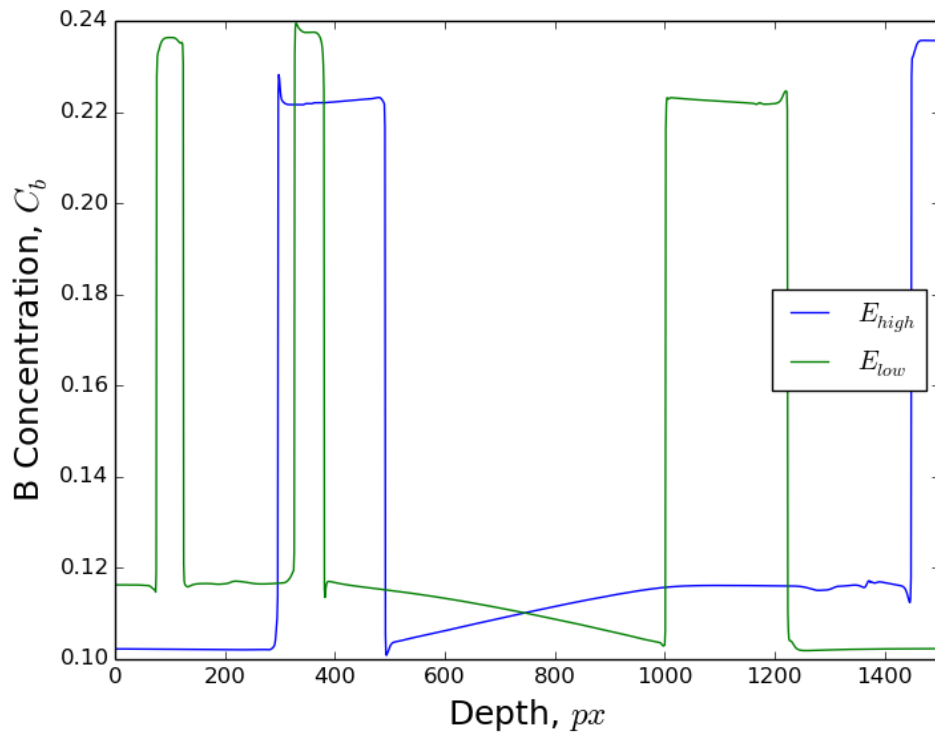


Figure 5.15: Concentration distribution profile across the microstructure for the low and high ion beam energy cases. The films and precipitates can be distinguished by the width of the “step”-like higher concentration. The irradiated surface is located at 1500  $px$  (top).

## CHAPTER VI

# Numerical Simulation of the Formation of Nano-Porous Networks

The main goal of this dissertation is the development of a computational model that is able to capture the multi-physical processes that lead to the formation of the nano-porous structures observed in irradiated amorphized-Ge. A deterministic-statistical hybrid model was developed in order to achieve this goal. This hybrid model couples a set of rate theory equations to a Potts Monte Carlo driven microstructural evolution model and a kinetic Monte Carlo (kMC) algorithm previously developed to simulate inter-granular bubble swelling Section 6.2. The hybrid model uses the set of partial differential equations to describe the evolution of the radiation induced point defects and Pott's energetics to drive mechanisms like void migration and surface smoothing. The kMC swelling model, while straightforward, is able to generate intricate microstructures, and simulate volume expansion of the simulation domain. These characteristics are well suited to the nano-porous network formation. Therefore, it makes a natural selection in the implementation of the coupled hybrid models. These advanced models are tested by simulating inter-granular bubble swelling (Section 6.2) and void swelling nano-porous structuring (Section 6.3). This chapter discusses the development and coupling of these models.

## 6.1 Introduction

The formation of the highly interlinked nano-porous networks is fairly convoluted with many mechanisms influencing the evolution of the microstructure. Experimental undertakings suggest that the mechanism leading to the structuring of the nano-pores can be considered as a series of radiation induced effects stages. As described in Section 1.3.1, the nano-structuring process as a function of irradiation dose (time with constant flux) goes as follows:

- amorphization of the target and continued damage build up,
- nucleation of small uniform voids,
- growth and coalescence of the smaller voids,
- and growth by surface migration leading to the formation of the stable nano-porous networks.

As expected from the formation of the highly porous structure, this is accompanied by substantial volumetric expansion. While swelling in crystalline materials has been extensively studied, the knowledge gained from these works is not immediately applicable to the nano-porous structuring phenomena since these were developed in amorphized semiconductors. This is a result of the amorphization of the target as a precursor for the formation of the nano-porous networks.

Several (qualitative and quantitative) models have been proposed in an attempt to describe the processes that lead to the formation of the complex porous networks. These have not been able to directly simulate the stages listed above. The present work approaches the problem by coupling two intrinsically different computational techniques. The model presented couples an exclusively kinetic Monte Carlo (kMC) model developed to simulate inter-granular bubble swelling and a set of partial differential equations similar to the ones developed by *Wiedersich et al.* This coupled



hybrid deterministic–statistical is able to leverage on each others’ inherit computational capabilities to sensibly evolve the microstructure. Since the kMC model drives the microstructural evolution, its application to the bubble swelling simulations is discussed first as an individual model.

## 6.2 Inter–granular Bubble Swelling

During service, neutron irradiation of nuclear fuel materials leads to the creation of fission gases. These gases can follow several “paths” before finding a stable arrangement, e.g. direct release, resolution into the matrix, and nucleation and/or growth of gas bubbles. Unfortunately, fission gases have very low solubility in the  $UO_2$  fuel matrix causing these gases to form intra– and/or inter–granular bubbles. This can in turn cause the fuel to swell, i.e. volumetric expansion. Examples of these are shown in Figure 6.1. Furthermore, these bubbles can interlink along the grain boundaries trijunctions and eventually reach the free surfaces. This is expected to cause the fission gas to be release by percolation from the fuel matrix into the fuel–clad gap. This can lead to several failure mechanisms, e.g. cladding ballooning and burst [120]. More importantly, it is desired for the fission gases to remain trapped within the fuel as a safeguard to releasing the toxic fission gases. Therefore, understanding the mechanisms that lead to the formation, evolution and interaction of these bubbles, and eventual release of its fission gas is of great interest.

The model presented here was based on the work developed by *Tikare et al.* [122] and extended by incorporating methods similar to those developed by *Garcia et al.* [123]. The main adaptation presented here is that the simulated microstructure is allowed to increase in volume, i.e. swell. In their work, Tikare et al. were able to study parameters like time for percolation, bubble evolution and distributions. An important observation was that at the time for percolation,  $\sim 0.5$  bubble coverage of the grain boundaries, about 0.057 of the gas in the inter–granular bubbles is expected

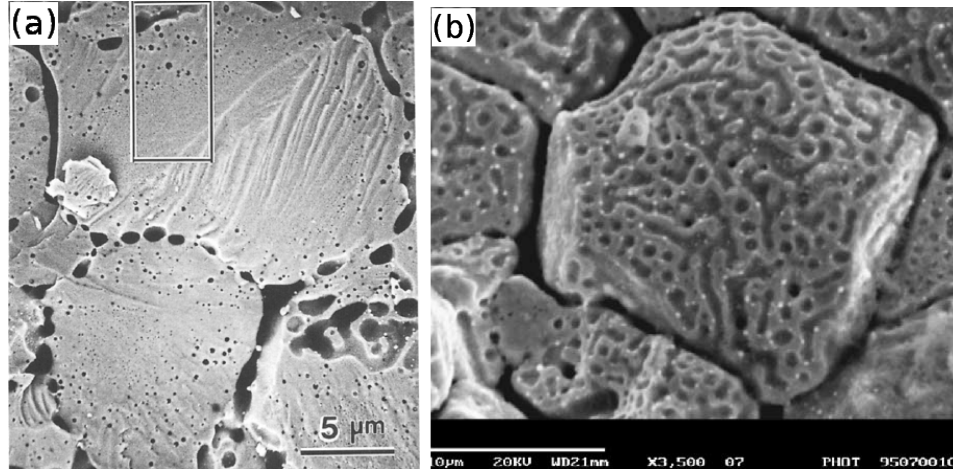


Figure 6.1: Micrographs showing inter- and intra-granular bubbles. (a) SEM fractographs of the fuel with burnup of 23 GWd/t after annealing at  $1800^{\circ} C \times 5 h$  [26]. (b) Advanced development of grain-boundary porosity: this fuel was ramped under similar conditions to that in Fig. 4 (of White) but maintained at  $1800^{\circ}C$  for 30 min [121].

to be released by percolation. This is particularly significant since current codes assume that all the fission gas is released upon percolation.

### 6.2.1 Model Framework

As with the sharp interface models discussed in Appendix E, the model considers a digitized 3 dimensional domain with sharp interfaces, Figure 2.1(a). The simulation space is digitized into a voxelated mesh, i.e. “volumetric pixels”. The order parameters being considered on this model are exclusively discrete features. These are differentiated by assigning “colors” (integer values) to each voxel. Essentially handling the microstructure as a standard Monte Carlo simulation space. The discrete features can represent: grain orientations, bubbles, vacuum/void or a frame. These features are used to define the system’s thermodynamic state and spatial confines.

### 6.2.1.1 Microstructural Representation

Unlike the models previously described, the models presented in this chapter apply non-periodic boundary conditions (nPBC) to the simulation domain. This is to allow the microstructure to undergo volumetric expansion (swelling). Since the simulations are performed within SPPARKS' static mesh, the simulation domain needs to accommodate this change in volume. Therefore, "extra empty" simulation space is allocated to serve as a vacuum space. These different regions that make up the simulation domain are termed the *microstructural* and *vacuum domains*. This are clearly observed in Figure 6.2. The microstructural domain is encased by the vacuum domain which is surrounded by a larger (blue) box, which defines the actual simulation space dimensions

$$\mathbf{x} = \{(x, y, z) : 0 \leq x \leq L_1, 0 \leq y \leq L_2, 0 \leq z \leq L_3\}. \quad (6.1)$$

The blue box represents a one voxel thick layer termed the *frame*. This domain serves as a computational spatial boundary that contains the simulation domain. The vacuum domain, which rests between the other two domains, is the empty space that allows the microstructure to swell.

The grain boundaries are important features since they are designated as the sole bubble nucleation sites, Table 6.1. They are represented by the interface between two differently colored grains, i.e. neighboring voxels with different colors. While grain boundaries could be defined as its own feature, Tikare found that this sharp interface definition is able to capture important kinetics and physics affiliated to inter-granular bubble swelling. It needs to be noted that intra-granular bubble could be easily incorporated in the model. However, Tikare found that not much is gained from this, other than prolonged temporal behavior. Therefore, this work only treats grain boundary sites as bubble nucleation sites.

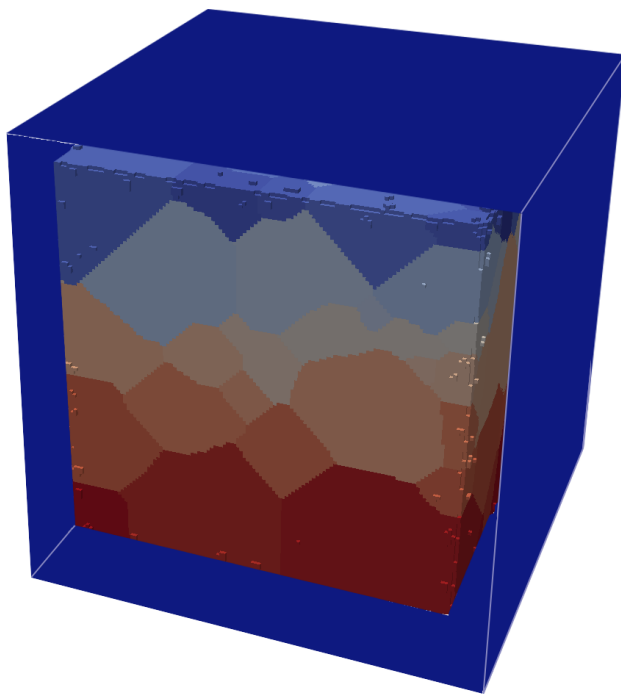


Figure 6.2: Simulation space showing the frame (blue outer box), microstructural domain (polycrystalline material) and empty space in between these two regions. The empty space, i.e. vacuum domain, allows swelling of the microstructural domain.

Table 6.1: Comparison of real life and computational modeling of fission gas behavior. These characteristics describe the fission gas generation and transport (based of [122]).

Reality	Model
○ Generated proportionally to fission events	○ Same as reality
○ Diffuse until precipitating in bubbles	○ Random walk with $D(T, \Phi, C, \dots)$
○ Intra- and inter-granular bubbles	○ Only inter-granular bubble nucleation simulated
○ Precipitate on trapping sites (irradiation defects) to form nano-sized intra-granular bubbles	○ Precipitate on trapping sites (stationary nucleation sites) diffusing along the surface
○ Nucleation and evolution of bubbles is complex and depends on gas concentration	○ Nucleation is a random event with a given frequency

### 6.2.1.2 Thermodynamics of the System

The kinetic evolution of the microstructure, e.g. surface migration, is dictated by the equation of state (EoS)

$$F_{EoS} = \underbrace{\sum_{i=1}^N (D_{i=ts} + G_{i=dg})}_{\text{Volumetric energy terms}} + \mathcal{J} \underbrace{\sum_{i=1}^N \sum_{j=1}^n (1 - \delta_{ij})}_{\text{Interfacial energy terms}} \quad (6.2)$$

where  $N$  is the number of sites in the microstructural domain, the volumetric terms include intrinsic energy from trapping sites ( $ts$ ) and the dissolved gases ( $dg$ ), and the interfacial energy is the Potts Monte Carlo energy. Since the volumetric term does not contribute to the behavior of the inter-granular bubbles kinetics, the interfacial energy is the only component accounted for in evaluating statistical changes of the microstructural configurations. The microstructural evolution is simulated by sta-

tistical rearrangements of the microstructural domain. The probability of accepting an attempted arrangement follows Boltzmann statistics where the EoS' interfacial energy drives the system to equilibrium.

### 6.2.1.3 Bubble Nucleation and Migration Mechanism

The generation of fission gases that are unable to escape or dissolve into the matrix will inevitably lead to the formation of inter- and intra-granular bubbles. Since this model focuses on the potential release of fission gases, the main feature of interest are the inter-granular bubbles. These are believed to be the more likely release mechanism of the gas encapsulated within the fuel matrix. Inter-granular bubble evolution is a complex multi-step process. Initially, intra-granular bubbles nucleate and grow by coalescence as the more mobile smaller bubbles diffuse. They also grow as fission gases are continuously supplied to the bubbles. They eventually migrate towards the grain boundaries where they become trapped and form the inter-granular bubble network. Although this multi-step process can be easily simulated with this model, Tikare found that allowing direct nucleation of the bubbles at the grain boundary yielded equivalent results, while saving computational overhead. Therefore, this model implements a direct inter-granular bubble nucleation mechanism by setting grain boundaries as nucleation sites. Another way of interpreting this is that the model assumes that intra-granular bubbles were nucleated and immediately migrated towards the trapping sites.

Bubbles nucleation is assumed to develop at a given frequency, which is related to the bubble nucleation probability. For site  $i$ , the probability of being sampled and that the site is a grain boundary site is

$$p_{i,gb} = p_i \cdot p_m \cdot p_{gb} = \begin{cases} N_m/N^2, & \sum_{j=1}^n (1 - \delta_{s_i s_j}) > 0 \\ 0, & \text{otherwise} \end{cases} \quad (6.3)$$

where  $N_m$  and  $n$  are the number of sites that make up the microstructural domain and surrounding site  $i$ , respectively. Once a grain boundary site is found, a bubble nucleation is attempted following standard Monte Carlo Metropolis methods

$$p_{nuc} = \begin{cases} 1, & \text{if } \omega_{nuc} > \mathcal{RN} \\ 0, & \text{otherwise} \end{cases} \quad (6.4)$$

where  $\mathcal{RN}$  is a random uniformly distributed number between 0 and 1. For example, Figure 6.3 shows a polycrystalline material with inter-granular bubble clusters and an isolated bubble (circled). This isolated bubble will migrate along the grain boundary until it becomes trapped by a larger bubble cluster. Migration takes place by exchanging sites with the surrounding grain boundary sites as described in Section 2.9. The bubble migration velocity can be defined as

$$v_b = \omega_{mig} \exp\left(-\frac{\Delta F}{k_B T}\right) \quad (6.5)$$

where  $\omega_p$  is the frequency of attempting a migration event and  $F$  is defined by Equation 6.2.

Another interesting characteristic shown in Figure 6.3 is the population of the larger bubbles in the tri-junctions (quadra-junctions in 3D). These configurations are attained by the deterministic migration of the bubbles along the grain boundaries. Further, the bubbles migrate along the grain boundaries' edges forming lenticularly shaped (elongated) bubbles. This shapes self-arrange due to surface energy considerations.

#### 6.2.1.4 Microstructural Swelling Algorithm

Fission gas bubbles nucleation is known to cause swelling of ceramic fuels in order to accommodate the volume occupied by the bubbles. The model treats each bubble

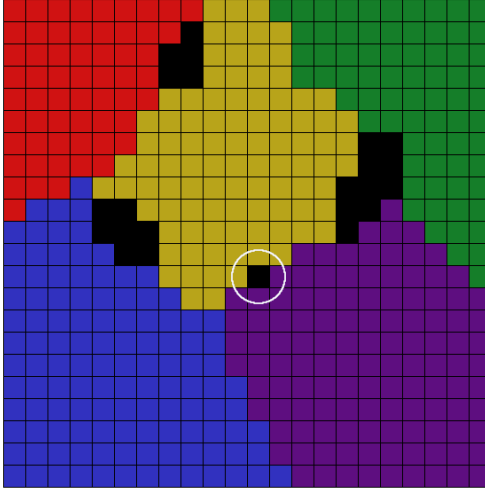


Figure 6.3: Microstructural representation of a bubble nucleation and coalescence in a polycrystalline material. Bubbles are nucleated along grain boundaries where they diffuse and form the interlinked bubble networks.

nucleation event as directly linked to a corresponding swelling event, i.e. each nucleated bubble will lead to a microstructural volumetric change. The algorithm used to simulate the swelling is based on the sintering model developed by *Garcia-Cardona et al.* [123]. In fact, the swelling algorithm can be in some ways considered a reverse sintering mechanism.

Swelling is simulated by a site exchange mechanism where at the end of the exchange sequence a bubble site is introduced at the grain boundary. Once a bubble has been nucleated, a random direction in  $4\pi$  space is calculated

$$\mathbf{p} = p_x \cdot \hat{i} + p_y \cdot \hat{j} + p_z \cdot \hat{k} = (\cos \phi \sin \theta, \sin \phi \sin \theta, \cos \theta) \quad (6.6)$$

determining in which direction the microstructure swells. This is illustrated in Figure 6.4 where the random direction is identified by the white arrow. While the exchange mechanism is shown to take place one voxel length at a time, the exchange length can be larger depending on the random direction.

Even though these models rely on SPPARKS to perform the message passing



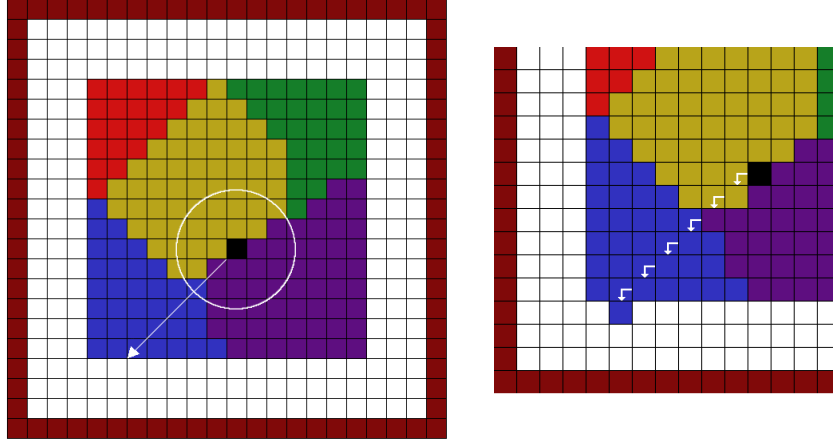


Figure 6.4: Schematic of the swelling algorithm. (left) A grain boundary site is flagged to undergo a swelling event, leading to the calculation of the random swelling direction. (right) The step-wise site exchange that leads to the swollen microstructure.

through processor interfaces, extra communication was required in order to communicate information when the swelling exchanges take place. This enables exchange between voxels that are not within the neighborhood of the exchanging site. In other words, not part of the processor's ghost sites. The additional communication is especially important when the exchange distance is larger than a voxel length. This is discussed in detail for the sintering algorithm [123], which is the basis of the developed the swelling algorithm.

### 6.2.2 Results and Discussion

The model was tested by simulating bubble swelling in a generic polycrystalline microstructure. The main objective was to study the microstructural and percolating bubble evolution. Three kinetic processes were incorporated into the model: bubble nucleation, pore migration and grain growth. The frequency at which each process occurs is given by

$$\omega_i = \frac{\nu_i}{\sum_{i=1}^3 \nu_i} \quad (6.7)$$

Table 6.2: Parameterization values used for the inter-granular bubble swelling simulation. The parameters correspond to nucleation, pore migration and grain growth rates, as identified.

Process	Parameterization Variable	Value
Nucleation	$\nu_{nuc}$	$1.25 \times 10^{-3}$
Migration	$\nu_{mig}$	$8.00 \times 10^{-1}$
Grain Growth	$\nu_{gg}$	$1.00 \times 10^{-1}$

where  $\nu_i$  is a parameterization value and the sum is performed over the three processes just defined. The parameterization values used for this simulation are given in Table 6.2.

The different features of a swollen microstructure are shown in Figure 6.5. The microstructure is shown at the time for percolation (a, c–d) or at an advanced swelling stage (b). The advanced swelling stage shows a particular view of a set of grains at a time much longer than the time for percolation. It qualitatively matches the micrographs shown in Figure 6.1, where we can identify bubbles along the grain boundaries and grain detachment. Further, the grain faces can be seen to be very porous and rough. Bubble networks can be observed in the grain faces, as in *Kashibe's* work, which are expected to contribute to the fission gas release paths. By examining the microstructural domain, it is evident that the domain has undergone uniform volumetric expansion. To the best of my knowledge, this is the first implementation of a kMC model that can genuinely show 3D swelling of the microstructural domain. The bubble microstructure shows a highly complex and interlinked network of inter-granular bubbles. It was found that at the time for percolation, the bubble density within the microstructural domain was  $\rho_b \sim 3\%$ . The percolating bubble was found to contain  $\sim 30\%$  of the bubble network volume. This was slightly larger than the volume fraction observed by *Tikare et al.* on their static microstructural domain simulation. The slightly larger percolating bubble could be due to the moving free

surfaces as the material swells. In other words, the bubble would need to grow further as to reach the advancing free surface. An interesting feature of the percolating bubble is that the bubbles interlink along the grain edges (trijunctions) forming a network of lenticular–shape bubbles. It should be noted, that even though the bubble is larger than the case of Tikare, the majority of the fission gases are still expected to remain trapped within the fuel matrix.

Since the volume of the microstructural domain is allowed to grow, swelling can be calculated by directly measuring the microstructural domain volumetric expansion from the simulation results. This was done by measuring the average distance between the surface grain voxels in any one direction of every plane and taking the average of all the distances

$$\frac{\Delta V}{V} = \left( \frac{\overline{\Delta x}}{L_1 - 2L_{b,1}} \right) \cdot \left( \frac{\overline{\Delta y}}{L_2 - 2L_{b,2}} \right) \cdot \left( \frac{\overline{\Delta z}}{L_3 - 2L_{b,3}} \right) \quad (6.8)$$

where the  $L_b$ 's are the symmetric border thickness for the vacuum domain in the respective directions. The measured swelling as a function of time is shown in Figure 6.6. From *Olander* [31], swelling by inter–granular bubbles can be calculated as

$$\frac{\Delta V}{V} = \frac{2(R_{gb}/a)(R_{gb}/\mathcal{R})^2}{1 - 2(R_{gb}/a)(R_{gb}/\mathcal{R})^2} \quad (6.9)$$

where  $R_{gb}$  is the spherical gas bubble radius,  $a$  is the grain radius and  $(R_{gb}/\mathcal{R})^2$  is the fraction of the grain boundary occupied by bubbles. By applying the respective parameters from the simulation results to Equation 6.9, it is observed that the simulated swelling is much lower than expected. This could be explained by the fact that the equation assumes that the bubbles are spherical. *Kagana* and *Rest* [124] showed that when accounting for the lenticular shape of the bubbles, swelling calculations yield results that are  $\sim 0.86$  lower than expected for percolation. Multiplying Equation 6.9 by 0.17 (0.83 reduction) the calculated and measured swelling give more comparable

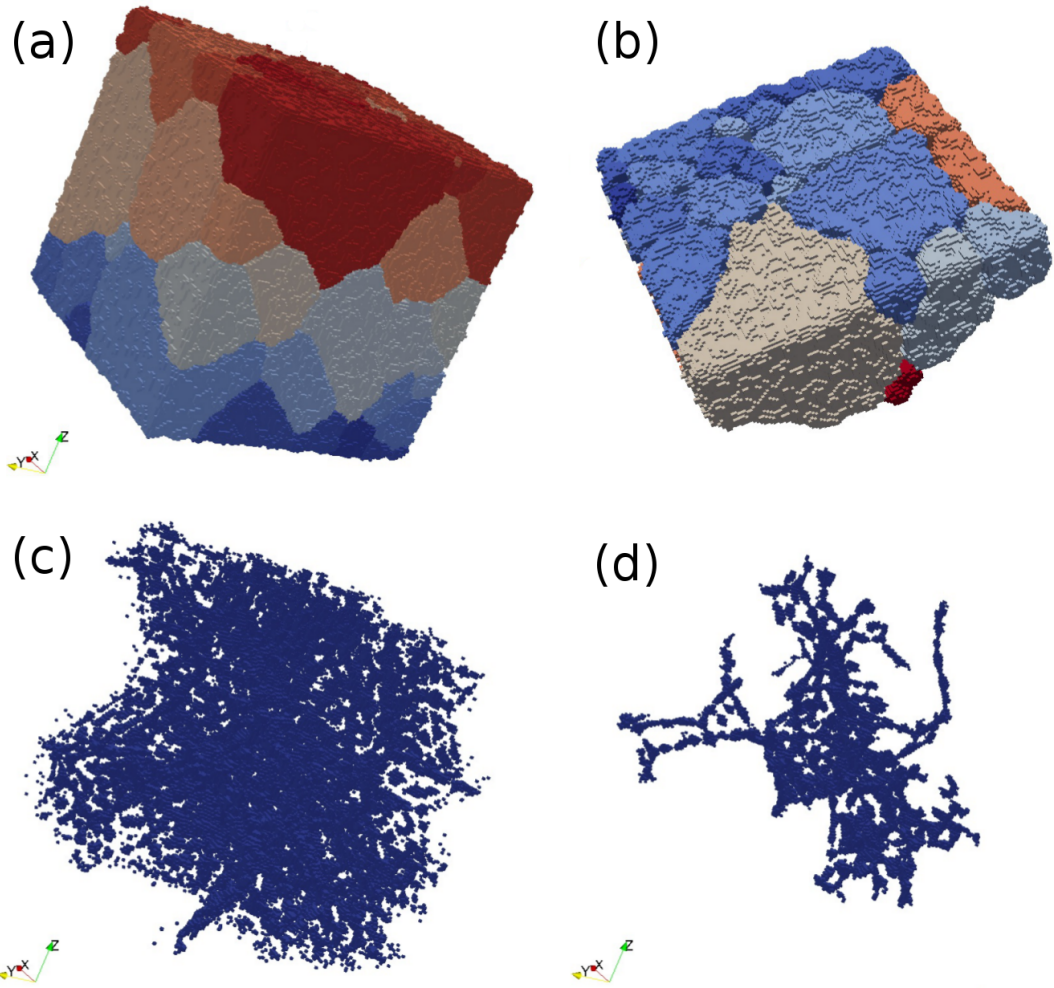


Figure 6.5: Microstructure after undergoing irradiation induced bubble swelling. (a) 3D swollen microstructure at time for percolation, (b) select view of grains showing advanced stage (well past percolation) swelling, (c) all the inter-granular bubbles present within the microstructural domain and (d) percolating bubble at time for percolation.

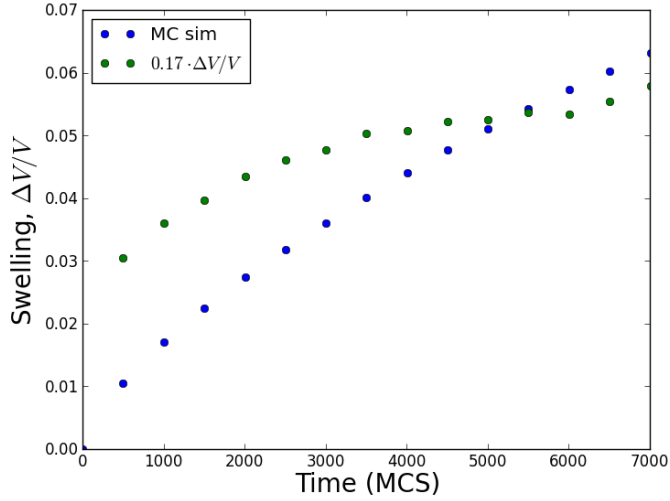


Figure 6.6: Measured swelling from the expanding microstructural domain dimensions as a function of time. The blue data represents the measured swelling and the green represents an 83% reduction in the calculated swelling times.

results.

Another parameter of interest when studying nuclear fuels is the microstructure initial porosity. Due to current fuel manufacturing practices, all fuels will have some amount of pores as a result of the sintering processes. A material with some initial porosity is expected to have a significant effect on the gas release kinetics. This was studied by comparing the previous results to a simulation of an equivalent microstructure (grain size and distribution), but with an initial density of  $\rho = 0.95$  (i.e. 5% porous). Figure 6.7 shows that by having an initial porosity of just 5% leads to a large reduction in the time for percolation

$$\frac{t_{perc}^{\rho=95\%}}{t_{perc}^{\rho=100\%}} \approx 33\%.$$

Further, in order to achieve percolation, the percolating bubble volume is significantly reduced to be about half of the fully dense microstructure

$$V_{\rho=95\%}(t_{perc}) \approx 0.5V_{\rho=100\%}(t_{perc}).$$

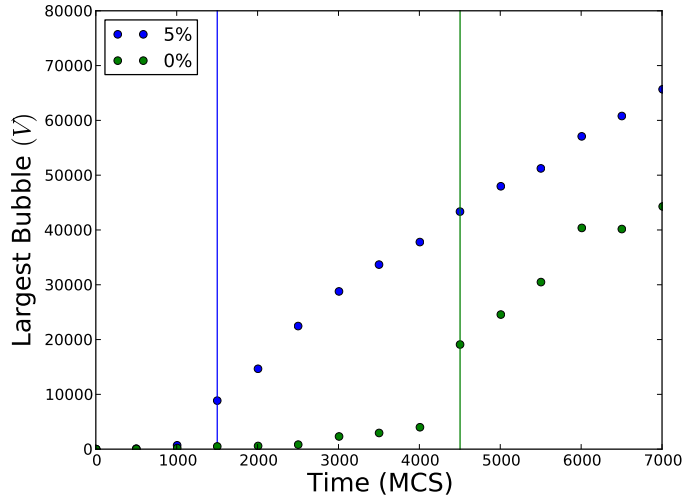


Figure 6.7: Comparison of the time for percolation between microstructures with initial porosities of 0% and 5%. The abrupt increase of largest the bubble volume (number of voxels) marked by the vertical lines denote the time for percolation.

Looking at the bubble size distributions, Figure 6.8, it is evident that the initially porous case requires a bubble content much lower than the perfectly dense case. It also shows that, as before, the vast majority of the bubble content is retained within the fuel matrix.

The implementation of the swelling algorithm to the study of inter-granular bubble swelling was able to corroborate several results reported by Tikare. More importantly, it is the first time that direct measurement of a swollen microstructural domain has been reported for a kinetic Monte Carlo model. This type of model could be applied to more realistic cases in order to better understand the fission gas behavior and trapping within inter- and intra-granular bubbles leading to improved performance of nuclear fuels.

### 6.3 Nano-porous Network Formation and Swelling

Ion irradiation of several semiconductors has lead to the formation of intricate nano-porous networks. Some examples were presented in Section 1.3.1.1. These net-

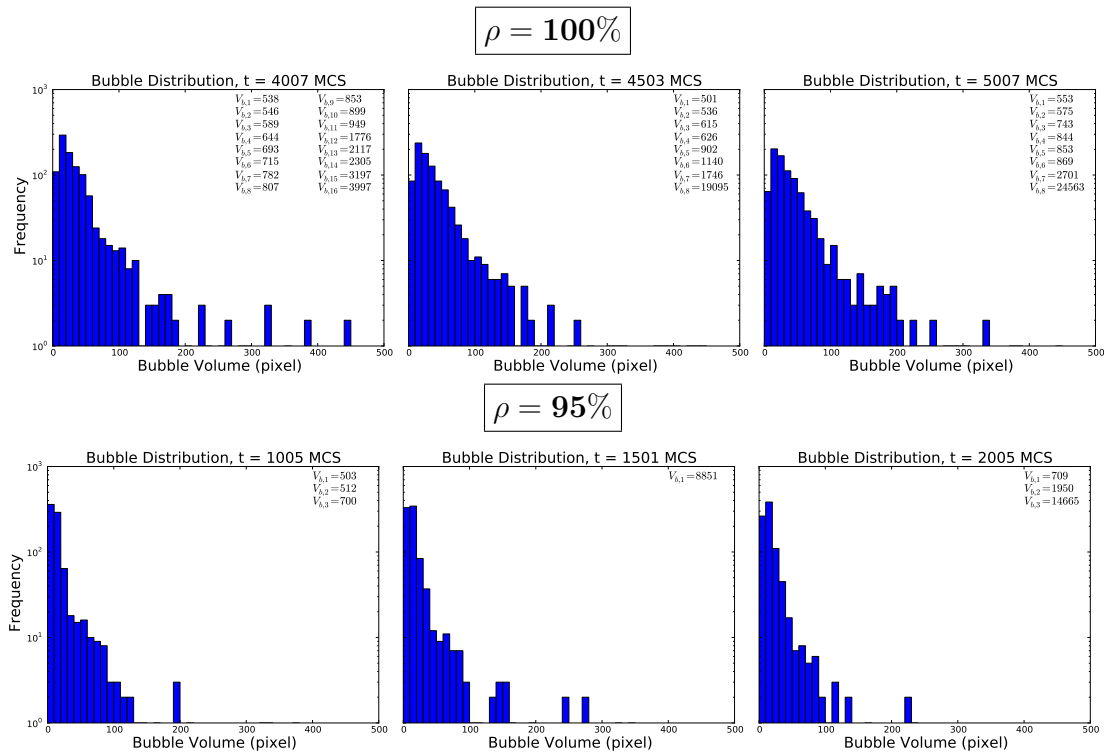


Figure 6.8: Bubble size distribution for the two cases simulated. It is evident that a much lower bubble content is needed for percolation to take place for the  $\rho = 95\%$  case. The inserts refer to bubbles that were larger than 500 voxels.

works have been deemed desirable due to their promising application to quantum-confined photoelectronic devices. While these structures have been easily developed and widely studied for ion irradiated of amorphized Ge, the controlling mechanisms are not wholly understood. Therefore, computational studies that elucidate the processes that lead to the formation of these structures are needed.

There have been attempts at modeling the formation of these nano-porous networks through the use of phase field models [72]. While they were able to generate structures that resemble the general shape of the networks developed experimentally, these models lack a direct link between the physical processes taking place and the ones being modeled. Therefore, a hybrid deterministic-statistical model has been developed that aims to capture real physical processes and implement them into irradiation simulations. This hybrid model employs rate theory and kinetic Monte Carlo methods to simulate point defect evolution and microstructural swelling of an irradiated material. Additionally, by not defining any properties pertinent to crystalline structure, the model virtually treats the irradiated microstructural domain as an amorphous material. This section outlines the model framework, development and generic simulation aspects.

### **6.3.1 Model Framework**

This model employs much of the same microstructural characteristics as defined for the previously discussed RIS models. Hence, for convenience and to avoid redundancy, the microstructural aspects for this model will be briefly considered. A noticeable difference is that a single valued microstructural domain is defined as a homogeneous target. This is because the irradiated material is assumed to be amorphized and the amorphous phase is treated as a uniform phase/state. As before, the simulation space is digitized into a 3D voxelated mesh. Further, it uses both continuum and discrete order parameters to fully describe the microstructure. The latter is very similar to



the microstructural framework discussed in Section 5.2.

### 6.3.1.1 Microstructural and Compositional Representation

The microstructure requires the definition of both continuum and discrete order parameters. The continuum order parameters include the radiation generated point defects, i.e. interstitials ( $C_i$ ) and vacancies ( $C_v$ ). These components are defined in term of compositional concentrations as defined in Chapter V. The continuum fields are *not* conserved as they are created by radiation collisions and reduced by recombination and annihilation at the sinks. Point defects in amorphous materials are an oxymoron as the definition of an amorphous material does not allow for their existence. Nonetheless, these defect density definitions are employed as computational approximations for radiation damage.

The discrete order parameter could be thought of as a homogeneous phase. Each voxel is assigned an integer value that describes its “type”. Similar to the bubble swelling model, these are: frame, void and matter. The main difference between the models’ microstructures is the lack of a reference to crystallinity, e.g. grain orientations. This is due to the fact that materials that have been shown to develop the nano-porous structures were amorphized by the time that void nucleation and swelling was observed. This has been repeatedly corroborated by work on several types of semiconductors, as discussed in Section 1.3.1. Another distinction is that evolution of the microstructural domain directly depends on the coupling of the order parameters. The discrete parameters strictly depend on the evolution of the continuum parameters and changes on the discrete microstructure will influence the how the continuum parameters diffuse. In other words, they are mutually dependent on defining the evolution of the system.

### 6.3.1.2 Thermodynamics of the System

While the thermodynamics of the system have been defined for this simulation, they do not drive the compositional evolution. The driving force is defined by the concentration gradients, as opposed to the chemical potential in Chapter V. However, the thermodynamics of the system does influence the microstructural kinetics as described in Section 6.2.1.3. The model is set up to use the same free energy functional as described in Section 5.2.4. The simplified EoS that solely uses the Pott’s interfacial energy defines the systems thermodynamics, Equation 6.2. If the void nucleation mechanism is replaced by a more rigorous approach, e.g. Boltzmann statistics, the EoS should be replaced by a free energy functional similar to the one discussed in Chapter V.

### 6.3.1.3 Void Nucleation and Migration Mechanism

Qualitative models have suggested that the nano-porous networks form due to the accumulation of the less mobile point defects, i.e. vacancies. These concepts are applied to the nucleation mechanism incorporated in this model. This means that the microstructural evolution needs to be directly linked to the compositional evolution of the point defects. Therefore, the kinetic Monte Carlo algorithm is driven by the evolution of the continuum order parameters.

In order to understand the nucleation of voids, it is important to discuss the point defect evolution. As detailed in Sections 5.2.2 and 2.2.1.2, point defects are introduced to the microstructure as a result of radiation damage. These defects are “removed” by allowing them to recombine and diffuse towards different sinks, e.g. free surface. Nonetheless, radiation processes lead to a net increase of defects until a steady state is reached. The presence of these oversaturated point defects lead to unstable microstructural configurations. It is to be expected that if the local defect concentration is too high, the system will try to find a more stable configuration by

nucleating *features*, e.g. dislocation loops and/or voids. Further, it is known that interstitials are usually faster and less thermodynamically probable than vacancies, as a general rule. This understanding is applied to the void nucleation mechanism.

The model assumes that there will be a net over saturation of vacancies which cause the local region to become “voided”. These are assumed to cluster into voids when a threshold concentration is surpassed. The nucleation of a void will lead defects to diffuse towards its surface, which then can cause the void growth by surface migration. Since it is expected for sites around a void (surface sites) to “nucleate” at a faster rate than bulk sites, the nucleation thresholds for these two types of sites is different. This assumption arises from the understanding that it is easier to grow a void as it consumes vacancies than to nucleate a new void within the bulk of the matrix. Then, the probability of nucleating a void is

$$p_{nuc} = \begin{cases} 1, & \text{if bulk site and } \Delta C_d(i) \geq C_{nuc,b}^{thres} \\ 1, & \text{if surface site and } \Delta C_d(i) \geq C_{nuc,s}^{thres} \\ 0, & \text{otherwise} \end{cases} \quad (6.10)$$

where  $\Delta C_d \equiv C_v - C_i$  is the change in defect concentration  $C_{nuc,b}^{thres} > C_{nuc,s}^{thres}$ . These conditions are applied to reflect the expectation that voids prefer to grow around existing voids than nucleate at the bulk.

It should be acknowledged that the exchange mechanism leads to an exchange of all the order parameters, i.e. concentrations and spin. Since this could become very unstable for crossing paths, whenever a swelling path becomes altered by an external swelling event it gets discarded and no void is nucleated. Further, a more realistic nucleation mechanism could be implemented by employing statistical methods, e.g. Boltzmann statistics. If this approach were applied, the EoS should be properly adapted as to capture the different contributing thermodynamic factors that could lead to a void nucleation.

### 6.3.1.4 Rate Theory Equations

The rate theory framework was used to simulate the evolution of the point defects. Similar to the work presented by *Wiedersich et al.*, different kinetic mechanisms influencing point defects are considered. The accumulation of point defects are modeled as described for the radiation-induced segregation hybrid model, but this model considers three atomic species: atoms ( $C_a$ ), interstitials ( $C_i$ ) and vacancies ( $C_v$ )

$$C_a + C_i + C_v = 1. \quad (6.11)$$

The simulations are applicable to a monatomic material ( $A$ ), which applies to ion irradiation of amorphized Ge. While this relationship suggests that the defects are conserved, this is not true. The number of lattice sites is conserved, hence, the  $C_a$  parameter can be considered to be the concentration of  $A$  atoms in its lowest energy configuration site. Since the materials are expected to be fully amorphized, these “lattice sites” do not correspond to atomic crystalline sites.

Once defects are created, they are assumed to undergo several types of kinetic reactions. The ones included in the model are: diffusion down the concentration gradient, recombination with dissimilar defects and annihilation at the void-matter interfaces. This can be mathematically expressed as

$$\frac{\partial N_i}{\partial t} = \nabla[D_i \nabla N_i] - K_{is} N_i (N - N_i - N_v) - K_{iv} N_i N_v \quad (6.12a)$$

$$\frac{\partial N_v}{\partial t} = \nabla[D_v \nabla N_v] - K_{vs} N_v (N - N_i - N_v) - K_{iv} N_i N_v \quad (6.12b)$$

where  $D_i$  is the diffusion coefficient for defect  $i$ ,  $K_{is}$  is the annihilation rate of defect  $i$  at the sink (surface) and  $K_{iv}$  is the rate at which interstitials and vacancies recombine. The model implements a simple adaptation where the rate of annihilation at the sink is proportional to number of atom sites on the surface. This assumes that the defects

reaching the surface will be removed either by a vacancy allowing an atom to take its place or an interstitial settling down on the thermodynamic stable atom “lattice” position at the surface.

For simplicity, it is desirable to relate the rate constants to the diffusion coefficients. Based on the work outlined by *Was* [11], the rate constants for recombination can be defined as

$$K_{iv} = \frac{z_{iv}\Omega(D_v + D_i)}{a^2} \quad (6.13)$$

and the rate constant for defect annihilation at the sink is, assuming a spherical sink,

$$K_{is} = \frac{4\pi R^2 D_i}{a} \quad (6.14)$$

where  $z_{iv}$  is the combinatorial factor,  $\Omega$  is the atomic volume,  $R$  is the radius of the sink and  $a$  is the lattice constant. Let’s keep in mind that the system is assumed to have been amorphized, then the  $a$  parameter is taken to be the average jump distance for defect annihilation. The latter rate is obtained by considering the amount of surface area available for a defect to annihilate.

Considering that the model’s free surface is represented as a flat voxel face, the number of “lattice” sites at the void–matter interface is given by

$$N_l = \frac{\text{voxel face area}}{a^2} = \frac{a_{vx}^2 \cdot \sum_{j=1}^n (1 - \delta_{s_i, s_j})}{a^2}$$

where  $a_{vx}$  is an assigned voxel–to–real dimension parameter,  $n$  is the number of surrounding voxel neighbors and  $a$  is the “lattice” constant. Then, the reaction rate coefficients between the defects and the void surface can be rewritten as

$$K_{is} = z_{is} N_l \Omega D_i = \frac{z_{is} a_{vx}^2 \Omega \sum_{j=1}^n (1 - \delta_{s_i, s_j}) D_i}{a^4} \quad (6.15a)$$

$$K_{vs} = z_{vs} N_l \Omega D_v = \frac{z_{vs} a_{vx}^2 \Omega \sum_{j=1}^n (1 - \delta_{s_i, s_j}) D_v}{a^4} \quad (6.15b)$$

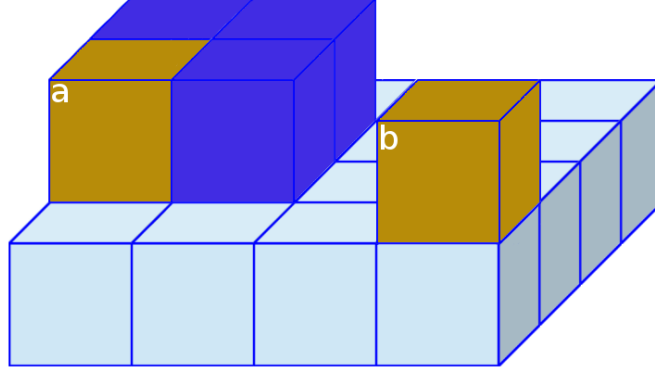


Figure 6.9: Schematic of a voxelated surface showing the difference in free surface area between two surface voxels. Site  $a$  will have a lower surface area, meaning that the more defects will be annihilated by site  $b$ . The arrangement shown indicates that voxel  $a$  and  $b$  have 3 and 5 free faces.

where  $z_{xs}$  are the combinatorial factors between the defects and the sinks. This concept of making the sink strength proportional to the surface area can be better understood by looking at Figure 6.9. Two voxel configurations are being considered: an agglomerated and isolated voxels. It is evident that the isolated voxel will have a larger surface area (highlighted in maize) exposed to the vacuum domain where defects can be annihilated.

As was done for the previous models, the evolution of the concentration is a more convenient parameter to study than the number density. Multiplying Equation 6.12 by the atomic volume and applying the definitions for the rate constants, we have

$$\begin{aligned} \Omega \frac{\partial N_i}{\partial t} = & \Omega \nabla [D_i \nabla N_i] - \frac{z_{is} a_{vx}^2 \Omega^2 D_i}{a^4} N_i (N - N_i - N_v) \sum_{j=1}^n (1 - \delta_{s_i, s_j}) \\ & - \frac{z_{iv} \Omega^2 (D_i + D_v)}{a^2} N_i N_v \end{aligned} \quad (6.16a)$$

$$\begin{aligned} \Omega \frac{\partial N_v}{\partial t} = & \Omega \nabla [D_v \nabla N_v] - \frac{z_{vs} a_{vx}^2 \Omega^2 D_v}{a^4} N_v (N - N_i - N_v) \sum_{j=1}^n (1 - \delta_{s_i, s_j}) \\ & - \frac{z_{iv} \Omega^2 (D_i + D_v)}{a^2} N_i N_v \end{aligned} \quad (6.16b)$$

where the Kronecker delta ( $\delta_{s_i, s_j}$ ) compares neighboring voxels' spin values. For the

simulation presented, the spin value is equivalent to the phase, i.e.  $s = q = n$ . If the microstructural domain is redefined to include several phases and/or polycrystals these equations should be adapted accordingly. In other words, the need to have different combinatorial factors for the different sinks should be considered. Lastly, since the concentration and the particle number density can be related by

$$N \equiv \frac{C}{\Omega},$$

and assuming that the atomic volume can be approximated by the jump distance,  $\Omega \sim a^3$ , Equations 6.16 can be re-written as

$$\begin{aligned} \frac{\partial C_i}{\partial t} = & \nabla[D_i \nabla C_i] - \frac{z_{is} a_{vx}^2 D_i}{a} C_i (1 - C_i - C_v) \sum_{j=1}^n (1 - \delta_{s_i, s_j}) \\ & - z_{iv} a (D_i + D_v) C_i C_v \end{aligned} \quad (6.17a)$$

$$\begin{aligned} \frac{\partial C_v}{\partial t} = & \nabla[D_v \nabla C_v] - \frac{z_{vs} a_{vx}^2 D_v}{a} C_v (1 - C_i - C_v) \sum_{j=1}^n (1 - \delta_{s_i, s_j}) \\ & - z_{iv} a (D_i + D_v) C_i C_v \end{aligned} \quad (6.17b)$$

It should be noted that if removal rates are much higher than the defect creation rate, the system will be driven to an un-physical configuration, e.g. defect concentration much lower than their thermal equilibrium concentration. This is commonly handled by bounding the concentrations, i.e. resetting to an assigned value if the order parameter strays from these bounds. The approach implemented in the model allows it to “self regulate” about the equilibrium concentrations. This is done by replacing the  $C$ 's with  $C - C^{eq}$  for the removal kinetics, e.g.

$$K_{iv} C_i C_v \rightarrow K_{iv} (C_i - C_i^{eq})(C_v - C_v^{eq}).$$

It should be noted that this approach does have its own flows. For instance, if the

defect concentration goes under the thermal equilibrium concentration, the system will be required to create point defects such that thermal equilibrium is achieved. On the other hand, this is not expected to happen as defects are created faster than removed during irradiation.

### 6.3.1.5 Void Swelling Algorithm

The algorithm that manages the actual volumetric expansion is very similar to the voxel exchange mechanism outlined in Section 6.2.1.4. In fact, the main difference between the models' swelling mechanism is the set of rules followed that dictate feature nucleation. Further, this model couples the swelling algorithm to the rate theory model, as just discussed. The rules for void nucleation are discussed in Section 6.3.1.3. The staged processes that lead to void swelling are sketched in Figure 6.10. Initially, the amorphized target undergoes defect accumulation in a random manner, as shown by the slightly different shades of the squares, Figure 6.10(a). The random distribution is due to the stochastic nature of radiation damage. Eventually enough damage builds up that a void is nucleated as defined by Equation 6.10. With the nucleation, a swelling event evolves the microstructure into a porous structure, Figure 6.10(b). The newly established internal free surface will act as a sink for defects in the surroundings and the void will tend to grow as more excess defects diffuse toward it, Figure 6.10(c-d). It is supposed that the equations will lead the smaller voids to grow into the convoluted large porous network experimentally observed.

### 6.3.2 Results and Discussion

The coupled hybrid swelling model was tested by considering the effects of the diffusivities and radiation damage profiles. The study of the former was done by changing both the defect diffusivities' ratio ( $D_i/D_v$ ) and changing the magnitudes while keeping the ratio fixed. The purpose of the simulations is to represent the



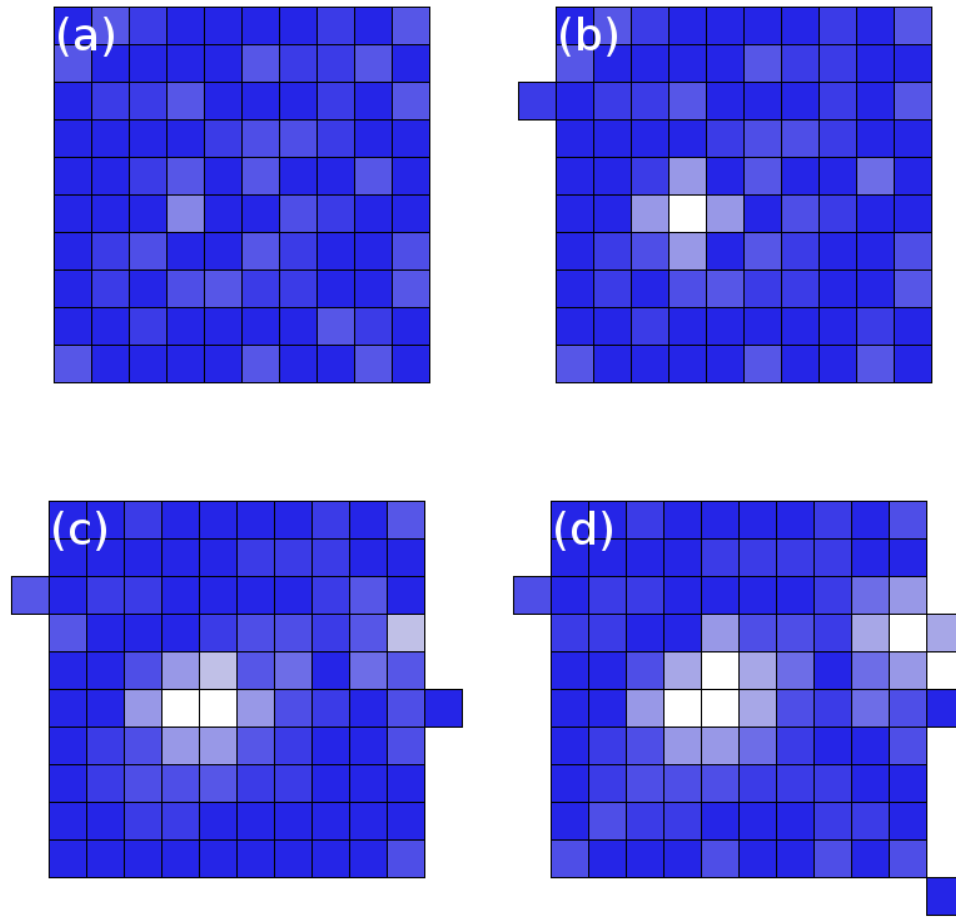


Figure 6.10: Example of the void swelling mechanism showing defect accumulation and volumetric expansion. As the material is irradiated, the defect density is increased as shown by the different shades of blue (lighter = more vacancies). Eventually enough defects are accumulated that a void is nucleated (white). Defects will then diffuse towards the newly created surface regions.

Table 6.3: Numerical values of the parameterization variables for the rate theory and kinetic equations. The units of the parameters have been set to represent  $cm$  and  $s$ .

<b>Parameterization Variable</b>	<b>Values</b>
$D_i$	$7.50 \times 10^{-4}$
$D_v$	$3.50 \times 10^{-4}$
$K_{iv}$	$1.00 \times 10^{-5}$
$z_{is}$	$1.00 \times 10^1$
$z_{vs}$	$1.00 \times 10^1$
$a_{vx}$	$2.00 \times 10^{-7}$
$a$	$7.43 \times 10^{-8}$
$C_i^{eq}$	$2.00 \times 10^{-6}$
$C_v^{eq}$	$2.00 \times 10^{-5}$
$C_{nuc,b}^{thres}$	$5.00 \times 10^{-4}$
$C_{nuc,s}^{thres}$	$5.00 \times 10^{-3}$
$\mathcal{J}$	$1.00 \times 10^0$

behavior of different materials (change in ratio) or the increase in temperature (proportional increase in magnitude). These simulations were subjected to the same uniform radiation conditions. As for the radiation damage profiles, a uniform radiation probability was compared to a (planar) probability distribution that peaked around the center of the target. A qualitative representation of the profiles used are shown in Figure 6.11. The uniform distribution translates into a uniform probability of damage, or a uniform distribution of defects being created on each voxel within the microstructural domain. The planar distribution defines a system where sites within any  $xy$ -plane have the same probability of damage. Hence, it only depends on the depth which peaks at the center of the microstructural domain, Figure 6.11(right). These simulations were performed as to show the general capabilities of the model and study the influence of certain parameterization variables. The parameters used for the simulations presented here are shown in Table 6.3. This section first considers the former of the damage profiles.

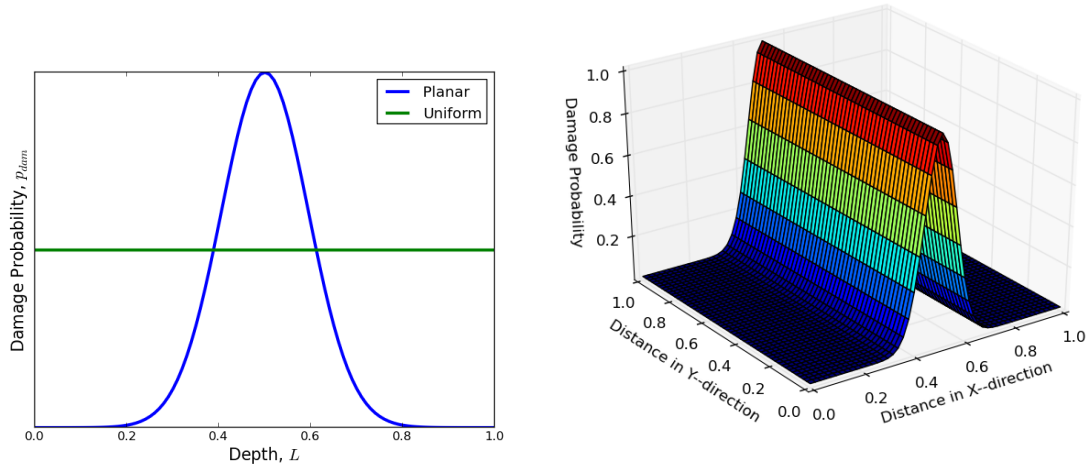


Figure 6.11: Qualitative representation of the radiation damage profiles used to assess the coupled swelling model. The uniform case considers an equal probability of damage and energy deposition regardless of the voxel location. The planar case sets a distribution that peaks at the center of the target in the depth direction, where  $z = L_3^l$  or  $z = L_3^h$  is the irradiated surface. The figure on the right helps visualizing the distribution along the  $xz$ - or  $yz$ -planes.

### 6.3.2.1 General Features of the Swollen Microstructures

Generic features shared by the different simulations of the nano-porous structuring processes is studied by considering the simplest case of uniform irradiation. The values used for the parameterization variables for this simulation are given in Table 6.3. The uniform radiation case treats each voxel as having the same likelihood of experiencing a collision event and leading to the creation of the same number of defects. This is analogous to a domain in the vicinity of a free surface irradiated by swift ions (high energy). Therefore, randomly distributed collision events lead to a random uniformly distributed radiation damage profile. Ultimately, after enough radiation events take place, the defect concentrations average into smooth profiles. The average defect concentration profile can be seen on Figure 6.12, which shows the average concentration for the vacancies (green) and the interstitials (blue). The profiles show a regime of linear defect build up, followed by a stabilization (saturation) of the

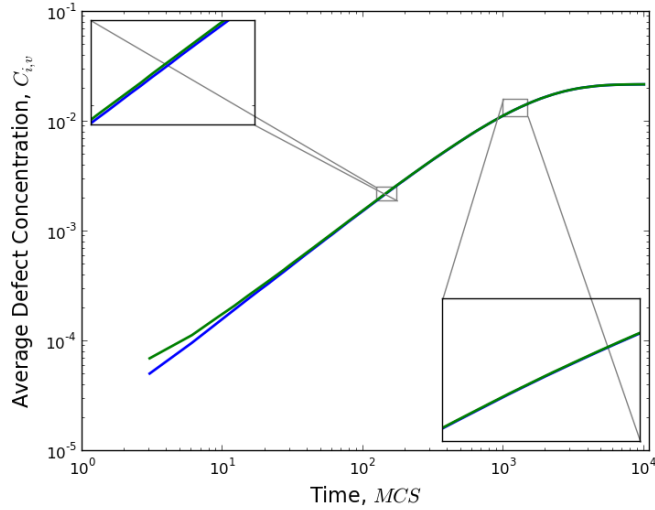


Figure 6.12: Average concentration for the point defects as a function of time. The green curve corresponds to the vacancy concentration ( $\bar{C}_v$ ) and the blue curve correspond to the interstitial concentration ( $\bar{C}_i$ ).

defects. After this regime, the microstructure is said to have reached a steady state. It is evident that these curves follow extremely similar trends with the vacancies being slightly higher. The similarity in these two distributions is due to the small differences between the sink strengths. Therefore, both defects will diffuse towards the sinks (free surfaces) and become annihilated at similar rates.

As in Section 6.2.2, each void nucleation event is followed by a swelling event. The resulting bulk microstructure is shown in Figure 6.13. Void nucleation within the microstructural domain starts at  $\tau \sim 90$  *MCS*, at which time enough damage has been built up. The microstructure quickly and uniformly expands in all directions until the microstructure starts transitioning into the saturation regime. Once the microstructure is within the steady state saturated regime, it becomes fairly stable with negligible swelling taking place. This can be better appreciated by looking at the interior cross section of the microstructure domain, Figure 6.14.

While the bulk outline of the microstructural domain shows swelling over the whole domain, looking at a cross section provides better insight as to the microstructural

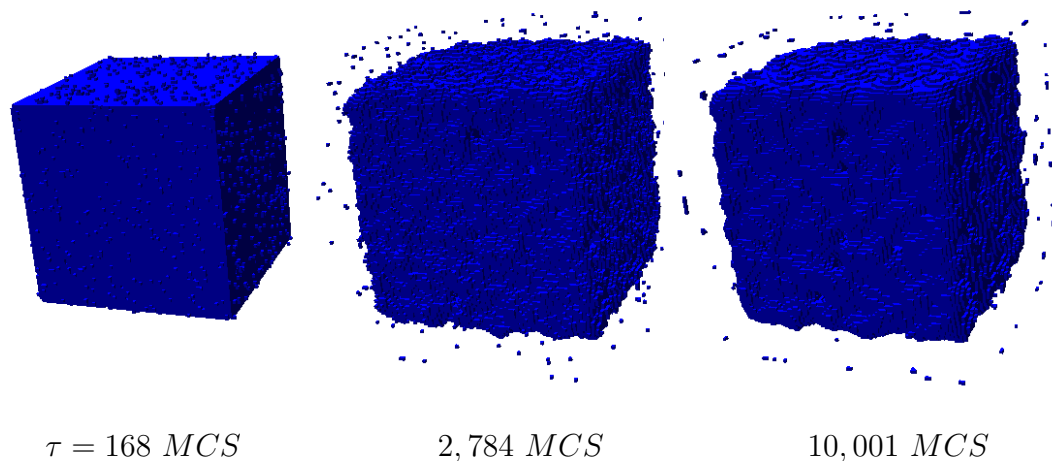


Figure 6.13: Evolution of the bulk microstructural domain at the onset of swelling, an intermediate time and at steady state. The microstructure seems to arrange into a stable configuration that remains generally unchanged for the last 4,000 *MCS*.

evolution. Figure 6.14 shows the formation of a complex interlinked nano-porous network. This starts with the onset of void nucleation and terminates with the formation of a stable porous microstructure. The initial stages show the nucleation of single site (voxel) voids that swell the microstructural domain. As more of these voids nucleate, the voids tend to cluster into larger uniform pseudo-spherical voids. The smaller mobile voids diffuse towards the stationary larger ones. These types of larger voids are the ones believed to have been initially observed by *Wang et al.* during their in-situ ion irradiation of amorphized Ge. The microstructure then continues to evolve into a highly intertwined porous network as these immobile voids keep growing by “consuming” the smaller voids. Furthermore, they grow due to defect diffusion towards the voids’ free surface. Eventually, the microstructure becomes very stable and negligible changes to the microstructure are observed, mostly surface diffusion. This stable microstructure self-assembles as the point defects reach a steady state saturation concentration. This is an important observation as the experiments have shown that further irradiation has a negligible effect on the generated nano-porous

structures.

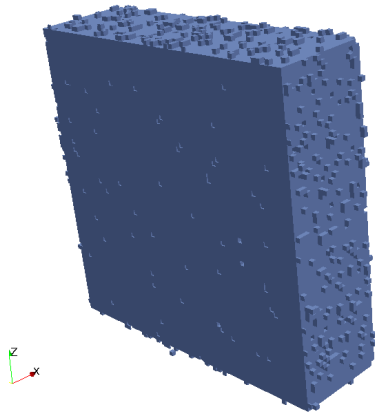
A general idea of how this nano-porous structure evolves can be obtained by studying the void size distribution. Figure 6.15 shows these distributions for experimental work by *Romano et al.* [125] and the uniform radiation simulation. The experimental case measures the void's radial distribution while the simulation presents the void volume in number of voxels. The volume distribution shows that initially there are few and mostly very small void clusters,  $V < 10$  voxels. As more voids are nucleated and pre-existing voids grow, the distribution starts "shifting" to the right. This leads to the void volume distribution to start taking the form of a *normal* distribution. Eventually, as the porous network becomes interlinked, a very large void forms and quickly overtakes the void volume as the whole network becomes interlinked. This behavior is not observed from the experimental measurements, and if present cannot be easily measured. This could be due to the manner in which the measurements were performed. Experimental measurements only consider cross sectional sections of the nano-porous structure where the complete complexity of the network cannot be appreciated.

### 6.3.2.2 Role of the Diffusivities

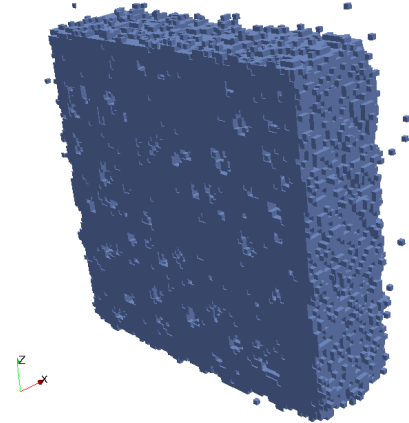
Parameterization studies on the diffusivities were performed to better understand their influence on microstructural evolution. Two relationships were considered: increased diffusivity magnitude with constant ratio ( $D_i/D_v$ ) and variation in the diffusivity ratio. Reaction rate constants shown in Equation 6.17 depend on multiple parameters, including the diffusivities. Hence, these parameterization studies do examine their influence to a lesser extent.

The diffusivity ratio was initially considered to be relatively close to unity,  $D_i/D_v \sim 2$ , to avoid a particular defect type from dominating the microstructural evolution. Interstitials were generally assumed to diffuse faster as they are usually considered

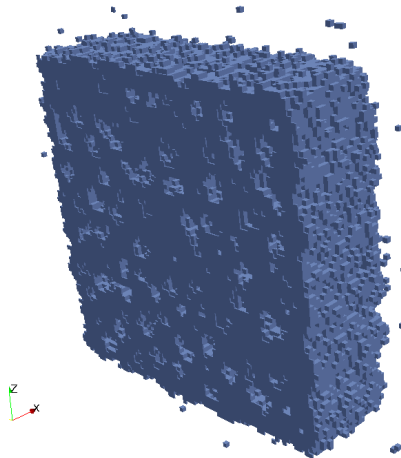
$\tau = 168 \text{ MCS}$



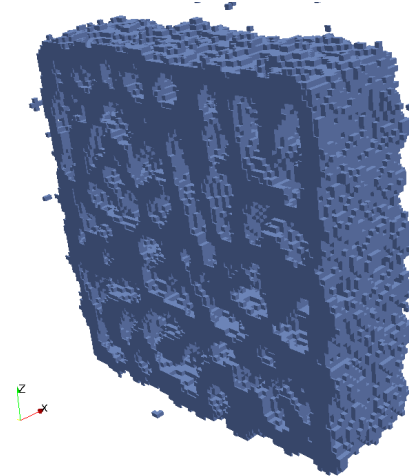
601 MCS



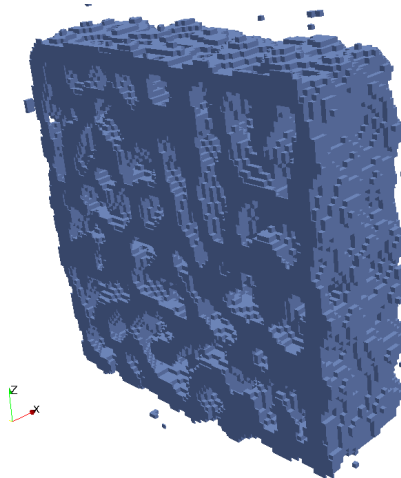
1,001 MCS



2,784 MCS



5,996 MCS



10,001 MCS

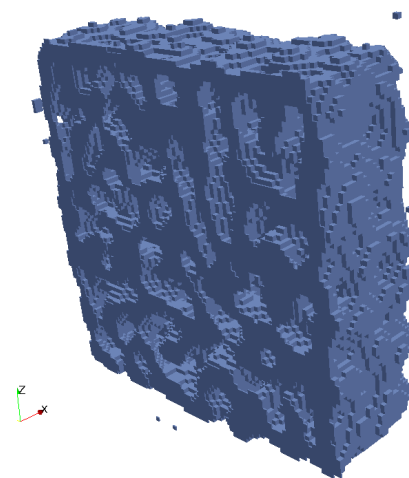


Figure 6.14: Cross sectional view of the microstructural evolution showing the development of the porous network. The stabilization of the porous network can be better appreciated from these views.

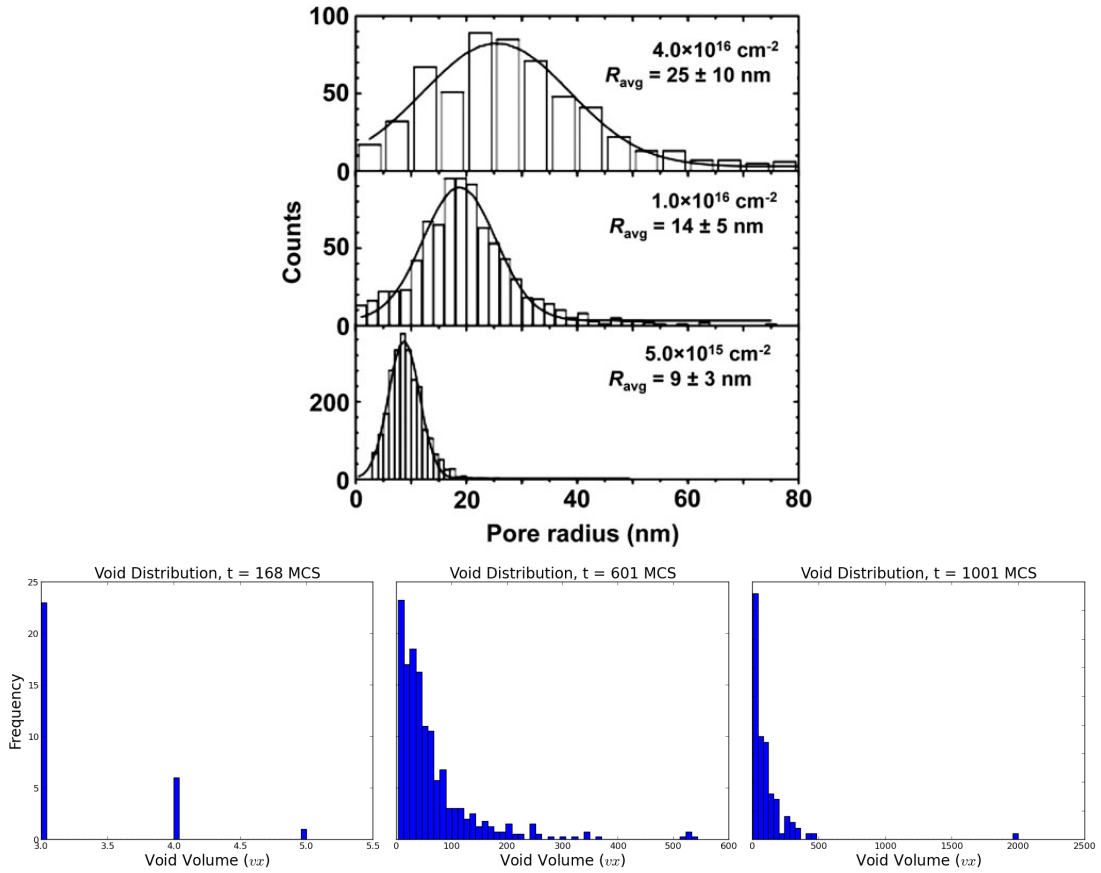


Figure 6.15: Void size distribution for (top) experimentally measured pore sizes [125], and (bottom) the uniform radiation simulation. The simulation distributions are able to capture the interlinkage between the individual voids while the is not straightforward for the experimental measurements. Notice that the experimental and computational distributions measure different parameters. Further, the simulations have “flexible” axes to allow for visualization of the data.



to be the more mobile defect, especially at higher temperatures. The magnitude of the diffusivities were then increased by orders of magnitude, which is equivalent to increasing the temperature. The resulting porous microstructures are shown in Figure 6.16. Visual comparison of these two cases shows that the porosity is largely reduced by increasing the diffusivities' magnitude. A simple quantitative approach of comparing the microstructural evolution is by plotting the porosity of the irradiated materials. The porosity is calculated by counting the number of voids within a fixed volume embedded in the bulk of the microstructural domain. The volume being considered is centered about

$$\mathbf{x}_c = \left( \frac{L_1}{2}, \frac{L_2}{2}, \frac{L_3}{2} \right).$$

These calculations are measured from a fixed volume of  $\sim 10\%$  of the fully dense microstructure. Then, the porosity is calculated as

$$\varrho = \frac{N_p - N_m}{N_p} = \frac{N_v}{N_p} = \sum_{i=1}^{N_p} \frac{\delta_{s(i),0}}{N_p} \quad (6.18)$$

where  $N_v$  and  $N_m$  are the number of void and matter voxels within the fixed volume and  $N_p$  is the total number of sites accounted for during the porosity calculation

$$N_p = N_m + N_v.$$

The porosity evolution for three different magnitudes is shown in Figure 6.17. Several feature in commonality can be observed as the diffusivities are increased, which is equivalent to increasing the temperature. First, there is exponential build up of pores as point defects are accumulated. Then, after saturation of the point defects is achieved, the porosity start to plateau. This means that the microstructure has achieved a stable configuration after which continued irradiation has minimal effect

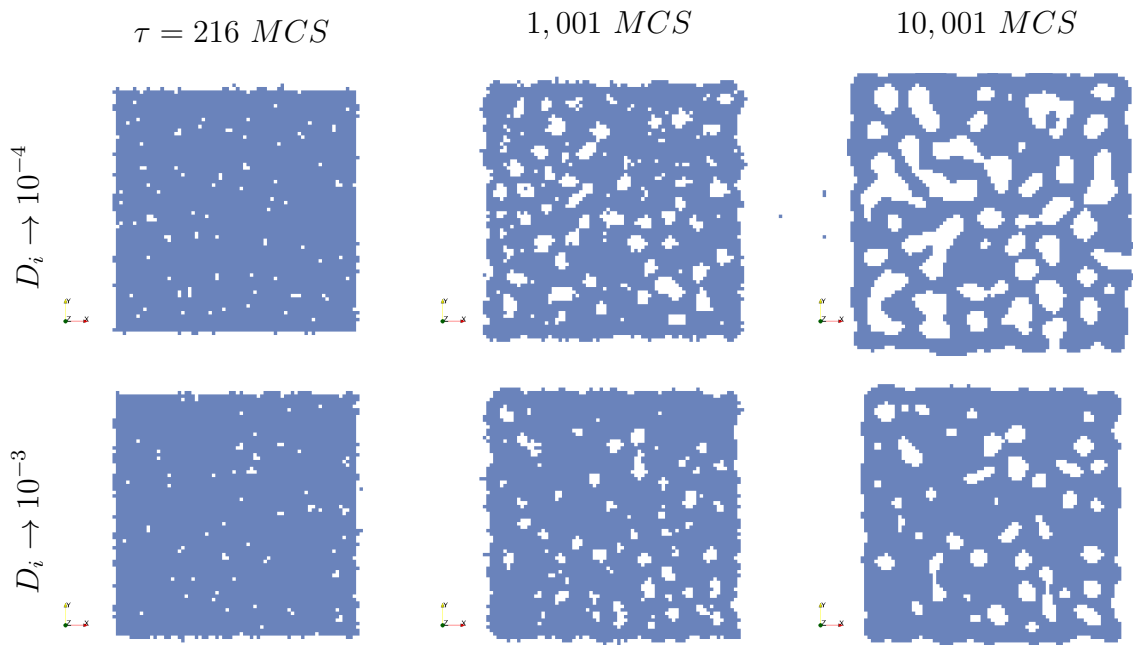


Figure 6.16: Single frame cross sectional views of the microstructural evolution of the void nucleated nano-porous structure. The simulations show the effects of the diffusivity magnitude. The three views represent different structuring stages: early initial void nucleation (left); preceding time step to reaching a stable configuration (center); and final configuration where steady state has been achieved (right).

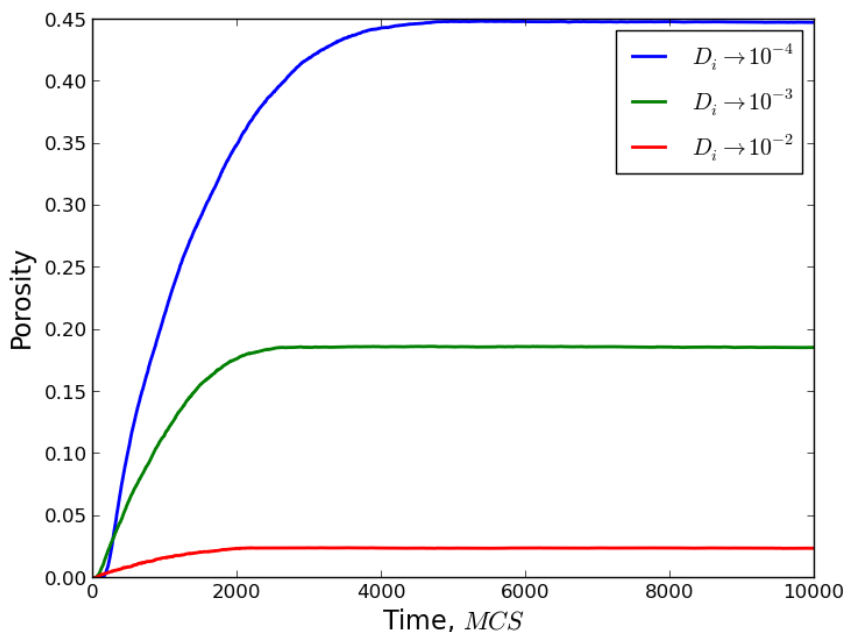


Figure 6.17: Porosity evolution for the different magnitude cases, identified by the order of magnitude of the given value. As the defects diffuse faster, a less porous stable microstructure is achieved. This is due to defects being removed faster and restraining void nucleation.

on the microstructural arrangement, as discussed in the previous section. The figure also shows that the microstructures' stable states are less porous and reached faster as the diffusivities are increased. This is explained by the fact that defects diffusing and reacting faster will mean that they are removed faster. Hence, defects will not have time to cluster and nucleate voids. This becomes accentuated as voids are nucleated, increasing the surface area.

The maximum (plateaued) porosity can be plotted as a function of interstitial diffusivity. This yields an obvious trend, as shown in Figure 6.18. This representation of the microstructural evolution enables the “mapping” of the expected wall size that separates pores, i.e. *fibers*. It should be noted that this approach could yield misleading interpretations. For instance, if the voids are not very mobile, as in these simulations, high porosity represents a complex microstructure. On the other

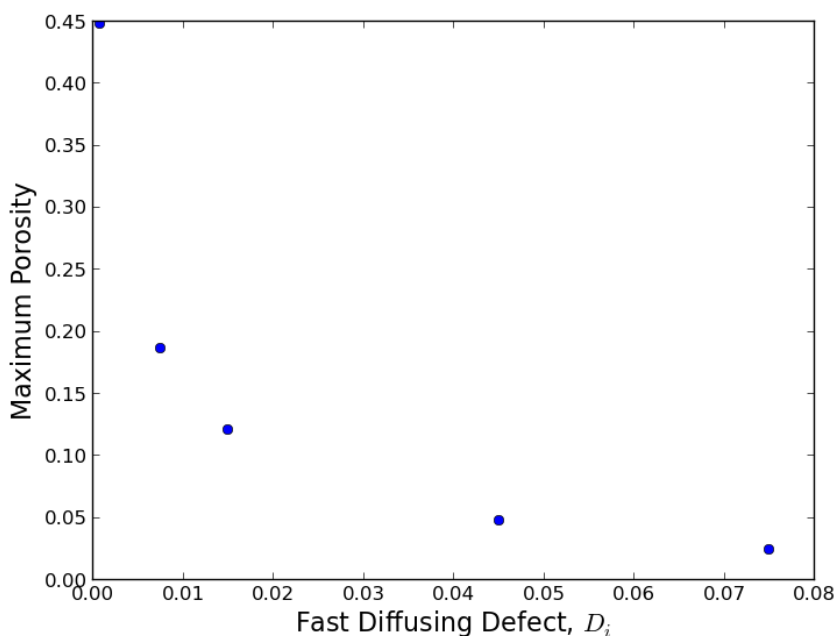


Figure 6.18: Porosity of the stable configuration as a function of the interstitial diffusivity. With less mobile defects, the microstructure is able to nucleate and grow more voids leading to a more porous configuration.

hand, if the individual voids are highly mobile they will diffuse and coalesce generating a highly porous microstructure consisting of a very large void. Nonetheless, this measurement does show that there is a clear relationship between the stable microstructure and the defect diffusivity.

Increasing the diffusivities' ratio has a less pronounced effect on the extent of the porosity as shown in Figure 6.19. This is especially true for cases where the interstitials are much faster than vacancies, i.e.  $D_i/D_v \geq 10$ . Figure 6.20 clearly shows this by comparing the porosity evolution for three different ratios ranging over several orders of magnitude. One of the simulations assumes the vacancies to be faster as this has been shown to be true for Si under certain conditions [126]. While all three simulations retain the usual evolution characteristics previously discussed, it is interesting to see that the case for faster vacancies leads to a more porous structure. A larger vacancy diffusivity means that they will reach the free surfaces

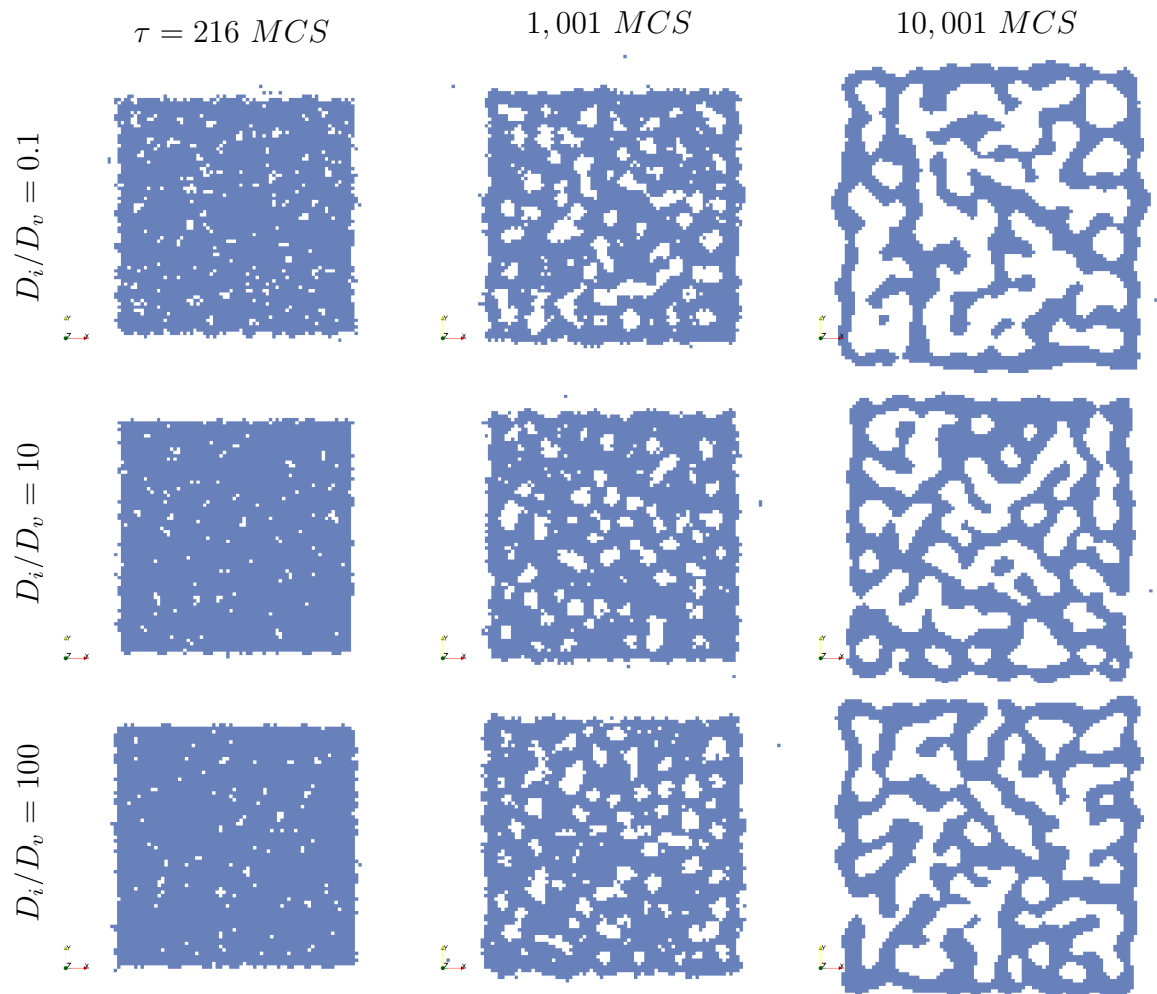


Figure 6.19: Single frame cross sectional views of the microstructural evolution of the void nucleated nano-porous structure. The simulations show the effects of the diffusivities' ratio. The three views represent different structuring stages: early initial void nucleation (left); preceding time step to reaching a stable configuration (center); and final configuration where steady state has been achieved (right).

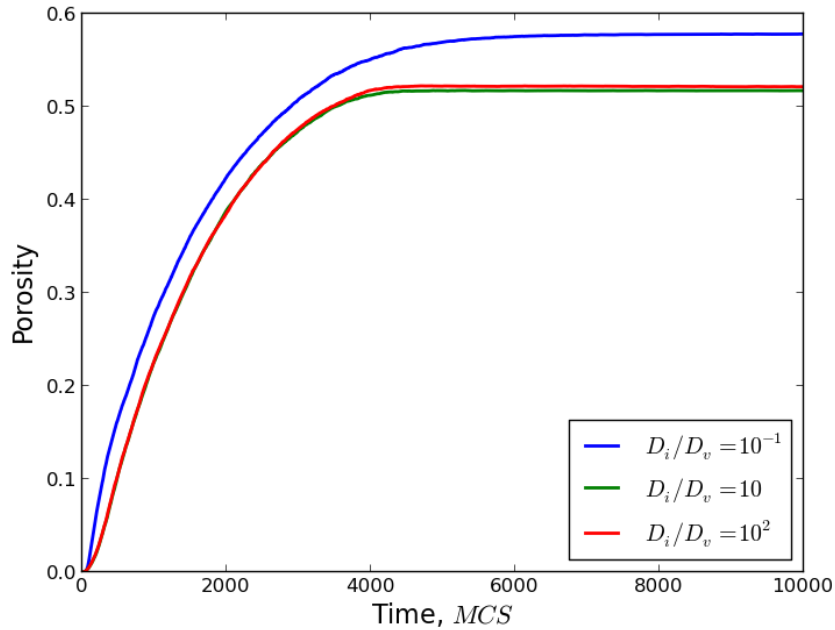


Figure 6.20: Porosity evolution for the varying diffusivities' ratio cases. The reference point used corresponds to the simulation that leads to the most porous microstructure for the diffusivity magnitude study, i.e.  $D_i \rightarrow 10^{-4}$ . It's interesting that while making the interstitials increasingly faster than vacancies barely influences the microstructural evolution, the case of faster vacancies has a very noticeable effect on the microstructure.

before interstitials. Hence, the nucleation threshold criteria will be attained less frequently in the bulk of the microstructure. On the other hand, as vacancies reach the surface before interstitials, the correct conditions for nucleation will be attained around free surfaces. Therefore, the void growth by surface migration mechanism is particularly important when the vacancies diffuse faster. Further, visual inspection of the cross sectional frames reveal that the faster diffusing vacancies case leads to thicker more interlinked nano-porous microstructures.

### 6.3.2.3 Qualitative Comparison to Experiments

One of the criteria to show the predictiveness of a computational model is its ability to recreate experimental results. The coupled hybrid model developed in this

dissertation does not claim to be modeling any physical system as it does not use specific material properties. Nonetheless, it is still useful to compare the simulated microstructural evolution to experimental results. The computational results correspond to the different parameterization studies. For the *change in magnitude* case, the diffusivities' ratio is about two,  $D_i/D_v \sim 2.1$ . Whereas for the *change in ratio* case, the  $D_i \rightarrow 10^{-3}$  condition is employed. In order to qualitatively compare these, TEM images from *Wang's* work [19] were filtered and compared to the simulation results previously discussed. These are shown in Figure 6.21, where the columns refer to:

- Early stage: soon after void nucleation has started.
- Preceding steady state: just before the steady state porous microstructure is attained
- Steady state: final stable configuration that barely changes with increased irradiation.

The three results yield very comparable microstructures during the first two stages where small voids are shown to have nucleated, and eventually grown and coalesced into complex pores. However, it is clear that the diffusivities' ratio is important in the development of the stable microstructural arrangement. Visual inspection of the steady state configurations show that the higher ratio case shares more similarities with the experimental results, e.g. voids spaced more uniformly, higher density of convoluted shaped voids, *inter alia*. Therefore, it is essential to have slow enough defects that lead to void nucleation *and* relatively faster interstitials to help achieve a more morphologically accurate nano-porous structures.

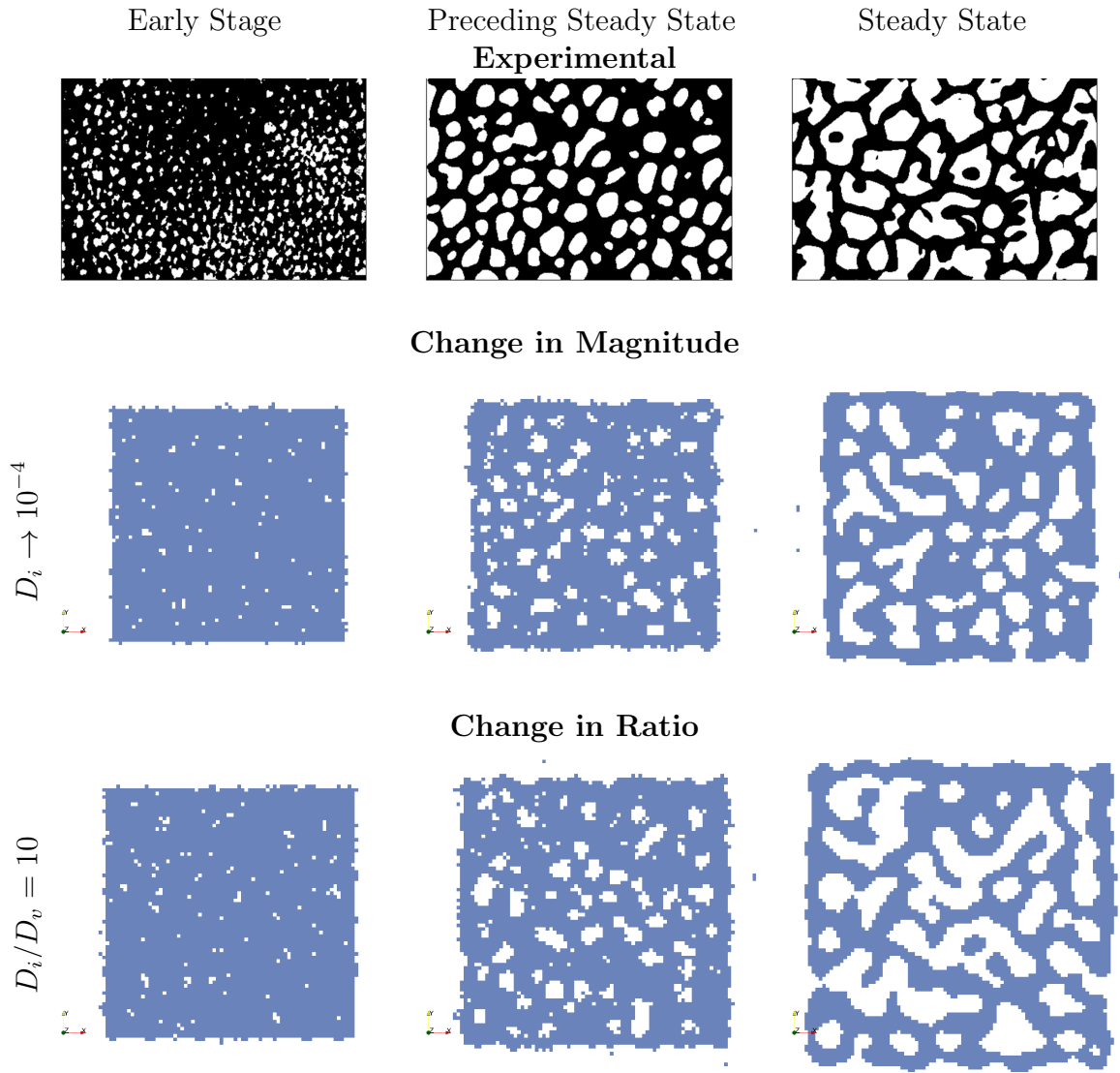


Figure 6.21: Qualitative comparison of the experimental [19] and the computational results (this dissertation). Visual inspection reveals that slow diffusing defects with slightly faster interstitials yield to a more sensitive and proper stable configuration. The computational results are from single frame cross sectional views of the previously discussed simulations. Notice that the experimental results were analyzed (computationally filtered) in order to obtain a sharper image that provides a more accurate description of a single frame cross sectional view.



#### 6.3.2.4 Case of the Planar Damage Distribution

To study the influence of radiation damage distribution on the microstructural evolution, a planar radiation damage profile was simulated. The profile peaks at a depth of  $\mathbf{x}_{peak} \sim (x, y, 0.5(L_3^h - L_3^l))$  where the microstructural domain is bounded by

$$\mathbf{x} = \{(x, y, z) : L_1^l \leq x \leq L_1^h, L_2^l \leq y \leq L_2^h, L_3^l \leq z \leq L_3^h\}.$$

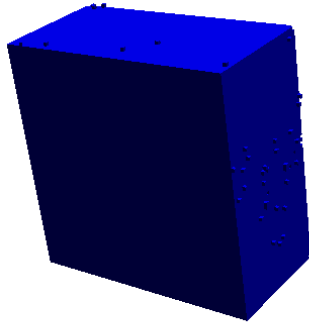
This would be equivalent to low energy ion irradiation of a relatively small target with exposed free surfaces. Figures 6.22 and 6.23 show tilted cross sectional views of the microstructural and vacancy concentration evolution, respectively. Since it was shown that the average concentrations of the defects behave similarly, only the vacancy distribution evolution is shown. The microstructural evolution, Figure 6.22, shows several peculiarities when compared to the uniform radiation damage case. First, in the initial stage of void nucleation, voids only nucleate in the peak radiation damage region. This is to be expected since the majority of the point defects have been created in this region. As voids nucleate and coalesce, this region starts to transform into an interlinked porous network. Interestingly, it appears as if this region experiences preferential swelling in the  $xy$ -plane directions, Figure 6.24. The model is able to capture this minute difference on the volumetric expansion inherently. This is a welcomed result as the volumetric expansion direction is randomly selected as discussed in Section 6.2.1.4. Ultimately, a quasi-stable porous network is formed in the peak dose region, which is accompanied by the formation of porous networks in the vicinity of the free surfaces. These form as defect created just off the porous region diffuse towards the free surfaces. This is more readily identifiable by examining the defect concentration distribution, Figure 6.23. These regions extend towards the center of the target where they eventually converge with the expansion of the first developed porous network. Thus forming a large interlinked porous network.

It should be noted that unlike the uniform radiation damage case, a wholly stable microstructure was not observed for up to 10,000 *MCS*.

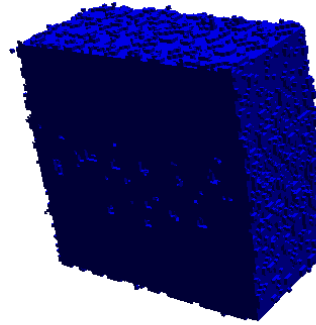
The planar view across the target depth, Figure 6.24, clearly shows the particular swelling characteristics for this simulation. The microstructural domain initially swells faster perpendicular to the  $xz$ - and  $yz$ -planes where most of the point defects are created. Eventually, the onset of void nucleation in the regions near the exposed surfaces lead to a uniformly swollen microstructure. Its clear that once swelling in these regions initiates, swelling in the peak damage region seems to stall. Another interesting feature is the difference in roughness of the surfaces for the  $xy$ -plane and the  $xz/yz$ -planes. This translates into the generation of smooth surfaces for high energy ion irradiation. This has been shown in GaSb where, an “intact” surface is reported [21]. Under the appropriate radiation conditions, the simulation is expected to form a stable smooth surface.

Lastly, the two simulated damage profiles are compared by looking at the internal porosity of the bulk microstructural domain. Again, these calculations employ a fixed volume of  $\sim 10\%$  of the fully dense microstructure. This fixed volume focuses on the region receiving the most damage for the “planar” damage distribution case. All other parameterization variables have the same values. The porosity evolution for both simulated cases is shown in Figure 6.25. The difference in the evolution is very noticeable. Firstly, the uniform radiation case leads to a slightly steeper increase in porosity than the planar case. This could be due to more net defects being created within the fixed volume under consideration. More importantly, at  $\sim 4,000$  *MCS*, the uniform irradiated microstructure is observed to find an equilibrium configuration. This was discussed when examining the microstructural evolution for the uniform damage case and observed to only experience minimal surface migration changes in the later stages of the simulation. Interestingly, the planar radiation damage case does not appear to have reached an equilibrium configuration after 10,000 *MCS*,

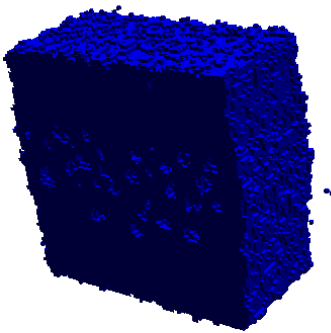
$\tau = 168 \text{ MCS}$



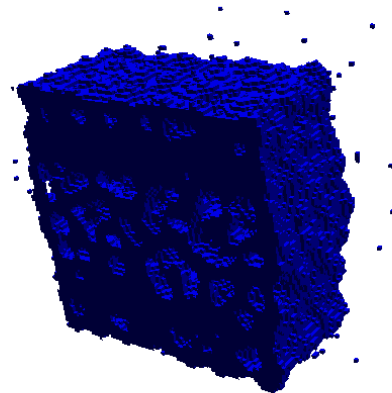
601 *MCS*



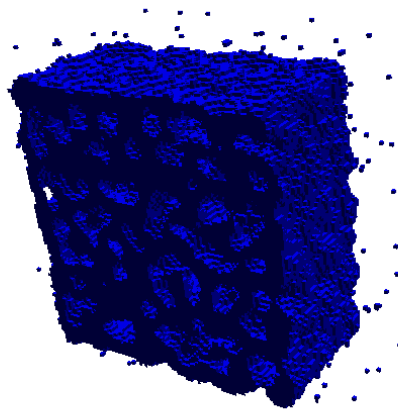
1,001 *MCS*



2,784 *MCS*



5,996 *MCS*



10,001 *MCS*

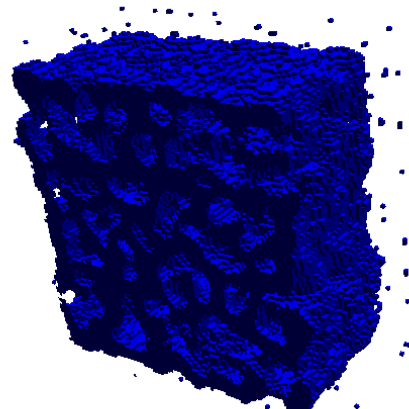
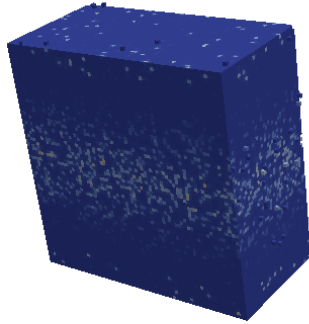
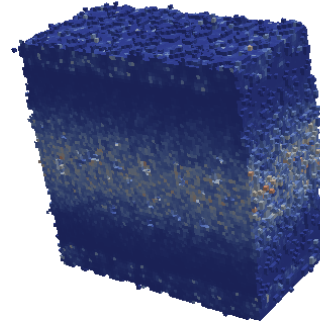


Figure 6.22: Cross sectional views of the microstructural evolution showing the development of the porous network. It is clear that the interlinked porous network forms in stages depending on the evolution of the defect concentration.

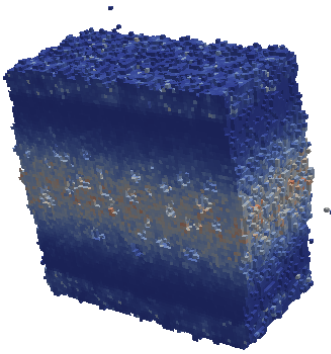
$\tau = 168 \text{ MCS}$



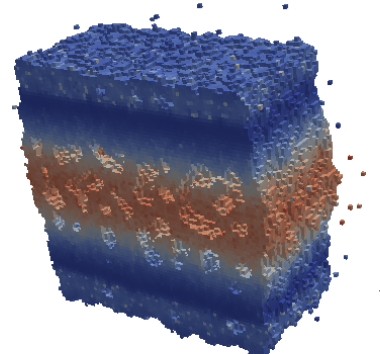
601 MCS



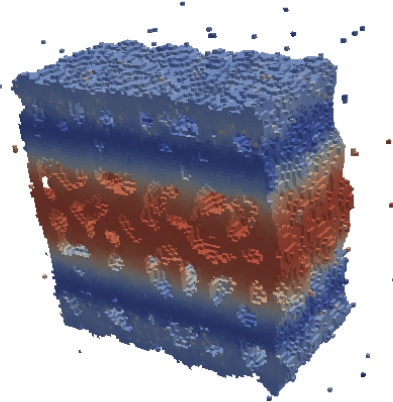
1,001 MCS



2,784 MCS



5,996 MCS



10,001 MCS

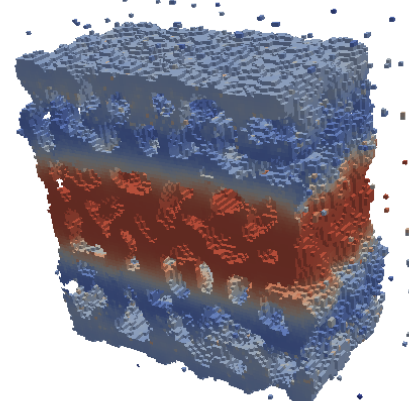


Figure 6.23: Cross sectional views of the microstructural evolution showing the vacancy compositional distribution. Since the average defect concentrations were shown to behave similarly for the uniform case, only the vacancy distribution is displayed. The defect distribution closely aligns with the radiation damage profile.

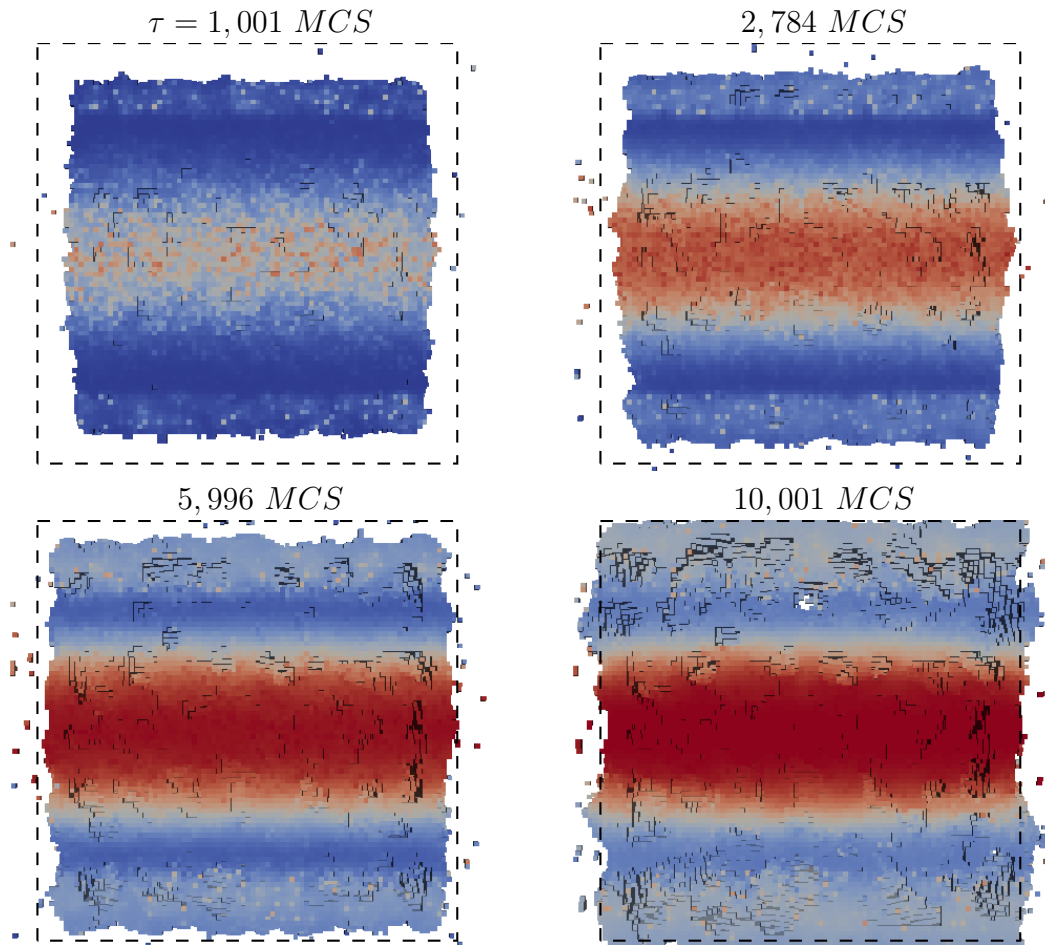


Figure 6.24: Planar views of the damaged microstructures exhibits a peculiar swelling behavior where expansion is faster in the region where the porous network forms. As the porous networks extend to the remaining region, the microstructural domain seems to reach a uniformly swollen configuration. The dashed box is fixed in location and size to compare the dimensional changes over time.

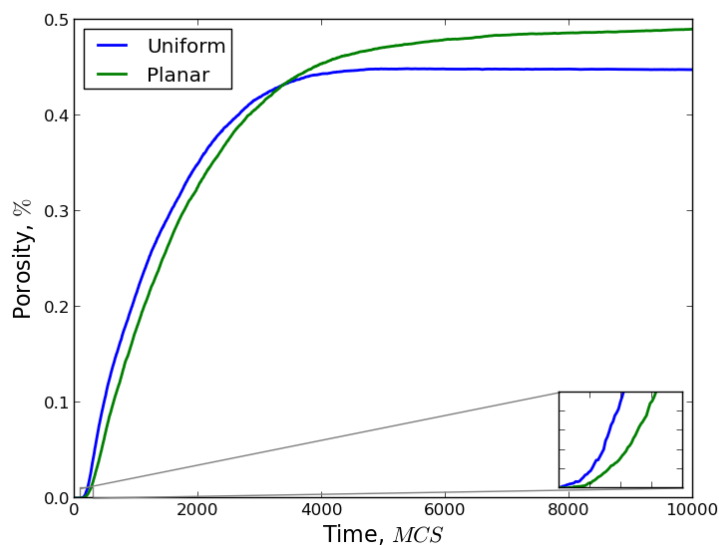


Figure 6.25: Porosity evolution is sensitive to the radiation damage distribution. An interesting observation is that while the uniform radiation seems to reach a stable configuration relatively quickly, the planar distribution does not achieve a stable microstructural arrangement.

Figure 6.25. While its increase in porosity is steadily dampened, an increase can still be measure up to 10,000 *MCS*. This can be attributed to the stage-like swelling behavior observed. These stages are: formation of a porous layer in the peak damage region; building of porous networks along the exposed surfaces; and extension of the porous regions in the low defect concentration layers.

## CHAPTER VII

### Summary

Several hybrid deterministic–statistical models were developed and applied to the study of different radiation influenced microstructural evolution in the nano–scale. These models help close the gap between the vast body of experimental work amassed on microstructural evolution of amorphized semiconductors and the shortcomings of the computational and theoretical counterparts. Developing models that are able to accurately account for the influence of radiation induced point defects on microstructural evolution presents many challenges. These range from solution stability to correctly interpreting the defects’ kinetic behavior. This is especially true for the amorphized structures considered in this dissertation where, by their nature, point defects are not well defined. The work presented herein addresses this by coupling deterministic and statistical computational techniques that treat these defects as “radiation defect densities”. The developed models were tested by simulating two particular radiation influenced behavior: precipitate evolution and void swelling.

The main objective of this dissertation is the development of a model that efficiently simulates the formation of nano–porous networks. Ion irradiation of semiconductors shows that the formation of these complex structures follow a staged process: *(i)* amorphization of the irradiated matrix, *(ii)* nucleation and growth of uniform spherical voids, and *(iii)* coalescence of the smaller voids until *(iv)* growth by surface

migration takes over generating the stable nano-porous networks. There have been previous attempts to simulate the microstructural evolution behavior presented in this dissertation, but these have been unable to capture the detailed staged transitions that lead to the nano-porous structure. The ability to capture these stages was explicitly addressed in this dissertation.

The simulation results clearly show that radiation induced point defects will influence the way in which microstructures evolve. These effects are shown and discussed for two types of radiation damage behavior:

- Chapter V: Irradiation of a binary two-phase material was simulated under different radiation damage distributions and dose rates. Precipitate growth kinetics was found to become dampened as the radiation dose rates increased. This is due to diffusion of radiation point defects towards the sinks (phase interfaces), which serves as a countering mechanism to capillarity driven precipitate growth. Therefore, it was shown that with increasing dose rate the system moved away from Ostwald ripening kinetics. An important observation was that in order to form full coverage of the grain boundary by the precipitated phase, the interfacial energy must be increased. This study demonstrates that radiation induced segregation is only partially responsible for the formation of precipitated films along the grain boundaries, unlike previously suggested. Furthermore, there is experimental precedent that show interfacial energy increases as a function of dose, with increases in energies comparable to the one used in the simulation.
- Chapter VI: Nano-porous structuring of a homogeneous amorphized phase is simulated. Parameterization studies of the radiation point defect diffusivities and damage distributions were performed to understand its influence in the nano-structuring behavior. Diffusivities' magnitude and ratio was shown to be of importance in the microstructural arrangement and degree of porosity. Faster diffusing defects lead to a less porous structure as these become annihilated



before they are able to accumulate and nucleate voids. Hence, once some voids are nucleated, the newly surviving defects will more likely become annihilated at the internal and/or external free surfaces than cluster into newer voids. The damage distribution profile was shown to influence the swelling behavior and microstructural stability. The uniform irradiation damage cases were found to reach stable configurations in relatively short times, while the non-uniform case was not observed to reach a true stable microstructure. Further, the non-uniform radiation damage case leads to a staged swelling behavior where the damage peak region swells first, followed by swelling of the exposed surfaces and ending with swelling of the complete microstructure. This is attributed to the high densities of defects in the high damage zone and diffusion of these defects towards the free surfaces once a quasi-stable microstructure is reached in the peak damage region.

The main achievement of this dissertation was the development of hybrid models that are able to simulate different aspects of radiation influenced microstructural evolution. These models are able to capture evolution of the microstructures and highlight the importance of some computational parameters that influence the final stable configurations. Several irradiation parameters were explored and approaches to quantifying their influence on the microstructural evolution were demonstrated. Nonetheless, more detailed parameterization studies would be beneficial to understanding the full capabilities of these model. Finally, it should be noted that the computational techniques developed in this dissertation could be implemented into existing models to enhance their efficiency and improve generally them.

## 7.1 Future Work

The developed hybrid models were shown to capture important aspects that enable the formation of the complex radiation influenced microstructures. However, the simulations were performed in order to demonstrate their general capabilities. Therefore, the models should be further studied and qualitatively correlated to direct experimental results to verify the validity of the models. Furthermore, the porous network structuring model can benefit from the implementation of the phase field model developed to study precipitate kinetics. Some suggested future work to enhance these models are:

- *Validation:* Any computational model is only as valuable as it is able to accurately simulate real physical phenomena. These models should be validate against experimental results by applying physical parameters that correspond to true material properties, as well as the exact experimental parameters. This presents several challenges that range from lack of material properties for the amorphized semiconductors to appropriate measurements of the complex microstructures. For the former, the irradiated semiconductors' properties have been extensively studied in their crystalline state, the same does not hold true for the amorphized counterparts. For now, the crystalline properties could work as a first-order approximation. Regarding direct comparison between experimental and computational results, two methods have been suggested: void size distribution and porosity level, which should be further explored. These issues need to be address in order to achieve a fully comprehensive model. For example, the model fails to describe the main difference observed between irradiated Ge and Si.
- *Statistical Void Nucleation:* The void swelling model uses a simplified threshold mechanism to simulate void nucleation that might need to be revisited. Use of

free energy functionals, of similar form to the ones implemented on Chapter V, to describe the evolution of the system might provide a more sensitive approach to nucleating the voids. Employing a thermodynamic description will enable the use of Boltzmann statistics to drive void nucleation. This would result in a more thermodynamically rigorous nucleation scheme.

- *Sharp Interfacial Energy:* By their nature, the types of microstructures discussed in this work are often better described by sharp interfaces. The sharp interfacial energy driven flux developed and presented in Appendix E could be used to better simulate diffusional processes. As shown in Appendix E, this sharp interface description is able to properly simulate grain growth by capillarity. The need for sharp interfaces is more definite for systems with voids and/or free surfaces where the diffuse order parameters become discontinuous. Further, the more mathematically rigorous definition of the curvature, Appendix B, should be implemented.
- *Accuracy of Radiation Damage:* Radiation damage is simulated by applying Gaussian-like distributions that represent the probability of colliding and/or the average expected amount of energy deposited per collision at a given depth. An approach that would simulate a more physically analogous process could be implemented by using pre-calculated collision paths. The SRIM software could be used to tabulate a statistically significant number of BCA paths, which would then be sampled to better simulate radiation damage. This could enhance the comprehensiveness of the model as more collision relevant properties would be directly linked to the modeled radiation processes.

The models developed for this dissertation represent the first time that we have been able to computationally capture the influence of some of the kinetic parameters have on irradiated microstructural evolution, e.g. staged nucleation of nano-porous

networks in an amorphous material. Regardless, there is always room for improvement. The suggested future work would lead to improved simulations that are able to simulate the processes in a more sensible fashion. Further, implementation of the phase field approach to the void swelling model could enable the addition of other thermodynamically relevant parameters that influence the kinetics of the system. Perhaps, being able to address the question of how to manipulate Si into generating the nano-porous networks.

## APPENDICES

## APPENDIX A

### Evolution Equations for a Quaternary System

Several of the thermodynamic concepts utilized in the development of the models presented in this thesis arrive from mathematical and/or physical principles. This appendix shows the full derivation of some of the more important concepts that lead to the derivation of important equations that describe behavior like the phenomenological equations. These have been developed for a quaternary system.

#### A.1 Regular Solution Equation for a Ternary System

One of the more common thermodynamical descriptions for the energy of mixing is given by the *regular solution equation*. This is an equation that moderately deviates from the ideal solution. Furthermore, it is used in the development of radiation-induced segregation model's entropic energy term. Defining the entropy as

$$\Delta S = k_B \ln Z \tag{A.1}$$

where the partition function is dependent on all the species present  $Z = f(N_1, N_2, N_3, N_4)$  and  $N = N_1 + N_2 + N_3 + N_4$ . The partition function is given by

$$Z = \frac{N!}{N_1!N_2!N_3!N_4!} = \frac{N!}{N_1!N_2!N_3!(N - N_1 - N_2 - N_3)!} \quad (\text{A.2})$$

which gives

$$\Delta S = k_B [\ln N! - \ln N_1! - \ln N_2! - \ln N_3! - \ln(N - N_1 - N_2 - N_3)!] \quad (\text{A.3})$$

Using the approximation  $\ln x! \approx x \ln x - x$  and rearranging the parameters, we have

$$\begin{aligned} \Delta S &= k_B [N \ln N - N - N_1 \ln N_1 + N_1 - N_2 \ln N_2 + N_2 - N_3 \ln N_3 + N_3 \\ &\quad - (N - N_1 - N_2 - N_3) \ln(N - N_1 - N_2 - N_3) + (N - N_1 - N_2 - N_3)] \\ &= -k_B N \left[ \frac{N_1}{N} \ln \left( \frac{N_1}{N} \right) + \frac{N_2}{N} \ln \left( \frac{N_2}{N} \right) + \frac{N_3}{N} \ln \left( \frac{N_3}{N} \right) \right. \\ &\quad \left. + \frac{N - N_1 - N_2 - N_3}{N} \ln \left( \frac{N - N_1 - N_2 - N_3}{N} \right) \right] \end{aligned} \quad (\text{A.4})$$

Since the concentration can be defined as the fraction of a species present in the system,

$$C_i = \frac{N_i}{N}$$

and the entropy can be rewritten as

$$\begin{aligned} \Delta S &= -k_B N [C_1 \ln C_1 + C_2 \ln C_2 + C_3 \ln C_3 \\ &\quad + (1 - C_1 - C_2 - C_3) \ln(1 - C_1 - C_2 - C_3)] \end{aligned} \quad (\text{A.5})$$

For a binary system where the interstitials and vacancies are considered to be atomic entities, this definition of the entropy can be used for the Gibbs free energy, which

gives

$$\begin{aligned}\Delta G &= \Delta H - T\Delta S \\ &= (E_i^f C_i + E_v^f C_v + C_a C_b \omega_{ab}) + Tk_B N [C_i \ln C_i + C_v \ln C_v + C_b \ln C_b \\ &\quad + (1 - C_i - C_v - C_b) \ln(1 - C_i - C_v - C_b)]\end{aligned}\quad (\text{A.6})$$

where  $E^f$  is the formation energy,  $\omega_{ab}$  is the interaction parameter between  $A$  and  $B$  atoms and

$$C_a = 1 - C_i - C_v - C_b.$$

This equation can then be employed in the calculation of the equation of state as shown in Chapter V.

## A.2 Derivation of the True Chemical Potential

Usually one can find in the literature that the chemical potential is defined simply as the slope of the bulk free chemical energy, i.e.  $\mu = \partial G / \partial C$ . Under conditions where the system consists of multiple components and phases, this definition does not fully describe the driving force of the system. The derivation presented here is based on the derivation by *Lupis* [86]. If the system has a total of  $N = \sum_{i=1}^n N_i$  moles, the total free energy is defined by the molar free energy

$$G = NG_m. \quad (\text{A.7})$$

For convenience, it is desired to change the molar free energy definition into molar fraction terms since materials properties are generally analyzed as such

$$G_m \equiv G_m(N_i, N_j, \dots, N_n) \equiv G_m(N, C_i, \dots, C_{n-1}) \quad (\text{A.8})$$



where the  $C_i$ 's are molar fractions of each  $i$  component. Applying the true thermodynamic definition of the chemical potential, we have

$$\mu_i = \frac{\partial G}{\partial N_i} = G_m \left( \frac{\partial N}{\partial N_i} \right)_{N_n} + N \left( \frac{\partial G_m}{\partial N_i} \right)_{N_n} \quad (\text{A.9})$$

where  $\partial N / \partial N_i = 1$  and  $N_i \neq N_n$ . The second term on the right hand side of Equation A.9 clearly will depend on the number of species  $n$  present. As an example, let's consider the quaternary system from before

$$G_m = G_m(N, C_i, C_v, C_b). \quad (\text{A.10})$$

Employing the chain rule, the last term of the right hand side of Equation A.9 can be rewritten in generic terms (here shown for interstitials)

$$\begin{aligned} \left( \frac{\partial G_m}{\partial N_i} \right)_{N_v, N_b} &= \left( \frac{\partial G_m}{\partial C_i} \right)_{N, C_v, C_b} \left( \frac{\partial C_i}{\partial N_i} \right)_{N_v, N_b} + \left( \frac{\partial G_m}{\partial C_v} \right)_{n, C_i, C_b} \left( \frac{\partial C_v}{\partial N_i} \right)_{N_v, N_b} \\ &+ \left( \frac{\partial G_m}{\partial C_b} \right)_{N, C_i, C_v} \left( \frac{\partial C_b}{\partial N_i} \right)_{N_v, N_b} + \left( \frac{\partial G_m}{\partial N} \right)_{C_i, C_v, C_b} \left( \frac{\partial N}{\partial N_i} \right)_{N_v, N_b} \end{aligned} \quad (\text{A.11})$$

Combining Equations A.9 and A.11, and since  $G_m$  only depend on the concentration and not the system size, i.e.  $\partial G_m / \partial N = 0$ , and recognizing that

$$\left( \frac{\partial C_j}{\partial N_i} \right)_{N_k} = \frac{\partial}{\partial N_i} \left( \frac{N_j}{N} \right) = \frac{\delta_{ij} N - N_j}{N^2} = \frac{\delta_{ij} - C_j}{N}, \quad (\text{A.12})$$

the chemical potential of species  $i$  can be written in a general form as

$$\mu_i = G_m + \sum_{j=1}^{n-1} (\delta_{ij} - C_j) \left( \frac{\partial G_m}{\partial C_j} \right)_{N, C_k} \quad (\text{A.13})$$

where  $\delta_{ij}$  is the Kronecker delta and  $C_k$  stands for all the species' concentrations that are being held constant. For the quaternary system, the true chemical potential for

each species is given by

$$\mu_i = G_m + (1 - C_i) \left( \frac{\partial G_m}{\partial C_i} \right)_{N, C_v, C_b} - C_v \left( \frac{\partial G_m}{\partial C_v} \right)_{N, C_i, C_b} - C_b \left( \frac{\partial G_m}{\partial C_b} \right)_{N, C_i, C_v} \quad (\text{A.14a})$$

$$\mu_v = G_m - C_i \left( \frac{\partial G_m}{\partial C_i} \right)_{N, C_v, C_b} + (1 - C_v) \left( \frac{\partial G_m}{\partial C_v} \right)_{N, C_i, C_b} - C_b \left( \frac{\partial G_m}{\partial C_b} \right)_{N, C_i, C_v} \quad (\text{A.14b})$$

$$\mu_b = G_m - C_i \left( \frac{\partial G_m}{\partial C_i} \right)_{N, C_v, C_b} - C_v \left( \frac{\partial G_m}{\partial C_v} \right)_{N, C_i, C_b} + (1 - C_b) \left( \frac{\partial G_m}{\partial C_b} \right)_{N, C_i, C_v} \quad (\text{A.14c})$$

$$\mu_a = G_m - C_i \left( \frac{\partial G_m}{\partial C_i} \right)_{N, C_v, C_b} - C_v \left( \frac{\partial G_m}{\partial C_v} \right)_{N, C_i, C_b} - C_b \left( \frac{\partial G_m}{\partial C_b} \right)_{N, C_i, C_v} \quad (\text{A.14d})$$

where the dependent species has set as  $n = a$ .

### A.3 Fully Coupled Diffusional Equations

With the true definition of the chemical potential, the true driving forces can be derived. This detailed derivation is especially important when a material with multiple phases is being simulated. As show by *Balluffi, Allen and Craig Carter* [127] for a generic framework, the flux for a given species is given as a function of all the driving forces

$$J_i = J_i(F_i, F_j, F_1, \dots, F_n) \quad (\text{A.15})$$

where the  $i$  and  $j$  subscripts stand for different type of non-atomic entities and the numbered subscripts denote atomic types from 1 to  $n$  for the *conjugate* forces,  $F_i$ . If the system is near equilibrium and the driving forces are small, Equation A.15 can be expanded in a Taylor series to a first order approximation,

$$J_i(F_i, F_j, F_1, \dots, F_n) = F_i \frac{\partial J_i}{\partial F_i} + F_j \frac{\partial J_i}{\partial F_j} + F_1 \frac{\partial J_i}{\partial F_1} + \dots + F_n \frac{\partial J_i}{\partial F_n} \quad (\text{A.16})$$

and the complete system evolution is described by a coupled set of partial differential equations formed of equations identical to Equation A.16 for each component. By setting the conjugate force to be given by the negative gradient of the chemical potential, we have

$$J_i = - \sum_{j=1}^n \frac{\partial J_i}{\partial F_j} F_j = - \sum_{j=1}^n M_{ij} \nabla \mu_j. \quad (\text{A.17})$$

*Balluffi et al.* show that from rate of entropy production considerations and if the sum of the fluxes is set to be equal to zero (conservation), Equation A.17 can be restated as

$$J_i = - \sum_{j=1}^{n-1} M_{ij} \nabla (\mu_j - \mu_n) \quad (\text{A.18})$$

where  $\mu_i$  are the true chemical potentials for species  $i$  as described in Section A.2. From Fick's second law, the diffusion rate of a species  $i$  can be related to its flux as

$$\frac{\partial C_i}{\partial t} = -\nabla \cdot J_i. \quad (\text{A.19})$$

Then, combining Equations A.18 and A.19 leads to the phenomenological equations

$$\frac{\partial C_i}{\partial t} = \nabla \cdot \left[ \sum_{j=1}^{n-1} M_{ij} \nabla (\mu_j - \mu_n) \right] \quad (\text{A.20})$$

Using the true definition of the chemical potential for the quaternary system, Equation A.14, and defining the difference in chemical potentials as the *effective chemical potential*,

$$\hat{\mu}_i \equiv \mu_i - \mu_a = \delta G_m / \delta C_i,$$

a set of PDE's that define the compositional evolution of the quaternary system can be defined as

$$\frac{\partial C_i}{\partial t} = \nabla \cdot [M_{ii} \nabla \hat{\mu}_i + M_{iv} \nabla \hat{\mu}_v + M_{ib} \nabla \hat{\mu}_b] \quad (\text{A.21a})$$

$$\frac{\partial C_v}{\partial t} = \nabla \cdot [M_{vi} \nabla \hat{\mu}_i + M_{vv} \nabla \hat{\mu}_v + M_{vb} \nabla \hat{\mu}_b] \quad (\text{A.21b})$$

$$\frac{\partial C_b}{\partial t} = \nabla \cdot [M_{bi} \nabla \hat{\mu}_i + M_{bv} \nabla \hat{\mu}_v + M_{bb} \nabla \hat{\mu}_b] \quad (\text{A.21c})$$

where the inter-diffusion mobilities are symmetrical, i.e.  $M_{ij} = M_{ji}$ .

### A.3.1 Comments on the Driving Force

A common misconception is that the mobility and diffusion coefficient are simply related by

$$M = \frac{CD}{k_B T}.$$

This is true for a very specific system, but not quite applicable to multi-phase multi-component systems. Therefore, it is of interest to obtain the appropriate relationship between these parameters. For convenience, the concentration gradient and the effective chemical potential are set as the driving forces

$$J = -D \nabla C = -M \nabla \mu$$

Applying the chain rule to the effective chemical potential to change parameters and working in 1D for simplicity, the relationship between the two driving force conjugates gives

$$\nabla \hat{\mu}_i = \frac{\partial \hat{\mu}_i}{\partial x} = \frac{\partial \hat{\mu}_i}{\partial C_i} \frac{\partial C_i}{\partial x} = \frac{\partial^2 G_m}{\partial C_i^2} \nabla C_i, \quad (\text{A.22})$$

By using Fick's second law,

$$\frac{\partial C_i}{\partial t} = \nabla \cdot \left[ \sum_{j=1}^{N-1} D_{ij} \nabla C_j \right] \quad (\text{A.23})$$

and comparing Equations A.20, A.22 and A.23, the accurate relationship between the diffusivities and mobilities is found to be

$$D_{ij} = \frac{\partial^2 G_m}{\partial C_j^2} M_{ij}. \quad (\text{A.24})$$

It should be noted that for the free energy functional

$$G = g_0 + k_B T C \ln C,$$

the two parameters can be related by the simple equation  $M = CD/k_B T$ .

## APPENDIX B

### Mathematical Formulation of a Continuum Surface's Curvature

Capillarity influenced microstructural evolution can be modeled by using the curvature as a driving force. While the work presented in this dissertation uses the analogous Cahn–Hilliard equation, it has been shown that a discrete definition of the curvature can be employed to obtain equivalent results [93]. A more accurate definition can be used to describe the microstructural evolution. The main goal is to obtain a full description of the curvature as a driving force in terms of the curved surface. The derivation of the required equation to achieve this are presented here.

From level set theory, the curvature of a continuum curved surface can be defined as

$$\kappa_s = \nabla \cdot \hat{\mathbf{n}} = \nabla \cdot \left( \frac{\nabla s}{|\nabla s|} \right) \quad (\text{B.1})$$

where  $\hat{\mathbf{n}}$  is the surface normal at the location where the curvature is calculated and  $s$  is the curved surface. Applying the chain rule, the curvature is given by

$$\begin{aligned}\kappa_s &= \nabla \cdot \left( \frac{\nabla s}{|\nabla s|} \right) \\ &= \frac{|\nabla s| \nabla \cdot \nabla s - \nabla s \nabla \cdot |\nabla s|}{|\nabla s|^2} \\ &= \frac{\nabla^2 s}{|\nabla s|} - \frac{\nabla s}{|\nabla s|^2} \left( \frac{\partial}{\partial x} \hat{i} + \frac{\partial}{\partial y} \hat{j} + \frac{\partial}{\partial z} \hat{k} \right) \cdot \sqrt{\left( \frac{\partial s}{\partial x} \right)^2 + \left( \frac{\partial s}{\partial y} \right)^2 + \left( \frac{\partial s}{\partial z} \right)^2}\end{aligned}\tag{B.2}$$

For simplicity, let's consider a 1D framework, e.g.  $x \rightarrow \nabla_x$ ,

$$\begin{aligned}\frac{\partial}{\partial x} \left( \sqrt{\left( \frac{\partial s}{\partial x} \right)^2 + \left( \frac{\partial s}{\partial y} \right)^2 + \left( \frac{\partial s}{\partial z} \right)^2} \right) \hat{i} = \\ \frac{1}{2|\nabla s|} (2\nabla_x s \nabla_{xx} s + 2\nabla_y s \nabla_{xy} s + 2\nabla_z s \nabla_{xz} s) \hat{i},\end{aligned}\tag{B.3}$$

and extended into a 3D space results in,

$$\begin{aligned}\kappa_s = \frac{\nabla^2 s}{|\nabla s|} - \frac{1}{|\nabla s|^3} \left[ (\nabla_x s)^2 \nabla_{xx} s + (\nabla_y s)^2 \nabla_{yy} s + (\nabla_z s)^2 \nabla_{zz} s \right. \\ \left. + 2(\nabla_x s \nabla_y s \nabla_{xy} s + \nabla_x s \nabla_z s \nabla_{xz} s + \nabla_y s \nabla_z s \nabla_{yz} s) \right]\end{aligned}\tag{B.4}$$

where the gradient nomenclature is

$$\nabla_i = \frac{\partial}{\partial i}\tag{B.5a}$$

$$(\nabla_i)^2 = \left( \frac{\partial}{\partial i} \right)^2 = \left( \frac{\partial}{\partial i} \right) \cdot \left( \frac{\partial}{\partial i} \right)\tag{B.5b}$$

$$\nabla_{ij} = \frac{\partial}{\partial i} \left( \frac{\partial}{\partial j} \right)\tag{B.5c}$$

The conjugate driving force has been shown to be proportional to the gradient of the curvature

$$\mathbf{F}_i \propto \nabla_s \kappa_s$$

where the gradient  $\nabla_s$  is the gradient along a free surface*i*

$$\nabla_s = \nabla - \hat{\mathbf{n}}(\hat{\mathbf{n}} \cdot \nabla).$$

This should result in a more accurate calculation of the curvature [103]. Performing the mathematical operations,

$$\begin{aligned} \nabla_s \kappa_s &= \nabla \kappa_s - \hat{\mathbf{n}}(\hat{\mathbf{n}} \cdot \nabla \kappa_s) \\ &= (\nabla_x \hat{i} + \nabla_y \hat{j} + \nabla_z \hat{k}) \kappa_s - (n_x \hat{i} + n_y \hat{j} + n_z \hat{k}) (n_x \nabla_x + n_y \nabla_y + n_z \nabla_z) \kappa_s \quad (\text{B.6}) \\ &= A \hat{i} + B \hat{j} + C \hat{k} \end{aligned}$$

where

$$\begin{aligned} A &= \nabla_x \kappa_s - n_x (n_x \nabla_x \kappa_s + n_y \nabla_y \kappa_s + n_z \nabla_z \kappa_s) \\ B &= \nabla_y \kappa_s - n_y (n_x \nabla_x \kappa_s + n_y \nabla_y \kappa_s + n_z \nabla_z \kappa_s) \\ C &= \nabla_z \kappa_s - n_z (n_x \nabla_x \kappa_s + n_y \nabla_y \kappa_s + n_z \nabla_z \kappa_s) \end{aligned}$$

Finally, since the compositional evolution is proportional to the divergence of the conjugate force

$$\frac{\partial C_i}{\partial t} \propto \nabla \cdot \mathbf{F}_i \propto \nabla^2 \kappa_s,$$

which results in

$$\begin{aligned} \nabla_s^2 \kappa_s &= \nabla_s \cdot \nabla_s \kappa_s = [\nabla - \hat{\mathbf{n}}(\hat{\mathbf{n}} \cdot \nabla)] \cdot [A \hat{i} + B \hat{j} + C \hat{k}] \\ &= \left[ (\nabla_x - n_x [n_x \nabla_x + n_y \nabla_y + n_z \nabla_z]) \hat{i} + (\nabla_y - n_y [n_x \nabla_x + n_y \nabla_y + n_z \nabla_z]) \hat{j} \right. \\ &\quad \left. + (\nabla_z - n_z [n_x \nabla_x + n_y \nabla_y + n_z \nabla_z]) \hat{k} \right] \cdot [A \hat{i} + B \hat{j} + C \hat{k}] \\ &= \nabla_x A + \nabla_y B + \nabla_z C - \left[ n_x (n_x \nabla_x A + n_y \nabla_y A + n_z \nabla_z A) \right. \\ &\quad \left. + n_y (n_x \nabla_x B + n_y \nabla_y B + n_z \nabla_z B) + n_z (n_x \nabla_x C + n_y \nabla_y C + n_z \nabla_z C) \right] \quad (\text{B.7}) \end{aligned}$$



andi where the derivatives of the  $A, B$  and  $C$  parameters

$$\begin{aligned}\nabla_i A &= \nabla_{ix} \kappa_s - \nabla_i n_x (n_x \nabla_x \kappa_s + n_y \nabla_y \kappa_s + n_z \nabla_z \kappa_s) \\ &\quad - n_x (\nabla_i n_x \nabla_x \kappa_s + n_x \nabla_{ix} \kappa_s + \nabla_i n_y \nabla_y \kappa_s + n_y \nabla_{iy} \kappa_s + \nabla_i n_z \nabla_z \kappa_s + n_z \nabla_{iz} \kappa_s)\end{aligned}$$

$$\begin{aligned}\nabla_i B &= \nabla_{iy} \kappa_s - \nabla_i n_y (n_x \nabla_x \kappa_s + n_y \nabla_y \kappa_s + n_z \nabla_z \kappa_s) \\ &\quad - n_y (\nabla_i n_x \nabla_x \kappa_s + n_x \nabla_{ix} \kappa_s + \nabla_i n_y \nabla_y \kappa_s + n_y \nabla_{iy} \kappa_s + \nabla_i n_z \nabla_z \kappa_s + n_z \nabla_{iz} \kappa_s)\end{aligned}$$

$$\begin{aligned}\nabla_i C &= \nabla_{iz} \kappa_s - \nabla_i n_z (n_x \nabla_x \kappa_s + n_y \nabla_y \kappa_s + n_z \nabla_z \kappa_s) \\ &\quad - n_z (\nabla_i n_x \nabla_x \kappa_s + n_x \nabla_{ix} \kappa_s + \nabla_i n_y \nabla_y \kappa_s + n_y \nabla_{iy} \kappa_s + \nabla_i n_z \nabla_z \kappa_s + n_z \nabla_{iz} \kappa_s).\end{aligned}$$

From examining these equations, there are three general operators to consider:  $\nabla_i$ ,  $\nabla_{ii} = \nabla_i^2$  and  $\nabla_{ij}$ . These can be numerically approximated by

$$\begin{aligned}\nabla_i f &= \frac{\partial f}{\partial i} = \frac{f(i) - f(i - \Delta i)}{\Delta i} \\ \nabla_{ii} f &= \frac{\partial^2 f}{\partial i^2} = \frac{f(i) - 2f(i - \Delta i) + f(i - 2\Delta i)}{(\Delta i)^2} \\ \nabla_{ij} f &= \frac{\partial^2 f}{\partial i \partial j} = \frac{f(i \pm \Delta i, j \pm \Delta j) - f(i \pm \Delta i, j) - f(i, j \pm \Delta j) + f(i, j)}{(\pm \Delta i) \cdot (\pm \Delta j)}\end{aligned}$$

where all of these have  $\mathcal{O}(h)$ . These approximations are considered since at the surface the continuum parameter  $s$  would become discontinued in at least one direction. For example, the  $x$ -component of the normal could be approximated as

$$\begin{aligned}n_x &= \frac{\nabla_x s}{\sqrt{(\nabla_x s)^2 - (\nabla_y s)^2 + (\nabla_z s)^2}} \\ &= \frac{s_i - s_{i-1}}{\sqrt{(s_i - s_{i-1})^2 + (s_j - s_{j-1})^2 + (s_k - s_{k-1})^2}}\end{aligned}\tag{B.8}$$

## APPENDIX C

### Comments on Numerical Approximation to the Phenomenological Equations

The models developed in this dissertation that incorporate diffusion due to a chemical potential force make use of a computational approximation. Instead of using the complete differentiation of the free energy functionals, an approximation is used where the individual slopes are considered. Hence, the phase dependence is only approximated by taking the slope of each curve into consideration. This approach was found to yield comparable results and slightly improve the computational efficiency. Nonetheless, the full derivation of the phase dependent chemical potentials is shown here for completeness.

Let's consider a phase dependent free energy functional that is defined by the Cahn–Hilliard equation as

$$F = \int_{\mathcal{V}} \left( G + \frac{\gamma}{2} |\nabla C|^2 \right) dV \quad (\text{C.1})$$

where  $G$  is a function of both the concentration,  $f(C)$ , and the thermodynamic phase,  $g(q)$ . A general description of the concentration and phase dependent free energy is

given by

$$G = \sum_{i=1}^N f(C_i)g(q_i) = \sum_{i=1}^N f_i g_i \quad (\text{C.2})$$

where  $f_i$  is the energy stored within a voxel and  $g_i$  is the thermodynamic state corresponding to site  $i$ . From Appendix A, it is clear that the compositional evolution is given by the effective chemical potential, which is related to the change in free energy as a function of concentration. Hence, applying concepts from variational calculus, we have

$$\frac{\partial C}{\partial t} = \nabla \cdot \left[ M \nabla \left( \frac{\delta F}{\delta C} \right) \right] = \nabla \cdot \left[ M \nabla (g(q) \cdot f'(C) - \gamma \nabla^2 C) \right] \quad (\text{C.3})$$

where  $F$  is the free energy functional and  $f'(C) \equiv f' \equiv \delta f(C)/\delta C$  is the variational derivative of  $f$  with respect to  $C$ . Applying the chain rule and assuming a constant mobility and interfacial gradient energy parameters, we get

$$\frac{\partial C}{\partial t} = M \left[ g \nabla^2 f' + 2 \nabla f' \cdot \nabla g + f' \nabla^2 g - \gamma \nabla^4 C \right] \quad (\text{C.4})$$

where both the free energy and phase are dependent on the simulation space. It is obvious that the actual evolution of the concentration does depend on the gradients of both concentration and phase order parameter. However, as mentioned before and corroborated by the different implementation presented in this dissertation, the diffusion equations can be approximated by omitting the phase gradients. This does introduce an error by propagating the original truncation error, but this error seems to be negligible. For the sake of completeness, the full discretization of this equation has been worked out.

For simplicity, let's re-write Equation C.4 in a one-dimensional form

$$\frac{\partial C}{\partial t} = M \left[ g \frac{\partial^2 f'}{\partial x^2} + 2 \frac{\partial f'}{\partial x} \frac{\partial g}{\partial x} + f' \frac{\partial^2 g}{\partial x^2} - \gamma \frac{\partial^4 C}{\partial x^4} \right]. \quad (\text{C.5})$$

As outlined in Section 4.2, we can use the FTCS scheme to numerically solve this equation, which gives

$$\frac{C_i^{t+1} - C_i^t}{\Delta t} = M \left[ g_i^t \frac{f_{i+1}^t - 2f_i^t + f_{i-1}^t}{h^2} + 2 \frac{f_{i+1}^t - f_{i-1}^t}{2h} \cdot \frac{g_{i+1}^t - g_{i-1}^t}{2h} + f_i^t \frac{g_{i+1}^t - 2g_i^t + g_{i-1}^t}{h^2} - \gamma \frac{C_{i+2}^t - 4C_{i+1}^t + 6C_i^t - 4C_{i-1}^t + C_{i-2}^t}{h^4} \right] \quad (\text{C.6})$$

For programming purposes, a convenient approach to rearranging this equation is to consider “fluxes” across the digitized element interfaces, i.e. 4 edges for 2D pixels and 6 faces for 3D voxels. Therefore, in a similar way to the one shown in Section 4.2.1, a *net* flux is defined as

$$\mathbf{J}_{n \Rightarrow i} = J_n - J_i \quad (\text{C.7})$$

where the  $J$ 's are the flux contribution from the neighbor ( $n$ ) or the site of interest ( $i$ ). For example, in the model implementation presented in Chapter V, these  $J$ 's are taken to be the slope of the polynomial curves. Applying this idea to Equation C.6, it can be re-written in the form of sums with some changes in notation for clarity, which can be directly applied to the computational algorithm

$$\frac{C_i^{t+1} - C_i^t}{\Delta t} = \frac{M}{h^2} \sum_{i=1}^D \left[ \sum_{\Delta}^{\{-1,1\}} \left( g_i^t (f_{i+\Delta}^t - f_i^t) + \frac{f_{i+\Delta}^t \cdot g_{i+\Delta}^t - f_{i+\Delta}^t \cdot g_{i-\Delta}^t}{2} + f_i^t (g_{i+\Delta}^t - g_i^t) - \gamma \frac{C_{i+2\Delta}^t - 4C_{i+\Delta}^t + 3C_i^t}{h^2} \right) \right] \quad (\text{C.8})$$

where  $D$  is the dimension and  $\Delta$  is the discretization direction with a value of  $\pm 1$ . This discretization is a suggested approach that has been found to be very efficient, but there are many other ways that these complex equations could be discretized.

## APPENDIX D

### Pseudocode and Output Data Layout

This section shows the a general idea of the C++ algorithms that were employed in the simulation of the radiation damage effects. The algorithms are implemented on the SPPARKS framework as *run alone* applications. The main algorithm for the hybrid Potts–phase field (hPPF) model is presented here. Similar variations run the other models developed under this dissertation.

The most important output file are known as “dump” files. These files provide importan data like the spin (i1), phase (i2) and concentrations (ds). These files can be altered to output the different types of SPPARKS’ defined arrays. An example is shown in Table D.1. It should be noted that when run as a parallel process the data does not necessarily output sequentially for the ID parameter.

---

**Algorithm 1** Basic algorithm of the hybrid Potts–phase field model showing the general operations followed.

---

```
BEGIN
while  $t < t_{end}$  do
  for  $i:=1$  to  $N$  do
    if  $\mathcal{RN} < \omega_{gg}$  then
      Adopt random neighbor spin
      if  $\Delta F \leq 0$  then
        Accept
      else if  $T > 0$  then
        Following Boltzmann statistics
        if  $\mathcal{RN} < \exp(-\Delta F/k_B T)$  then
          Accept
        end if
      else
        Reject
      end if
    else
      Continue
    end if
  end for
  for  $i:=1$  to  $N$  do
    Calculate new  $C$ 
     $C_{new} \leftarrow$  forward–time central–space solution
  end for
  for  $i:=1$  to  $N$  do
    Update  $C$ 
     $C^{t+1} \leftarrow C_{new}$ 
  end for
end while
```

---

Table D.1: Typical dump output file. This dump file outputs data showing the site ID,  $x, y$  and  $z$  position, spin, and vacancies and interstitials concentrations for a SPPARKS' time of  $\sim 168$  MCS. The values correspond to the frame region.

```

ITEM:                TIMESTEP
15                   168.42
ITEM:                NUMBER OF ATOMS
1000000
ITEM:                BOX BOUNDS
0                    100
0                    100
0                    100
ITEM: ATOMS id      x  y  z  i1  d1  d2
1  0  0  0  -1  0  0
2  1  0  0  -1  0  0
3  2  0  0  -1  0  0
4  3  0  0  -1  0  0
5  4  0  0  -1  0  0
6  5  0  0  -1  0  0
7  6  0  0  -1  0  0
8  7  0  0  -1  0  0
9  8  0  0  -1  0  0
10 9  0  0  -1  0  0
  ⋮ ⋮ ⋮ ⋮ ⋮ ⋮ ⋮

```

## APPENDIX E

### Sharp Interface hybrid Potts–phase field

This appendix presents the development of a hybrid model for sharp interfacial driven microstructural evolution. Capillarity driven diffusion is simulated with the implementation of a discrete curvature parameter developed. The full description and development of the model is presented here and appeared in the journal *Scripta Materialia* [93]. In fact, the description provided here is more detailed than the one presented in the journal.

#### E.1 Scripta Materialia: Manuscript

Many microstructural evolution processes have been simulated by the Cahn–Hilliard (CH) based phase field model. The Cahn–Hilliard equation was originally developed to model spinodal decomposition [64] of glass with interfacial energy introduced by a gradient in the composition of the glass. Since then, many have adapted this to simulate a wide range of microstructural evolution mechanisms with “order parameters” introduced by *Khachaturyan* [59] to represent many other materials characteristics, such as grains and precipitates with a gradient in the parameters representing the interfaces. Recently, *Homer et. al.* [88, 89, 90] introduced a hybrid Potts–Phase field (hPPF) model, which uses both the Cahn–Hilliard (CH) smoothly



varying interfacial energy and the Potts sharp interfacial energy terms to calculate the interfacial energy. In this work, we show that the CH–interfacial energy term can be eliminated; we can determine the interfacial energy the sharp interface between discrete particle and the bulk free energy by the compositional field. We will compare our results to those of the hPPF model, which has been extensively studied. The benefit of such a model is that it affords direct control over the thermodynamics of interfaces. The interfaces between microstructural features is a sharp interface with the associated interfacial energy,  $\gamma S$ . Then, the bulk energy equation is a function of phase and composition.

Several types of computational techniques have been used to model the evolution of microstructures, e.g. Potts Monte Carlo (PMC) and phase field (PF) models. The former uses a discretized ensemble of particles, while the latter uses continuum fields, or order parameters, to define the microstructure. Hence, the PMC and PF models have sharp and diffuse interfaces, respectively. While these models have been extensively used for different types of microstructural evolution, both have intrinsic drawbacks. The PMC model struggles to simulate smoothly varying continuous fields like concentrations. While, in order to accurately capture diffuse interface evolution, the PF model requires a large set of coupled partial differential equations with sufficiently refined meshes. These issues can easily become prohibitively computationally expensive. Therefore, *Homer et. al.* developed the hPPF model that enables efficient and accurate simulation of microstructural evolution where microstructure is characterized by both continuous fields and discrete particles.

Many applications of the PF model uses the Cahn–Hilliard equation [64, 61, 62, 63], where the interfacial energy is a function of the gradients in the continuous fields. The hybrid model developed by *Homer et al.*, incorporates both this interfacial energy and the Potts interfacial energy. In this work, we implement a simpler, yet robust, approach to calculating the interfacial energy with more direct control over its charac-

teristics. An added benefit is the slight improvement in computational efficiency over the hPPF model under certain conditions, which itself was an improvement over the conventional PF models. In essence, our model uses a discretized curvature, where the digitized microstructure is used to calculate the interfacial energy, as opposed to gradients on the concentration field.

Our model runs in a digitized voxelated mesh with a continuum concentration field overlaid on it. The voxels are populated by an ensemble representing grain orientation and phase. The microstructure is represented by a set of discrete fields, grain id ( $s$ ) and phase ( $q$ ), and a continuum field, concentration ( $C$ ). The concentration,  $C \in \mathbb{R} : 0 \leq C \leq 1$ , defines the fraction of component A at a point in the continuum field. The grain id and phase are integer discrete values that represent the particular type of microstructural feature. We have a two-phase binary system where each phase is allowed a set of grain orientations.

The thermodynamic state of the system is given by an equation of state (EoS), which has volumetric and interfacial terms. The hPPF model uses a free energy functional that incorporates the gradient in composition term used by the CH equation and the Potts term, i.e. total number of dissimilar neighboring voxels,

$$F = \int_{\mathcal{V}} f_0 dV + \int_{\mathcal{S}} \gamma dS = \int_{\mathcal{V}} f_0 dV + \frac{\gamma_{CH}}{2} \int_{\mathcal{V}} |\nabla C|^2 dV + \gamma_{Potts} \int_{\mathcal{S}} dS \quad (\text{E.1})$$

where  $f_0$  is the bulk chemical free energy and the  $\gamma$ 's are the interfacial or surface energy. The CH term goes to zero as we move away from the interface

$$\lim_{d_{int} \rightarrow \infty} \nabla C = 0 \quad (\text{E.2})$$

where  $d_{int}$  is the distance to the sharp interface. Our model only uses the Potts term to account for the interfacial energy induced by the curved surface (curvature), which

gives us

$$F = \int_{\mathcal{V}} f_0 dV + \gamma_{Potts} \int_{\mathcal{S}} dS \quad (\text{E.3})$$

We use polynomial (quadratic) equations to describe the bulk chemical free energies

$$f = \int f_0 dV = \sum_{i=1}^N f_i(q_i) \quad (\text{E.4})$$

where  $N$  is the total number of sites (voxels) in the simulation system and each site  $i$  with  $q$ -phase stores energy

$$f_i = \begin{cases} \lambda_0 [(C - C_1)^2 + (C - C_2)^2] + \lambda_1 (C - C_3)^2, & q = \alpha \\ \lambda_0 [(C - C_1)^2 + (C - C_2)^2] + \lambda_1 (C - C_4)^2, & q = \beta \end{cases} \quad (\text{E.5})$$

where  $f_i$  is the bulk free energy for the  $\alpha$ - and  $\beta$ -phases, and the  $\lambda$ 's and  $C_i$ 's constants are the parameterization variables chosen to match the work by *Homer*, Table E.1.

The general microstructural evolution for multi-state systems has been simulated by the Potts Monte Carlo model [50], which we incorporate to calculate the sharp interfacial energy, given by

$$\int_{\mathcal{S}} \gamma_{Potts} dS \equiv J \sum_{j=1}^n (1 - \delta_{s(i)s(j)}) \quad (\text{E.6})$$

where  $J$  is the interaction energy between adjacent elements,  $N$  is the number of surrounding particles,  $\delta$  is the Kronecker delta, and  $s(i)$  and  $s(j)$  are the grain id for the  $i$  and  $j$  sites. Then, introducing Equations E.5 and E.6 to Equations E.1 and E.3, we get the following discretized equations of state

$$F_{CH,i} = \sum_{i=1}^N \left( f_0(q_i, C_i) + \frac{\gamma}{2} |\nabla C_i|^2 + J \sum_{j=1}^n (1 - \delta_{s(i)s(j)}) \right) \quad (\text{E.7})$$

$$F_{dC,i} = \sum_{i=1}^N \left( f_0(q_i, C_i) + \sum_{j=1}^n (1 - \delta_{s(i)s(j)}) \right) \quad (\text{E.8})$$

where  $N$  is the number of particles (voxels) in the simulation system.

To simulate grain growth and phase coarsening, we minimize the EoS by means of the standard Metropolis algorithm. For each site  $i$ , we choose a neighboring, site  $j$  at random, and adopt its grain id and phase. Following Boltzmann statistics, the probability of accepting the microstructural change is given by

$$P_i = \begin{cases} 1, & \Delta F_i \leq 0 \\ \exp\left(-\frac{\Delta F_i}{k_B T}\right), & \Delta F_i > 0 \end{cases} \quad (\text{E.9})$$

where  $\Delta F_i$  is the change of energy for the event calculated using Equations E.7 or E.8,  $k_B$  is the Boltzmann constant and  $T$  is the absolute simulation temperature. For the concentration evolution, we use the phenomenological equation

$$\frac{\partial C}{\partial t} = \nabla \cdot (M \nabla \mu) \quad (\text{E.10})$$

where  $\mu$  is the chemical potential and  $M$  is the mobility. The chemical potential is defined as  $\mu \equiv \delta F / \delta C$ . Incorporating Equations E.1 and E.3 into Equation E.10 and non-dimensionalizing, for the hPPF model we get

$$\frac{\partial C}{\partial \tilde{t}} = \tilde{\nabla} \cdot \left[ \tilde{\nabla} \left( \frac{\partial \tilde{f}_0}{\partial C} - \tilde{\nabla}^2 C \right) \right] \quad (\text{E.11})$$

where  $\tilde{t}$ ,  $\tilde{\nabla}$  and  $\tilde{f}_0$  are the non-dimensionalized time, spatial gradient and bulk chemical free energy, respectively. Then, for the discrete curvature model we get

$$\frac{\partial C}{\partial \tilde{t}} = \tilde{\nabla} \cdot \left[ \tilde{\nabla} \left( \frac{\partial \tilde{f}_0}{\partial C} + \tilde{\kappa} \right) \right] \quad (\text{E.12})$$

where  $\tilde{\kappa}$  is the non-dimensionalized surface curvature <sup>1</sup>.

Curvature of a continuous field is commonly defined as the divergence of the unit normal to the surface,  $\kappa = \nabla \cdot \bar{n}$ . We should note that if we define the Cahn–Hilliard interfacial energy term as  $\gamma_{CH} = -1/|\nabla C|$ , we get  $\kappa = \nabla^2 C$ , which is consistent with the common curvature definition. We define a discrete curvature that is given directly by the digitized microstructural features. The discrete curvature is defined as

$$\kappa_i = \frac{\sum_{j=1}^{n_s} (1 - \delta_{q(i)q(j)}) - n_{base}}{n_s} \quad (\text{E.13})$$

where  $n_s$  is the number of surrounding neighbors being considered on the curvature calculation <sup>2</sup> and  $n_{base}$  is the reference state that yields a curvature of zero for a flat surface

$$n_{base} = \mathcal{N}(1 + 2\mathcal{N})^{D-1} \quad (\text{E.14})$$

where  $\mathcal{N}$  is the number of neighbors “shells” and  $D$  is the simulation dimension. Similar definitions for the discretized curvature have been extensively used by Potts Monte Carlo simulations. This concept of “neighbor shells” can be explained by the sketch in Figure E.1. In this example, we have  $\mathcal{N} = 2$ , hence we look at two shells of surrounding neighbors. Then, the sum of all unlike phase neighbors gives the curvature of site  $i$ .

---

<sup>1</sup>If the energy associated to a curved surface is given by  $F = \gamma S$ , the variational energy is given by

$$\frac{\delta F}{\delta C} = \gamma \frac{\delta S}{\delta C}.$$

Adding mass to the surface leads to a change in volume,  $\delta V = 4\pi R \delta r$ , and in surface area,  $\delta S = 4\pi \delta r$ . Defining the amount of volume added per change in concentration as  $\delta V/\delta C = \Omega$  and applying the chain rule, we have

$$\frac{\delta F}{\delta C} = \gamma \Omega \frac{4\pi \delta r}{4\pi R \delta r} = \frac{\gamma \Omega}{R} \equiv \gamma \Omega \kappa.$$

We should also point out that in order to accurately compare the two models, we scaled the normalized curvature by 1/10 as to obtain comparable interfacial kinetics.

<sup>2</sup>The number of sites accounted for the curvature calculation can be computed by

$$n_s = (1 + 2\mathcal{N})^D - 1.$$

To test our model, we compare its performance to that of the hPPF model. The first tests consist of computing the compositional evolution of an initially stoichiometric matrix–precipitate system, and compare our model to the hPPF model. We do not allow growth or shrinkage of the precipitate such that the effect of interfacial (curvature) energy on compositional evolution can be evaluated. Figure E.3 shows the concentration profile after the system reaches equilibrium under these conditions. As we can see, the discretized curvature is able to accurately simulate the compositional evolution and is comparable to the hPPF model. We should point out that under these conditions, the hPPF model is identical to a single order parameter CH model.

We performed a more complex simulation of grain growth controlled by diffusion–limited kinetics in order to verify that the model maintains its accuracy as the microstructural evolution scales in complexity. The simulations were run at a finite temperature,  $k_B T = 0.3$  to avoid grain growth pinning effects. The microstructural evolution can be easily appreciated from Figure E.4 where we illustrate both grain growth and compositional evolution. Grain growth curves obtained from the hPPF model are compared to those from our model for shells  $\mathcal{N} = 1$  and  $2$  in Figure E.5. The grain growth is virtually identical for all three cases. By fitting the data to the grain growth equation,  $\bar{R} = (mt + R_0^n)^{1/n}$ , we obtained a grain growth exponent of  $n = 3$  for all three simulations, as shown in Table E.2. This grain growth exponent  $n = 3$  is characteristic of diffusion–controlled Ostwald ripening–like grain growth kinetics. Since  $\mathcal{N} = 1$  and  $\mathcal{N} = 2$  give virtually identical results, the additional computational expense of considering more neighbors for the curvature calculations is not necessary.

Finally, we also simulated the evolution of a polycrystalline material in a 3D system. Figure E.6 shows the concentration and microstructural (grain orientation) evolution of an initially randomly oriented microstructure. It is evident that our method

is able to simulate this type of realistic microstructural evolution while preserving the correct physics and kinetics of the system.

## Conclusion

We have shown that using the discretized curvature approach with continuum thermodynamic description of the bulk energy is accurate and robust for simulation of microstructural evolution. It has been successfully applied to continuum thermodynamic and kinetic equations to simulate microstructural evolution by capillarity. The implementation of the discretized curvature to the deterministic–statistical hybrid model is able to improve the computational efficiency slightly without compromising the physics. When compared to the hPPF model, and it was shown to yield some computational savings while retaining the correct kinetics and physics, especially for the  $\mathcal{N} = 1$  case. More importantly, we showed that the discretized curvature approach grants us a direct method for calculating the thermodynamic state, rather than using the CH, which was originally developed for spinodal decomposition. Furthermore, a limit to the efficiency enhancement and applicability was shown to depend on the microstructural physics. Lastly, we showed that the model is robust and can be extended to a 3D scheme and more complex microstructural evolution scenarios.

## Acknowledgement

Sandia National Laboratories is a multi–program laboratory managed and operated by Sandia Corporation, a wholly owned subsidiary of Lockheed Martin Corporation, for the U.S. Department of Energy’s National Nuclear Security Administration under contract DE–AC04–94AL85000.

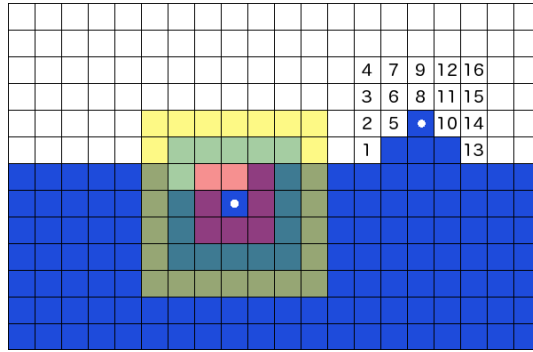


Figure E.1: Sketch illustrating methodology used to calculate discrete curvature. The lower-left white dot shows the concept of neighbor shells, where each color surrounds the neighbors considered for a given  $\mathcal{N}$ -shell: red corresponds to 8 neighbors ( $\mathcal{N} = 1$ ), green to 24 ( $\mathcal{N} = 2$ ) and yellow to 48 ( $\mathcal{N} = 3$ ). For  $\mathcal{N} = 2$ , the curvature of the upper-right white dot is proportional to 16, which gives  $\kappa = 0.25$  calculated using Equation E.13.

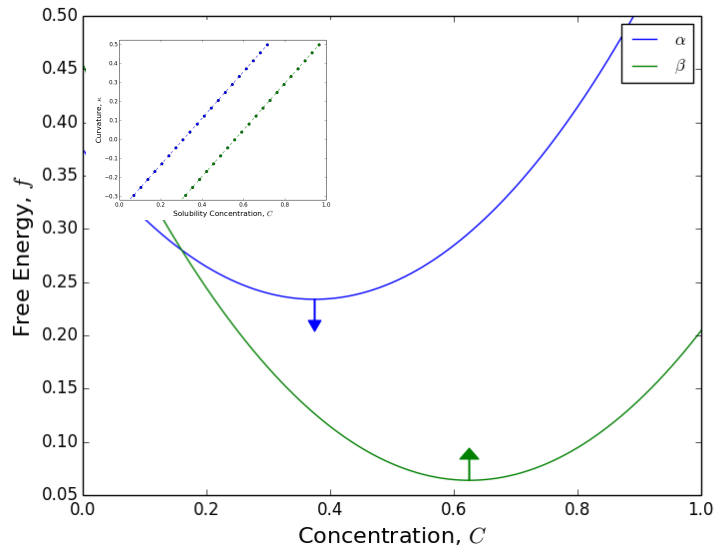


Figure E.2: Free energy curves for the minimum curvature configuration. As the curvature changes, these curves move and the solubility changes (insert for  $\mathcal{N} = 2$ )



Table E.1: Numerical values of the model’s parameterization variables used in the presented simulations.

Parameterization Variable	$C_1$	$C_2$	$C_3$	$C_4$	$\lambda_0$	$\lambda_1$
Values	0.25	0.75	0.05	0.95	0.3	0.5

Table E.2: Summary of the grain growth exponential inverse,  $1/n$ , for the hPPF model and a series of discrete curvature calculations with varying  $\mathcal{N}$ .

hPPF	$\mathcal{N}$		$\mathcal{N}_{3D} = 1$
	1	2	
0.350	0.337	0.345	0.386

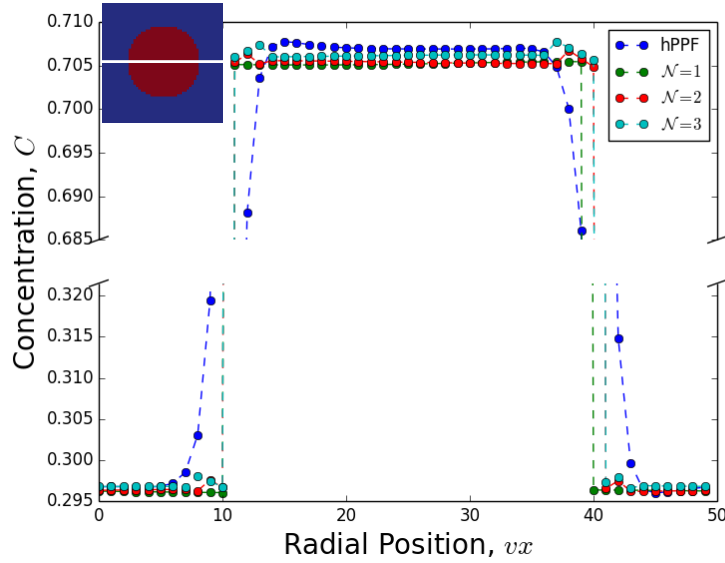


Figure E.3: Concentration profile for the matrix–precipitate (insert) system after equilibrium has been reached. The concentration is taken across the center of the precipitate, as shown by the white line in the insert. The concentration at the interfaces for all cases are very similar and is highlighted by the high resolution of the y–axis.

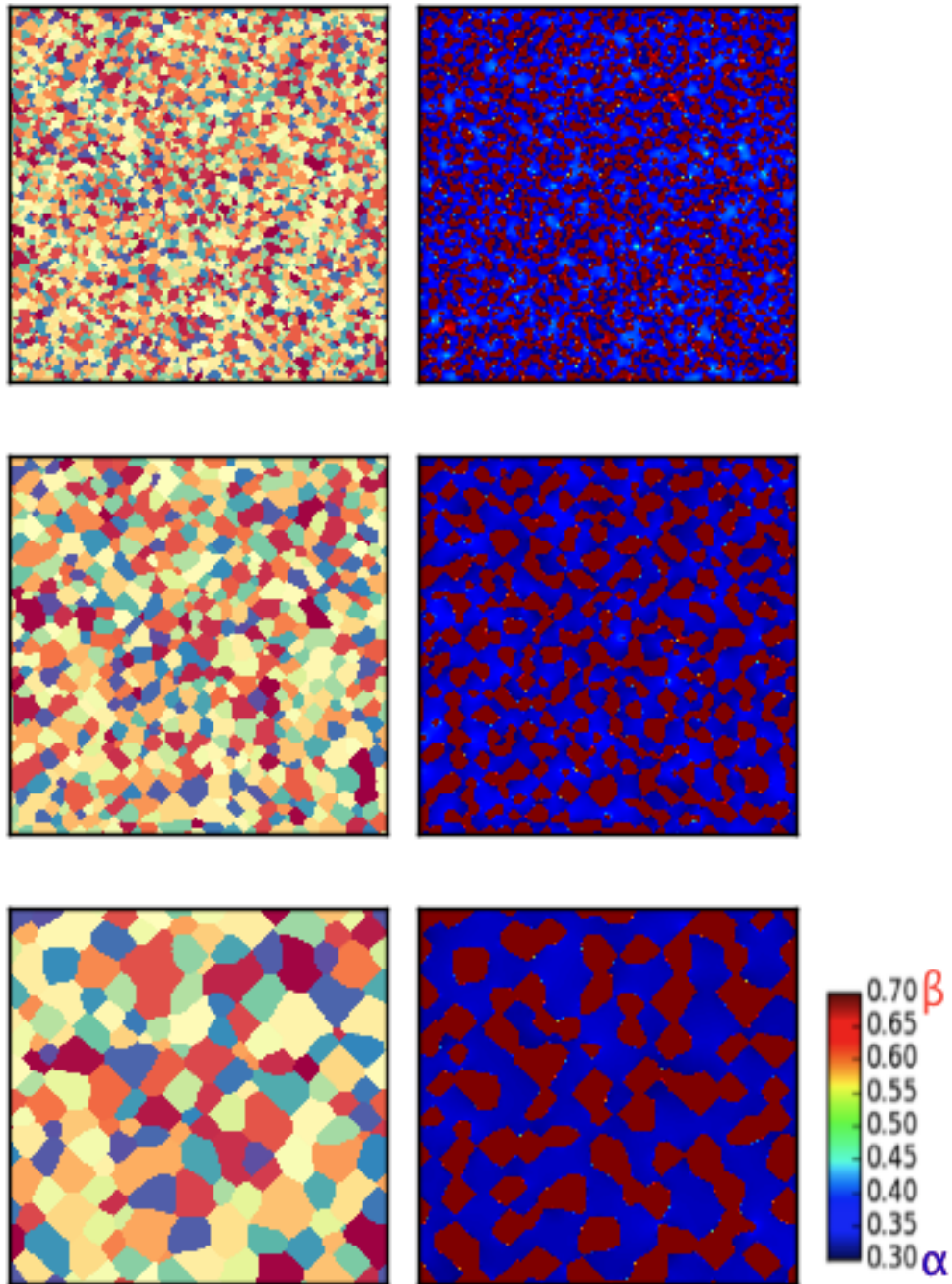


Figure E.4: Microstructural evolution showing grain growth on the left, and concentration evolution and coarsening of the  $\alpha$  (blue) and  $\beta$  (red) phases on the right for the  $\mathcal{N} = 1$  case. We show the spin and concentration distributions for: (top to bottom)  $t = 464, 4640$  and  $46416$  *MCS*.

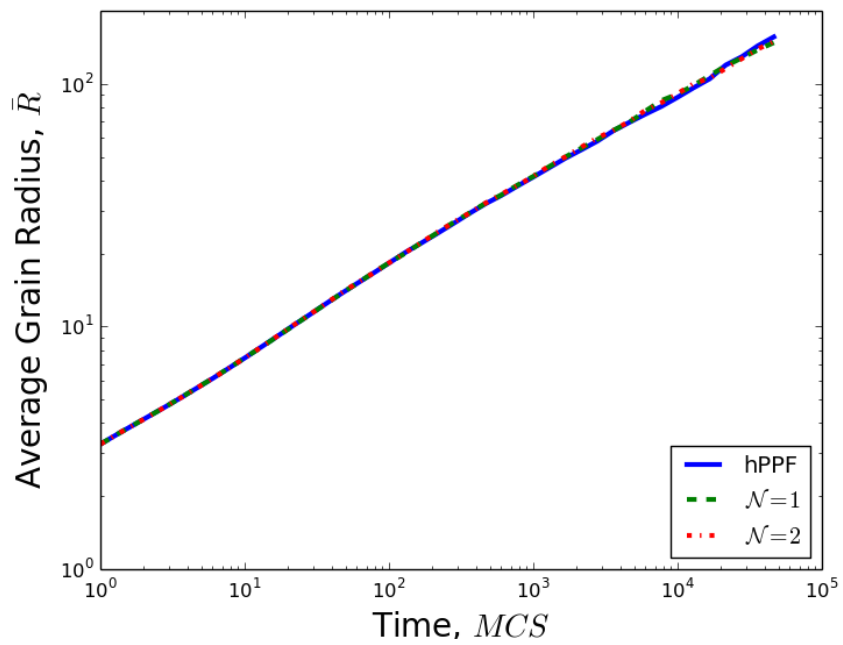


Figure E.5: Grain growth curves for hPPF and our simplified model with shells  $\mathcal{N} = 1$  and 2. We can see that all three curves are virtually identical.

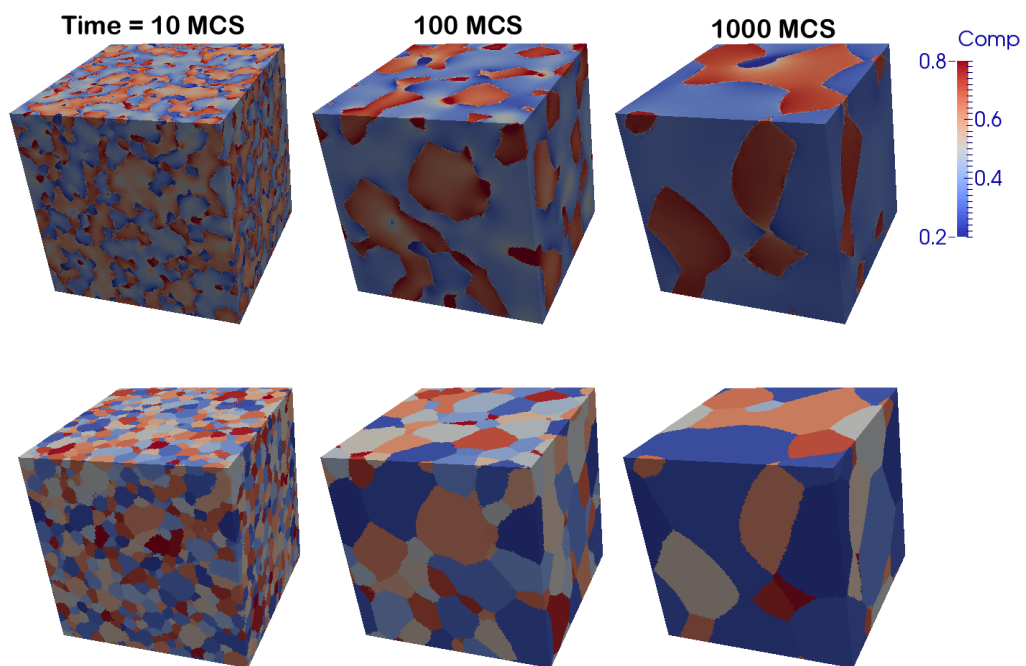


Figure E.6: 3D simulation of a polycrystalline microstructural evolution using the discrete curvature definition ( $\mathcal{N}_{3D} = 1$ ). The top figures show the concentration evolution, while the bottom shows the microstructural (grain id) evolution. The grain growth exponential was found to be in good agreement with the 2D cases, Table E.2.

## APPENDIX F

### Comments on the Dependence of *Fiber* Diameter on Diffusivity

This section compares the self diffusivities of semiconductors that are known to generate nano-porous/fibrous structures when irradiated by high energy ions.

From Perez-Bergquist's dissertation [27], Figure F.1, the size for several experimental results are plotted as a function of fluence. A clear trend observed is that the Ge samples resulted in slightly smaller *fibers/walls*. If we consider the diffusivities of Ge and GaSb, Figure F.2, we can see that Ge self diffusion is expected to be much slower than diffusion in GaSb. Figure F.2 shows the calculated self diffusivities for a wide range of temperatures. These were plotted assuming that the diffusivities follow the Arrhenius equation and with data from [128]. This qualitatively agrees with the computational results as it was shown that slower diffusion is needed in order to create the nano-porous structures.

Lastly, it must be noted that these diffusivities correspond to crystalline materials, which likely do not apply to the amorphized states. Nonetheless, due to lack of the amorphized state data, these values can be used as a first order approximations.

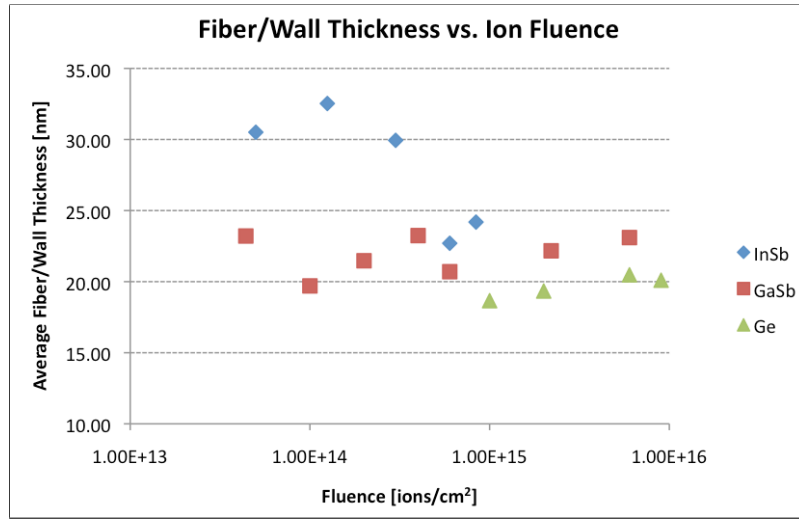


Figure F.1: Fiber or cell wall thickness as a function of ion fluence for InSb, GaSb, and Ge irradiated with 1 MeV Au+ ions.

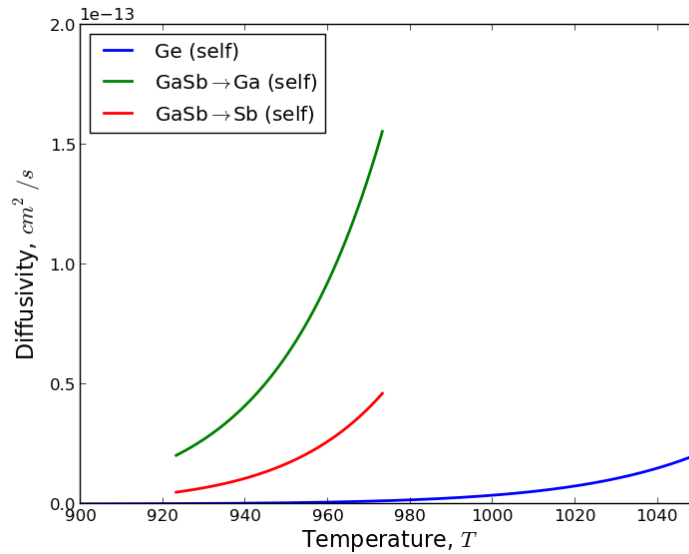


Figure F.2: Self diffusivities for crystalline Ge and GaSb as a function of temperature.

## BIBLIOGRAPHY

## BIBLIOGRAPHY

- [1] V. Schmidt, J. V. Wittemann, S. Senz, and U. Gsele, “Silicon nanowires: A review on aspects of their growth and their electrical properties,” *Advanced Materials*, vol. 21, no. 25-26, pp. 2681–2702, 2009.
- [2] P. Sigmund, “Sputtering by ion bombardment theoretical concepts,” in *Sputtering by Particle Bombardment I* (R. Behrisch, ed.), vol. 47 of *Topics in Applied Physics*, pp. 9–71, Springer Berlin Heidelberg, 1981.
- [3] M. Nastasi, J. Mayer, and J. Hirvonen, *Ion-Solid Interactions: Fundamentals and Applications*. Cambridge Solid State Science Series, Cambridge University Press, 1996.
- [4] P. Sigmund, “Theory of sputtering. i. sputtering yield of amorphous and polycrystalline targets,” *Phys. Rev.*, vol. 184, pp. 383–416, 1969.
- [5] J. F. Ziegler, J. P. Biersack, and M. D. Ziegler, *The Stopping and Range of Ions in Matter*. LuLu Press Co., 2008.
- [6] M. Nastasi and J. Mayer, “Surface erosion during implantation: Sputtering,” in *Ion Implantation and Synthesis of Materials*, pp. 159–178, Springer Berlin Heidelberg, 2006.
- [7] H. Andersen and H. Bay, “Sputtering yield measurements,” in *Sputtering by Particle Bombardment I* (R. Behrisch, ed.), vol. 47 of *Topics in Applied Physics*, pp. 145–218, Springer Berlin Heidelberg, 1981.
- [8] N. Lam and H. Wiedersich, “Bombardment-induced segregation and redistribution,” *Nuclear Instruments and Methods in Physics Research Section B: Beam Interactions with Materials and Atoms*, vol. 18, no. 1–6, pp. 471–485, 1986.
- [9] H. Wiedersich, H. Andersen, N. Lam, L. Rehm, and H. Pickering, “Surface modification and alloying by laser, ion, and electron beams,” in *NATO conference series: Materials science* (J. Poate, G. Foti, and D. Jacobson, eds.), p. 261, Published in cooperation with NATO Scientific Affairs Division [by] Plenum Press, 1983.
- [10] Z. Liau and J. Mayer, *Ion bombardment effects on material composition*, vol. 18 of *Treatise on Materials Science and Technology*. Academic Press, 1980.



- [11] G. S. Was, *Fundamentals of Radiation Materials Science: Metals and Alloys*. Berlin Heidelberg New York: Springer, 1st ed., 2007.
- [12] L. Rehn, P. Okamoto, D. Potter, and H. Wiedersich, "Effect of solute misfit and temperature on irradiation-induced segregation in binary ni alloys," *Journal of Nuclear Materials*, vol. 74, no. 2, pp. 242 – 251, 1978.
- [13] L. Kornblit and A. Ignatiev, "The size effect in radiation-induced segregation of solutes in binary metallic alloys," *Journal of Nuclear Materials*, vol. 126, no. 1, pp. 77 – 78, 1984.
- [14] P. Okamoto and H. Wiedersich, "Segregation of alloying elements to free surfaces during irradiation," *Journal of Nuclear Materials*, vol. 53, no. 0, pp. 336 – 345, 1974.
- [15] L. Rehn, "Surface Modification and Radiation-Induced Segregation," in *Symposium E Metastable Materials Formation by Ion Implantation*, vol. 7 of *MRS Proceedings*, 1 1981.
- [16] R. C. Ewing, A. Meldrum, L. Wang, and S. Wang, "Radiation-induced amorphization," vol. 39, pp. 319–361, (in Transformation processes in minerals) Reviews in Mineralogy and Geochemistry, 2000.
- [17] W. Weber, "Models and mechanisms of irradiation-induced amorphization in ceramics," *Nuclear Instruments and Methods in Physics Research Section B: Beam Interactions with Materials and Atoms*, vol. 166167, no. 0, pp. 98–106, 2000.
- [18] P. R. Okamoto, N. Q. Lam, and L. E. Rehn, "Physics of crystal-to-glass transformations," vol. 52 of *Solid State Physics*, pp. 1–135, Academic Press, 1999.
- [19] L. M. Wang and R. Birtcher, "Radiation-induced formation of cavities in amorphous germanium," *Applied Physics Letters*, vol. 55, no. 24, pp. 2494–2496, 1989.
- [20] L. M. Wang and R. C. Birtcher, "Amorphization, morphological instability and crystallization of krypton ion irradiated germanium," *Philosophical Magazine A*, vol. 64, no. 6, pp. 1209–1223, 1991.
- [21] A. G. Perez-Bergquist, K. Sun, L. Wang, and Y. Zhang, "Formation of gasb core-shell nanofibers by a thermally induced phase decomposition process," *Journal of Materials Research*, vol. 24, no. 07, pp. 2286–2292, 2009.
- [22] S. Kluth, D. Llewellyn, and M. Ridgway, "Irradiation fluence dependent microstructural evolution of porous insb," *Nuclear Instruments and Methods in Physics Research Section B: Beam Interactions with Materials and Atoms*, vol. 242, no. 1-2, pp. 640–642, 2006.

- [23] A. G. Perez-Bergquist, K. Li, Y. Zhang, and L. Wang, “Ion irradiation–induced bimodal surface morphology changes in insb,” *Nanotechnology*, no. 32, p. 325602, 2010.
- [24] Q. Wei, J. Lian, W. Lu, and L. Wang, “Highly ordered ga nanodroplets on a gaas surface formed by a focused ion beam,” *Phys. Rev. Lett.*, vol. 100, p. 076103, 2008.
- [25] C. Cawthorne and E. Fulton, “Voids in irradiated stainless steel,” *Nature*, vol. 216, p. 575, 1967.
- [26] S. Kashibe, K. Une, and K. Nogita, “Formation and growth of intragranular fission gas bubbles in UO<sub>2</sub> fuels with burnup of 683 GWd/t,” *Journal of Nuclear Materials*, vol. 206, no. 1, pp. 22 – 34, 1993.
- [27] A. G. Perez-Bergquist, *Ion Irradiation-Induced Nanoscale Porous Structures in Semiconductors*. PhD thesis, The University of Michigan, 2010.
- [28] T. Steinbach and W. Wesch, “Porous structure formation in ion irradiated germanium,” *Nuclear Instruments and Methods in Physics Research Section B: Beam Interactions with Materials and Atoms*, vol. 319, no. 0, pp. 112 – 116, 2014.
- [29] P. G. Shewmon, “Radiation-induced swelling of stainless steel,” *Science*, vol. 173, no. 4001, pp. pp. 987–991, 1971.
- [30] L. Jenkins and A. Kirk, *Characterisation of Radiation Damage by Transmission Electron Microscopy*. Series in Microscopy in Materials Science, Taylor & Francis, 2000.
- [31] D. Olander, *Fundamental aspects of nuclear reactor fuel elements: prepared for the Division of Reactor Development and Demonstration, Energy Research and Development Administration*. ERDA Technical Information Center Series, Technical Information Center, Office of Public Affairs, Energy Research and Development Administration, 1976.
- [32] J. Brimhall, H. Kissinger, and G. Kulcinski, *EFFECT OF TEMPERATURE ON VOID FORMATION IN IRRADIATED PURE AND IMPURE METALS*. 1971.
- [33] W. Xu, Y. Zhang, G. Cheng, W. Jian, P. C. Millett, C. C. Koch, S. N. Mathaudhu, and Y. Zhu, “In-situ atomic-scale observation of irradiation-induced void formation,” *Nature Communications*, vol. 4, no. 2288, 2013.
- [34] A. Perez-Bergquist, S. Zhu, K. Sun, X. Xiang, Y. Zhang, and L. Wang, “Embedded Nanofibers Induced by High-Energy Ion Irradiation of Bulk GaSb,” *Small*, vol. 4, no. 8, pp. 1119–1124, 2008.

- [35] A. P. Alivisatos, “Semiconductor Clusters, Nanocrystals, and Quantum Dots,” *Science*, vol. 271, no. 5251, pp. 933–937, 1996.
- [36] N. G. Rudawski and K. S. Jones, “Nanostructured germanium prepared via ion beam modification,” *Journal of Materials Research*, vol. 28, no. 13, pp. 1633–1645, 2013.
- [37] B. Darby, B. Yates, N. Rudawski, K. Jones, A. Kontos, and R. Elliman, “Insights for void formation in ion-implanted ge,” *Thin Solid Films*, vol. 519, no. 18, pp. 5962 – 5965, 2011.
- [38] E. M. Bringa, J. D. Monk, A. Caro, A. Misra, L. Zepeda-Ruiz, M. Duchaineau, F. Abraham, M. Nastasi, S. T. Picraux, Y. Q. Wang, and D. Farkas, “Are nanoporous materials radiation resistant?,” *Nano Letters*, vol. 12, no. 7, pp. 3351–3355, 2012.
- [39] R. Gago, L. Vázquez, O. Plantevin, J. A. Sánchez-García, M. Varela, M. C. Ballesteros, J. M. Albella, and T. H. Metzger, “Temperature influence on the production of nanodot patterns by ion beam sputtering of si(001),” *Phys. Rev. B*, vol. 73, p. 155414, 2006.
- [40] B. Ziberi, F. Frost, and B. Rauschenbach, “Pattern transitions on ge surfaces during low-energy ion beam erosion,” *Applied Physics Letters*, vol. 88, no. 17, p. 173115, 2006.
- [41] S. Facsko, T. Dekorsy, C. Koerdt, C. Trappe, H. Kurz, A. Vogt, and H. L. Hartnagel, “Formation of ordered nanoscale semiconductor dots by ion sputtering,” *Science*, vol. 285, no. 5433, pp. 1551–1553, 1999.
- [42] S. Le Roy, E. Barthel, N. Brun, A. Lelarge, and E. Sondergard, “Self-sustained etch masking: A general concept to initiate the formation of nanopatterns during ion erosion,” *Journal of Applied Physics*, vol. 106, no. 9, pp. –, 2009.
- [43] T. Allmers, M. Donath, and G. Rangelov, “Pattern formation by erosion sputtering on gasb: Transition from dot to ripple formation and influence of impurities,” *Journal of Vacuum Science & Technology B*, vol. 24, no. 2, pp. 582–586, 2006.
- [44] K.-D. Li, A. Perez-Bergquist, Q. Wei, L. Wang, and W. Lu, “Energy-Dependant Irradiation-Induced Nanostructure Formation in Amorphous Germanium,” *Journal of Computational and Theoretical Nanoscience*, vol. 7, no. 3, pp. 522–527, 2010.
- [45] P. Sigmund, “A mechanism of surface micro-roughening by ion bombardment,” *Journal of Materials Science*, vol. 8, no. 11, pp. 1545–1553, 1973.
- [46] “Self-organized ripple and dot patterns induced by low energy ion erosion.” <http://www.hzdr.de/db/Cms?pOid=24344&pNid=2707>. Image based on Figure 3 of this article.

- [47] C. S. Madi, E. Anzenberg, K. F. Ludwig, and M. J. Aziz, “Mass redistribution causes the structural richness of ion-irradiated surfaces,” *Phys. Rev. Lett.*, vol. 106, p. 066101, 2011.
- [48] J. Venables, *Introduction to Surface and Thin Film Processes*. Cambridge University Press, 2000.
- [49] S. M. Wise, *Diffuse Interface Model for Microstructural Evolution of Stressed, Binary Thin Films on Patterned Substrates*. PhD thesis, University of Virginia, 2003.
- [50] E. A. Holm and C. C. Battaile, “The computer simulation of microstructural evolution,” *JOM*, vol. 53, no. 9, pp. 20–23, 2001.
- [51] B. Radhakrishnan, G. Sarma, and T. Zacharia, *Coupled finite element-Monte Carlo simulation of microstructure and texture evolution during thermomechanical processing*. 1998.
- [52] A. Baskaran, J. Devita, and P. Smereka, “Kinetic monte carlo simulation of strained heteroepitaxial growth with intermixing,” *Continuum Mechanics and Thermodynamics*, vol. 22, no. 1, pp. 1–26, 2010.
- [53] Y. Li, S. Hu, R. Montgomery, F. Gao, X. Sun, M. Tonks, B. Biner, P. Millett, V. Tikare, B. Radhakrishnan, and D. Andersson, “Mesoscale benchmark demonstration problem 1: Mesoscale simulations of intra-granular fission gas bubbles in UO<sub>2</sub> under post-irradiation thermal annealing,” *DOE-FCR&D-MDSM-2012-000098*, 2012.
- [54] R. B. Potts, “Some generalized order-disorder transformations,” *Mathematical Proceedings of the Cambridge Philosophical Society*, vol. 48, pp. 106–109, 1952.
- [55] E. Ising, “Beitrag zur theorie des ferromagnetismus,” *Zeitschrift fr Physik*, vol. 31, no. 1, pp. 253–258, 1925.
- [56] V. Tikare, *Numerical simulation of grain growth in liquid phase sintered materials*. PhD thesis, Case Western Reserve University, 1995.
- [57] M. Miodownik, “Monte Carlo Potts model,” in *Computational Materials Engineering* (K. G. Janssens, D. Raabe, E. Kozeschnik, M. A. Miodownik, and B. Nestler, eds.), pp. 47 – 108, Academic Press, 2007.
- [58] C. Battaile, T. Buchheit, E. Holm, M. Neilsen, and G. Wellman, *Coupled Simulations of Mechanical Deformation and Microstructural Evolution Using Polycrystal Plasticity and Monte Carlo Potts Models*. USDOE, 1999.
- [59] A. Khachaturyan, *Theory of Structural Transformations in Solids*. Dover Books on Engineering Series, Dover PublKhach, 2008.

- [60] C. K. III and L.-Q. Chen, “Computer simulation of 3-d grain growth using a phase-field model,” *Acta Materialia*, vol. 50, no. 12, pp. 3059 – 3075, 2002.
- [61] J. W. Cahn and J. E. Hilliard, “Free energy of a nonuniform system. i. interfacial free energy,” *The Journal of Chemical Physics*, vol. 28, no. 2, pp. 258–267, 1958.
- [62] J. W. Cahn, “Free energy of a nonuniform system. ii. thermodynamic basis,” *The Journal of Chemical Physics*, vol. 30, no. 5, pp. 1121–1124, 1959.
- [63] J. W. Cahn and J. E. Hilliard, “Free energy of a nonuniform system. iii. nucleation in a twocomponent incompressible fluid,” *The Journal of Chemical Physics*, vol. 31, no. 3, pp. 688–699, 1959.
- [64] J. W. Cahn, “On spinodal decomposition,” *Acta Metallurgica*, vol. 9, no. 9, pp. 795 – 801, 1961.
- [65] S. M. Allen and J. W. Cahn, “A microscopic theory for antiphase boundary motion and its application to antiphase domain coarsening,” *Acta Metallurgica*, vol. 27, no. 6, pp. 1085 – 1095, 1979.
- [66] K.-D. Li, Q. Wei, L. Wang, and W. Lu, “DYNAMICS OF NANOSCALE VOID-FIBER ASSEMBLY FORMATION IN IRRADIATED AMORPHOUS MATERIALS,” *International Journal for Multiscale Computational Engineering*, vol. 10, no. 1, pp. 109–116, 2012.
- [67] P. C. Millett, A. El-Azab, and D. Wolf, “Phase-field simulation of irradiated metals: Part II: Gas bubble kinetics,” *Computational Materials Science*, vol. 50, no. 3, pp. 960 – 970, 2011.
- [68] S. Rokkam, A. El-Azab, P. Millett, and D. Wolf, “Phase field modeling of void nucleation and growth in irradiated metals,” *Modelling and Simulation in Materials Science and Engineering*, vol. 17, no. 6, p. 064002, 2009.
- [69] P. C. Millett, S. Rokkam, A. El-Azab, M. Tonks, and D. Wolf, “Void nucleation and growth in irradiated polycrystalline metals: a phase-field model,” *Modelling and Simulation in Materials Science and Engineering*, vol. 17, no. 6, p. 064003, 2009.
- [70] P. C. Millett, A. El-Azab, S. Rokkam, M. Tonks, and D. Wolf, “Phase-field simulation of irradiated metals: Part I: Void kinetics,” *Computational Materials Science*, vol. 50, no. 3, pp. 949 – 959, 2011.
- [71] N. Nitta, M. Taniwaki, Y. Hayashi, and T. Yoshiie, “Formation of cellular defect structure on gas ion-implanted at low temperature,” *Journal of Applied Physics*, vol. 92, no. 4, pp. 1799–1802, 2002.
- [72] K.-D. Li, A. Perez-Bergquist, and L. Wang, “Computer simulation of radiation-induced nanostructure formation in amorphous materials,” *Nucl. Instr. Methods Phys. Res. B*, vol. 267, no. 18, pp. 3063–3066, 2009.

- [73] M. T. Robinson and I. M. Torrens, “Computer simulation of atomic-displacement cascades in solids in the binary-collision approximation,” *Phys. Rev. B*, vol. 9, pp. 5008–5024, Jun 1974.
- [74] T. de la Rubia and M. Guinan, “Progress in the development of a molecular dynamics code for high-energy cascade studies,” *Journal of Nuclear Materials*, vol. 174, no. 23, pp. 151 – 157, 1990.
- [75] C.-C. Fu, J. D. Torre, F. Willaime, J.-L. Bocquet, and A. Barbu, “Multiscale modelling of defect kinetics in irradiated iron,” *Nature Materials*, vol. 4, pp. 68–74, 2005.
- [76] M. T. Robinson, *MARLOWE Binary Collision Cascade Simulation Program, Version 15b, A Guide for Users*, 2002.
- [77] W. D. Wilson, L. G. Haggmark, and J. P. Biersack, “Calculations of nuclear stopping, ranges, and straggling in the low-energy region,” *Phys. Rev. B*, vol. 15, pp. 2458–2468, Mar 1977.
- [78] J. Biersack and L. Haggmark, “A monte carlo computer program for the transport of energetic ions in amorphous targets,” *Nuclear Instruments and Methods*, vol. 174, no. 12, pp. 257 – 269, 1980.
- [79] S. M. Foiles, *Comparison of binary collision approximation and molecular dynamics for displacement cascades in GaAs*. USDOE, 2011.
- [80] L. Bukonte, F. Djurabekova, J. Samela, K. Nordlund, S. Norris, and M. Aziz, “Comparison of molecular dynamics and binary collision approximation simulations for atom displacement analysis,” *Nuclear Instruments and Methods in Physics Research Section B: Beam Interactions with Materials and Atoms*, vol. 297, no. 0, pp. 23 – 28, 2013.
- [81] G. H. Kinchin and R. S. Pease, “The Displacement of Atoms in Solids by Radiation,” *Reports on Progress in Physics*, vol. 18, no. 1, p. 1, 1955.
- [82] G. Hobler, A. Simionescu, L. Palmetshofer, C. Tian, and G. Stinger, “Boron channeling implantations in silicon: Modeling of electronic stopping and damage accumulation,” *Journal of Applied Physics*, vol. 77, no. 8, pp. 3697–3703, 1995.
- [83] K. M. Klein, C. Park, and A. F. Tasch, “Modeling of cumulative damage effects on ion-implantation profiles,” *Nuclear Instruments and Methods in Physics Research Section B: Beam Interactions with Materials and Atoms*, vol. 59-60, Part 1, no. 0, pp. 60–64, 1991.
- [84] M. Jaraiz, J. Arias, L. Bailn, and J. Barbolla, “Detailed computer simulation of damage accumulation in ion irradiated crystalline targets,” *Vacuum*, vol. 44, no. 3-4, pp. 321–323, 1993.
- [85] R. Balluffi, S. Allen, and W. Carter, *Kinetics of Materials*. Wiley, 2005.

- [86] C. Lupis, *Chemical Thermodynamics of Materials*. Prentice Hall, 1993.
- [87] N. Metropolis, A. W. Rosenbluth, M. N. Rosenbluth, A. H. Teller, and E. Teller, “Equation of State Calculations by Fast Computing Machines,” *The Journal of Chemical Physics*, vol. 21, no. 6, pp. 1087–1092, 1953.
- [88] V. Tikare, E. R. Homer, and E. A. Holm, *A Model for Simulation of Coupled Microstructural and Compositional Evolution*, pp. 145–157. John Wiley & Sons, Inc., 2012.
- [89] E. R. Homer, V. Tikare, and E. A. Holm, “Hybrid Potts-phase field model for coupled microstructural-compositional evolution,” *Computational Materials Science*, vol. 69, pp. 414 – 423, 2013.
- [90] J. J. Cox, E. R. Homer, and V. Tikare, “Coupled microstructural-compositional evolution informed by a thermodynamic database using the hybrid potts-phase field model,” *MRS Proceedings*, vol. 1524, 1 2013.
- [91] S. Plimpton, C. Battaile, M. Ch, L. Holm, A. Thompson, V. Tikare, G. Wagner, X. Zhou, C. G. Cardona, and A. Slepoy, “Crossing the mesoscale no-mans land via parallel kinetic monte carlo,” 2009.
- [92] “Spparks kinetic monte carlo simulator.” <http://spparks.sandia.gov/>. Accessed: 2014-10-28.
- [93] E. HernándezRivera, V. Tikare, L. Noirot, and L. Wang, “Direct handling of sharp interfacial energy for microstructural evolution,” *Scripta Materialia*, vol. 92, no. 0, pp. 11 – 14, 2014.
- [94] Y. Ugurlu and D. Kaya, “Solutions of the calnhilliard equation,” *Computers & Mathematics with Applications*, vol. 56, no. 12, pp. 3038 – 3045, 2008.
- [95] S. Chapra and R. Canale, *Numerical methods for engineers*. No. v. 2 in McGraw-Hill international editions, McGraw-Hill, 1988.
- [96] E. Kreyszig, H. Kreyszig, and E. J. Norminton, *Advanced Engineering Mathematics*. Hoboken, N.J.: Wiley, 10th ed., 2011.
- [97] D. A. ANDERSON, J. C. TANNEHILL, and R. H. PLETCHER, *Computational Fluid Mechanics and Heat Transfer*. Washington, DC: Taylor & Francis, 2nd ed., 1997.
- [98] W. H. Press, S. A. Teukolsky, W. T. Vetterling, and B. P. Flannery, *Numerical Recipes in C (2Nd Ed.): The Art of Scientific Computing*. New York, NY, USA: Cambridge University Press, 1992.
- [99] J. J. Eggleston, *Phase-Field Models for Thin Film Growth and Ostwald Ripening*. PhD thesis, Northwestern University, 2001.

- [100] W. Ostwald, “Studien über die Bildung und Umwandlung fester Körper: Übersättigung und Überkaltung,” *Zeitschrift für Physikalische Chemie*, vol. 22, pp. 289–330, Feb. 1897.
- [101] “Ostwald ripening.” [http://en.wikipedia.org/wiki/Ostwald\\_ripening](http://en.wikipedia.org/wiki/Ostwald_ripening). Accessed: 2014-11-01.
- [102] J. A. Sethian, “Theory, algorithms, and applications of level set methods for propagating interfaces,” *Acta numerica*, vol. 5, pp. 309–395, 1996.
- [103] P. Smereka, “Semi-Implicit Level Set Methods for Curvature and Surface Diffusion Motion,” *J. Sci. Comput.*, vol. 19, pp. 439–456, Dec. 2003.
- [104] K. Kremeyer, “Cellular Automata Investigations of Binary Solidification,” *Journal of Computational Physics*, vol. 142, no. 1, pp. 243 – 262, 1998.
- [105] A. Delehouz, G. L. Vignoles, J.-F. Epherre, and F. Rebillat, *A New Kinetic Monte-Carlo/Volume-of-Fluid Solver for the Anisotropic Surface Recession of C/C Composites by Ablation*, pp. 55–64. John Wiley & Sons, Inc., 2014.
- [106] P. Boyanova and M. Neytcheva, “Efficient numerical solution of discrete multi-component CahnHilliard systems,” *Computers & Mathematics with Applications*, vol. 67, no. 1, pp. 106 – 121, 2014.
- [107] K. Russell, “Phase stability under irradiation,” *Progress in Materials Science*, vol. 28, no. 34, pp. 229 – 434, 1984.
- [108] M. Nastasi and J. Mayer, “Thermodynamics and kinetics of phase transformations induced by ion irradiation,” *Materials Science Reports*, vol. 6, no. 1, pp. 1 – 51, 1991.
- [109] R. Sizmann, “The effect of radiation upon diffusion in metals,” *Journal of Nuclear Materials*, vol. 69-70, pp. 386–412, 1978.
- [110] S. Rogers, “Radiation Damage to Satellite Electronic Systems,” *IEEE Transactions on Nuclear Science*, vol. 10, pp. 97–105, Jan 1963.
- [111] H. Wiedersich, P. Okamoto, and N. Lam, “A theory of radiation-induced segregation in concentrated alloys,” *Journal of Nuclear Materials*, vol. 83, no. 1, pp. 98 – 108, 1979.
- [112] P. Okamoto and L. Rehn, “Radiation-induced segregation in binary and ternary alloys,” *Journal of Nuclear Materials*, vol. 83, no. 1, pp. 2–23, 1979.
- [113] D. Potter, L. Rehn, P. Okamoto, and H. Wiedersich, “Ni<sub>3</sub>Si surface-film formation caused by radiation-induced segregation,” *Scripta Metallurgica*, vol. 11, no. 12, pp. 1095 – 1099, 1977.
- [114] T. Massalski, P. Subramanian, H. Okamoto, and L. Kacprzak, *Binary Alloy Phase Diagrams*. Materials Park, OH: ASM International, 2nd ed., 1990.



- [115] E. Hernandez-Rivera, V. Tikare, and L. Wang, “Simulation of Radiation-Induced Segregation by the Hybrid Potts-Phase Field Model,” in *Materials Science Forum*, vol. 783-786, pp. 1872–1879, in THERMEC 2013, 2014.
- [116] R. Nelson, J. Hudson, and D. Mazey, “The stability of precipitates in an irradiation environment,” *Journal of Nuclear Materials*, vol. 44, no. 3, pp. 318 – 330, 1972.
- [117] P. Wilkes, “Phase stability under irradiation a review of theory and experiment,” *Journal of Nuclear Materials*, vol. 83, no. 1, pp. 166 – 175, 1979.
- [118] J.-S. Cho, W.-K. Choi, K. H. Yoon, H.-J. Jung, and S.-K. Koh, “Changes of Wettability and Surface Energy of Polymer by keV Ar+ Ion Irradiation,” in *Symposium A Ion-Solid Interactions for Materials Modification and Processing*, vol. 396 of *MRS Proceedings*, 1 1995.
- [119] Z. Zhao, C. Wang, M. Li, L. Wang, and L. Kong, “The effects of pulsed Nd:YAG laser irradiation on surface energy of copper,” *Applied Surface Science*, vol. 252, no. 12, pp. 4257 – 4263, 2006.
- [120] M. Flanagan, “Mechanical Behavior of Ballooned and Ruptured Cladding,” Tech. Rep. NUREG-2119, U.S. Nuclear Regulatory Commission, Washington, DC, February 2012.
- [121] R. White, “The development of grain-face porosity in irradiated oxide fuel,” *Journal of Nuclear Materials*, vol. 325, no. 1, pp. 61 – 77, 2004.
- [122] V. Tikare and P. Medvedev, “Modeling of Fission Gas Release in LWR Fuel Using the Potts Kinetic Monte Carlo Technique,” September 2010. Presented at the LWR Fuel Performance Meeting in Orlando, FL, USA.
- [123] Cristina Garcia Cardona and Veena Tikare and Steven J. Plimpton, “Parallel simulation of 3D sintering,” *International Journal of Computational Materials Science and Surface Engineering*, vol. 4, no. 1, pp. 37–54, 2011.
- [124] G. Kaganas and J. Rest, “A physical description of fission product behavior fuels for advanced power reactors,” Tech. Rep. ANL-07/24, Florida International University and Nuclear Engineering Division, Argonne National Laboratory, Argonne, IL, September 2007.
- [125] L. Romano, G. Impellizzeri, M. V. Tomasello, F. Giannazzo, C. Spinella, and M. G. Grimaldi, “Nanostructuring in Ge by self-ion implantation,” *Journal of Applied Physics*, vol. 107, no. 8, p. 084314, 2010.
- [126] M. Tang, L. Colombo, J. Zhu, and T. Diaz de la Rubia, “Intrinsic point defects in crystalline silicon: Tight-binding molecular dynamics studies of self-diffusion, interstitial-vacancy recombination, and formation volumes,” *Phys. Rev. B*, vol. 55, pp. 14279–14289, 1997.

- [127] R. Balluffi, S. Allen, and W. Carter, *Kinetics of Materials*. Wiley, 2005.
- [128] W. Haynes, *CRC Handbook of Chemistry and Physics, 93rd Edition*. CRC Handbook of Chemistry and Physics, Taylor & Francis, 95th ed., 2014–2015.